國立中山大學材料科學研究所

博士論文

經高比率擠型 AZ31 鎂合金之低溫高速超塑性研發與變形機構之分析

Development and Analysis of Low Temperature and High Strain Rate Superplasticity in High-Ratio Extruded AZ31 Mg Alloys

研究生：林鉉凱 撰

指導教授：黃志青 博士

中華民國 九十四 年 四 月

Table of Content

LIST OF TABLES

LIST OF FIGURES

Abstract

There have been numerous efforts in processing metallic alloys into fine-grained materials, so as to exhibit high strain rate superplasticity (HSRSP) and/or low temperature superplasticity (LTSP). The current study is to apply the most simple and feasible one-step extrusion method on the commercial AZ31 magnesium billet to result in low temperature and high strain rate superplasticity (LT&HSRSP). The one-step extrusion was undertaken using a high extrusion ratio at 250-350^{o}C, and the grain size after one-step extrusion became ~1-4 μm. The processed AZ31 plate exhibited high room temperature tensile elongation up to 50%, as well as superior LTSP and/or HSRSP up to 1000%. Meanwhile, the AZ31 alloy was also conducted by equal-channel angular pressing (ECAP). It is demonstrated that an elongation of 461% may be attained at a temperature of 150^{o}C, equivalent to 0.46 T_m where T_m is the absolute melting temperature. This result clearly demonstrates the potential for achieving low temperature superplasticity.

A detailed investigation, using x-ray diffraction (XRD), electron back scattering diffraction (EBSD), and transmission electron microscopy / selected area diffraction (TEM/SAD), revealed different textures in the as-extruded and as-ECAP bars. These dominant textures were characteristic of $<10\bar{1}0>$//ED in the extruded bars and $<\bar{2}\,\bar{5}76>$//ED in the ECAP condition, where ED is the extrusion direction. The results show that the basal planes tend to lie parallel to the extrusion axis in the extruded bars but there is a rearrangement during ECAP and the basal planes become reasonably aligned with the theoretical shearing plane. As to the extruded plates, the {0002} planes tended to lie on the plane that contains the extrusion axis.

At different tensile temperatures, different deformation mechanisms would be dominant. Over the lower loading temperatures within 150-200^{o}C, the true strain rate sensitivity, m_t, after extracting the threshold stress is determined to be 0.28, suggesting that power-law dislocation

creep but the Q_t value is not related to any creep mechanism. It should be partly due to thermal activated dislocation slip mechanism. However, more data need to be tested systematically this part in the future study in order to define the correct deformation mechanism. As to the loading temperatures over 250-300^{o}C, the m_t value and the true activation energy for the extruded specimens are calculated to be ~0.4-0.5 and ~90-100 kJ/mol, implying that the major deformation mechanism is grain boundary sliding plus minor solute drag creep, with the rate controlling diffusion step being the magnesium grain boundary diffusion.

中文提要

本研究將商用 AZ31 鎂合金經簡易擠型加工後，可使該合金呈現低溫及高速超塑性。經擠型後的晶粒可細化至 1-4 μm。加工後的鎂板可得到 50%優異的室溫伸長量，在高速超塑性測試條件下也獲得 1000%的伸長量。同時鎂合金也利用等徑轉角擠製法(ECAP)來達到合金內部晶粒細化。在 125 及 150^{o}C 低溫條件下可達到 200%和 461%的伸長量，該測試溫度分別為 0.43 與 0.46 鎂合金熔點溫度。結果顯示經由加工後的鎂合金可以達到低溫超塑性。

利用 x-ray 繞射圖形,背向散射電子繞射(EBSD)以及穿透式電子顯微鏡(TEM)選區繞射的方法，針對擠型及等徑轉角擠製後的材料，研究其織構行為及高角度晶界之比率。經一系列實驗分析，從結果可觀察到擠型棒材的主要織構為<10$\bar{1}$0>平行擠型方向，等徑轉角擠製後的織構為<$\bar{2}$ $\bar{5}$76>平行擠型方向。至於擠型板材，主要織構則為{0002}基面平行擠型方向。

本實驗透過不同的拉伸溫度測試，觀察不同溫度區間的變形機構。在 150 ~ 200^{o}C，變形機構以差排滑移為主，計算後之活化能所對應機構為熱活化差排滑移。在 250 ~ 300^{o}C 之測試區間，變形機構則以晶界滑移為主，控制速率之主要擴散步驟為晶界擴散。

誌謝

再多的言語也無法表達內心對於恩師 黃志青老師的感激。吾師的學識淵博及待人處事的氣度都讓學生深深地佩服，並以身為黃幫一員為榮。六年的研究生活裡，從吾師身上所學到為學做人的大智慧將令我終生受用不盡。另外，也感謝學生的口試委員 何扭今教授、高伯威教授、黃永茂教授、侯春看教授以及張六文博士，在論文審查過程中，給予學生的教導與指正，由於您們的寶貴意見使得本論文更加充實，在此對老師們致上我最由衷的謝意。

也感謝所上各實驗室的技術員王良珠學姊、陳貴香小姐、王國強先生、林明政先生、古錦松學長、李秀月小姐、行政上朱小姐、顏小姐以及熱心的華大哥。謝謝您們的協助及幫忙。

在黃幫大家庭裡，所需謝謝的人員實在太多了，包括已畢業的一清、建超、木城學長及凱琳、佩汝學姊在學識的開導；博班的英博、敬仁在實驗及生活上的幫忙以及子翔、志溢、宇庭、家豪、政信和碩一學弟的鼓勵都讓我留下美好的回憶。另外，也感謝國科會提供學生留學獎學金、USC T. G. Langdon 教授提供學生在美期間儀器使用以及學問上的解惑。Monash University Chamini Mendis 提供鎂合金 TEM 試片製作方法，瘦忠義學長、吳玉娟同學及丁仕旋學弟在 Instron 及 TEM 的指導與協助都讓本論文得以順利進行。同時也謝謝我多年的好友義凱、以德、振福、志龍、永興、之德在我低潮時總是適時的鼓勵我。謝謝你們，好友。

最後在這感謝我最親愛的家人由於你們的支持，並且給予我一個很溫暖的家，可以讓我無後顧之憂而專注於學業上。並且謝謝雪娥一直默默地支持著我，不斷地鼓勵我。謹以此文獻給所有關心愛護我的人。

林鉉凱

2005.05.25

於 高雄西子灣

Chapter 1

Introduction

1.1 The basic character of superplastic materials

Superplasticity is referred to the ability of certain materials to attain a large tensile elongation without pronounced local necking within the gauge length prior to failure. In general, under uniaxial tension, a failure elongation over 200% is usually an indication of superplasticity [1]. Materials exhibiting superplasticity include metals, ceramics, intermetallics, and composites [2-3]. The high ductility can be utilized in terms of superplastic forming (SPF) routines. In industry, the SPF technology offers an easy mean in forming complicated shapes. Meanwhile, it can result in decreased spring back phenomenon, and also reduced cost from simplified forming practices with minimum welding or fastening.

The flow stress of the superplastic materials has been seen to be highly sensitive to the deformation rate at elevated temperatures, and there is a relationship between the flow stress and strain rate. Superplastic materials have the common characters in exhibiting high values of strain rate sensitivity, m, during deformation. The relationship, under the most simple power low behavior, is characterized by the constitutive equation,

$$\sigma = K\dot{\varepsilon}^m, \tag{1-1}$$

where σ is the true flow stress, K a material constant, and $\dot{\varepsilon}$ the true strain rate. The exponent m is the strain rate sensitivity of the material, and defined as

$$m = \frac{\partial \ln \sigma}{\partial \ln \dot{\varepsilon}} = \frac{\dot{\varepsilon}}{\sigma}\frac{d\sigma}{d\varepsilon} \quad . \tag{1-2}$$

Most metals and alloys normally exhibit m<0.05 as tested at room temperature and strain rates less than 10^1 s^{-1}, but superplastic materials possess m values greater than 0.3 at elevated temperatures.

The typical superplastic materials need to satisfy the following requirements [4-5]:

(1) Fine and stable grain size: Typically the grain sizes are less than 10 μm for metals and less than 1 μm for ceramics.

(2) High tensile temperature: The loading temperature for conventional high temperature superplastic materials is usually around 0.8 T_m (the melting point expressed in Kelvin), because superplasticity is related to the diffusion-controlled process. To maintain a fine grain size under high temperature SPF regimes, a second phase to impede grain growth is generally needed.

(3) Low strain rate: For conventional low strain rate superplastic materials, the strain rate is below $1x10^{-3}$ s^{-1}.

The factors that may be of concern with respect to superplasticity of the materials are listed below:

(1) The character of grain boundary: The high angle and random boundaries are available for carrying out grain boundary sliding (GBS); but the low angle boundaries are not. The superplastic materials are first processed by various thermomechanical treatments (TMT) so as to refine the grain sizes, but the resulting grain boundaries may or may not be high angle boundaries. Whether the low angle boundaries can be successfully transformed into high angle boundaries ready for GBS is another key issue for the development of superior superplastic materials.

(2) The relationship among stress, strain and strain rate: As stated above, the strain rate sensitivity m is important for superplasticity. A higher m value will usually accompanied by a

higher tensile superplastic elongation. In addition, the relation between stress and strain, or the work hardening exponent, also impose positive influence on the tensile elongation, though the effect becomes less obviously at elevated temperatures. Higher strain rate sensitivity and work hardening exponent will both reduce the tendency of local necking during tensile deformation.

(3) The tendency of grain growth: In superplastic loading range, a rapid grain growth will obstruct continuous and smooth GBS.

(4) The tendency of cavitation: Cavities are inevitable during tensile deformation to large strains, but the control of cavity growth and coalescence rates will prevent premature failure.

1.2 Types of superplasticity

There are a number of different types of superplastic behavior, including the fine structure superplasticity, internal stress superplasticity, high strain rate superplasticity, low temperature superplasticity, coarse-grained superplasticity, and some other mechanisms.

1.2.1 Fine-structure superplasticity (FSS)

There are three principle modes of deformation explaining the creep behavior of FSS [6]: (1) diffusional flow, (2) GBS accommodated by diffusional flow, and (3) GBS accommodated by dislocation slip. An accommodation process to accompany GBS is prerequisite or extensive cavities particularly near the triple junctions would cause premature fracture. The accommodation process that could avoid early fracture might be grain-boundary migration, diffusional flow, or some dislocation slip processes.

The high-temperature deformation behavior of fine-grained materials might reveal three stages in their stress and strain rate curves, i.e., regions I, II and III as shown in Fig. 1-1 [4][6]. There are two competing independent process in explaining the trend of Fig. 1-1. The dashed line indicates the creep rate of a fine-grained material when GBS (with an operating threshold stress) is the deformation process and the solid line represents the creep rate when dislocation creep is the rate controlling process. These two processes are thought to be independent or parallel, therefore the faster one is the rate-controlling route. The rate-controlling process at region III is power-law creep. The threshold stress and lower ductility can be observed at region I with lower m-values of ~0.2. At intermediate strain-rates (region II) the strain rate sensitivity values are the highest, around 0.5 or even higher. The tensile elongation can achieve several hundreds or thousands percent. The experimental evidence offered by the offset of scratch lines on the sample surface after tensile test support the activation of GBS [7].

Normally, the strain rate is inversely proportional to the grain size, therefore a simple relationship between the strain rate and grain size can be defined as [8]

$$\dot{\varepsilon} \propto d^{-p} \exp(-1/T), \tag{1-3}$$

where the grain size exponent p may be 2 or 3, dependent on the dominant diffusion process involved. Thus, the refinement of grain size will directly result in an increase in working strain rate for optimum superplastic performance. In addition, the finer grain size under a fixed strain rate will correspond to a lower superplastic temperature or a lower flow stress.

1.2.2 Internal stress superplasticity (ISS)

Internally stress induced superlasticity is developed upon repeated thermal cycling. In general, the internal stress induced superplastic materials need not to be fine grained and the

strain rate sensitivity usually equals 1. In most cases, there are some guidelines [6]. (1) The polymorphic materials undergo phase transformation during thermal cycling or pressure cycling procedures. (2) Pure metals or single phase alloys need to have anisotropic thermal expansivity coefficients. And (3) during thermal cycling procedures, materials, which have different thermal expansivities of constituents, will lead to internal stress; such internal stresses will promote extensive deformation during consecutive thermal cycles.

1.2.3 High strain rate superplasticity (HSRSP) or low temperature superplasticity (LTSP)

In fact, both high strain rate superplasticity and low temperature superplasticity are extensions of FSS. HSRSP is an important topic because traditional superplasticity would proceed at low strain rates about 10^{-4} to 10^{-3} s^{-1}. In contrast, HSRSP takes place at much faster strain rates of 10^{-1} to 10^{1} s^{-1}, an increase of 1000 times in speed. Grain size is obviously the prime parameter. Table 1-1 summarizes the typical HSRSP materials reported since its first discovery in 1984 [9-20].

On the other hand, the superplastic temperature is typically around 0.8 T_m. As for the magnesium alloys (T_m~650^{o}C or 923 K) and aluminum alloys (T_m~660^{o}C or 933 K), the superplastic temperatures for conventional superplastic alloys are about 500^{o}C or 733 K (~0.8 T_m). Due to severe grain refinement, the superplastic temperature can be lowered down to about 0.50-0.65 T_m, or 200-350^{o}C for magnesium or aluminum alloys. For nano-grained materials (~20 nm) fabricated by electrodeposition [21] or severe deformation by torsion [21-23], the superplastic temperatures may be reduced to 0.3 T_m. Table 1-2 lists the reports on LTSP since its first publication in 1986 [24-29].

1.2.4 Coarse grained superplasticity (CGSP)

There are some materials that show superplastic-like behaviors in coarse grained materials such as some Class I solid solution alloys [30]. In certain alloys, creep is controlled by the glide mechanism because solute atoms impede dislocation motion. It is also called as the solute drag mechanism [31]. The dislocation slip itself determines the deformation rate, therefore the grain size is no longer the only important factor to attain larger elongation, as in the GBS mechanism. The strain rate sensitivity is usually equal to 0.33 and the tensile elongation obtained is about 400%.

Recently, coarse grained superplasticity has also been observed in alloys with initial grain sizes of ~300 μm [32]. The grain size became smaller to less than 100 μm upon tensile straining via dynamic recrystallization. A few hundreds of tensile elongation can be achieved. It appears to be an interesting research topic.

Liu et al. [33-34] studied the superplastic behavior of coarse-grained AZ31 magnesium alloys tested at $0.5x10^{-2}$ s^{-1} and 350~500^{o}C. It was found that the average initial grain size of 250 μm was reduced down to 50 μm after tensile deformation, as the deformation temperature was below 400^{o}C. If the temperature was above 400^{o}C, the grain size changed to about 100 μm. The maximum elongation of 170% has been obtained at 500^{o}C and $5x10^{-3}$ s^{-1}. Most of the grain boundaries were high angle ones. Because of dislocation emission and absorption from the grain boundaries, the dislocation density after deformation was found to be low. This study implied that grain boundary migration resulted in grain growth and grain refinement resulted from dynamic recrystallization. The microstructural evolution was attributed to continuous recovery and recrystallization, and the suggested deformation mechanisms during tension included power law creep and diffusional creep.

1.2.5 Other mechanisms

Sufficient tensile elongations can possibly achieved in some coarse grained materials when loaded at low strain rates with m=1 through Coble creep (grain boundary diffusion controlled), Nabarro-Herring creep (lattice diffusion controlled), and Harper-Dorn creep (slip controlled).

1.3 The development and application of magnesium alloys

Because of resource shortage and strict environment regulations, the utilization of lightweight materials in many areas of transportation vehicles becomes essential. Magnesium is the lightest metal used as the basis for constructional alloys, though heavier than Li and Be but these two are highly active and the latter is toxic. Meanwhile, the use of magnesium in electronic industry is growing steadily, and enhanced by the light and small requirement for the computer, communication and consumer (3C) electronic products. As a structural material, magnesium has numerous advantageous over steels, cast irons, copper, aluminum alloys and engineering plastics, as compared in Table 1-3 [35]. The advantages of magnesium and magnesium alloys are listed as below.

(1) Lower density: In terms of density, Mg is about 2/3 of Al, only 20% of steel, and is the lowest of all metallic constructional materials.

(2) Better heat dissipation: In comparison with to plastics, magnesium has excellent heat dissipation capability.

(3) Good damping and crash resistance: The damping capability of magnesium is better than plastics and aluminum, and the crash resistance is much superior to plastics.

(4) The thickness: The thickness of Mg enclosures used for 3C products can be reduced to 0.5 mm for sufficient strength.

(5) Good castability: Mg can be easily die cast into complicated shape with minimum wall thickness.

(6) Excellent electromagnetic shielding capabilities: Plastic cannot shield electromagnetic wave generated by the 3C electronic products, but Mg can. A thin Mg wall can effectively shield electromagnetic wave.

(7) Recycling abilities: The same as Al, Mg can be easily and economically recycled through proper remelting procedures. This factor imposes a strong benefit over the competing plastics.

Due to these characters, magnesium alloys have potentials in replacing the aluminum alloys or plastics to become the main material for electronic products. In spite of the numerous advantages, however, magnesium alloys generally exhibit poor workability because of their hexagonal close-packed (HCP) crystal structure. Therefore, it is essential to improve the workability for developing feasible forming technologies as currently used in Al and steel industry.

There have been numerous forming methods developed for Mg alloys, including die-casting, thixomolding and rheomolding [36-38]. Die-casting has been a principal technique over the past ten years for the fabrication of magnesium alloys for vehicles and 3C enclosures, due to the high productivity, strength, quality and dimensional control. However, the yield rate currently is usually around 30%, so that a high percentage of waste materials will be generated which causes great need for in-site recycle capability. The fabrication has also been performed by thixomolding, a technique similar to the injection molding used for plastics. Thixomolding is a much more expensive routine compared with die-casting, but the yield rate and the product quality are both superior.

Fabrication by conventional plastic deformation means used for Al and steel factory, such as stretching, forging, stamping, tubing, press forming, press forging, or superplastic forming, have also been pursued for Mg forming. It is well known that the wrought materials are typically more strong and ductile than the cast counterparts [39]. For this reason, the wrought typed (or even cast typed) Mg alloys have been processed by various means so as to be suitable for subsequent plastic deformation. Among the above plastic deformation means, press forming [40] and press forging are actually a variation form of superplastic forming, the former two both use upper tools to press or forge the worked piece at elevated temperatures while the latter usually use uniform gas bulging. All these three techniques can greatly improve the quality of the products and can fabricate a hard-to-form material into complex shapes. Therefore these methods can reduce the cost and save overall forming time.

1.4 Properties of magnesium alloys

According to recent research literature, different solute additions or contents, thermomechanical treatments, and process will all result in variations in material properties. In what follows, a review on the grain size, solute additions and contents, and process means is presented.

1.4.1 The classification of magnesium alloys

Before discussing magnesium alloys, the physical and mechanical characteristics need to be realized, as shown in Table1-4 [41]. The designations of Mg alloys are based on the solute elements and contents. For example, the most common and low priced “AZ91” Mg base alloy means that the alloy contains solute elements of Al (A) for nominally 9 wt% and Zn (Z) for

nominally 1 wt%. Other important Mg alloys include the ZK (Zn and Zr), AM (Al and Mn) and WE (Y and Re) systems. Table 1-5 [42] represents the standard four-part ASTM designation system of alloy and temper for the magnesium alloys.

1.4.2 Grain size

Narutani et al. [43] reported the Hall-Petch relationship for magnesium alloys as

$$\sigma = \sigma_0 + kd^{-1/2}, \tag{1-4}$$

where σ is the flow stress, d the grain diameter, σ_o material constant, and k the slope equal to 280-320 MPa.$m^{1/2}$. It should be mentioned that the k slope or the grain size strengthening efficiency of the Mg alloys is much higher than that of the Al alloys (~68 MPa.$m^{1/2}$), meaning that grain refinement in Mg alloys will be more beneficial [44]. Lahaie et al. [45] demonstrated that grain refinement in AZ91 to about 1 μm might provide an excellent property with high strength and light weight. Nussbaum et al. [44] applied rapid solidification processes to AZ91 magnesium alloys and then deformed the resulting alloys under various extrusion temperatures, extrusion ratios and ram speeds. The structure in the as-extruded alloys possessed fine equiaxed grains. The relationship between grain size and mechanical properties is listed in Table 1-6 [45]. The hardness values of ingots of pure Mg, AZ31 (Mg-3Al-1Zn) and AZ91 (Mg-9Al-1Zn) are 28, 47 and 60 kg/mm^2, respectively. According to this result, solution hardening by Al is apparent. Yue et al. [46] have shown that the mechanical properties and the fatigue strength for AZ91 would be improved as the grain size decreased. Mabuchi et al. [17] also showed a finer grain size in a powder metallurgy (PM) processed alloys, compared to the ingot metallurgy (IM) ones.

1.4.3 Solute content in magnesium alloys

In fact, the addition of different solute contents was effective in improving mechanical properties. The effects of various solute additions on the mechanical properties are listed in Table 1-7 [41]. The most common Mg alloys used in vehicles and 3C products are the AZ series alloys, containing various portions of Al and Zn. The addition of Al into Mg matrix was mainly aimed for solution and/or precipitation hardening, while the inclusion of a small amount of Zn will improve casting capability. So far, the best systematic study on the addition of Al and Zn in the AZ or ZA series alloys was given by Kaneko et al. [47] in 1999. They fabricated a number of Mg-Al-Zn ternary alloys containing 1 to 10% Al and 5 to 12% Zn by both rapid solidification and powder metallurgy processes. The strengths of the resulting alloys were primarily originated from the dispersion of second phase particles. In their paper, the AZ105, ZA84, AZ88, ZA101 and ZA128 alloys were first processed by rapid solidified PM or rapid solidified IM routes, and then both extruded at 300^{o}C with a reduction ratio of 100:1. The hardness, tensile properties and superplastic properties of the PM and IM materials were discussed [47].

(a) Hardness of the PM and IM materials

Hardness of the as-extruded PM materials was always higher than that of the IM ones. Also, increasing the Al+Zn content would increase the hardness, resulting from the denser and finer dispersion of the second phase particles. The hardness would decrease appreciably while the temperature increases through recovery, recrystallization and grain growth. Figure 1-2 shows the variation of hardness with increasing annealing temperature.

(b) Tensile properties of the PM and IM materials

In general, the tensile strength (UTS) of those of cast materials of AZ105, ZA84, AZ88, ZA101, ZA124 and ZA128 ranges 110-120 MPa, which is lower than that of the above PM or IM materials. The UTS will increase to 170-319 MPa when the materials were further extruded. For the PM ZA128 alloy, a high strength of 447 MPa has been attained. The tensile strength of

the PM materials was consistently larger than that of the IM ones by ~50 MPa. Figure 1-3 shows the tensile strength and elongation of the PM and IM materials at different test temperatures. The tensile strength of the PM materials became lower than that of the IM materials at 200 and 300^{o}C due to the operation of GBS, the reversed as the trend at room temperature.

(c) Superplastic properties of the PM materials

The PM materials were tensile tested at 200 and 300^{o}C at various strain rates between $2x10^{-4}$ to $2x10^{-1}$ s^{-1}. All materials showed the maximum superplastic elongation at $2x10^{-2}$ s^{-1}. The maximum elongation values were about 900% for AZ105, 800% for AZ88, 500% for ZA124 and ZA128 at 300^{o}C. It seemed that a higher Al content would lead to a higher superplastic elongation, possibly due to the pinning effect from the β ($Mg_{17}Al_{12}$) phase. Over the experimental range the m value tended to increase with increasing strain rate and reached a high level of 0.65.

The mechanical properties of pure Mg and an Mg-0.9%Al alloy at room temperature could be improved by imposing these materials to severe plastic deformation. According to their experimental results, it was concluded that the presence of dilute Al lead to higher ductility under the un-deformation condition, and ECAP for one or more passes was effective in increasing elongations [48].

1.4.4 Grain refining processes

In order to gain excellent mechanical properties, different processes can be applied to refine the grain size, which would in-turn affect the superplastic properties. In what follows, the rapid solidification, powder metallurgy, rolling, equal channel angular pressing, forging, and extrusion will be discussed separately.

1.4.4.1 Rapid solidification (RS)

Solberg et al. [49] studied the superplastic properties of conventionally cast and rapidly solidified magnesium alloy AZ91. Through rapid solidification, a foil of 100 μm in thickness and 12 mm in width was made. The RS material was then subjected to extrusion to a ratio of 40:1 at 300^{o}C. Samples of the conventionally cast material was also conducted under similar conditions. The grain size of the conventionally cast material was about 3-20 μm after extrusion, but that of the RS material was ~1.2 μm. The microstructure could maintain stable at elevated temperatures below 300^{o}C. The grain size after tempering for 21 h at 300^{o}C still remained about 1.9 μm. The tensile elongation of the RS and conventionally cast materials were 1000% and 170% at 3.3x10^{-3} s^{-1} and 300^{o}C, respectively. The superplastic behavior of the RS materials was much better than that of the cast counterparts. In both materials cavities aligned in the tensile direction were formed during superplastic deformation. A fewer pores were present in the RS materials. A high density of pores would result in reduced strength and ductility at room and elevated temperatures. Although, the RS process might render outstanding superplastic performance, it is a complicated and expensive process, and produces only small or thin specimens not suitable for common industry applications.

1.4.4.2 Powder metallurgy (PM)

Mabuchi et al. [17] studied for the PM-AZ91, IM-AZ91, PM-ZK61 and IM-ZK60 alloys processed by the PM and IM routes. The grain sizes of the magnesium alloys after extrusion to a ratio of 100:1 at 300^{o}C became much finer. The four specimens were further received static annealing at 300^{o}C for half hour, and the grain sizes were 1.4 μm, 5 μm, 1.4 μm and 2.4 μm, respectively. It is obvious that the PM process could render a smaller grain size than the IM ones

under the same processing routes. The PM Mg alloys exhibited HSRSP, while the IM alloys did not. The origin of HSRSP at 300^{o}C in the PM Mg alloys was considered to be different from the previous argument for HSRSP at high temperatures related to the presence of a liquid phase [17].

1.4.4.3 Rolling

Mohir and his co-workers [50] reported microstructural evolution and superplasticity of a rolled AZ91 alloy. The AZ91 alloy rolled at 400^{o}C and constant velocity tensile tests were carried out at 300^{o}C and 1.5x10^{-3} s^{-1}. The grain size of the as-rolled AZ91 alloy was 39.5 μm but that of the specimen deformed to a true tensile strain of 0.6 became 9.1 μm. The grain refinement was considered to result from dynamically continuous recrystallization during tension. Because of grain refinement, GBS occurred significantly and the maximum elongation of 604% could be attained. Lin [51] and Huang [52] have also tested the extruded and then rolled AZ91 alloys in tension at 300^{o}C and 1x10^{-3} s^{-1}. The grain size was reduced from 13 to 2.5 μm and the grain refinement was also attributed to dynamical recrystallization.

1.4.4.4 Equal channel angular pressing (ECAP)

The ECAP is a new method to produce an ultrafine-grained structure by shearing the sample through a channel. A schematic drawing of ECAP is illustrated in Figure 1-4. It is recognized that the origin of superplasticity is associated with a fine grain size [53]. Smaller grain size may cause superplasticity at higher strain rates or at lower temperatures. The ECAP method has been efficiently used in reducing the grain size and improving the LTSP or HSRSP performance. With the significant success achieved on the Al base alloys [54], there have been however very limited reports on the advances in Mg alloys [48,55-58].

Yamashita et al. [48] applied ECAP onto the pure Mg and an Mg-0.9%Al alloy. The ECAE process seemed to offer a useful improvement in both strength and ductility; however, such improvement was attained after only one pass through ECAP and there was little improvement with later passes.

Mabuchi et al. [55] have studied an ingot rod of AZ91 solution-treated at 415^{o}C for 2 hours. The grain size after 8 passes of ECAP (ε=8.05) at 175^{o}C was 1 μm. Tensile tests were conducted at $2x10^{-5}$-$1x10^{-3}$ s^{-1} and 175 and 200^{o}C. A LTSP elongation of 661% was obtain at 200^{o}C and 6.2 x 10^{-5} s^{-1}. The grain boundaries of the ECAP processed fine-grained AZ91 alloy were revealed to be of a non-equilibrium state. The grain boundaries were mostly curved or wavy and corrugated with regular or irregular arrangements of facet and steps, and the crystal lattice were seriously distorted near the grain boundaries [57]. The sample was then annealed at 225^{o}C for 12 hours. The grain boundaries changed from the non-equilibrium into the equilibrium state, and the grain size grew from 0.7 μm to 3.1 μm. The alloy with an equilibrium grain boundary structure exhibited higher superplastic elongations than the alloy with non-equilibrium grain boundaries. This was due to the fact that the accommodation process for GBS was hampered by the long-range stresses associated with the non-equilibrium grain boundaries [57]. Matsubara et al. [62] showed a cast Mg-9%Al alloy through the use of a two-step processing procedure that involves the application of extrusion and ECAP. An initial grain size of the Mg-9%Al alloy is about 50 μm after casting but this is reduced to ~12 μm after extrusion and this is further reduced to ~0.7 μm when the extruded alloy is undertaken using ECAP for 2 passes at 200^{o}C.

Similar ECAP work was performed on the AZ31 Mg alloy at 200^{o}C, also resulting in fine grain size around 1 μm [58]. The ECAP AZ31 specimens were further annealed at 300^{o}C for 24 h in order to form well-defined equiaxed grains with the desired grain orientation; and the room temperature tensile elongation reached an outstanding level of ~50%.

Table 1-8 [59-68] shows a summary of the major investigations of Mg alloys using ECAP. Ultrafine grain sizes cannot be achieved in pure Mg or Mg-based solid solution alloys when pressing in a cast or rolled condition. An additional extrusion step is required in order to produce a reasonably small grain size (typically ~10-20 μm) that can be even further refined using ECAP. This two-step process is designated EX-ECAP (Matsubara et al. [62]). When using extruded Mg alloys, the grain size is typically refined to ~1 μm. This value is significantly larger than the grain sizes of ~0.2-0.3 μm associated with many Al-based alloys.

Attempts have been made to achieve superplasticity in Mg alloys after ECAP and the results are summarized in Table 1-9. Some of the ductilities are very high, for example, 1083% in ZK60 after ECAP (Watanabe et al. [64]). However, all of these high elongations occur at fairly slow strain rates and, without exception, all of the results were obtained at strain rates below 10^{-2} s^{-1}. Therefore, none of these results demonstrate the occurrence of high strain rate superplasticity, which requires a strain rate at or above 10^{-2} s^{-1}. The testing temperatures are typically in the vicinity of 200^{o}C but this temperature is still slightly above 0.5 T_m and therefore it is not within the generally recognized low temperature superplasticity. The best evidence to date for the occurrence of low temperature superplasticity at reasonably rapid strain rate is the elongation of 391% reported for a Mg-Li-Zn alloy tested at 150^{o}C with a strain rate of 1×10^{-3} s^{-1} (Yoshida et al. [67]).

The properties of the as-ECAPed material at room temperature are summarized in Table 1-10. Although the YS and the UTS are reasonably high, the total elongations are low and often below 20%.

Table 1-11 summarizes the results from other investigations [69-77] where there have been

attempts to achieve superplastic properties without the use of ECAP. Some of these results show high elongations that fall just within the strain rates associated with high strain rate superplasticity. In general, the results are fairly similar to those achieved through ECAP processing. It can be concluded that the results to date do not clearly demonstrate any major advantage in using the ECAP process. Nevertheless, more careful and detailed experiments are needed to more fully characterize the capabilities of the ECAP processing procedure.

1.4.4.5 Forging

Chino et al. [78] have conducted a series of examinations on the as-received and as-extruded AZ31 specimens, both followed by forging. The as-received specimens consisted of both elongated coarse grains and equiaxed small grains, and the as-extruded ones consisted of equiaxed small grains. The characteristics of open-die forging and the relation between resulting microstructure and mechanical properties were investigated. The as-received and as-extruded specimens were forged at 50 to 400^{o}C, from 18 mm down to 2.5 mm in thickness at forging temperatures above 150^{o}C. If the grains were first refined by extrusion prior to forging, the specimen could be forged without surface cracks. However some cracks for the as-received specimens were observed at the edge of the specimens when forged at temperatures below 300^{o}C. The grain size of the forged specimens decreased with decreasing forging temperature, and the tensile strength of the forged specimens increased.

1.4.4.6 Extrusion

Lee et al. [79] investigated the tensile properties and microstructural evolution of the hot extruded AZ91 alloy with and without the reinforcement of SiC particles. The extrusion parameters considered included the extrusion ratio and extrusion temperature. This study

reported the composite and alloy both contained fine equiaxed grains due to dynamic recrystallisation during hot extrusion. The tensile strength of both the composite and alloy increased with increasing extrusion ratio, and the former was higher than the latter in strength.

Mabuchi et al. [73] also extruded the machined chips of an AZ91 alloy at 300, 400 and 480^{o}C with an extrusion ratio of 100:1. The grain sizes of the alloys extruded at these three temperatures were 7.6, 15.4 and 66.1 μm, respectively. Machined chips after extrusion showed both high room-temperature ultimate tensile strengths of 320-410 MPa and elongations to failure of 5~12%. Over the test range (300^{o}C and $2x10^{-5}$-$2x10^{-1}$ s^{-1}), the m values decreased with increasing extrusion temperature, ranging from 0.5 down to 0.2. Furthermore, the tensile elongations at 300^{o}C decreased from 310% to 30%. According to this study, the specimens extruded at 300^{o}C exhibited reasonable superplasticity. Because the magnesium alloys are unfavorable to be rolled at lower temperatures, the extrusion process becomes a good method for refining grains. Mostly rod-shaped products were unfavorable for large quantity applications. Therefore, the plate extrusion method may be feasible and simple for industry practices.

Lin and Huang [52] reported that the most simple and feasible one- or two-step extrusion methods with a high extrusion ration on the AZ91 alloy could result in superior low temperature superplasticity. The grain size was effectively reduced to ~2.5 μm after extrusion, resulting in superior low temperature superplastic elongation of ~1200% at 300^{o}C and $1x10^{-3}$ s^{-1}.

1.4.4.7 Double extrusion and cyclic (reciprocal) extrusion

In order to homogenize and refine the microstructure, the ZK60/17vol%SiC composite subjected to simple extrusion was further extruded. This further extruded process is denoted as double extrusion. The grain size of the magnesium composite after double extrusion became 1.7

μm. The annealed grain sizes increased slightly below 350^{o}C, but they grew above 350^{o}C. In addition, the material showed an m-value of 0.5 and an activation energy of 81 kJ/mol in the superplastic region. According to the results, it implied that the domination mechanism was GBS accommodated by a grain boundary diffusion process. The maximum elongation occurred at 350^{o}C and 1x10^{-1} s^{-1} was 450%. Therefore, the material exhibited HSRSP [80].

Chang [74] applied reciprocal extrusion to process the AZ91 alloy. Reciprocating processes were performed on the billets to 1, 5 and 10 times at 275^{o}C, respectively. Increasing extrusion times can refine the grain of alloys to 3.5 μm. The optimum superplastic condition was occurred when using the reciprocal extrusion at 275^{o}C for 10 times. The maximum elongation attained was about 1000%, as tested at 300^{o}C and 1x10^{-3} s^{-1}.

1.4.4.8 A two-step processing route

A two- or three-step processing route is good method to produce fine-grained material especially; the simple equipment will be needed. Galiyev [81] reported the ZK60 alloy after three thermomechanical processing involving extrusion; compression and isothermal rolling exhibited excellent superplastic ductility. An elongation of 1330% was achieved at a temperature of 250^{o}C and an initial strain rate of 1.4x10^{-4} s^{-1}. Matsubara [62] showed a new processing procedure was applied a cast Mg-9% Al alloy and this processing route consisted of extrusion and ECAP. The grain size can be efficiently refined after the processing route combining extrusion and ECAP. After superplastic tensile testing, it is shown that the alloy is capable of producing both low temperature superplasticity and high strain rate superplasticity. Lin [52] also reported an AZ91 Mg alloy processed by two-step extrusion. The initial grain size in the purchased AZ91D ingot was 125 μm, and that after two-step high extrusion ratio extrusion became ~2.5 μm, resulting in excellent superplastic elongation up to ~1200% at 300^{o}C and

$1x10^{-3}$ s^{-1}.

1.4.5 Room temperature tensile properties

It is well known that magnesium alloys exhibit limited ductility because of their HCP structure. It is difficult to manufacture structural components with a wrought alloy. If the magnesium alloys could obtain larger elongations at about 100^{o}C or even room temperature, forming and injection molding will become practical techniques to fabricate a hard-to-form material into complex shapes.

Mabuchi et al [73] in 1995 reported that the AZ91 magnesium alloys conducted by extrusion would exhibit improved mechanical properties. Cast materials generally exhibited a lower stress of 121 MPa and elongation of 3% at room temperature. The extruded material showed a good combination of a high stress of 400 MPa and elongation of 12% [82]. Magnesium alloys containing different elements were investigated [83,84]. The elongation-to–failure of AZ31 and WE43 was seen to be generally higher than those of AZ91. This phenomenon is owing to the fact that the structure of the magnesium matrix is HCP but that of $Mg_{17}Al_{12}$ phase is BCC, leading to the fragility of the Mg/$Mg_{17}Al_{12}$ interface. Therefore, the microcrack initiation starts from the Mg/$Mg_{17}Al_{12}$ interface [87-88].

A summary of tensile elongation of Mg based materials at room temperature is presented in Table 1-9 [82-86].

1.5 Superplastic behavior in Magnesium alloys

The research and development for HSRSP and LTSP in the Mg base alloys have been newly

emerged over the past five years, predominantly in Japan. This is because that the applications of Mg alloys were gradually shifted and spread from the transportation industry only into the rapidly growing 3C industry. The fabrication of light, thin and small enclosures for 3C products needs to be fast and economic, so that the conventional low strain rate and high temperature superplasticity would be no longer accepted, as ever did in the aerospace and aircraft industry. In general, HSRSP is defined as superplasticity occurring at strain rates at or greater than 10^{-2} s^{-1}. This will allow an increment in fabrication speed by 100-1000 times. On the other hand, LTSP at temperatures lower than $0.6T_m$ is attractive since the lower working temperature would directly lead to lower energy consumption, longer life time for tools and dies, easier handling and operation, and much better post-form mechanical properties. The following sections introduce the limited reports on the related topics.

1.5.1 HSRSP in magnesium alloys

Although there have been a number of publications reporting the HSRSP in the Mg base composites at temperature above the temperatures for incipient partial melting [89-90], there are very limited demonstrations on the HSRSP behavior of magnesium alloys. From the industrial point of view, HSRSP magnesium alloys should be produced by conventional working techniques, such as extrusion and rolling. Watanabe et al. [91] first reported HSRSP in an AZ91 alloy. The ingot was extruded at 250^{o}C with a reduction ratio of 44:1. The fine grain size of 1.7 μm was stable below 300^{o}C. The maximum elongation was over 300% at 275^{o}C and $1x10^{-2}$ s^{-1}. The ZK61 magnesium alloy produced by powder metallurgy also revealed HSRSP [92]. The powders were sintered at 250^{o}C, and then extruded at 250^{o}C with a reduction ratio of 100:1. The grains were equiaxed with a fine grain size of 500 nm, and an elongation of 283% was achieved at 200^{o}C and $1x10^{-2}$ s^{-1}.

1.5.2 LTSP in magnesium alloys

From economical point of view, the low temperature superplasticity is necessary. However, there are only few works on low temperature superplasticity in magnesium alloys. Mabuchi et al [55-57] reported the AZ91 was extruded at 250^{o}C and then was conducted at 175^{o}C with a total strain intensity of 8.05 by ECAP. The grain size after annealing at 200^{o}C for 30 min was about 1 μm and the grains were almost equiaxed. The alloy showed a large elongation of 661% and the specimen deformed to fracture at 200^{o}C with 6.2x10^{-5} s^{-1}. The ZK60 magnesium alloy also showed low temperature superplastic behavior. The material was extruded with a reduction ration of 100:1 at 310^{o}C. The grain was equiaxed and the grain size was measured to 6.5 μm. It is clearly observed that the large elongation of 430% was attained at 200^{o}C and 2x10^{-6} s^{-1} [76]. The ZK61 magnesium alloy produced by powder metallurgy or grain refinement also showed LTSP [93].

A summary of HSRSP and LTSP (< 200^{o}C) of Mg based materials is presented in Table 1-13.

1.5.3 Deformation mechanisms

A number of papers on the creep mechanisms of magnesium alloys have been published during the past years. The superplastic deformation mechanisms would change under different conditions, such as different materials, temperatures, strain rates, and grain sizes. For the AZ91 alloy, grain boundary sliding with an accommodation process was the most commonly considered mechanism [17]. However, the proposed mechanism for AZ31 was claimed to be the glide-controlled creep and the m value was close to 0.33 [97]. If there is only creep mechanism without any accommodation process, cavitations and grain overlapping will be present in the

neighboring grains. Therefore, the accommodation process is necessary to avoid premature fracture of the loaded specimens. The activation energy for lattice diffusion of magnesium is 135 kJ/mole and the activation energy for grain boundary diffusion of Mg is 92 kJ/mole [94]. In literature, the extruded activation energies from the deformation mechanism analyses mostly range from 90 to 130 kJ/mole.

A summary of superplastic behaviors, deformation mechanisms, and activation energy of Mg based materials is presented in Table 1-14 [95-98].

1.6 Cavitation

Cavitation takes place in a wide range of materials during superplastic tensile flow. There are three different stages of cavitation during tensile deformation, namely, cavity nucleation, growth of individual cavities, and cavity coalescence. Cavities may nucleate at grain boundaries or grain triple points. The cavities may perhaps be pre-existed or nucleated at preferred sites because of the lack of accommodation for grain boundary sliding. Their subsequent growth, coalescence, and interlinkage will lead to premature fracture, and the presence of cavities in superplastically formed parts may have unfavorable effect on its service behavior [99-101].

It is clear that cavity growth is dominated by matrix plastic flow, and that coalescence plays an essential role in the development of large cavity. Hence, it is necessary to prevent cavitation from nucleating, and to avoid the presence of pre-existing defects by careful control of the processing used to produce the superplastic microstructure. The influence of cavity nucleation includes both the microstructural features and deformation conditions. The former includes grain size, grain size distribution and second-phase particles, and the later includes strain rate and

temperature [100].

Minimizing cavitation during superplastic flow is important for gaining satisfactory superplasticity. The small and stable equiaxed grains of uniform size containing second phase particles in a finely dispersed form are advantageous for SPF. Higashi et al. [89,90] also reported that the presence of a small amount of liquid would suppress the cavity growth, and the resulting low cavity growth rate was attributed to the change in the stress state at the liquid boundaries. The volumes of cavities formed via different diffusion processes are different, and their study showed the cavity volume for lattice diffusion is higher than that for lattice diffusion.

1.7 Crystal orientation and overview of techniques for microtexture determination

The factors influencing the fine-grain superplasticity include the grain size, second phase, grain boundary property, texture, and grain shape. It is essential to trace the microstructure and texture evolution during thermomechanical treatment, annealing, or tensile loading. Texture can be divided into two categories by the manners of how they were formed. The first kind of the preferred orientation is called deformation texture, which is produced by the forming process itself (wire drawing or sheet rolling). The second kind of the preferred orientation is recrystallization texture or annealing texture. When the cold-worked metal is recrystallized by annealing, the orientation of the new grain structure might be different from that of the-worked material. The polycrystalline materials with completely random crystal orientations will reveal isotropic mechanical properties. In fact, the preparation of aggregate with completely random crystal orientations is a difficult task. Textures are a result of crystal lattice preferred orientation, but are independent of grain shape [104].

1.7.1 Overview of techniques for microtexture determination

There are several techniques available for microstructure and crystallography characterization. In general, the techniques for analyzing microstructure include optical microscopy (OM), scanning electron microscopy (SEM), transmission electron microscopy (TEM), X-ray diffraction (XRD), and electron backscattered diffraction (EBSD). OM and SEM could observe the grain size or shape of the materials but could not gain the information of crystallography. Furthermore, the reactions between some low angle grain boundaries and etching solution are not very active so sometimes the special boundaries are not easy to be exposed. For X-ray method, the drawback is only to obtain overall or qualitative information on the orientation distribution. On the contrary, it is easy for TEM method to gain local or quantitative information but the range of observation is limited, which cannot gain a great deal of information. The texture analyses by EBSD method involving microtexture and quantitative information became a useful technique for investigating the grain structure and texture evolution.

1.7.2 The basic principles and setup of typical EBSD system

The simplified explanation for the principle of EBSD is illustrated in Fig. 1-5 [105]. As the incident electron beam bombards at point P, inelastic scattering occurs. The Kikuchi lines are formed by Bragg diffraction of inelastic scattered electrons of the plane. The parallel Kikuchi lines can be formed on the phosphor screen, similar to the Kikuchi lines in TEM. From these parallel Kikuchi lines, crystallographic orientations can be obtained.

The setup of an EBSD system is illustrated in Fig. 1-6 [106]. EBSD is an additional instrument attached to SEM. The optimum angle between the incident electron beam and

specimen normal needs to be adjusted to approximately 70.5^{o}. Hence, the major signal is backscattered rather than absorbed. These electron-backscattered patterns will be detected by a phosphor screen and viewed with a low-light TV camera. The real-time picture of the diffraction pattern is viewed on a monitor and analyzed using a computer driven cursor and dedicated software [107]. There are several kinds of information which can be obtained from EBSD such as (a) pole figure and inverse pole figure, (b) orientation distribution functions (Fig.1-7) and (c) misorientation distribution (Fig.1-8).

1.7.3 The study of texture in magnesium alloy

It is well know that magnesium is lack of ductility at room temperature owing to its HCP structure and it is generally fractured with a limited elongation-to-failure less than 10%. Mukai et al. [58] have reported a commercial AZ31 magnesium alloy processed by ECAP, and found the development of a different texture compared with the conventionally extruded alloy. In order to avoid the grain-size effect, the ECAP-processed alloy was annealed to the same grain size as the extrusion-processed one. The X-ray diffraction spectra of both specimens were obtained for the planes perpendicular and parallel to the extrusion direction. The texture of the ECAP/annealed alloy was obviously different from that of extruded alloy. The elongation of the former reached ~50%, which was about twice higher than the latter case. Barnett [108] also studied the influence of texture and deformation mode on the flow stress of magnesium AZ31. The specimens were tested in torsion, uniaxial compression and channel die compression. It is clear that the flow stress was strongly dependent on texture and deformation mode. The influence of texture and deformation mode at low strain levels was more obvious than at high strain levels, and it was rationalized in terms of the influence of prismatic slip, twinning and dynamic recrystallisation on the deformation stress and structure [107].

Perez-Prado et al. [109] demonstrated texture evolution during annealing of an AZ31 alloy sheet. A through-thickness texture gradient has been investigated in the as-received material. On the surface, $\{0001\}$ basal and $\{11\bar{2}0\}$ prismatic components predominated, and the texture plane in the mid-layer includes $\{0001\}$, $\{10\bar{1}0\}$and $\{11\bar{2}0\}$ prismatic. Upon moderate annealing, normal grain growth occurred in the mid-layer and $\{11\bar{2}0\}$ planes parallel to the sheet plane developed at the depletion of randomly oriented grains. On the outer surface, secondary recrystallization started to take place during annealing and $\{11\bar{2}0\}$ planes parallel to the sheet plane developed abnormally. Upon severe annealing, the process of secondary recrystallization continued until a homogeneous texture is completed throughout the thickness.

1.8 Motive of the research

The current research and development of LTSP and/or HSRSP in the Mg base alloys is among the first generation study of the overall exploration on processing, heat treatment, microstructure, microtexture, mechanical properties, deformation mechanisms, as well as joining and forming in terms of superplastic gas forming, press forming, or hydroforming for the processed rod-shaped bars, thin sheets or thin tubes. As introduced in previous sections, the achievements of LTSP or HSRSP in the Mg alloys have been reported in a number of papers, mostly authored by the Japanese investigators.

Most successes on LTSP or HSRSP in the Mg base alloys were based on the ECAP processing route, which produced small rod specimens only suitable for laboratory uses. The current proposal is intended to conduct systematic studies on the simple processing route of high ratio extrusion, which is feasible for regular foundry and is expected to fabricate large bars, sheets or tubes for structural applications. The characterization of the resulting specimens

through high ratio extrusion will cover basic microstructures, microtextures, as well as room and elevated temperature mechanical properties. The results will be compared with those obtained from the parallel study on ECAP processed Mg alloys. In this research, the work is designed as what summarized below:

(1) To develop LTSP and HSRSP in magnesium alloys by proper grain refining processes of high ratio extrusion and ECAP.

(2) To reveal microstructure evolution, cavity and texture during deformation, and to relate to the superplastic behavior for HCP material.

(3) To determine the superplastic characteristic parameters, such as the stress-strain curves, strain rate sensitivity m values, and activation energy, and to explain the deformation mechanisms in magnesium alloys.

Chapter 2

Experimental Method

2.1 Materials

The AZ31 alloys used in this study were purchased from CDN Company, Canada. The as-received alloy was fabricated through semi-continuous casting and has the form of extruded billet measuring 178 mm in diameter and 300 mm in length. The chemical composition of AZ31 alloy is shown in Table 2-1. The as-received alloys contained coarse grains and did not exhibit any LTSP or HSRSP characteristics. The grain size in the casting condition was ~75 μm. The as-received alloys contained coarse grains and did not exhibit any LTSP or HSRSP characteristics. Microstructural examination was conducted using optical microscopy (OM) and transmission electron microscopy (TEM).

For OM, samples were observed in the longitudinal direction, they were ground mechanically to a mirror-like surface using abrasive papers with water and alumina powders, and the surface were then etched by immersing 100 ml ethanol, 5 g picric acid, 5 ml acetic acid and 10 ml water by volume. For TEM samples were sliced perpendicular to longitudinal direction and ground to give disks with diameters of 3 mm and thickness of ~150 μm. The samples were prepared using a twin-jet polishing facility with a solution of 22.32 g magnesium perchlorate, 10.6 g lithium chloride, 200 ml 2-butoxy ethanol and 1000 ml methanol electrolyte. Microstructural observations by TEM were undertaken using a Jeol-3010 electron microscope operating at 200 kV.

2.2 Grain refining process

The initial materials will be undertaken a series of solution treatment and hot working. The hot working includes extrusion and ECAP. After hot working, the materials will be tested in tension. Microstructure of specimens will be examined for figuring out the specific properties in magnesium alloys. Figure 2-1 shows the processing routes for this research.

2.2.1 Extrusion

In order to receive the refined grain structure, extrusion process was performed at temperatures ranging from 200 to 350^{o}C. It is well known that grain refinement resulted in a decrease in superplastic temperature and an increase in strain rate during superplastic tensile loading. The input rod-shaped ingot for laboratory extrusion, with a diameter of 65 mm, was extruded into bars of diameter of 10-6.5 mm or a plate width of 10 mm and plate thickness of 2 mm, resulting in extrusion ratios of 25-166 (or a true extrusion strain of 3.2-5.1). In this study the extrudor is made by Kong-Yi Company and the maximum power is about 350 ton. To scale up for industrial applications, the diameter of the input rod ingot can be raised to 200 mm. Extrusion into a plate with a cross-sectional area of 150x1.5 mm^2 will correspond to an extrusion ratio of 140. However, a more powerful extrusion machine up to 3000 ton is needed to proceed with such routine practices. Parallel experiments on the AZ91D alloys also showed that the one-step extrusion could be replaced by two-step extrusion with the same total accumulated strain [52], and slightly degraded but still compatible superplastic results could also be achieved. For two-step extrusion, a regular industry extrudor ~1000 ton can be applied.

Extrusion ratio is defined as ER = A_0/A_f, where A_0 is the initial area of the billet and A_f the final area of the extruded specimens. The extrusion ratios of different diameters are assigned

below:

$ER1=(65/2)^2\,\pi : (10/2)^2\,\pi=42 : 1$ ($\varepsilon=3.74$), (2-1)

$ER2=(65/2)^2\,\pi : (6.5/2)^2\,\pi=100 : 1$ ($\varepsilon=4.61$), (2-2)

$ER3=(65/2)^2\,\pi : (20)=166 : 1$ ($\varepsilon=5.11$). (2-3)

The reduction ratio in area is defined below:

$RA1=\{(65/2)^2\,\pi-(10/2)^2\,\pi\}/(65/2)^2\,\pi=97.6\%$ *extrusion ratio 42:1,* (2-4)

$RA2=(65^2-6.5^2)/65^2=99.0\%$ *extrusion ratio 100:1,* (2-5)

$RA3=(65^2-20)/65^2=99.5\%$ *extrusion ratio 166:1.* (2-6)

According to different processes, the AZ31 specimens examined in this study could be roughly classified as Table 2-2.

2.2.2 Processing route of equal-channel-angular pressing

The ECAP is an attractive and simple method to produce an ultrafine–grained material by using intense plastic straining. An AZ31 alloy will also be processed by ECAP to achieve the ultrafine grain structures and the results will be compared to those obtained from the above as-extruded AZ31 alloy. The E1 rod specimens were machined for ECAP with diameters of 10 mm and lengths of 60 mm. ECAP was conducted by the die with an angle of 110^o between the two channels. For processing through more than one pass, each sample was rotated by 90^o in the same direction for each pass. The specimen was pressed via route Bc (rotate 90^o in the same direction for each pass) at 200^oC.

The principles of ECAP have been described [110]. As indicated in Figure 1-4, the angle Φ is the angle at which two channels intersect, and the angle Ψ is the arc of curvature at the outer point of intersection of the two channels. The strain accumulated in ECAP (ε_N) can be expressed

as [110].

$$\varepsilon_N = N/\sqrt{3}[2\cot(\Phi/2+\Psi/2)+\Psi\csc(\Phi/2+\Psi/2)], \quad (2\text{-}7)$$

where N is the number of pressings through the die. In this study, the values of Φ and Ψ are 110^o and 20^o, respectively. In this case, it follows from Equation (2-7) that a strain ~0.76 is introduced into the sample during each pass through the die, so that a total of 8 passes will give an accumulated strain of ~6.

2.3 Evaluation of superplasticity behavior

2.3.1 Tensile tests

The optimum temperature, strain rate, and elongation of all processed materials were characterized by tension tests in this study. Constant crosshead speed tensile tests were conducted using an Instron 5582 universal testing machine equipped with a three-zone furnace. The temperature was controlled within $\pm 2^oC$. It usually took 60 min for the tested specimens to reach the desired loading temperature without thermal fluctuations. Different heating rates were tried, and 60 min seemed to be optimum in terms of LTSP elongation performance and instrument stability. The temperature range of 100-300^oC and the constant initial strain rates in the range of 10^{-4} to 10^{-1} s^{-1} were chosen for most materials. The geometry of extruded alloys was in the form of rod or plate specimens, as presented in Figures 2-2 (a)(b). The tensile specimens had a gage length of 5.5 mm. For the sheet specimens, the gage width was 3 mm and the gage thickness was 1-2 mm. As for the rod tensile specimens, the gage length was 8.3 mm and the gage diameter was 3-10 mm. The specimens were machined from the as-extruded material with tensile axis parallel to the extrusion direction.

2.3.2 Strain uniformity

The constant strain rate tests were carried out at a temperature of 300^{o}C and a strain rate of 10^{-3} s^{-1}. The tensile tests were stopped at several fixed strains. Varieties of thickness, width and area in the gage length were measured at different strains. According to results, the uniform deformation can be defined.

2.3.3 Strain rate sensitivity (m-value)

In general, there are two methods used to determine the m-value. The first one is the jump-strain-rate test during which a periodic increase in strain rate is superimposed on a base strain rate. The strain rate difference between the base and the jump is small and the elevated strain rate is maintained for a short time. Hence, the microstructural difference due to the jump is considered to be negligible. Therefore, the relationship between the m-value and strain for a given constant strain-rate can be determined by the jump-strain-rate test. An example of this kind of test is shown in Fig. 2-3. The second method is the step-strain-rate test during which the strain rate was increased or decreased until a 'reasonably steady flow' is attained at each strain rate [111]. From this information, the relationship between stress (at fixed strain) and strain rate will be established and then plotted logarithmically. The slope of the logσ-log$\dot{\varepsilon}$ curve represents the strain rate sensitivity of the flow stress.

2.4 Microstructure observations

2.4.1 Grain size and cavitation

The grain size distribution and cavitation will be examined by a Nikon Microphoto-FXL optical microscopy (OM) or a Jeol 6400 scanning electron microscopy (SEM). Both the microstructures before and after superplastic loading are investigated and compared. Besides, the specimens after tension tests in different strain levels will be also examined. The specimens were mechanically ground using emery papers with water, then polished with a diamond paste and etched with an aqueous, containing 100 ml ethanol, 5 g picric acid, 5 ml acetic acid and 10 ml water by volume.

2.4.2 TEM

It has been recognized that the dislocation substructure formed during superplastic tensile tests. In this study, the morphology of grains/subgrains and the dislocations activity will be examined by TEM. The specimens loaded to different will be prepared into thin foil specimens for TEM microstructural characterization. Thin foil specimens will be twin-jet electropolished using a solution of 22.32 g magnesium perchlorate, 10.6 g lithium chloride, 200 ml 2-butoxy ethanol and 1000 ml methanol at 90 V while keeping the electrolyte at about –40^{o}C. After polishing finished, samples were taken out immediately and washed in ethanol and then soaked in ethanol for about 1 min and then let them dry and store in a dry environment to prevent any oxidation.

2.4.3 Thermal stability

In order to examine the grain size stability during static annealing and dynamic loading, the E3 specimens extruded by a high extrusion ratio were further heated to 150, 200, 250, 300 and 350^{o}C and held for 0-10 hour, followed by subsequent tensile loading under various loading conditions. The E1, E1B and E2 samples were further heated to 150, 200, 250 and 300^{o}C and

held for 1 hour. The grain microstructures and post-annealing superplastic properties were characterized and compared. The grain structures of the etched specimens were revealed by OM or SEM observations.

2.4.4 Fractography examinations

The fracture surface was examined using SEM. The fracture surface of the as-deformed specimens will provide the information about which deformation mechanism occurred during superplastic flow. The fracture surface of the specimens, which were tested at different temperatures and strain rates, appeared different morphology. The appearance of grain boundaries might indirectly account for the occurrence of GBS mechanism.

2.5 Microhardness measurements

The microhardness was performed in a Shimadzu HMV-2000 hardness indentor. The Vickers microhardness of those H_v was measured after extruded and ECAP processes for the sample with a diameter of 10 mm. Measurements were taken at cross-sectional of the samples and on the surfaces of the samples, using a load of 100 g for 15 s for each separate measurement. Figure 2-4 is a schematic illustration of these measurement locations. The average microhardness value was determined from two separate measurements clustered around the selected position.

2.6 Texture characterization

2.6.1 X-ray diffraction

The crystalline orientations of the as-extruded as well as the annealed specimens were examined by X-ray diffraction. For the rod ingot billet, the cross-sectional plane was placed to receive the incident Cu K_α X-ray. In contrast, for the extruded plate the plane facing to the X-ray was the flat extrusion surface. Besides, the crystalline orientations after extrusion with different extrusion ratios and after tension tests to different strain levels will be also traced. According to the information, the relationship between texture and mechanical properties is intended to be established. X-ray pole figure will also be generated in center for Nanoscience & Nanotechnology, NSYSU.

2.6.2 EBSD

On the other hand, EBSD will also be employed to analyze the crystalline orientation of the specimens. There are several kinds of useful information generated by the EBSD technique, such as pole figures, inverse pole figures, orientation distribution functions, orientation image, grain boundary misorientation distribution and the coincidence site lattices. In comparison of the results of X-ray and EBSD, integrated crystalline orientation information will be attained.

2.6.3 TEM

There are a number of methods to determine the local grain orientations by TEM. In this case, the selected area diffraction (SAD) was used to extract the mutual misorientation of neighboring grains in the illuminated. There are standard equations to calculate the misorientation angle [112]. The result of misorientation distribution determined by EBSD and TEM will be compared and systematic characterizations of texture and grain boundary mutual misorientation angles will also be defined.

Chapter 3

Experimental Results and Discussions

3.1 Microstructure characterization

3.1.1 Grain size evolution

The as-received AZ31 Mg billets were processed by both extrusion and ECAP. The appearances of samples after extrusion and ECAP are shown in Fig. 3-1. No crack is observed at surfaces of the extruded plates or extruded rods processed at 300^{o}C, but there are slight surface defects for the E1B ECAP specimens due to lower processing temperature of 200^{o}C.

The microstructure of the as-received AZ31 billet, seen from the cross-sectional plane, is shown in Fig. 3-2. The grain size measured by the liner intercept method is about 75 μm. The change in grain size often differs from various processes. In general, larger processing strain would result in finer grain size. Figure 3-3 shows the OM micrographs of the E1, E1B, E2, E2B and E3B specimens. With high extrusion ratios from 42:1 to 166:1, the grain size could be easily refined. The average grain sizes of the E1, E2B and E3 are 2.5, 3 and 2.5 μm, respectively. The OM micrographs of as-extruded E3 materials are shown in Figs. 3-4 (a)(b)(c) taken from the flat, longitudinal and cross-section plane, respectively. The grain size of AZ31 alloy after a high extrusion ratio of 166:1 became ~2.5 μm. Furthermore, the grain boundaries are observed to be well defined. In addition, Fig. 3-5 (a)(b) shows the grain structure of the as-extruded E1 and as-ECAP E1B condition. The grain size of E1 and E1B specimens measured by the linear intercept method are 2.5 and 0.7 μm, respectively. Parameters such as grain size and room

temperature tensile properties of billet, high ratio extruded and ECAP specimens are all listed in Table 3-1.

3.1.2 Influence of annealing temperature and time

The thermal stability of the grains in the processed E1 and E1B specimens was examined by heating the samples at temperatures up to 350°C and subsequently annealed for 1 hour. The results are shown in Fig. 3-6 and it is apparent that reasonable grain stability is maintained up to 200°C for the E1B sample but there is pronounced grain growth at higher temperatures. On the other hand, the E1 sample is reasonably stable up to 300°C. The different thermal stabilities are due to the different processing temperatures of the E1 (300^{o}C) or E1B (200^{o}C) specimens.

The author's co-worker, Lee [113], also reported the similar grain growth phenomenon. The extruded AZ31 plates similar to the E2B specimens contain a grain size about 3 μm after subjecting to static annealing and superplastic loading at 200-400^{o}C, the grain size would gradually increase. Grain growth under the dynamic loading condition appears to be severer than the static annealing. It is noted that the grains have grown to about 20 μm at the later stage of superplastic straining at 400^{o}C and 6x10^{-4} s^{-1}, which is considered as a higher temperature and a lower strain rate. In contrast, the grain size maintained nearly unchanged (or even refined further) at lower holding temperatures of 200 and 250^{o}C, irrespective of static annealing or dynamic straining at low or high strain rates.

In addition, the grain boundaries of the E3 specimen extruded at 300^{o}C after static annealing at 150-350^{o}C for 1 h appeared to be well defined. The variation of grain size as a function of temperature in the E3 specimen after holing for 1 h in the furnace is shown in Fig. 3-7. It is apparent that with the annealing temperature ranges within 150-300^{o}C, the grain size

increased slightly to the region of 2.6 to 2.8 μm, suggesting that the grain size was fairly stable upon exposure at temperatures below 300^{o}C. Nevertheless, the extensive grain growth would occur at above 300^{o}C. Figure 3-8 shows that variation of grain size as a function of time in the E3 specimen at 300^{o}C and the grain sizes of E3 specimens after static annealing at 300^{o}C for 1 to 10 h exhibited slightly increase from 2.8 to 3.9 μm, as listed in Table 3-2. This implies that the grain structure in heavily extruded AZ31 alloy can remain its grains at T< 300^{o}C for a long period of loading or forming time. However, at an even higher temperature of 350^{o}C for 1 or 10 h, the grains grew appreciably to 5.2 or 6.5 μm. In comparison with the AZ31 magnesium alloy, the AZ91 alloy also has the same phenomenon in maintaining a stable grain size below 300^{o}C [51]. Meanwhile, both the AZ31 [71] and AZ91 [52] alloys were extruded at 300^{o}C using the simple high-ratio extrusion method. During static annealing process over 25-300^{o}C, the grain size remained highly stable. Wang [114] in our group also reported a commercial AZ61 alloy, which was extruded using a medium extrusion ratio at a temperature of 350^{o}C. Limited grain growth occurred at the optimum superplastic temperature of 350^{o}C, which corresponds to the transition temperature between limited and pronounced grain coarsening. From all results, it can be seen that stable grain size could be maintained below the processing temperature.

3.1.3 Microstructures in specimens subject to different superplastic strains and temperatures

Selected E2B specimens were tensile-strained and then stopped at true strain levels of ~0.3-2 to observe the development of microstructure and cavitation. The typical SEM surface topography micrographs taken from the E2B specimens loaded at 200 and 300^{o}C to different strains are shown in Figs. 3-9 and 3-10, respectively. It is apparent that the grains still maintained nearly equiaxed throughout the straining until fracture at 200^{o}C. Some microcracks are observed at the grain boundaries or triple points when the E2B specimen deformed to a strain around 0.29. In contrast, only few cavity numbers were observed when the E2B specimen deformed to the

same strain at 300^{o}C. It is evident to show that a higher temperature would enhance accommodation and suppress cavitation. From the results in Fig. 3-10, it can be seen the evolution of GBS when the E2B specimens are strained to different true strains at 300^{o}C and $6x10^{-4}$ s^{-1}. GBS could be readily seen from the large number of grain boundary "steps". It should be noted that almost all surface grains in the E2B specimen have been involved in GBS operation; namely; individual grain boundary sliding rather than cooperate grain-boundary sliding was undertaken from the very early stage of superplastic straining. With increasing deformation strain, GBS offsets at individual grains were progressively further developed. The deformation mechanism will be not discussed in this Chapter, and a detailed mechanism calculated is given in Chapter 4 in order to describe the GBS phenomenon.

The microstructures of the E3 specimens also deformed at 300^{o}C and $1x10^{-3}$ s^{-1} to tensile strains of 0.25, 0.47, 0.93, and 1.23 are shown in Fig. 3-11. During the initial stage of tensile test, up to a true strain of 0.25, it is seen that there is a mixed structure, which is composed of two structural components. One is the region of recrystallized grains with an average size of about 6 μm and the other region comprises crystallites with about 3 μm. With increasing strain, the average grain sizes of the specimens gradually grew.

3.2 Microhardness

The mean H_v reading of the as-received AZ31 billet is about 55. The microhardness results are illustrated in Fig. 3-12 for samples processed by extrusion and ECAP, respectively. Inspection of these data reveals that all measured values of the microhardness of the extruded E1 and ECAP E1B processed samples are significantly higher than the values of the unprocessed AZ31 billet, suggesting that grain size is effectively refined after extrusion and ECAP. The plot

also shows basically homogeneous microhardness measurements of extrusion and ECAP processed samples. With a smaller grain size in the E1B specimens, the H_v readings (~95) are higher than those (~82) of the E1 specimens. Table 3-1 also shows the hardness of the E2B, E3 and E3B specimens and the values are 81, 82 and 83, respectively. Microhardness of the AZ31 alloy as a function of grain size is shown in Fig. 3-13. With refining grain size, the microhardness in all specimens increase. Wu [115] reported the Hall-Petch relationship for the AZ31 alloy expressed as

$$H_{v,\,AZ31} = 33 + 95\, d^{-1/2}. \tag{3-1}$$

The microhardness readings of the extruded specimens match approximately for the equation but that of ECAP specimens (E1B) was not. It is inferred that when grain size was below specific value or the structure had different texture, the equation must be modified.

3.3 Tensile properties

3.3.1 Room temperature tensile properties

Typical stress-strain curves are shown in Fig. 3-14 for tests conducted at room temperature and $1x10^{-3}$ s^{-1} using samples in the as-received, extruded and ECAP conditions. The values of the tensile yield stress (YS), ultimate tensile stress (UTS) and elongation (e) to failure are summarized in Table 3-1. The room temperature YS and UTS data shown in Fig. 3-15 were seen to follow the Hall-Petch relationship. Using the unit of MPa for the YS and UTS data and μm for the grain size d, the relationship can be expressed by

$$\sigma_{YS} = 56 + 348 d^{-1/2}, \tag{3-2}$$

and

$$\sigma_{UTS} = 133 + 307d^{-1/2}. \quad (3\text{-}3)$$

The K-slope of these equations might be somewhat higher than the value reported in literature [44], usually less than 250 MPa·μm$^{1/2}$. This might be due to the fact that those stress data corresponding to small grain sizes included some work hardening contribution, thus raising the K-slope. Recent research by Mabuchi et al. [82] also suggested the importance of microscopic orientation effect on the K-value. It should be noted that the K-slope for Mg base alloys is much higher than that for Al base alloys (~60 MPa·μm$^{1/2}$) [116], so that the benefic grained from grain refinement in Mg alloys will also be much higher.

In general, the room temperature YS and UTS data followed the Hall-Petch relationship. Mechanical properties in most extruded specimens are consistent with the relationship. However, such grain size dependency of the UTS and the YS could not be observed from the as-ECAP results. Although the grain size is the smallest in the ECAP condition, it is noted that the YS and UTS are both lower than those in the extruded condition. Since slip is caused by shear stresses, the yield stress for crystals is best expressed in terms of a shear stress resolved on the slip plane and in the slip direction. Orientation factors such as the Schmid factor would affect the strongest texture component. Figure 3-16 shows the macro-fracture surface of the E1 and E1B specimens. The fracture plane of the E1B specimen lies approximately 45^{o} angles with the tensile direction. Therefore, it is inferred that the tensile properties must have been influenced by the crystallographic texture due to strong anisotropy of the slip system at room temperature. The Schmid factors will be discussed in Chapter 4.

In order to improve the ductility at room temperature, an annealing process has been conducted for the E3 specimen. After warm extrusion to 166:1, the tensile data on the

as-extruded E3 specimen increased to 280 MPa, 323 MPa and 27%. Upon static annealing at 150-300^{o}C for 1-10 h, the room temperature tensile strength and elongation did not change much. It is evident from the data in Table 3-3. The maximum tensile elongation of 35% for the E3 specimens was obtained in specimens after static annealing at 200^{o}C for 1 h. However, tensile elongations higher than 30% can be achieved by numerous annealing practices. The room temperature strength was not severely affected by annealing at 300^{o}C or below, a result consistent with the measured grain size and texture evolution. Annealing at 350^{o}C for 10 h will however reduce the UTS strength and elongation to 268 MPa and 21%, a level closer to commercial coarse-grained AZ31 alloys.

Basically, the extruded plate or rod could attain good ductility at room temperature. The E3B specimens especially exhibit excellent ductility and large ultimate tensile stresses. The engineering stress versus engineering strain curves tensile-loaded at RT and the appearance of the E3B specimens after tensile testing is shown in Fig. 3-17. The maximum elongation and UTS were about 50% and 283 MPa, as compared in Table 3-4. The as-extruded specimen showed low work hardening at room temperature. Compared with the as-extruded 5083 Al alloys exhibiting room temperature tensile elongation of ~15% and ill-defined (sub)grains, the AZ31 Mg alloy possesses much higher room temperature tensile elongation. The high elongation of 50% for the as-extruded AZ31 specimens, much higher than the 15-25% for commercial coarse-grained AZ31 alloys or similarly processed 5083 Al alloys, was derived from the uniform and well-defined fine grain structures.

3.3.2 Superplastic behavior over 150-300^{o}C and 10^{-4}-10^{-1} s^{-1}

3.3.2.1 Comparison of LTSP in the E1 and E1B specimens

The tensile test results at 150-250^{o}C of the E1 and E1B processed rods are presented in Table 3-5. According to these results, there are two things that must be noticed. First, the E1B specimen could attain low temperature superplasticity. Second, both E1 and E1B specimens can also achieve sufficient elongations at a high strain rate of $1x10^{-2}$ s^{-1}. At 150^{o}C, equivalent to ~0.46 T_m, the highest tensile elongation of the E1 specimens was only 130% but the superplastic elongation of 461% could attain in the E1B specimen. Figure 3-18 shows the typical true stress versus true strain curves for the E1 and E1B specimens at 150 and 200^{o}C. It is clear to see that the elongation to failure in the E1 specimen is merely about 130% but that in the E1B specimen achieved under these conditions is 461% at a strain rate of $1x10^{-4}$ s^{-1} and 150^{o}C. Tensile specimens of the E1 and E1B conditions tested at $1x10^{-4}$ s^{-1} and 150^{o}C are shown in Fig. 3-19. It can be noted that local necking phenomenon occurred in the E1 specimens, but the E1B specimens show uniform deformation in gage area. It is inferred that the deformation mechanism would have proceeded smoothly in the E1B specimens under this condition. A summary of the tensile elongations is given in Fig. 3-20 where the results are plotted against the testing strain rate at different temperatures. In Figs. 3-20(a), reasonably high elongations appear only at 250°C for the extruded condition. By contrast, Fig. 3-20(b) shows that superplasticity occurs in the ECAP condition at 150°C but only at the lowest strain rate. It is also apparent from inspection of Fig. 3-6 that the elongation reduction of the E1B specimens at 250°C is a consequence of extensive grain growth at this temperature. The average grain sizes in the gauge sections of the ECAP specimens strained to failure at 150, 200 and 250°C at a strain rate of $1x10^{-4}$ s^{-1} were ~1, ~3 and ~8 μm, respectively. The larger grain size would lead to less smooth operation of GBS and a longer distance for diffusion or dislocation accommodation.

In addition, the grain boundary of the E1B specimen after static annealing at 125^{o}C for 7 h appeared to be well defined and then the sample was tensile-loaded at 125^{o}C and $1x10^{-4}$ s^{-1}. The true stress versus true strain curves and the appearance of the E1B specimen are shown in Fig.

3-21. This E1B specimen still maintained superplastic elongation ~200%. It is clear to show that the samples processed by ECAP easily attain low temperature superplasticity.

3.3.2.2 Comparison of the E1 and E2 specimens processed to different extrusion ratios

The E1 and E2 rod specimens were processed using the same extrusion method at 280-300^{o}C but different extrusion ratios of 42 and 100. In general, larger processing strain would result in finer grain size. The average grain sizes for the E1 and E2 specimens were 2.5 and 2 μm, respectively. Table 3-6 shows the elongations of the E1 and E2 samples at various tensile temperatures and strain rates. From the results, it is apparent to show that the tensile elongation of both E1 and E2 specimens increased with increasing test temperature. The variation in elongation to failure as a function of test temperature is shown in Fig. 3-22. Over the test temperature ranges of 150-250^{o}C examined, the elongations of the E2 specimens are much higher than those of the E1 specimen. Figure 3-23 shows the variation in elongation to failure as a function of strain rate. From these results, it is apparent the elongation will increase with decreasing strain rate when tensile test at low temperature of 150^{o}C. The E1 specimens could not attain LTSP but the E2 specimen exhibited both LTSP ($\leq$200^{o}C) and HSRSP ($\geq 10^{-2}$ s^{-1}). It should be noted that the high elongation is attained in a low temperature range of 0.46 T_m. The LTSP elongation occurred at 150^{o}C and $1x10^{-4}$ s^{-1} was achieved 437%. It is inferred that the materials were extruded with high extrusion ratio, the LTSP would easily attain. Furthermore the HSRSP at 250^{o}C and $1x10^{-2}$ s^{-1} was achieved for E2 specimen and the elongation was 405%.

3.3.2.3 Comparison of the E2 and E2B specimens processed into different geometric shapes

Table 3-7 shows the elongations of the extruded AZ31 alloy at various temperatures and strain rates. The difference between the E2 and the E2B specimens is the extruded geometric

shapes. The E2 specimen is an extruded rod but the E2B specimen is an extruded plate. They were both subject to the extrusion process with an extrusion ratio of 100:1 at 300^{o}C. From Table 3-7, there are two points to be noted. Firstly the UTS for E2 is less than E2B shown in Fig. 3-24, and the grain size for both specimens listed in Table 3-1 can easily explain that the superplasticity behavior in E2 is better than E2B. Secondly, the elongation to failure for E2 is higher than that for E2B. Furthermore, only the E2 specimen could achieve LTSP and the elongation is 437% at the test temperature of 150^{o}C. It is difficult to say that the difference for both specimens is owing to different grain sizes because their sizes were close. Figure 3-25 shows the variation in elongation to failure as a function of temperature at constant strain rate of $1x10^{-2}$ s^{-1}. It is observed that HSRSP could easily attain for both E2 and E2B when test temperature is above 200^{o}C. However, the cavitation behavior is a good way to describe that the higher elongation attained in the E2 specimen. Most superplastic materials after large tensile strains are susceptible to extensive internal cavitation. The elongation to failure is inversely proportional to the level of cavitation. Cavitation in the E2B plate specimen is more extensive than that in the E2 rod specimen because the geometric shapes for both samples are different. The tensile ductility of E2B is limited by cavity interlinkage in a direction perpendicular to the tensile axis during superplastic deformation because one direction of gauge area in the E2B specimens is thinner than that in the E2 specimen. The fact is that cavity interlinkage resulted in fracture occurred during an early stage.

It is especially pointed out that excellent elongations could be attained when superplastic temperature is above 200^{o}C. The incipient melting temperature for AZ31 is 644^{o}C. Only the E2 specimens exhibit LTSP and the elongations were 437%. However, HSRSP was achieved for both E2 and E2B specimens. The elongations were 1000% and 481%, respectively. The maximum elongation value of 1000% was obtained at 300^{o}C and at a high strain rate of $1x10^{-2}$ s^{-1}. The tested specimen is shown in Figs. 3-26 and 3-27. It is apparent that the elongations in E2

and E2B would increase with increasing tensile temperatures in this test range. Uniform deformation in the gauge section can be seen for most samples. This also indicates that HSRSP in AZ31 can be obtained without the liquid phase. This is in contrast to HSRSP in aluminum-based alloys and their composites, in which the liquid phase plays an important role for relaxation of stress concentrations caused by GBS as an accommodation helper [117].

3.3.2.4 Comparison of the E2B and E3 specimens processed to different extrusion ratios

The E2B and E3 extruded 2 mm plates were proceeded using the same extrusion method at 280-300^{o}C but the difference is only the different extrusion ratios of 100:1 and 166:1, respectively. Basically, the average grain size for the E2B (3 μm) and the E3 (2.5 μm) specimens were very close. Table 3-8 lists the elongations of the E2B and E3 extruded plates at various temperatures and strain rates. It appears that both LTSP and HSRSP can be attained for the E3 extruded plates. Figures 3-28 shows the typical true stress and strain curves for the E3 specimens recorded from tensile tests at different initial strain rates for the loading temperatures of 150-300^{o}C. Only the E3 specimens exhibit LTSP and the elongation was 215%, but both E2B and E3 specimens can achieve HSRSP with elongations of 481% and 294%, respectively. The UTS variations against tensile temperatures for the E2B and E3 specimens are shown in Fig. 3-29. The UTS levels of E3 are lower than those of E2B. It is inferred that superplasticity would occur more easily in the E3 specimens. With heavy extruded in the E3 specimens, low temperature superplasticity easily occurred because of finer grain size (2.5 μm).

3.3.2.5 Comparison of the E3 and E3B specimens to different plate thicknesses

Figure 3-30 shows the typical true stress and strain curves for the E3B specimens recorded from tensile tests at different initial strain rates for the loading temperatures of 150^{o}C to 300^{o}C.

From the results, it could be observed that the UTS value in E3B would decrease with increasing test temperature and decreasing strain rate. Table 3-9 shows the elongations of the extruded E3 (2 mm), and E3B (1.5 mm) plates at various temperatures and strain rates. Over the test temperature ranges of 150-300^{o}C examined, the extruded plates exhibited low temperature and/or high strain rate superplasticity at 150-300^{o}C. The variation of superplastic elongation as a function of strain rate at 150-300^{o}C is depicted in Fig. 3-31. The maximum elongation of 900% for the E3 specimens occurred at 280^{o}C and 1x10^{-4} s^{-1}. At a low temperature of 150^{o}C (~0.46 T_m), the tensile elongations for the E3 and E3B specimens were 215% and 300%, suggesting that the alloy exhibited LTSP as well. An elongation of 520% can also be achieved at 300^{o}C and 8x10^{-3} s^{-1}. At 300^{o}C and higher strain rates of 2x10^{-2} and 1x10^{-1} s^{-1}, the elongation still maintained at ~300% and ~210%, suggesting that the current processed AZ31 plates have processed HSRSP. The tested specimens are shown in Figs. 3-32 and 3-33. It is observed that uniform deformation in gauge length for all test samples, suggesting the dominant deformation mechanism proceeded smoothly. The high elongation occurred at low temperatures and high strains in the current Mg base alloy has exceeded all published data in the literature. Figure 3-34 shows the tensile elongations at a reasonable strain rate of 1x10^{-3} s^{-1} from room temperature to 300^{o}C, the elongation increased from around 30% to above 500%.

The difference for both E3 and E3B specimens is the plate thickness. The former in thickness is 2 mm, and the later is 1.5 mm. The grain sizes for both specimens were very close, being 2.5 μm and 2.3 μm. Basically, the E3 and E3B specimens could attain both LTSP and HSRSP. The LTSP elongations of the E3 and E3B specimen at 150^{o}C were 215% and 300%, and the HSRSP elongations at 300^{o}C were 294% and 281%, respectively. However, the elongation at room temperature in E3B (50%) is better than E3 (27%). It is inferred that the microstructure in the thinner extruded E3B specimens seems to be more homogenous.

Two exciting things were also found from the tensile testing that the elongation-to-failure of E3B specimen at room temperature exhibited around 50%, which is similar to the ECAP/annealed alloy [58]. The other is that the UTS of the E3 specimen was 320 MPa, which was twice larger than for the billet condition. It is obvious to show that mechanical properties will efficiently improved through one-step high ratio extrusion. To achieve a minimum tensile elongation of ~100% for forming a cell phone enclosure, the alloy needs to be heated to ~75^{o}C. The results imply that the simple one pass high-extrusion ratio extrusion method might be a feasible processing mean for industrial applications.

3.3.3 Plastic anisotropy

During superplastic tensile tests, the distribution of sample cross-sectional area within the gauge length to different strains was measured. According to this information, the deformation uniformity for the specimens will be defined. The variations of cross-sectional area for the E3 specimens tensile deformed at 300^{o}C and 1x10^{-3} s^{-1} to tensile strains of 0.25, 0.47, 0.93, and 1.23 are shown in Figure 3-35. The specimens showed uniform deformation, no apparent local necking. In addition, the plastic anisotropy ratio R ($R=R_W/R_T$) could also describe the degree of uniform deformation. The width reduction rate is defined as $R_W=[(W_f-W_o)/W_o]$, where W_o and W_f are the initial and final width for the cross-section in the gage length. The specimen thickness reduction rate is defined as $R_T=[(T_f-T_o)/T_o]$, where T_o and T_f are the initial and final thickness for the cross-section in the gage length [99]. If the grain structure gradually tended to be equiaxed and uniformed grains, the value of R would maintain a constant closed to 0.8~0.9. Figure 3-36 shows the variation of R for the E3 specimens to different tensile strains. The AZ31 Mg alloy tested at 300^{o}C and at 1x10^{-3} s^{-1} exhibited fairly uniform deformation. That implies that GBS has been undertaken smoothly as the specimen as deform with no serious local necking.

Furthermore, the variations of cross-sectional area for the E2B specimens deformed at various temperatures and strain rates to different tensile strains are shown in Fig. 3-37. From the results, it is apparent to observe the local neck phenomenon occurred when the E2B specimen deformed to tensile strain of 0.04 at the lower temperature of 200^{o}C. However, at higher temperature of 300^{o}C the local neck phenomenon did not occur until a tensile strain of 1.6. It is inferred that deformation mechanism (GBS or dislocation creep) will easily occur at higher temperature. From the viewpoint of strain rate, it is clear to show that local neck phenomenon would occur in an early deformation stage at higher strain rates. Figure 3-38 shows the variation of R for the E2B specimens to different tensile strains. The value of R of the E2B specimen maintained a constant closed to 0.9 at 300^{o}C but is below 0.8 when tested at 200^{o}C. That implies the deformation mechanism is different at 200 and 300^{o}C. At a fixed temperature of 300^{o}C, the variation of R would be moderately affected by strain rate. It appears that strain rate effect is less pronounced than the temperature influence.

3.3.4 Fractography after tensile testing

Figure 3-39 shows the SEM fractographs taken from the billet and E3B specimens after tensile test at room temperature. The as-received billet specimen is brittle and fewer ductile dimples are observed in the fracture surface of this sample. However, the fracture surface of the E3B specimens shows complete grain boundaries, and it is inferred that a specific mechanism would easily occur for finer grain samples. Ohyama et al. [118] reported that when the fine-grained AZ31 Mg alloy was subjected to tensile test at RT and the occurrence of GBS at RT was observed by the displacement of submicron lines drawn across the grain boundaries of deformed samples. It explains that the higher elongation in the E3B specimen could attain via a certain level of GBS at RT.

The macro-fracture surfaces of the E1 and E1B specimens were different (cf. Fig. 3-16), but the similar elongation of ~30% could obtain. SEM fractographs of the E1 and E1B specimens after tensile test at room temperature are shown in Fig. 3-40 and it is observed that small ductile dimples in E1 and smooth areas in E1B. This implies the mechanisms such as GBS and ductile dimple would contribute different degrees for RT tensile elongations for these samples.

The fracture surfaces of the E1B specimens tested at 150^{o}C and various strain rates are investigated, as shown in Fig. 3-41. The exposure of a number of finer grains and ductile dimples were also observed simultaneously. It is evident that both GBS and ductile dimple mechanisms would proceed in the deformation stage. One thing should be noted is that, at lower strain rate of $1x10^{-4}$ s^{-1}, smaller ductile dimples appear and more fine grains are exposed in the fracture area. It indicates directly that the GBS mechanism becomes dominant and that seems to be the reason why the E1B specimen could attain excellent LTSP.

The fracture surface of the E3 specimens tested at various temperatures and strain rates was investigated. The exposure of a number of finer grains indirectly indicated that grain boundaries had slid at the tensile conditions. Figures 3-42 (a)(b)(c) show the fracture surface of the E3 specimen after tensile testing at 300^{o}C and different strain rates. When tested at the higher strain rate of $1x10^{-1}$ s^{-1}, the fracture surface of the E3 specimens showed ductile dimple structure. In contrast, the fracture surface of E3 specimens tested at a strain rate below $8x10^{-3}$ s^{-1} showed complete grain boundaries. It is inferred that different deformation mechanisms will occur at different strain rates. In later sections, the average apparent strain rate sensitivity m data determined by the jump strain rate tests will offer reasonable evidence to describe the phenomenon.

On the other hand, the fracture surface of the E3B specimens tested at various temperatures

and strain rates was investigated. Figure 3-43 shows the fracture surface of the E3B specimens after tensile testing at 150^{o}C and different strain rates. When tested above the strain rate of 1x10^{-3} s^{-1}, the fracture surface of the E3B specimens showed ductile dimple structure but tested at a strain rate below 1x10^{-4} s^{-1} the fracture surface of E3 specimens showed complete grain boundaries. It is inferred that different deformation mechanisms (e.g. GBS) will occur at a low strain rate of 1x10^{-4} s^{-1}. The phenomenon explains that E3B could attain LTSP because of more smooth deformation mechanism undergoing. Figure 3-44 shows the fracture surfaces of the E3B specimens at a fixed strain rate of 1x10^{-3} and different test temperatures. The fracture surface of the E3 specimens showed complete grain boundaries when test temperature is above 200^{o}C. That is why the higher elongation achieves at higher temperature, suggesting specific mechanism such as GBS occurred easily.

3.4 Texture characterization

3.4.1 Texture determined by X-ray diffraction patterns

The X-ray diffraction pattern simulated by computer for completely random Mg powders is presented in Fig. 3-45 (a); the $(10\bar{1}1)$ diffraction is the highest peak. In comparison, Fig. 3-45 (b) shows the experimental X-ray diffraction taken from the cross-sectional plane of the as-received billet. The $\{11\bar{2}0\}$ planes tended to lie on the cross-sectional plane. In other words, the {0002} planes tended to lie on the extruded plate that contains the extrusion axis. This has been typically observed in extruded or rolled Mg alloys [100]. The $\{10\bar{1}1\}$ peak predicted to be the strongest X-ray peak for completely randomly-oriented samples, still ranked second in intensity, suggesting that the overall texture intensity was not significantly strong. In contrast, only one single strong and dominant texture was observed in the severely extruded plate, with

predominantly {0002} basal planes lying on the flat surface of the extruded plate, as seen in Fig. 3-45 (c).

Figure 3-46 shows the X-ray diffraction patterns taken from the E1 rod sample processed with an extrusion ratio of 42:1 at 300^{o}C for the longitudinal and transverse cross-sectional planes, respectively. From Fig. 3-46 (b), the $\{10\bar{1}0\}$ planes are strongly perpendicular to the plane containing the extrusion axis. In other words, the (0002) basal plane should be parallel to the plane contain the extrusion axis. Figure 3-47 shows the X-ray diffraction patterns taken from the E1B sample processed by ECAP for 8 passes at 200^{o}C for the longitudinal and transverse cross-sectional planes, respectively. The (0002) basal planes do not seem to lie on the longitudinal or transversal planes; they seem to lie some angles with respect to the ECAP axis.

3.4.2 Texture evolution during static annealing

The strong {0002} texture did not evolve much during static annealing at 150-300^{o}C for 1-10 h. However, appreciable evolution can be seen in specimens annealed at 350^{o}C, especially after 10 h annealing. Examples of the X-ray diffraction for the annealed E3 specimens are shown in Fig. 3-48. The ratios of the peak intensity of the (0002) reflection and two other peaks, $(10\bar{1}1)$ and $(10\bar{1}3)$, for the AZ31 alloy under various processing and annealing conditions are listed in Table 3-10.

From Table 3-10, it can be seen that the strong {0002} texture induced during severe extrusion was further enhanced by static annealing at 150-300^{o}C for a short period of time for 1 h. Figures 3-49 show X-ray diffraction patterns taken from the severely extruded E3 specimen after further annealing for 1 h at 150, 250, 300, and 350^{o}C. The peak ratio of (0002)/$(10\bar{1}1)$ increased from 14.6 for the as-extruded sample to 23 after annealing at 150^{o}C for 1 h; it was

even further increased up to 60 for the sample annealed at 150^{o}C for 10 h. This suggests that recovery has occurred during the whole annealing treatment at 150^{o}C and during the initial annealing stage at 250 and 300^{o}C. Partial recrystallization seemed to proceed at higher annealing temperatures and longer annealing time. Annealing at 250-300^{o}C for 2-5 h seemed to involve initial recovery and subsequent partial recrystallization, resulting in the optimum grain size and mutual orientation. As described later, this condition happened to correspond to the regime for optimum low temperature and high strain rate superplasticity. At 350^{o}C, the ratios of (0002)/($10\bar{1}1$) and (0002)/($10\bar{1}3$) both decreased to 4-8, meaning more recrystallized grains with orientations other than {0002} have emerged and the overall grain size increased appreciably.

X-ray diffraction texture analysis has also been conducted by Mukai et al. [58] on the AZ31 alloy processed by ECAP. It was reported that the {0002} planes were not preferentially parallel to the extrusion direction, and the room temperature tensile ductility was greatly improved. In this study, the as-extruded or further annealed AZ31 specimens all contained strong {0002} texture, and high tensile elongations at 25-300^{o}C were similarly achieved. It seems that the fine grain size is the most critical factor in obtaining the superior tensile ductility. The strong initial texture was found to be substantially evolved and weakened into more random manner during the tensile straining in Al base alloy [119], and it is interesting to explore whether this also occur in the Mg base alloys.

3.4.3 Texture determined by X-ray pole figures

The X-ray (0002), ($10\bar{1}0$) and ($10\bar{1}1$) pole figures are given in Fig. 3-50 for the E1 (on left) and the E1B (on right) specimens: it should be noted that, in order to protect the X-ray detector, only the poles within 0-80° are constructed. It is apparent as indicated also by the X-ray

diffraction patterns that most of the $\{10\bar{1}0\}$ planes in the extruded condition lie perpendicular to the extrusion axis and it follows therefore that the (0002) planes generally lie parallel to the extrusion axis. By contrast, the (0002) basal planes in the ECAP condition lie primarily within the angular range from 40° to 50° with respect to the pressing direction (or the normal direction, ND, assigned in the pole figures). Since ECAP processing in this investigation was undertaken using a die with a channel angle of 110°, it is reasonable to anticipate the basal planes in the majority of grains rearrange during processing to become close to the theoretical shearing plane as the billet passes through the die.

The X-ray (0002) pole figures for the E2B and the E3 specimens (both 2 mm plates) are shown in Fig. 3-51. It can be seen that the strong {0002} texture induced during severe extrusion process. The {0002} planes tended to lie on the plate that contains the extrusion axis. The X-ray pole figure result is consistent with that of X-ray diffraction pattern. It is clear to know that texture evolution will be changed with process route. In other words, the similar texture will be observed using the same TMT (e.g. extrusion) process.

3.4.4 Texture determined by EBSD

Parallel pole figures were constructed by EBSD for some local regions on the transverse cross-sectional planes in the E1 and E1B specimens and these are shown in Fig. 3-52. In the E1 specimen, it is evident that the $\{10\bar{1}0\}$ planes are perpendicular to the plane containing the extrusion axis. The result is also consistent with the result of the X-ray pole figure and X-ray diffraction pattern. In the E1B specimen, it is noted that most of basal planes depart from the extrusion direction. The distribution of basal plane is similar for the parallel and perpendicular to extrusion direction based on X-ray diffraction pattern. EBSD result of the E1B specimen clearly shows that most basal planes are close to 40-50^{o} from the extrusion and transverse directions.

These EBSD results are similar to the X-ray pole figures and the diffraction patterns thereby providing additional confirmation of these general conclusions.

3.4.5 Texture determined by TEM

Since the XRD and EBSD were both examined on the transverse cross-sectional plane of the extruded or ECAP rods, TEM SAD analysis was also performed on this plane. Figures 3-53 shows that the TEM bright field images and TEM diffraction patterns in the E1 extruded specimen. Around 50 diffraction patterns were collected for each sample. For examples, the $[1\bar{1}00]$ zone is shown in Figs. 3-53 (d)(f)(i) and the angle against the [0001] direction is 90^o. Meanwhile, the $[\bar{1}2\bar{1}0]$ zone is shown in Figs. 3-53 (c)(e), the $[1\bar{5}40]$ shown in Fig. 3-53 (j), $[01\bar{1}1]$ shown in Fig. 3-53 (g) and $[5\bar{1}\bar{4}3]$ shown in Fig. 3-53 (h), the angles against the [0001] are 90^o, 90^o, 47^o and 59^o, respectively. Form all of these results, it is apparent that most angles against the [0001] are close to 90^o. Figure 3-54 shows that the TEM bright field images and TEM diffraction patterns in the E1B ECAP specimen. The angles against the [0001] are also calculated via the same analysis method and the most angles against [0001] are 50^o.

The TEM bight field images and TEM diffraction patterns for the E2 and E3 specimens are also shown in Figs. 3-55 and 3-56, respectively. The most angles against the [0001] are 90^o in the E2 specimen and the {0002} planes in the E3 specimen are parallel to the extrusion direction. These TEM diffraction pattern results are similar to the X-ray and the EBSD pole figures, thereby providing additional confirmation of these general conclusions.

All TEM diffraction patterns were analyzed and all results were marked in the inverse pole figures. There are not enough data on the E3 specimen, hence the inverse pole figures for the preferred orientations can not be constructed. In the constructed inverse pole figures, the texture

tendency for both E1 and E1B could be easily observed. Figure 3-57 shows the inverse pole figures determined by TEM diffraction pattern analysis in the E1 and E1B specimens. A strong preference tended to be perpendicular to (0001) in the E1 extruded rod sample but the strong texture in the E1B ECAP specimen lie primarily with the angular range from 40^{o} to 50^{o} with respect to the pressing direction. Figure 3-58 shows the inverse pole figures determined by TEM diffraction pattern analysis in the E2 specimen. A strong preference tended to be perpendicular to (0001) in the E2 extruded rod sample, which is similar to E1. The average angles for the E1 and E1B specimens against the [0001] direction are around 76 ± 5^{o}C and 50 ± 5^{o}C, respectively. On the other hand, the average angle for the E2 specimens against the [0001] direction is around 80 ± 5^{o}C. These TEM results are similar to the X-ray pole figures and the diffraction patterns thereby providing additional confirmation.

Base on this texture characterization, the situation may be illustrated schematically by showing the predominant grain orientations for the extruded and ECAP conditions as in Fig. 3-59. It is apparent that these different types of texture will impose an influence on the room and low temperature stress-strain curves for the extruded and ECAP conditions. The results for the extruded condition are consistent with earlier reports demonstrating an alignment of the basal planes in the extrusion direction in various Mg alloys [58].

3.4.6 Grain misorientation distributions

With the information of the texture in the AZ31 Mg under the extruded and ECAP conditions, it is essential to learn the local grain misorientation for the adjacent grains, as well as the relative fractions of the low and high angle boundaries (LAB and HAB). It is well known that the grain boundary structure is related to the characteristic interfacial energy, rate of mobility, and the capability of GBS. High angle grain boundaries, which are not of the coincident site

lattice form, are desirable for superplastic flow by GBS.

There are a number of methods to determine the local grain orientations by TEM. In this case, the selected area diffraction (SAD) was used to extract the mutual misorientation of neighboring grains in the illuminated area, using the standard equations to calculate the misorientation angle [112], i.e., the cosine of the angle ϕ between two planes ($h\ k\ i\ l$) and ($d\ e\ f\ g$) is given by the below equation.

$$\cos\phi = [hd + ke + (he + kd)/2 + 3lg*(a/c)^2/4]/ \\ \{[h^2 + k^2 + hk + 3l^2(a/c)^2/4]^{1/2} * [d^2 + e^2 + de + 3g^2(a/c)^2/4]^{1/2}\} \quad . \qquad (3\text{-}4)$$

The above equation is feasible for rough estimation of the mutual angle between two neighboring grains with two well-defined diffraction zone axes. Nevertheless, for most cases, the grains are oriented in directions that are slightly deviated from the in-zone axis. In such a case, the deviations can be calculated on the base of specimen X and Y tilt angles θ that can shift back the specimen to the in-zone axis:

$$\theta = [(X_1 - X_2)^2 + (Y_1 - Y_2)^2]^{1/2}, \qquad (3\text{-}5)$$

where X_1 and Y_1 are the X and Y tile angles for grain 1, and X_2 and Y_2 are the X and Y tile angles for grain 2. Since the indices for a grain has equivalent values such as $(10\bar{1}0)$ or $(0\bar{1}10)$, the extracted mutual angle may exceed 120^o with the inappropriate indices of the grain zone. With the symmetry concept for the HCP crystals, the calculated mutual grain misorientation angles, or $\phi \pm \theta$, can be reduced into the minimum equivalent angular relationship within the stereographic triangle of (0001), $(\bar{1}010)$ and $(\bar{2}110)$ for the HCP crystals.

Since the XRD and EBSD were both examined on the transverse cross-sectional plane of the extruded or ECAP rods, TEM SAD analysis was also performed on this plane. Examples of the SAD patterns taken from various adjacent grains in AZ31 Mg under the as-extruded and as-ECAP conditions are shown in Figs. 3-60 and 3-61, respectively. For instance, the mutual misorientation angle between grains A and B was carefully calculated to be 30^o in the E1 specimen, with the consideration of both ϕ and θ. Around 40 grain boundaries were included for the analysis of grain misorientation distribution. It is known that a meaningful statistic should include more boundaries, but manual identification of the exact grain orientation one by one for a HCP crystal in TEM is tedious and time-consuming. Figure 3-62 presents two representative misorientation distributions determined by TEM for the E1 and E1B specimens, as compared with the theoretical prediction for complete random HCP crystals. It can be seen that the AZ31 Mg extruded at 300^oC to an extrusion ratio of 42:1 possesses a high fraction of 79% for HAB with misorientation angles greater than 15^o. Nevertheless, the HAB fraction for the ECAP specimen also occupies a high value of 69%. The slightly lower HAB faction of the ECAP specimen is a result of a lower processing temperature at 200^oC, during which a certain level of the grains have not completely recrystallized. It follows that some of the low angle boundaries are still retained.

Figure 3-63 presents representative misorientation distributions determined by TEM for the E2 specimen. It can be seen that the AZ31 Mg extruded at 300^oC to an extrusion ratio of 100:1 possesses a high fraction of 76% for HAB with misorientation angles greater than 15^o. The result in the E2 specimen is similar to that in the E1 specimen. It is inferred that the high fraction of HAB with misorientation angles would slightly be changed. Nevertheless, the influence of processing temperature on the fraction of HAB is apparent.

Figure 3-64 shows two representative misorientation distributions for the E1 and E1B

specimens using EBSD. Parallel construction of the grain misorientation distribution has also been conducted using EBSD. Nevertheless, due to both the ease in oxidation on the polished Mg surface and the low backscattering efficiency from the light Mg, the identification of individual grain orientation one by one, and thus the calculation of mutual misorientation and rotation axis become difficult. By scanning over a larger area, the ratio of solved Kikuchi patterns was frequently lower than 50%, making the continuous calculation of mutual misorientation for neighboring fine grains less convincing. Another factor is the spatial resolution of the field emission gun SEM/EBSD, which is about 0.5 μm, close to average grain size of 0.7 μm for the ECAP specimen. As long as one Kikuchi pattern for a particular grain is not properly identified, the mutual misorientation angles for all neighboring grains would fail. Figure 3-64 shows the examples of grain misorientation distributions obtained by EBSD. The low angle portions are frequently unidentified, especially for the extra-fine grains in the ECAP samples. Due to the underestimate of LAB populations, the HAB fractions determined by EBSD of the extruded and ECAP specimens are 94 and 95%, respectively. Even with the apparent error, the EBSD results show consistent grain misorientation distribution for the medium and high angle boundaries. Judging from the TEM and EBSD data, it is evident that there are a sufficient amount of high angle boundaries for the operation of GBS during the superpalstic flow at 150-300^{o}C.

Chapter 4

Analyses on Deformation Mechanisms

4.1 Temperature dependence of elastic modulus

In the analysis of high temperature deformation mechanisms, the temperature dependence of elastic modulus should be taken into account for normalizing the applied stress. From the physical viewpoint, the elastic modulus is related to the bonding energy between atoms. Grain boundaries are considered as defects causing a decrease in the observed bulk elastic modulus. At the temperature around the T_m, the liquid phase is expected to be present at grain boundaries. This might further reduce the value of elastic modulus. The reduction in elastic modulus resulting from the two above defects does not affect the deformation within the grain interior. In the view of classic definition, the change in elastic modulus results from the change in the equilibrium spacing between atoms due to thermal vibration. The elastic modulus used to normalize the stress values at each test temperature was obtained from the relationship for pure magnesium [94-95]. The temperature dependence of elastic modulus (E) is express as

$$E\ (MPa) = 4.3x10^{4}*[1-5.3x10^{-4}\ *(T-300)], \qquad (4\text{-}1)$$

where T is the absolute temperature. The tensile temperatures in the range of 150 to 300^{o}C for the AZ31 Mg alloy are below the incipient partial melting temperature. Therefore, the E is calculated in accordance with the equation.

4.2 Analysis of deformation mechanisms

Typically, when a plastic deformation process occurs in metallic fine-grained solids at elevated temperatures, three possible mechanisms should be considered. The dominating first mechanism is grain boundary sliding, accompanied by accommodation process, e.g. diffusional flow or dislocation slip. Plastic deformation by grain boundary sliding is characterized by n=2 (n=1/m=1/0.5). Grain boundary sliding has strong grain size dependency. The mathematical expression is [8]:

$$\dot{\varepsilon} = A\frac{Eb}{kT}D_{eff}\left(\frac{b}{d}\right)^{p}\left(\frac{\sigma-\sigma_{th}}{E}\right)^{2}, \tag{4-2}$$

where A is a coefficient related to grain boundary structure, k the Boltzmann's constant; D_{eff} the effective diffusion coefficient, including lattice diffusion (D_l) and grain boundary diffusion (D_{gb}), d the grain size, b the Burgers vector; p the grain size exponent, σ_{th} the threshold stress, and E the elastic modulus.

The second acting mechanism might be the power law dislocation creep with an average m value around 0.2 (or n~5) and no grain size dependence. The mathematical expression is [120]:

$$\dot{\varepsilon} = B\frac{Eb}{kT}D_{eff}\left(\frac{\sigma-\sigma_{th}}{E}\right)^{5}, \tag{4-3}$$

where B is another coefficient correspond to dislocation creep.

The last mechanism is the glide controlled creep. In certain alloys, creep is controlled by the glide step in the glide/climb mechanism mainly because solute atoms impede dislocation motion. The value of strain rate sensitivity m is about 0.33 (or n~3). The mechanism also has no grain size dependence. The mathematical expression is [30]:

$$\dot{\varepsilon} = C\frac{kT}{E}D_{s}\left(\frac{\sigma}{E}\right)^{3}, \tag{4-4}$$

where D_s is the diffusion coefficient of the solute atom in the alloy.

From the tensile data on the E1B specimen, it can be seen that the ECAP specimens would attain larger elongations below 200^{o}C. However, the elongation decreased when the tensile temperature was above 250^{o}C. From microstructure results, the grain stability is maintained up to 200^{o}C and the average grain size is below 2 μm. With increasing test temperature, grain growth could easily occur. Therefore, a larger elongation is not achieved. The mechanism for the ECAP E1B specimen will be calculated first for different test temperatures.

On the other hand, from the tensile test on the extruded specimens, it would exhibit excellent elongations in the temperature ranges of 250 to 300^{o}C. With decreasing test temperature below 150^{o}C, the tensile elongation decreased, possibly due to the difficulty is accommodation for GBS. Nevertheless, the excellent elongations for the E2, E3 and E3B specimens could attain at 150^{o}C and a lower strain rate of $1x10^{-4}$ s^{-1}. On the basis of tensile test results and microstructural observations, deformation mechanisms will be examined in two temperature ranges, namely, 150^{o}C to 200^{o}C and 250^{o}C to 300^{o}C. Basically, the deformation mechanism of the ECAP E1B specimens will be analyzed at lower temperature. Furthermore, both the extruded E2 and E3 specimens will be discussed at higher temperatures.

4.2.1 Apparent strain rate sensitivity, m_a

The tensile testing for the E1B specimens were conducted at temperature ranging from 150 to 200^{o}C and initial strain rates from $1x10^{-4}$ to $1x10^{-2}$ s^{-1}. To select the flow stress value for extracting the apparent strain rate sensitivity value, it is necessary to choose a suitable strain level from the true stress-strain curves, and is usually selected at the balance stage between strain hardening and strain softening. In the current case, the flow stress for each strain rate was

determined at a fixed strain of 0.3, and the flow stress as a function of strain rate is plotted in Fig. 4-1. The data in Fig. 4-1 indicate that the flow stress decreases with increasing temperature. At low temperatures (150-200^{o}C), the apparent strain rate sensitivity exponent, m_a, is measured to be around 0.2. Meanwhile, the flow stress for each strain rate for the E1, E2 and E3 specimens was determined at a fixed strain of 0.3, and the flow stress as a function of strain rate over 150 to 200^{o}C is plotted in Fig. 4-2 (a)(b)(c), respectively. It is apparent m_a value increases with increasing test temperature.

At higher superplastic temperatures of 250-300^{o}C, the E3 and E3B extruded exhibited large elongations, and the alloy tended to be strain-hardened first until ε~0.7, followed by rapid softening. Figure 4-3 shows the flow stress at ε~0.3 versus strain rate at various temperatures for the E2 and E3 specimens. At the optimum superplastic temperature within 250-300^{o}C, the apparent strain rate sensitivity m_a values are around 0.3-0.4, suggesting that both GBS and solute drag creep might be involved.

Table 4-1 showed the apparent strain rate sensitivity m_a for all specimens. From the data, it is clear to know that the value increases with increasing test temperature. At lower temperature of 150^{o}C, the m_a value is mostly below 0.2. However, when the tensile temperature is above 250^{o}C, the m_a value is above 0.3. It is inferred that the dominant deformation mechanisms might be different between the lower and higher temperature ranges. It is apparent that similar deformation mechanism would occur in the high-ratio extruded samples.

To understand the variation of the m_a values as a function of strain, the jump-strain-rate test performed by changing strain rate is a promising method (Fig. 2-3). By examining the m_a values measured from the E2 specimens tested at the 200 and 300^{o}C, over $6x10^{-4}$-$1x10^{-3}$ s^{-1}, it is found that the average apparent strain rate sensitivity m_a value are 0.36 and 0.45, respectively (Fig. 4-4).

The m_a value determined by the step-strain-rate test is slightly higher than those measured by the jump-strain-rate test. Presumably, due to the narrow and lower regime of strain rate for the jump tests ($6x10^{-4}$ – $1x10^{-3}$ s^{-1}) than the step tests (10^{-4} – 10^{-1}). From these results, it seems that the dominant deformation mechanisms might be different at these two temperatures. From Fig. 4-4, it is clear to observe that the m_a value generally increased with increasing strain when the samples tested at 300^{o}C. However, when the sample tested at 200^{o}C, the m-value decreased with increasing the strain. According to the results, two things would be noted. First, after considering the threshold stress [121], the true strain rate sensitivity was mostly around 0.4-0.5 (except for the cases at 150 and 200^{o}C), suggesting that GBS was the dominant deformation mechanism at the current test regimes. Second, the GBS proceed smoothly to the total strain when the sample tested at 300^{o}C but the phenomenon would not be observed at 150^{o}C. It is conceivable that excellent superplastic elongation could be attained at 300^{o}C.

The m_a values show in Table 4-1 were measured at around medium strain rate of $1x10^{-3}$ s^{-1} because they would be changed with different strain rates. Table 4-2 shows the measured strain rate sensitivity m_a value for the E2B samples based on the jump strain rate tests. From the results, it is noted that with increasing testing temperature or decreasing testing strain rate, the m-value will increase slightly. The stain rate sensitivity was mostly around 0.5 when tested at 300^{o}C, suggesting that GBS was the dominant deformation mechanism. The typical surface topography SEM micrographs taken from the E2B specimens load 300^{o}C and $6x10^{-4}$ s^{-1} to a strain around 1.28 are shown in Fig. 3-10. Therefore, it is also suggested that the grain boundary sliding occurred at 300^{o}C. Finally, the m_a value for the E2 sample is close to that for E2B. It was shown that the similar deformation mechanism would occur during the same test condition. On the basis of tensile test results and microstructural observations, deformation mechanisms (e.g. σ_{th}, m_t and Q_t) will be examined in two temperature ranges, namely, 150-200^{o}C and 250-300^{o}C.

4.2.2 Threshold stress (σ_{th}) and true stain rate sensitivity (m_t)

The threshold stress could be appreciably high at low deformation temperatures and decreases gradually with increasing temperature [121]. The value of σ_{th} was determined using a linear extrapolation on a double-linear plot $\dot{\varepsilon}^{1/n}$ against σ for selected values of n at each temperature. The fitted straight line intersects the stress axis at zero strain rate and gives the value of σ_{th}. In the higher temperature range of 250^{o}C to 300^{o}C, numerous selections using such as n = 2 and 2.5 were tried. Over the test range, the most probable true stress exponent n_t seems to be 2.5 (or a true strain rate sensitivity m_t of ~0.4), corresponding to higher correlation coefficients R, as shown in Fig. 4-5 for ε = 0.3 but correlation coefficients between n_t ~2 (m_t~0.5) and n_t ~2.5 (m_t~0.4) are very close. For this reason, these two values would be considered individually.

The true stress exponent n_t in the lower temperature range of 150^{o}C to 200^{o}C were also extracted and the examples using n=3 and 3.5 are shown in Fig. 4-6. The true stress rate exponent n_t is found to be close to 3.5 (or m_t~0.28). The result is different from that extracted from the high temperature regime. In general, the stress exponent values found in different classes of polycrystalline solids are n_t~5 for power-law dislocation creep, n_t =3 for solute drag creep and n_t =2 for grain boundary sliding. It is clear to know that different dominating deformation mechanisms have been operating and competing during the lower and higher tensile temperature regimes. The extracted σ_{th} values in E1B for 150 and 200^{o}C at ε = 0.3 are 40.0 and 3.7 MPa (with n_t=3.5) and the values in E3 for 250, 280 and 300^{o}C at ε = 0.3 are 8.6, 6.2 and 1.6 MPa (with n_t=2.5). On the other hand, using the true stress exponent n_t of 2, the extracted σ_{th} values for E3 at 250, 280 and 300^{o}C are 13.7, 10.6 and 4.5 MPa. Park and Mohamed [122] have proposed the following relationship:

$$\frac{n_a}{n_t} = \frac{\sigma}{\sigma - \sigma_{th}}, \tag{4-5}$$

or

$$\frac{m_t}{m_a} = \frac{\sigma}{\sigma - \sigma_{th}}. \tag{4-6}$$

For example, using the true stress exponent n_t of 2.5, the true stress is 12 MPa at 300^{o}C and 1x10^{-3} s^{-1}, and the effective stress σ - σ_{th} would be 10.42 MPa, so the value of $\sigma/(\sigma - \sigma_{th})$ is around 1.15, very close to n_a / n_t. Meanwhile, the true stress is 40.7 MPa at 250^{o}C and 2x10^{-3} s^{-1}, and the effective stress σ - σ_{th} would be 32.1 MPa, so the value of $\sigma/(\sigma - \sigma_{th})$ is around 1.29, also very close to n_a / n_t. Thus, the estimated value of true stress exponent should be reasonable. On the other hand, the true stress exponent n_t of 2 is also considered, the true stress is 12 MPa at 300^{o}C and 1x10^{-3} s^{-1}, and the effective stress σ - σ_{th} would be 7.49 MPa, so the value of $\sigma/(\sigma - \sigma_{th})$ is around 1.6, again very close to n_a / n_t. It appears that the values of n_t of 2.5 and 2 would reach highly similar results. It is conceivable that the appropriate n_t values lie in between 2.5 and 2, thereby both values are tried in the following analyses.

4.2.3 True activation energy, Q_t

Taking the effective flow stress (σ - σ_{th}) into account, the m_t value could be extracted from the slope of the double logarithm plot of the flow stress versus the strain rate, as demonstrated in Fig. 4-7. The m_t values are larger than the m_a values. Without accounting for the temperature-dependent elastic constant term E(T) since the temperature internal for these temperature regime is only 50^{o}C, the true activation energy can be evaluated according to the equations of

$$Q_t = -R\frac{\partial(\ln \dot{\varepsilon})}{\partial(\frac{1}{T})}\Big|_{\sigma-\sigma_{th}}, \quad (4\text{-}7)$$

or

$$Q_t = nR\frac{\partial[\ln(\sigma-\sigma_{th})]}{\partial(\frac{1}{T})}\Big|_{\dot{\varepsilon}}. \quad (4\text{-}8)$$

Using the true stress exponent n_t of 2.5 and taking (σ - σ_{th}) = 8 MPa, the slope of the double linear plot of ln $\dot{\varepsilon}$ against 1000/RT based on Eq. (4-7) is 100 kJ/mole. On the other hand, taking m_t = 0.4 and $\dot{\varepsilon}$ = 8x10^{-4} s^{-1}, the estimated activation energy under constant strain rate based on Eq. (4-8) is 104 kJ/mole (Fig. 4-8). Meanwhile, using the true stress exponent n_t of 2 and taking (σ - σ_{th}) = 10 MPa, the slope of the double linear plot of ln $\dot{\varepsilon}$ against 1000/RT based on Eq. (4-7) is 91 kJ/mole. On the other hand, taking m_t = 0.5 and $\dot{\varepsilon}$ = 8x10^{-4} s^{-1}, the estimated activation energy under constant strain rate based on Eq. (4-8) is 100 kJ/mole (Fig. 4-9). Both of these two values of Q_t over 250 to 300^{o}C were much lower than lattice diffusion of magnesium (135 kJ/mole), higher than grain boundary diffusion of aluminum (84 kJ/mole), but close to grain boundary diffusion of magnesium (92 kJ/mole) [94]. Based on the preceding analysis, it is suggested that the dominant superplastic deformation mechanism over 250 to 300^{o}C in the current AZ31 magnesium alloy includes both GBS (m_t=0.5) and solute drag creep (m_t=0.33) accommodated by dislocation slip and climb, the latter are in turn controlled by grain boundary diffusion.

However, the deformation mechanism is power-law dislocation creep in lower temperature range of 150-200^{o}C. Taking (σ - σ_{th}) = 50 MPa, the slope of the double linear plot of ln $\dot{\varepsilon}$ against 1000/RT based on Eq. (4-7) is 44 kJ/mole. On the other hand, taking m_t = 0.28 and $\dot{\varepsilon}$ = 8x10^{-4} s^{-1}, the estimated activation energy under constant strain rate based on Eq. (4-8) is 45 kJ/mole (Fig. 4-10), which does not correspond to any diffusion process. One thing should be noted that excellent elongations could be achieved in the E1B ECAP specimens at low

temperatures, with a low m_t value. The reason might be due to the fact that the m value is extracted over the strain rate range of 10^{-4} to 10^{-2} s^{-1}. We do not have enough data to extract the m value over the optimum LTSP regime of 10^{-5} to 10^{-4} s^{-1}. Currently, there are not enough ECAP samples for such systematic tests to be run, therefore the correct deformation mechanism for the ECAP specimens at 150-200^{o}C cannot be proven at this stage. Future study is needed.

4.3 Comparison with specimens processed by ECAP

Another processing method used in reducing the grain size and improving the LTSP or HSRSP performance is the ECAP process. The first report might be the result on the AZ91 Mg alloy by Mabuchi et al. in 1997 [55]. The grain size after 8 passes of ECAP (ε = 8.05) at 175^{o}C was 1 μm and a LTSP elongation of 661% was obtained at 200^{o}C and 6 x 10^{-5} s^{-1}. Similar ECAP work was performed on the AZ31 Mg alloy at 200^{o}C, also resulting in fine grain size around 1 μm [58]. The ECAP AZ31 specimens were further annealed at 300^{o}C for 24h in order to form well-defined equiaxed grains with the desired grain orientation [58]; and the room temperature tensile elongation reached an outstanding level of ~50%. In addition, recent ECAP work on pure Mg and dilute Mg-Al binary alloy [48] also showed appreciable improvement of the room temperature mechanical properties.

Table 4-3 compares the previous ECAP work [55,57,58] with the current high-ratio extrusion processing. The true strain experienced by the one-step high-ratio extrusion (ε ~ 5) was slightly lower than that during multiple-pass ECAP (ε ~ 6-8). Also, the working temperature for high-ratio extrusion (250-350^{o}C) was higher than that for ECAP (~200^{o}C). The slight differences in processing strain and working temperature were also reflected by the slightly larger grain size observed in the as-extruded specimens than that in the ECAP ones. However, the current optimum LTSP results based on the high-ratio extrusion experiment appeared to be compatible to

those fabricated by ECAP, both above 600% at low temperatures and low strain rates. The room temperature tensile elongation in specimens processed by high-ratio extrusion or ECAP followed by low-temperature annealing both increased to 35-50%, much higher than commercial larger-grained Mg alloys (mostly < 15%). It should be noted that the high room temperature elongation of 50% obtained in AZ31 specimens subjected to ECAP plus full annealing was due to texture control (with relatively more random texture and a larger grain size of ~ 20 μm) [58], but the current case was mainly due to grain refinement (with strong basal texture and a fine grain size of ~2.5 μm). In any case, it appears that thermomechanical processing using severe plastic deformation means of either high-ratio extrusion or ECAP will be effective in improving the mechanical properties.

4.4 Comparison between extruded AZ31 and AZ91 alloys

Table 4-3 also includes the comparison between the AZ31 and AZ91 Mg alloys processed by the same high-ratio extrusion method. With the higher Al content, and thus with the presence of β ($Mg_{17}Al_{12}$) precipitates, the AZ91 alloy exhibited a higher room temperature tensile strength but lower elongation than the AZ31 counterpart. Meanwhile, the presence of fine β precipitates seemed to be highly effective in controlling the grain size during superplasticity loading at ~300^{0}C. This effect resulted in the superior superplasticity elongation of 1200% at 300^{o}C and 1×10^{-3} s^{-1} observed in the high-ratio extruded AZ91 alloy [52], an elongation which is higher than the 900% at 280^{o}C and 1×10^{-4} s^{-1} obtained from the high-ratio extruded AZ31 alloy. Parallel work on the AZ91 alloys also showed that the one-step extrusion could be replaced by two-step extrusion with the same total accumulated strain [52].

4.5 Texture evolution during thermomechanical treatment

Based on this texture characterization, the situation may be illustrated schematically by showing the predominant grain orientations for the extruded and ECAP conditions (Figure 3-59). It is obviously shown that texture will be changed owing to different process routes. It is apparent that these different types of texture will impose an influence on the room and low temperature stress-strain curves for the extruded and ECAP conditions. Using the stereographic projections for pure Mg, it is concluded that <10$\bar{1}$0>//ED and <$\bar{2}$ $\bar{5}$76>//ED correspond to the extruded and ECAP conditions, respectively, where ED is the extrusion direction. Thus, considering the three primary slip systems in hexagonal structures, namely (i) basal {0001} <11$\bar{2}$0>, (ii) prismatic {10$\bar{1}$0}<11$\bar{2}$0>, and (iii) pyramidal {10$\bar{1}\bar{1}$}<11$\bar{2}$0>, the average Schmid factors may be calculated for each system as summarized in Table 3-11. In the present work, the non-basal slip systems, namely, the prismatic slip system, and pyramidal slip system are all considered in addition to the basal slip system. These calculations show there is a high Schmid factor of 0.27 for basal {0001} <11$\bar{2}$0> slip in the ECAP condition. Because the yielding of materials is dominated by a slip system having higher Schmid factor, it is anticipated these ECAP specimens will exhibit both a lower YS and a higher elongation than for the extruded condition at room temperature.

Ohyama et al. [118] reported that the grain size of the as-rolled sheet of AZ31 Mg alloy was 8 μm. When the samples were subjected to tensile test at room temperature and elevated temperatures, the occurrence of GBS at RT and elevated temperatures was observed by the displacement of submicron lines drawn across grain boundaries of deformed samples. The ratio of GBS strain to total strain increased with increasing test temperature. Based on the results, the AZ31 Mg alloys were subjected to tensile testing at RT and elevated temperatures and GBS is attributed to plastic elongation. As for our superplastic tensile testing at 150-200^{o}C, the partial mechanism for superplastic deformation is grain boundary sliding accommodated by dislocation slip. The mobility of intragranular dislocations also plays an important role in the mechanism. A

reasonable explanation for the superplasticity in the present textured AZ31 Mg alloy would be contributed to the mobility of dislocations in the differently oriented samples. Based on the Schmid factor analysis on the slip systems, it can be realized that the mobility of dislocations in as-ECAP samples is the highest. This means that the overlap of grains and the stress concentration can be more readily relieved by the movement of high mobility of dislocations, at least in the initial stage of superplastic deformation, because the textural structure is little altered by the small amount of grain boundary sliding and grain rotation at this stage. For this reason, the accommodation with respect to the grain boundary sliding and rotation is expected to occur more smoothly, and grain boundary sliding can continue as the partial deformation process. This will lead to lower stress concentrations at the triple points and less occurrences of cavity nucleation, favorable for achieving higher superplastic elongations than as-extruded sample. By contrast, at the higher temperature of 250°C the influence of this more favorable texture is lost through grain growth.

4.6 Design for continuous industry processing line

Basically, the extruded plate could attain excellent elongations and the maximum elongation at room temperature is around 50%. The specimen also could achieve LTSP and HSRSP. At 150^{o}C, the elongation to failure is about 300%. To achieve a minimum tensile elongation of ~100% for forming a cell-phone enclosure, the current severely extruded AZ31 plate need to be heated (for example in boiled water or oil bath) to ~75^{o}C for press forming or press forging. The present results imply that the simple high-ratio extrusion method might be a feasible processing mean for industry applications.

Figure 4-11 shows a design of the continuous press forming using heated oil or water bath. If the oil temperature is heated to 150^{o}C or 75^{o}C and the material tensile elongation could

achieve above 300% or 75%, respectively. The press forming would not need to operate at temperature higher than 300^{o}C. Due to the LTSP of the severely extruded AZ31 plates, the heating temperature could be reduced and the die life could also increase as a result of such lower deformation temperatures. Continuous industrial system is effective in increasing the output of production. There are four parts for the continuous processing system, including the extrudor, transportation, forming machine and grinding machine are shown in Fig. 4-12. Besides, the details of the forming machine are shown in Fig. 4-13 and the apparatus have considered how to filter the bits and pieces. Through the system, the case of electrical production would be efficiently fabricated; meanwhile the deformation efficiency is also improved.

Chapter 5

Conclusions

(1) There have been numerous efforts in processing metallic alloys into fine-grained materials, so as to exhibit HSRSP and LTSP. The current study applied the most simple and feasible one-step extrusion method on the commercial AZ31 magnesium billet to result in HSRSP and LTSP. The one-step extrusion was undertaken using a high extrusion ratio at 280-300^{o}C, and the grain size after one-step extrusion became ~1-4 μm.

(2) The grain size of the AZ31 alloy was reduced from ~75 μm in the billet condition to 2.5 μm by one-step extrusion at 300^{o}C and to 0.7 μm through additionally processing by ECAP for 8 passes at 200^{o}C.

(3) The processed AZ31 specimen exhibited high room temperature tensile elongation of 30-50%.

(4) The extruded plate or bar could easily attain HSRSP and LTSP. Following extrusion and ECAP, the E1B specimen exhibited LTSP with a maximum elongation of ~461% when using a strain rate of $1x10^{-4}$ s^{-1} at 150^{o}C, equivalent to $0.46T_m$. With high-ratio extrusion, the E3B extruded plate also attained higher elongation of 300% at $1x10^{-4}$ s^{-1} and 150^{o}C. Meanwhile, the E1B specimen could attain HSRSP at a strain rate of $1x10^{-2}$ s^{-1} and relatively lower temperature of 200^{o}C and the elongation was 233%. As to the extruded plate or rod, they also could easily attain HSRSP when test temperature is above 200^{o}C. The E2 specimen could achieve excellent elongation of 1000% at $1x10^{-2}$ s^{-1} and 300^{o}C.

(5) A detailed investigation revealed different textures in the extruded and ECAP conditions. These dominant textures were characteristic of $<10\bar{1}0>$//ED in the extruded condition and $<\bar{2}\,\bar{5}\,76>$//ED in the ECAP condition, where ED is the extrusion direction. The results show that the basal planes tend to lie parallel to the extrusion axis in the extruded condition but there is a rearrangement during ECAP and the basal planes become reasonably aligned with the theoretical shearing plane. As to extruded plates, the $\{0002\}$ planes tended to lie on the plane that contains the extrusion axis.

(6) The AZ31 Mg extruded at 300^{o}C to an extrusion ratio of 42:1 possesses a high fraction of 79% for HAB with misorientation angles greater than 15^{o}. Nevertheless, the HAB fraction for the ECAP specimen also occupies a high value of 69%. The slightly lower HAB faction of the ECAP specimen is a result of a lower processing temperature at 200^{o}C, during which a certain level of the grains have not completely recrystallized.

(7) Using the measured textures and the calculated Schmid factors, it is anticipated that the ECAP specimens will exhibit lower yield stresses and higher elongations to failure at room temperature when dislocation slip is the dominant rate-controlling process. This is consistent with the experimental observations.

(8) At loading temperature over 150-200^{o}C, the true strain rate sensitivity, m_t, is determined to be 0.28, suggesting that power-law dislocation creep is the rate-controlling mechanism. However, the true activation energy, Q_t, determined to be ~44 kJ/mole, do not correspond to any accommodation processes. It should be partly due to thermal activated dislocation slip mechanism. In addition excellent elongation could achieve at lower temperature but the m_t value is relatively low. The reason is that experimental strain rate is higher resulting

in measuring the lower m_t value. Currently no enough ECAP samples could be offered and therefore the correct deformation mechanism was not proved.

(9) At loading temperatures over 250-300^oC, the m_t value for extruded specimens is measured to be ~0.4-0.5, implying the major deformation mechanism is grain boundary sliding and minor one is solute drag creep. The true activation energy, Q_t, is determined to be ~90-100 kJ/mole, the dominant diffusion process is grain-boundary diffusion.

(10) To achieve a minimum tensile elongation of ~100% for forming a cell-phone enclosure, the current severely extruded AZ31 plate need to be heated (for example in boiled water or oil bath) to ~75^oC for press forming or press forging. The present results imply that simple high-ratio extrusion method might be a feasible processing mean for industry applications.

References

[1] S. Hori, M. Tokizane and N. Furushiro, Superplasticity in Advanced Materials. The Japan Society of Research on Superplasticity, Osaka Japan, (1991).

[2] H. Chokshi, A. K. Mukherjee and T. G. Langdon, Mater. Sci. Eng., R10 (1993) p.1.

[3] T. G. Nieh, J. Wadsworth and O. D. Sherby, in Superplasticity in Metals and Ceramics, (1997).

[4] M. Kawazoe, T. Shibata, T. Mukai and K. Higashi, Scripta Mater., 36 (1997) p. 699.

[5] J. W. Edington, Metall. Trans. A, 13A (1982) p. 703.

[6] O. D. Sherby and J. Wadsworth, Prog. Mater. Sci., 33 (1989) p. 169.

[7] I. C. Hsiao and J. C. Huang, Metall. Trans. A, 33A, (2002) p.1373.

[8] O. D. Sherby and J. Wadsworth, in Deformation, Processing and Structure, ed. G. Krauss, ASM, Metal Park, Ohio, (1984) p. 355.

[9] T. G. Nieh and J. Wadsworth, Scripta Mater., 28 (1993) p. 1119.

[10] Z. Cui, W. Zhong and Q. Wei, Scripta Mater., 30 (1994) p.123.

[11] H. S. Cho, H. G. Jeong, M. S. Kim and H. Yamagata, Scripta Mater., 42 (2000) p. 221.

[12] M. Mabuchi, K. Higashi, K. Inoue and S. Tanimura, Scripta Mater., 26 (1992) p. 1839.

[13] M. Mabuchi, K. Higashi, Y. Okada, S. Tanimura, T. Imai and K. Kubo, Scripta Mater., 25 (1991) p. 2517.

[14] M. Mabuchi, K. Higashi, Y. Okada, S. Tanimura, T. Imai and K. Kubo, Scripta Mater., 25 (1991) p. 2003.

[15] T. G. Nieh, C. A. Henshall and J. Wadsworth, Scripta Mater., 18 (1984) p.1405.

[16] R. S. Mishra, R. Z. Valiev, S. X. McFadden, R. K. Islamgaliev and A. K. Mukherjee, Scripta Mater., 40 (1999) p. 1151.

[17] M. Mabuchi, T. Asahina, H. Iwasaki and K. Higashi, Mater. Sci.Tech., 13 (1997) p. 825.

[18] T. G. Nieh and J. Wadsworth, Scripta Mater., 32 (1995) p. 1133.

[19] T. G. Nieh, A. J. Schwartz and J. Wadsworth, Mater. Sci. Eng., A208 (1996) p. 30.

[20] S. W. Lim, T. Imai, Y. Nishida and T. Choh, Scripta Mater., 32 (1995) p. 1713.

[21] S. X. McFadden, R. S. Mishra, R. Z. Valiev, A. P. Zhilyaev and A. K. Mukherjee, Nature, 398 (1999) p. 684.

[22] R. Z. Valiev, A. V. Korznikov and R. R. Mulyukov, Mater. Sci. Eng., A168 (1993) p.141.

[23] A. V. Sergueeva, V. V. Stolyarov, R. Z. Valiev and A. K. Mukherjee, Scripta Mater., 43 (2000) p. 819.

[24] H. P. Pu and J. C. Huang, Scripta Metall. Mater., 28 (1993) p. 1125.

[25] I. C. Hsiao and J. C. Huang, Scripta Mater., 40 (1999) p.697.

[26] H. Watanabe, T. Mukai, T. G. Nieh and K. Higashi, Scripta Mater., 42 (2000) p.249.

[27] T. K. Ha, W. B. Lee, C. G. Park and Y. W. Chang, Metall. Mater. Trans. 28A (1997) p.1711.

[28] V. M. Imayev, G. A. Salishchev, M. R. Shagiev, A. V. Kuznetsov, R. M. Imayev, O. N. Senkov and F. H. Froes, Scripta Mater., 40 (1999) p.183.

[29] T. R. McNelley, A. V. Korznikov and R. R. Mulyukov, Metall. Trans., 17A (1986) p. 1035.

[30] J. Weertman, J. Appl. Phys., 28 (1957) p. 1185.

[31] W. R. Cannon and O. D. Sherby, Metall. Trans., 1 (1970) p. 1030.

[32] X. Wu and Y. Liu, Scripta Mater., 46 (2002) p. 269.

[33] Y. Liu, X. Wu, Z. Li and Y. Xu, in Proceedings of International Symposium on Materials Science and Technology, 1 (2000) p. 127.

[34] Xin Wu, Yi Liu and Hongqi Hao, Mater. Sci. Forum, 357-359 (2001) p. 363.

[35] 陳錦修，工業材料，186 期，(2002) p. 148.

[36] 林景扶， 工業材料，152 期，(1999) p. 81.

[37] 楊智超， 工業材料，152 期，(1999) p. 72.

[38] S. Spigarelli, Scripta Mater., 42 (2000) p. 397.

[39] H. Watanabe, H. Tsutsui, T. Mukai, K. Ishikawa, Y. Okanda, M. Kohzu and K. Higashi, Mater. Sci. Forum, 350-351 (2000) p. 171.

[40] H. Somekawa, M. Kohzu, S. Tanabe and K. Higashi, Mater. Sci. Forum, 350-351 (2000) p.177.

[41] R. W. Cahn, P. Haasen and E. J. Kramer, Materials Science and Technology, Structure and Properties of Nonferrous Alloys, 8 (1996) p. 131.

[42] T. Lyman, H. E. Boyer, P. M. Unterweiser, J. E. Foster, J. P. Hontas and H. Lawton, in Metals Handbook, Metals park, Ohio, (1975).

[43] T. Narutani and J. Takamura, Acta Mater., 39 (1991) p. 2037.

[44] G. Nussbaum, P. Sainfort and G. Regazzoni , Scripta Mater., 23 (1989) p. 1079.

[45] D. Lahaie, J. D. Embury, M. M. Chadwick and G. T. Gray, Scripta Mater., 27 (1992) p. 139.

[46] T. M. Yue, H. U. Ha and N. J. Musson, J. Mater. Sci., 30 (1995) p. 2277.

[47] J. Kaneko, M. Sugamata and N. Hisata, Mater. Sci. Forum, 304-306 (1999) p. 85.

[48] A. Yamashita, Z Horita and T. G. Langdon, Mater. Sci. Eng., A300 (2001) p. 142.

[49] J. K. Solberg, J. Torklep, O. Bauger and H. Gjestland, Mater. Sci. Eng., A134 (1991) p. 1201.

[50] T. Mohri, M. Mabuchi, M. Nakamura, T. Asahina, H. Iwasaki, T. Aizawa, K. Higashi, Mater. Sci. Eng., A290 (2000) p. 139.

[51] 林鉉凱，“析出型 AZ91 低溫超塑性之研究”，國立中山大學材料科學與工程研究所碩士論文，2000。

[52] H. K. Lin and J. C. Huang, Key Engineering Materials, 233-236 (2002) p. 875.

[53] T. G. Langdon, Metal. Trans., 13A (1982) p. 689.

[54] S. Lee, A. Utsunomiya, H. Akamatsu, K. Neishi, M Furukawa, Z. Horita and T. G. Langdon, Acta Mater., 50 (2002) p. 553.

[55] M. Mabuchi, H. Iwasaki, K. Yanase and K. Higashi, Scripta Mater., 36 (1997) p. 681.

[56] M. Nabuchi, M Nakamura, K. Ameyama, H. Iwasaki and K. Higashi, Mater. Sci. Forum, 304-306 (1999) p. 67.

[57] M. Mabuchi, K. Ametama, Iwasaki and K. Higashi, Acta mater., 47 (1999) p. 2047.

[58] T. Mukai, M. Yamanoi, H. Watanabe and K. Higashi, Scripta Mater., 45 (2001) p.89.

[59] L. Cisar, Y. Yoshida, S. Kamado, Y. Kojima and F. Watanable, Mater. Sci. Forum, 419-422 (2003) p. 249.

[60] Y. Yoshida, L. Cisar, S. Kamado and Y. Kojima, Mater. Trans., 44 (2003) p. 468.

[61] K. J. Kim, S. I. Hong, Y. S. Kim, S. H. Min, H. T. Jeong and J. D. Lee, Acta Mater., 51 (2003) p. 3293.

[62] K. Matsubara, Y. Miyahara, Z. Horita, T. G. Langdon, Acta Mater., 51(2003) p. 3037.

[63] H. Watanabe, T. Mukai, S. Kamado, Y. Kojima and K. Higashi, Mater. Trans., 44 (2003) p. 463.

[64] H. Watanabe, T. Mukai, K. Ishikawa and K. Higashi, Scripta Mater., 46 (2002) p. 851.

[65] T. Liu, W. Zhang, S. D. Wu, C. B. Tiang, S. X. Li and Y. B. Xu, Mater. Sci. Eng., A360 (2003) p. 345.

[66] Z. Horita, K. Matsubara, K. Makii and T. G. Langdon, Scripta Mater., 47 (2002) p. 255.

[67] Y. Yoshida, L. Cisar, S. Kamado and Y. Kojima, Mater. Tran., 43 (2002) p. 2419.

[68] H. K. Lin, J. C. Huang and T. G. Langdon, submitted to Mater. Sci. Eng., A., (2005).

[69] H. Watanabe, T. Mukai, K. Ishikawa, Y. Okanda and K. Higashi, J. Jpn. Inst. Light Metals, 49 (1999) p. 401.

[70] H. watanabe, H. Tsutsui, T. Mukai, K. Ishikawa, Y. Okanda, M. Kohzu and K. Higashi, Mater. Sci. Forum, 350-351 (2000) p. 171.

[71] H. K. Lin and J. C. Huang, Mater. Trans., 43 (2002) p. 2424.

[72] Y. N. Wang and J. C. Huang, Scripta Mater., 48 (2003) p. 1117.

[73] M. Mabuchi, K. Kubota and K. Higashi, Mater. Trans., JIM, 36 (1995) p. 1249.

[74] R. G. Chang (under the guidance of J. W. Yeh): Mater Thesis, Tsing Hua University, 2000.

[75] H. Watanabe, T. Mukai and K. Higashi, Scripta Mater., 40 (1999) p. 477.

[76] H. Watanabe, T. Mukai and K. Higashi, Mater. Sci. Forum, 304-306 (1999) p.303.

[77] H. Watanabe, T. Mukai, M. Mabuchi and K. Higashi, Scripta Mater., 41 (1999) p. 209.

[78] Y. Chino, M. Mabuchi, K. Shimojima, Y. Yamada, C. Wen, K. Miwa, M. Nakamura, T. Asahina, K. Higashi and T. Aizawa, The Autumn-Metting of the Japan Institute of Metals in Nagoya (2000).

[79] D. M. Lee, B. K. Suh, B. G. Kim, J. S. Lee and C. H. Lee, Mater. Sci. Tech., 13 (1997) p. 590.

[80] T. Mukai, T. G. Nieh, H. Iwasaki and K. Higashi, Mater. Sci. Tech., 14 (1998) p. 32.

[81] A. Galiyev and R. Kaibyshev, Scripta Mater., 51 (2004) p. 89.

[82] M. Mabuchi, Y. Chino, H. Iwasaki, T. Aizawa and K. Higashi, Mater. Trans. 42 (2001) p. 1182.

[83] K. Nakashima, H Iwasaki, T. Mohri, M. Mabuchi, M. Nakamura, T. Asahina and K. Higashi, Mater. Sci. Forum, 350-351 (2000) p. 87.

[84] R. Kariya, H. Iwasaki, T. Mohri, M. Mabuchi, M. Nakamura, T. Asahina and K. Higashi, Mater. Sci. Forum, 350-351 (2000) p. 93.

[85] T. Mohri, M. Mabuchi, N. Saito and M. Nakamura, Mater. Sci. Eng., A257 (1998) p. 287.

[86] S. Kamado, T. Ashie, H. Yamada, K. Sanbun and Y. Kojima, Matre. Sci. Forum, 350-351 (2000) p. 65.

[87] Y. Z. Lu, Q. D. Wang, W. J. Ding, X. Q. Zeng and Y. P. Zhu, Mater. Letters, 44 (2000) p. 265.

[88] R. E. Reed-Hill, Physical Metallurgy Principles, PWS publishing company, Boston, America (1994) p. 729.

[89] T. Imai, S. W. Lim, D. Jiang and Y. Nishida, Scripta Mater., 36 (1997) p. 611.

[90] M. Mabuchi, K. Kubota and K. Higashi, Scripta Mater., 33 (1995) p.331.

[91] H. Watanabe, T. Mukai, K. Ishikawa and K. Higashi, Mater. Trans., 43 (2002) p. 78.

[92] M. Mabuchi, K. Shimojima, Y. Yamada, C. E. Wen, M. Nakamura, T. Asahina, H. Iwaski, T. Aizawa and K. Higashi, Mater. Sci. Forum, 357-359 (2001) p. 327.

[93] H. Watanabe, T. Mukai, K. Ishikawa and K. Higashi, Scripta Mater., 46 (2002) p. 851.

[94] H. J. Frost and M. F. Ashby, in Deformation Mechanism Maps, Pergamon, Oxford, (1982).

[95] W. J. Kim, S. W. Chung, C. S. Chung and D. Kum, Acta mater., 49 (2001) p. 3337.

[96] H. Watanabe, T. Mukai, M. Kohzu, S. Tanabe and K. Higashi, Acta mater., 14 (1999) p.3753.

[97] H. Watanabe, H Tsutsui, T. Mukai, M. Kohzu, S. Tanabe, K. Higashi, Inter. J. Plasticity, 17 (2001) p. 387.

[98] K. Kubota, M. Mabuchi and K. Higashi, J. Mater. Sci., 34 (1999) p. 2255.

[99] C. M. Lombard, A. K. Ghosh and S. L. Semiatin, Metall. Mater. Trans., 32A (2001) p. 2769.

[100] J. Pilling and N. Ridley, Superplasticity in Aerospace, H. C. Heikkenen and T. R. McNelley, eds., TMS, Warrendale, PA, (1988) p. 183.

[101] A. H. Chokshi and A. K. Mukherjee, Mater. Sci. Eng., A110 (1989) p. 49.

[102] J. V. Aguirre, H. Hosokawa and K. Higashi, The Fourth Pacific Rim International Conference on Advanced Materials and Processing, (2001) p. 2039.

[103] H. Iwaskai, T. Mori, M. Mabuchi and K. Higashi, The Fourth Pacific Rim International Conference on Advanced Materials and Processing, (2001) p. 1995.

[104] B. D. Cullity, Elements of X-Ray Diffraction, Addison-Wesley publishing company, America (1978) p. 295.

[105] Link Opal Operater's Guide, Opalman 3.0, Issue 1, Oxford Instruments plc, Buckingghamshire, UK, (1997).

[106] V. Randle, Oxford Guide Book Series, Electron Backscatter Diffraction, (1996), p. 3.

[107] V. Randle, Microtexture Determination and Its Applications, Institute of Materials, London, (1992), p. 20.

[108] M. R. Barnett, Journal of Light Metals, 1 (2001) p. 167.

[109] M. T. Perez-Prado and O. A. Ruano, Scripta Mater., 46 (2002) p. 149.

[110] M. Furukawa, Y. Iwahashi, Z. Horita, M. Nemoto, T. G. Langdon, Mater. Sci. Eng., A257 (1998) p. 328.

[111] 普翰屏，“8090 鋁鋰合金低溫與高溫超塑板材之製程開發與形變機構分析”， 國立中山大學材料科學與工程研究所博士論文，1995.

[112] D. B. Williams and C. B. Carter. Transmission Electron Microscopy. Plenum Pub. Press, New York. (1996).

[113] C. J. Lee and J. C. Huang, Acta Mater., 52 (2004) p. 3111.

[114] Y. N. Wang and J. C. Huang, Metall. Mater. Trans. 35A (2004) p. 555.

[115] S. H. Wu, J. C. Huang and Y. N. Wang, Metall. Mater. Trans. 35A (2004) p. 2455.

[116] T. Mukai, K. Ishikawa and K. Higashi, Mater. Sci. Eng., A204 (1995) p. 12.

[117] B. Y. Lou, J. C. Huang, T. D. Wang and T. G. Langdon, Mater. Tran. 43 (2002) p. 501.

[118] R. Ohyama, J. Koike, T. Kobayashi, M. Suzuki and K. Maruyama, Mater. Sci. Forum Vols. 419-422 (2003) p. 237.

[119] I. C. Hsiao, S. W. Su and J. C. Huang, Metall. Mater. Trans. 26A (2000) p. 2169.

[120] A. Ball and M. M. Hutchinson, Met. Sci. J., 3 (1969) p. 1.

[121] R. S. Mishra, T. R. Bieler and A. K. Mukherjee, Acta Metall. Mater., 43 (1995) p. 877.

[122] K-T. Park and F. A. Mohamed, Metall. Mater. Trans. 26A (1995) p. 3119.

Table 1-1 Summary of the typical HSRSP materials [9-20].

Material	Grain size (μm)	Temperature (^{o}C)	Strain rate (s^{-1})	Elongation (%)	Reference
A2124-0.6Zr	1	425-500	$3x10^{-1}$	500	[9]
AL-Li-Mg-Cu-Zr	4	490-580	$1.4x10^{-1}$	250	[10]
Al-16Si-5Fe	0.8	520	$1.38x10^{-1}$	400	[11]
5052Al-20Si_3N_{4p}	1	545	1	700	[12]
6061Al-20Si_3N_{4p}	1	560	2	620	[13]
6061Al-20Si_3N_{4p}	3	545	$1x10^{-1}$	450	[14]
2124Al-20SiC_w	--	525	$3x10^{-1}$	300	[15]
2009Al-15SiC_w	1	525	$1x10^{-1}$	230	[16]
PM AZ91	1	300	$1x10^{-2}$	280	[17]
IM AZ91	4.1	300	$2x10^{-2}$	250	[17]
		275	$2x10^{-2}$	330	[17]
ZK60/SiC	0.5	400	1	350	[18,19]
Mg/5Zn/10TiC	2-5	470	$0.67x10^{-2}$	340	[20]

Table 1-2 List of the reports on LTSP [24-29].

Material	Processing	Grain size (μm)	Temperature (^{o}C)	Strain rate (s^{-1})	Elongation (%)	Reference
Al-10Mg-0.5Mn	TMT	--	300	$1x10^{-3}$	400	[29]
Al-4Cu-0.5Zr	Torsion	0.3	220	$3x10^{-4}$	250	[22]
Al-8090	TMT	0.7	350	$8x10^{-4}$	710	[24]
Al-5083	TMT	0.5	230	$2x10^{-3}$	511	[25]
Mg-AZ91	ECAE	1	200	$6x10^{-5}$	661	[55]
Mg-ZK60/SiC	Extrusion	1.7	190	$1x10^{-2}$	337	[26]
Zn-0.3Al	TMT	1	25	$2x10^{-4}$	1400	[27]
Ti-6Al-4V	Torsion	0.15	650	$1x10^{-2}$	305	[23]
Ti-48Al	Forging	0.7	800	$8x10^{-4}$	355	[28]
Ni	Deposition	0.02	350	$1x10^{-3}$	300	[21]
Ni_3Al	Torsion	0.05	650	$1x10^{-3}$	375	[21]

Table 1-3 Some characters compared among magnesium, steels, cast irons, copper, aluminum alloys and engineering plastics [35].

Material	Cast Mg	Wrought Mg	Cast Iron	Steel	Cast Al	Wrought Al	Plastics (PC/ABS)
Alloy	AZ91	AZ31-H24	Class 40	Galva-Nized	380	6061-T6	Dow Pulse 2000
Process	Die cast	Sheet	Sand cast	Sheet	Die cast	Extrusion	Injection
Density (g/cm^3)	1.81	1.77	7.15	7.8	2.68	2.7	1.13
Elastic modulus (GPa)	45	45	100	210	71	69	2.3
Yield stress (MPa)	160	220	--	200	159	275	53
Tensile Stress (MPa)	240	290	293	320	324	310	55
Elongation (%)	3	15	0	40	3	12	125
Thermal conductivity (W/m K)	51	77	41	46	96	167	--
Coeff. Of thermal expansion (mm/m K)	26	26	10.5	11.7	22	23.6	74
Melting point (^oC)	598	630	1175	1515	595	652	160 (Tg)

Table 1-4 The physical or mechanical characters in magnesium [41].

Property	Temperature (^{o}C)	Value
Atomic number		12
Relative atomic mass		23.3050
Natural isotopes		79%$_{12}{}^{24}$Mg 10%$_{12}{}^{25}$Mg 11%$_{12}{}^{26}$Mg
Melting point		(650±0.5)^{o}C
Boiling point		1090 ^{o}C
First ionization energy		7.646 eV
Structure	25	Hexagonal (hP2)
a	25	0.32094 nm
c	25	0.52107 nm
c/a	25	1.6236
Density	25	1736 kg/m^3
Electrical resistivity	20	4.46*10^{-8} Ωm
(polycrystalline)	600	17.0*10^{-8} Ωm
Elastic moduli C_{11}	25	59.3 GPa
Elastic moduli C_{33}	25	61.5 GPa
Elastic moduli C_{44}	25	16.4 GPa
Elastic moduli C_{12}	25	25.7 GPa
Elastic moduli C_{13}	25	21.4 GPa
Young's modulus of polycrystalline Mg	25	45 GPa
Poisson's ratio of polycrystalline Mg	25	0.35
Coeff. of thermal expansion parallel to a	25	24.7*10^{-6} /K
Coeff. of thermal expansion parallel to a	25	29.8*10^{-6} /K
Coeff. of thermal expansion parallel to c	27	25.7*10^{-6} /K
Coeff. of thermal expansion parallel to c	527	30.5*10^{-6} /K
Coeff. of thermal expansion polycrystalline	27	25.0*10^{-6} /K
Coeff. of thermal expansion polycrystalline	527	30.0*10^{-6} /K
Linear contraction	650-20	1.9%
Volume contraction liquid-solid	650	4.2%
Heat capacity C_p	27	24.86 J/mol K
Heat capacity C_p	527	31.05 J/mol K
Entropy S	27	32.52 J/mol K
Entropy S	527	59.72 J/mol K
Enthalpy H-$H_{25\,^{o}C}$	527	14057 J/mol K
Thermal conductivity	27	156 W/m K
Thermal conductivity	527	1456 W/m K
Thermal diffusivity	27	0.874 cm^2/s
Electrochemical potential (Normal hydrogen electrode)		-2.37 V
Rel. machining power Mg alloy: Al alloy		1:1.8
Rel. machining power Mg alloy: cast iron		1:3.5
Rel. machining power Mg alloy: Ni alloy		1:10

Table 1-5 The standard four-part ASTM alloy designation system and the temper for the magnesium alloys [42].

First part	Second part	Third part	Fourth part
Indicates the two principal alloying element	Indicates the amounts of the two principal	Distinguishes between different alloys with the same percentages of the two principal alloying elements	Indicates condition (temper)
Consists of two code letters representing the two main alloying elements arranged in order of decreasing percentage (or alphabetically if percentages are equal)	Consists of two numbers corresponding to rounded-off percentages of the two main alloying elements and arranged in same designations in first part	Consists of a letter of the alphabet assigned in order as compositions become standard	Consists of a letter followed by a number (separated from the third part of the designation by a hyphen)
A-Aluminum E-Rare Earth H-Thorium K-Zirconium M-Manganese Q-Sliver S-Silicon T-Tin W-Yttrium Z-Zinc	Whole numbers	Letters of alphabet except I and O	F-AS fabricated O-Annealed H10 and H11-Strain hardened H23, H24 and H26-Strain hardened and partially annealed T4-Solution heat treated T5-Artificially aged only T6-Solution heat treated and artificially aged

Table 1-6 The relationship between grain size and mechanical properties of AZ91 [45].

Heat treatment	Grain size	Volume fraction of the β phase	Yield stress
Rapidly solidified and extruded	1.2 μm	0.18	445 MPa
Annealed at 400^{o}C for 1 hour and air cooled	15 μm	0.06	320 MPa

Table 1-7 The effect of separate solute additions of elements on the mechanical properties [41].

Element	Melting and casting behavior	Mechanical and technological properties	Corrosion behavior I/M produced
Ag		Improves elevated temperature tensile and creep properties in the presence of rare earths	Detrimental influence on corrosion behavior
Al	Improves castability, tendency to microporosity	Solid solution hardener, precipitation hardening at low temperatures (< 120^{o}C)	Minor influence
Be	Significantly reduces oxidation of melt surface at very low concentrations (< 30 ppm), leads to coarse grains		
Ca	Effective grain refining effect, slight suppression of oxidation of the molten metal	Improves creep properties	Detrimental influence on corrosion behavior
Cu	System with easily forming metallic glasses, improves castability		Detrimental influence on corrosion behavior, limitation necessary
Fe	Magnesium hardly reacts with mild steel crucibles		Detrimental influence on corrosion behavior, limitation necessary
Li	Increases evaporation and burning behavior, melting only in protected and sealed furnaces	Solid solution hardener at ambient temperatures, reduces density, enhances ductility	Decreases corrosion properties strongly, coating to protect from humidity is necessary
Mn	Control of Fe content by precipitating Fe-Mn compound, refinement of	Increases creep resistivity	Improves corrosion behavior due to iron control effect

	precipitates		
Ni	System with easily forming metallic glasses		Detrimental influence on corrosion behavior, limitation necessary
Rare earths	Improve castability, reduce microporosity	Solid solution and precipitation hardening at ambient and elevated temperature tensile and creep properties	Improve corrosion behavior
Si	Decreases castability, forms stable silicide compounds with many other alloying elements, compatible with Al, Zn and Ag, weak grain refiner	Improves creep properties	Detrimental influence
Th	Suppresses microporosity	Improves elevated temperature tensile and creep properties, improves ductility, most efficient alloying element	
Y	Grain refining effect	Improves elevated temperature tensile and creep properties	Improves corrosion behavior
Zn	Increases fluidity of the melt, weak grain refiner, tendency to microscopy	Precipitation hardening, improves strength at ambient temperatures, tendency to brittleness and hot shortness unless Zr refined	Minor influence, sufficient Zn content compensates for the detrimental effect of Cu
Zr	Most effective grain refiner, incompatible with Si, Al, and Mn, removes Fe, Al and Si from the melt		

Table 1-8 Summary of the ECAP applications for Mg alloys.

Material subjected to ECAP							
Material	Condition before ECAP	Original grain size (μm)	ECAP T (^{o}C)	ECAP Processing route	ECAP Number pass	Final grain size (μm)	Reference
Pure Mg	Rolled	Annealing 500^{o}C, 1h 400 μm	400	Bc	2	110	[48]
Mg-0.9%Al	Rolled	Annealing 400^{o}C, 1h 100 μm	200	Bc	2	17	
			300	Bc	2	48	
			400	Bc	2	78	
AZ31	Extruded	---	250	180-90-180	4	---	[59]
AZ31	Wrought Mg	---	200	Bc	8	1	[58]
AZ31	Extruded	11	200	180	2	2.4	[60]
			250	180	2	2.9	
			300	180	2	4.1	
			200	180-90-180	4	1.9	
			250	180-90-180	4	2.7	
			300	180-90-180	4	3.4	
AZ61	Extruded	24.4	275	Bc	1	15.8	[61]
					4	10.6	
					8	8.4	
AZ91	Extruded	---	175	---	Strain intensity of 6.343	0.7	[55,57]
Mg-9%Al	Cast + extruded	12	200	Bc	2	0.7	[62]
			300	Bc	4	10	
WZ73	Extruded	---	350	Bc	6	1.6	[63]
ZK60	Extruded	---	160	Bc	8	Annealing 200^{o}C, 1.8ks 1.4	[64]

Mg-8%Li-1%Al	Cast+ Extruded	α Phase 25	130	A	1	1-5	[65]
			130	A	4	0.5	
		β Phase 18	130	A	4	0.2	
Mg-0.6%Zr	Extruded	11	300	---	1	1	[66]
Mg-10%Li-1%Zn	Cast	---	50	180-90-180	6	---	[67]
AZ31	Extruded	2.5	200	Bc	8	0.7	[68]

Table 1-9 Evidence of superplasticity at low temperatures after ECAP.

Material	Grain size (μm)	Strain rate (s^{-1})	T (^oC)	UTS (MPa)	Elongation (%)	Reference
ZK60	1.4	$1x10^{-5}$	200	---	1083	[64]
AZ91	0.7	$6.2x10^{-5}$	200	22	661	[55,57]
Mg-9%Al	0.7	$3.3x10^{-4}$	200	50	840	[62]
Mg-0.6%Zr	1	$3.3x10^{-4}$	300	38	>400	[66]
Mg-10%Li-1%Zn	---	$1x10^{-3}$	150	28	391	[67]
AZ31	0.7	$1x10^{-4}$	150	81	461	[68]

Table 1-10 Room temperature tensile properties after ECAP.

Material	Grain size (μm)	YS (MPa)	UTS (MPa)	Elongation (%)	Reference
Pure Mg	110	105	125	2.5	[48]
Mg-0.9%Al	17	145	230	12	
	48	70	210	17.5	
	78	95	198	15	
AZ31	---	190	280	33	[59]
AZ31	1	---	270	46	[58]
AZ31	2.4	---	200	8	[60]
	2.9	---	275	25	
	4.1	---	285	17	
	1.9	---	225	27	
	2.7	---	230	35	
	3.4	---	275	20	
AZ61	8.4	154	310	55	[61]
	10.6	191	317	42	
	15.8	193	302	34	
WZ73	1.6	293	350	18	[63]
Mg-8%Li-1%Al	1-5	170	201	13	[65]
	0.5	198	224	26	

Table 1-11 Comparison of superplastic properties in commercial AZ and ZK series Mg alloys without ECAP.

Alloy	Processing Mean	Grain size (μm)	Test temp (^{o}C)	Strain rate (s^{-1})	Elongation	Ref.
AZ31	Extrusion	5	325	$1x10^{-4}$	608%	[69]
AZ31	Extruded rod	---	450	$1x10^{-5}$	596%	[70]

	Extruded sheet	---	375	$6x10^{-5}$	200%	
AZ31	HR extrusion	2.5	280	$1x10^{-4}$	900	[71]
AZ61	Extrusion	6	350	$1x10^{-4}$	920	[72]
AZ91	RS+extrusion	---	250	$3.3x10^{-3}$	>500%	[49]
			275		>1000%	
			300		>1000%	
AZ91	PM+extrusion	1.4	300	$1x10^{-2}$	280%	[17]
	IM+extrusion	4.1	250	$3x10^{-4}$	430%	
AZ91	Extrusion	7.6	300	$1x10^{-5}$	310%	[73]
AZ91	Extrusion	15.4	300	$1x10^{-5}$	150%	
AZ91	Reciprocal extrusion		300	$1x10^{-3}$	1000%	[74]
AZ91	HR extrusion	2.5	300	$1x10^{-3}$	>1000%	[52]
AZ105	PM+extrusion	-----	200	$2x10^{-3}$	53%	[47]
			300	$2x10^{-3}$	400%	
			300	$2x10^{-2}$	900%	
AZ105	IM+extrusion	----	200	$2x10^{-3}$	75%	
			300	$2x10^{-3}$	120%	
ZK60	IM+extrusion	3.3	325	$1x10^{-2}$	544%	[75]
			400	$1x10^{-3}$	340%	
	PM+extrusion +annealing	6.5	200	$3x10^{-6}$	430%	
			212	$8x10^{-6}$	430%	
			225	$1x10^{-5}$	400%	
ZK60		3.2	300	$4x10^{-3}$	730%	[17]
ZK61		1.8	350	$1x10^{-1}$	450%	[17]
ZK60	Extrusion	3.3	523	$1x10^{-1}$	130%	[75]
			523	$1x10^{-2}$	544%	[76]
			523	$1x10^{-3}$	370%	
			350	$1x10^{-1}$	150%	
			350	$1x10^{-2}$	320%	
			350	$1x10^{-3}$	420%	
			400	$1x10^{-1}$	60%	
			400	$1x10^{-2}$	100%	
			400	$1x10^{-3}$	230%	
ZK60	Extrusion+ annealing	6.5	200	$1x10^{-5}$	240%	[76]
			212	$1x10^{-5}$	320%	
			225	$1x10^{-5}$	430%	

ZK61	PM+extrusion	0.5	200	$1x10^{-1}$	100%	[77]
			200	$1x10^{-2}$	283%	
			200	$1x10^{-3}$	659%	
			200	$1x10^{-4}$	410%	

Table 1-12 Summary of tensile elongations of Mg based materials at room temperature.

Material	Process	Grain size, μm	Ultimate tensile stress (MPa)	Elongation, %	Reference
AZ91	As-cast	125	146	4.3	[51]
	Cast+T6	--	195	5.4	
	Extrusion	5	340	15.5	
AZ91	Extrusion	7.6	343	8	[73]
	Extrusion	15.4	378	7.7	
	Extrusion	66.1	334	12.3	
AZ91	Extrusion	1.2	400	1.9	[82]
	Extrusion	2.1	302	1.4	
	Extrusion	15.6	325	7.1	
	Extrusion	59.1	274	11	
	ECAP	0.5	313	3.2	
	ECAP	1	318	2.5	
	ECAP	2	298	5.2	
	ECAP	12.6	320	12.4	
	ECAP	60.9	293	11	
Mg-5Y-6Re	P/M +Extrusion	0.5	536	2	[83]
Mg-4Y-3Re	Extrusion + solution treatment	1.5	233	16	[84]
	Extrusion + peak aging	1.5	301	6	
WE43	Extrusion	1.5	336	27	[85]
	Extrusion + aging	--	368	7.5	
AZ31	ECAE+ annealing	--	260	38	[86]
AZ31	ECAE + annealing	15	250	50	[58]

Table 1-13 HSRSP and LTSP in the Magnesium alloys.

Material	Grain size, (μm)	Temperature, (^{o}C)	Strain rate, (s^{-1})	Elongation (%)	Reference
PM AZ91	1	300	$1x10^{-2}$	280	[17]
		270	$1x10^{-2}$	140	
IM AZ91	4.1	300	$2x10^{-2}$	250	
		275	$2x10^{-2}$	330	
PM ZK61	1.2	250	$1x10^{-2}$	350	
		300	$1x10^{-1}$	420	
		250	$1x10^{-1}$	310	
IM ZK60	2.2	300	$1x10^{-2}$	400	
		250	$1x10^{-2}$	250	
		300	$1x10^{-1}$	150	
		250	$1x10^{-1}$	200	
AZ91	1.7	275	$1x10^{-2}$	300	[91]
PM ZK61	0.6	300	$1x10^{-2}$	260	[92]
IM ZK60	1.2		$1x10^{-2}$	360	
AZ105	--	300	$2x10^{-2}$	900	[47]
AZ91	0.7	200	$6x10^{-5}$	661	[55-57]
	1	175	$6x10^{-5}$	326	
	3.1	200	$7x10^{-5}$	956	
ZK60	6.5	200	$2x10^{-6}$	430	[76]
ZK61	0.5	200	$1x10^{-3}$	640	[77]
ZK60	1.4	200	$1x10^{-5}$	1083	[93]

Table 1-14 Summary of superplastic behaviors, deformation mechanisms, and activation energy of Mg based materials.

Alloy, reference	Grain size, (μm)	Temperature (^{o}C)	Strain rate (s^{-1})	Stress exponent, n	Activation energy for plastic flow, Q (kJ/mol)
AZ61 [95]	16	300-420	10^{-4}-$3x10^{-3}$	2	124
AZ61 [96]	17	325-400	10^{-5}-10^{-3}	2	143
AZ61 [95]	8.7	325-400	$2x10^{-4}$-10^{-2}	2	91
AZ91 [97]	5	300	$3x10^{-4}$-$1.5x10^{-1}$	2	121
AZ91	9	300	$3x10^{-4}$-$1.5x10^{-1}$	2	--
AZ91	16	300	$3x10^{-4}$-$1.5x10^{-1}$	2	--
ZK60 [17]	2	250-500	$2x10^{-4}$-10^{-1}	2	118
ZK61	~1	250-350	10^{-3}-10^{1}	2	118
AZ91	~1	270-400	10^{-5}-10^{0}	2	121
ZK61/SiC_p [73]	~1.7	325-500	10^{-1}-10^{1}	2	81
AZ61 [95]	16	325-400	$1x10^{-3}$-$3.5x10^{-3}$	5	159
AZ61	8.7	325-350	$5x10^{-3}$-10^{-1}	7	80
AZ31 [95]	150	300-375	$2x10^{-4}$-$7x10^{-2}$	3	122
AZ31 [98]	130	325-400	$1x10^{-5}$-10^{-3}	3	127

Table 2-1 Chemical composition of the AZ31 (in wt%).

	Mg	Al	Zn	Mn	Si	Fe	Cu	Ni	Be
AZ31B	Bal.	3.02	1.01	0.3	0.0067	0.0028	0.0031	0.0001	--

Table 2-2 The AZ31 specimens in this study.

Specimen name	Process	Reduction ratio in area	True strain
Billet	As-received material	---	---
E1 (42R-rod)	The rod (d=10 mm) with an extrusion ratio of 42:1 at 300^{o}C	97.6%	3.74
E1B (ECAP)	The rod (d=10 mm) with an extrusion ratio of 42:1 at 300^{o}C and then ECAP at 200^{o}C	>97.6%	>3.74
E2 (100R-rod)	The rod (d=6.5 mm) with an extrusion ratio of 100:1 at 300^{o}C	99.0%	4.61
E2B (100R-plate)	The plate (t=2 mm) with an extrusion ratio of 100:1 at 300^{o}C	99.0%	4.61
E3 (166R-plate)	The plate (t=2 mm) with an extrusion ratio of 166:1 at 300^{o}C	99.5%	5.11
E3B (166R-plate B)	The plate (t=1.5 mm) with an extrusion ratio of 166:1 at 300^{o}C	99.5%	5.11

Table 3-1 Grain size and room temperature tensile properties of the AZ31 billet, extruded and ECAP specimens.

	Billet	E1	E1B	E2	E2B	E3	E3B
Grain size, μm	75	2.5	0.7	2	3	2.5	2.3
YS, MPa	100	265	217	290	268	280	275
UTS, MPa	160	319	282	338	329	323	310
Hardness, H_v	55	82	95	90	81	82	83
e, %	9	28	30	38	43	27	50

Table 3-2 The variation of the grain size for the E3 (166R-plate) specimens after static annealing.

	As-extruded	150°C	200°C	250°C	300°C	350°C
	2.5	---	---	---	---	---
Held 1 h	---	2.57	2.7	2.8	2.80	5.2
Held 3 h	---	---	---	---	2.82	---
Held 5 h	---	---	---	---	3.75	---
Held 10 h	---	---	---	---	3.85	6.5

Table 3-3 Room temperature tensile properties at $1x10^{-3}$ s^{-1} for the E3 (166R-plate) specimens after extrusion and post-annealing.

Material condition	YS, MPa	UTS, MPa	e, %
As-received billet	100	160	9
As-extruded plate (E3, 2 mm)	280	323	27
As-extruded plate (E3B, 1.5 mm)	250	280	50
As-extruded bar (E2)	290	338	38
Post-annealed at 150^{o}C for 1 h for E3	265	324	32
Post-annealed at 150^{o}C for 10 h	280	323	28
Post-annealed at 200^{o}C for 1 h	275	318	35
Post-annealed at 200^{o}C for 10 h	280	317	32
Post-annealed at 250^{o}C for 1 h	272	327	28
Post-annealed at 250^{o}C for 10 h	276	316	29
Post-annealed at 300^{o}C for 1 h	260	306	30
Post-annealed at 300^{o}C for 3 h	255	302	31
Post-annealed at 300^{o}C for 5 h	235	297	32
Post-annealed at 300^{o}C for 10 h	232	290	33
Post-annealed at 350^{o}C for 1 h	205	275	32
Post-annealed at 350^{o}C for 10 h	190	268	21

Table 3-4 Room temperature tensile properties at $1x10^{-3}$ s^{-1} for the E3B (166R-plate B) specimens after extrusion and post-annealing.

Annealing (temperature and time)	UTS, MPa	e, %
As-extruded	283	50
150°C, 1 h	312	37
200°C, 1 h	303	42
250°C, 1 h	306	36
300°C, 1 h	298	35
350°C, 1 h	269	36
150°C, 10 h	317	36
200°C, 10 h	310	34
250°C, 10 h	320	35
300°C, 10 h	285	36
350°C, 10 h	256	34
300°C, 30 h	272	36

Table 3-5 Comparison of the mechanical properties of the E1 and E1B AZ31 specimens with and without ECAP.

	E1 (42R-rod)		E1B (ECAP)	
Test condition	UTS, MPa	e, %	UTS, MPa	e, %
150°C, 1x10^{-4} s^{-1}	**114**	**130**	**81**	**461**
150°C, 1x10^{-3} s^{-1}	156	107	118	153
150°C, 5x10^{-3} s^{-1}	197	107	143	141
150°C, 1x10^{-2} s^{-1}	193	114	149	119
150°C, 1x10^{-1} s^{-1}	207	58	---	---
200°C, 1x10^{-4} s^{-1}	---	---	49	247
200°C, 1x10^{-3} s^{-1}	79	205	68	290
200°C, 5x10^{-3} s^{-1}	104	218	87	329
200°C, 1x10^{-2} s^{-1}	**123**	**164**	**98**	**233**
200°C, 1x10^{-1} s^{-1}	126	83	---	---
250°C, 1x10^{-4} s^{-1}	---	---	42	129
250°C, 1x10^{-3} s^{-1}	49	293	53	207
250°C, 5x10^{-3} s^{-1}	60	355	61	212
250°C, 1x10^{-2} s^{-1}	**73**	**377**	**70**	**227**
250°C, 1x10^{-1} s^{-1}	91	120	---	---

Table 3-6 Comparison of the mechanical properties of the E1 and the E2 specimens processed to different extrusion ratios.

	E1 (42R-rod)		E2 (100R-rod)	
Test condition	UTS, MPa	e, %	UTS, MPa	e, %
$150^{o}C$, $1x10^{-4}$ s^{-1}	**114**	**130**	**106**	**437**
$150^{o}C$, $1x10^{-3}$ s^{-1}	156	107	131	180
$150^{o}C$, $5x10^{-3}$ s^{-1}	197	107	166	127
$150^{o}C$, $1x10^{-2}$ s^{-1}	193	114	206	126
$150^{o}C$, $1x10^{-1}$ s^{-1}	207	58	240	87
$200^{o}C$, $1x10^{-4}$ s^{-1}	---	---	50	290
$200^{o}C$, $4x10^{-4}$ s^{-1}	---	---	129	445
$200^{o}C$, $6x10^{-4}$ s^{-1}	---	---	75	596
$200^{o}C$, $1x10^{-3}$ s^{-1}	79	205	80	352
$200^{o}C$, $5x10^{-3}$ s^{-1}	104	218	---	---
$200^{o}C$, $1x10^{-2}$ s^{-1}	123	164	135	191
$200^{o}C$, $1x10^{-1}$ s^{-1}	126	83	174	105
$250^{o}C$, $1x10^{-4}$ s^{-1}	---	---	23	386
$250^{o}C$, $1x10^{-3}$ s^{-1}	49	293	43	515
$250^{o}C$, $5x10^{-3}$ s^{-1}	60	355	63	220
$250^{o}C$, $1x10^{-2}$ s^{-1}	**73**	**377**	**76**	**405**
$250^{o}C$, $1x10^{-1}$ s^{-1}	91	120	118	183

Table 3-7 Comparison of the mechanical properties of the E2 and the E2B specimens processed into different geometric shapes.

	E2 (100R-rod)		E2B (100R-plate)	
Test condition	UTS, MPa	e, %	UTS, MPa	e, %
150°C, 1x10^{-4} s^{-1}	**106**	**437**	**133**	**159**
150°C, 1x10^{-3} s^{-1}	131	180	168	121
150°C, 5x10^{-3} s^{-1}	165	127	---	---
150°C, 1x10^{-2} s^{-1}	207	126	210	75
200°C, 1x10^{-4} s^{-1}	50	290	---	---
200°C, 4x10^{-4} s^{-1}	129	445	---	---
200°C, 6x10^{-4} s^{-1}	75	596	87	300
200°C, 1x10^{-3} s^{-1}	80	352	100	248
200°C, 1x10^{-2} s^{-1}	135	191	140	179
200°C, 1x10^{-1} s^{-1}	174	105	202	117
250°C, 1x10^{-4} s^{-1}	23	386	---	---
250°C, 1x10^{-3} s^{-1}	43	515	72	296
250°C, 5x10^{-3} s^{-1}	63	220	---	---
250°C, 1x10^{-2} s^{-1}	**76**	**405**	**87**	**250**
250°C, 1x10^{-1} s^{-1}	118	183	145	131
300°C, 1x10^{-4} s^{-1}	20	335	---	---
300°C, 4x10^{-4} s^{-1}	53	1093	---	---
300°C, 6x10^{-4} s^{-1}	---	---	25	657
300°C, 1x10^{-3} s^{-1}	29	711	34	738
300°C, 5x10^{-3} s^{-1}	45	353	---	---
300°C, 1x10^{-2} s^{-1}	**51**	**1000**	**86**	**481**
300°C, 5x10^{-2} s^{-1}	**70**	**534**	**---**	**---**
300°C, 1x10^{-1} s^{-1}	**78**	**331**	**90**	**259**

Table 3-8 Comparison of the mechanical properties of the E2B and the E3 specimens processed to different extrusion ratios.

	E2B (100R-plate)		E3 (166R-plate)	
Test condition	UTS, MPa	e, %	UTS, MPa	e, %
150°C, 1x10^{-4} s^{-1}	**133**	**159**	**60**	**215**
150°C, 1x10^{-3} s^{-1}	168	121	127	142
150°C, 2x10^{-2} s^{-1}	---	---	208	90
200°C, 6x10^{-4} s^{-1}	87	300	---	---
200°C, 1x10^{-3} s^{-1}	100	248	73	425
200°C, 1x10^{-2} s^{-1}	140	179	---	---
200°C, 2x10^{-2} s^{-1}	---	---	133	118
200°C, 1x10^{-1} s^{-1}	202	117	---	---
250°C, 1x10^{-4} s^{-1}	---	---	42	640
250°C, 1x10^{-3} s^{-1}	72	296	49	310
250°C, 1x10^{-2} s^{-1}	**87**	**250**	**---**	**---**
250°C, 2x10^{-2} s^{-1}	---	---	76	196
250°C, 1x10^{-1} s^{-1}	145	131	106	140
300°C, 1x10^{-4} s^{-1}	---	---	20	633
300°C, 6x10^{-4} s^{-1}	25	657	---	---
300°C, 1x10^{-3} s^{-1}	34	738	30	396
300°C, 1x10^{-2} s^{-1}	**86**	**481**	**---**	**---**
300°C, 2x10^{-2} s^{-1}	**---**	**---**	**55**	**294**
300°C, 1x10^{-1} s^{-1}	**90**	**259**	**85**	**207**

Table 3-9 Comparison the E3 and the E3B specimens to different thicknesses.

	E3 (166R-plate)		E3B (166R-plate B)	
Test condition	UTS, MPa	e, %	UTS, MPa	e, %
150°C, 1x10^{-4} s^{-1}	**60**	**215**	**111**	**300**
150°C, 1x10^{-3} s^{-1}	127	142	126	144
150°C, 2x10^{-3} s^{-1}	---	---	147	103
150°C, 8x10^{-3} s^{-1}	---	---	195	98
150°C, 2x10^{-2} s^{-1}	208	90	224	94
150°C, 1x10^{-1} s^{-1}	---	---	239	92
200°C, 1x10^{-3} s^{-1}	73	425	67	365
200°C, 2x10^{-3} s^{-1}	---	---	78	250
200°C, 8x10^{-3} s^{-1}	---	---	107	165
200°C, 2x10^{-2} s^{-1}	133	118	135	127
200°C, 1x10^{-1} s^{-1}	---	---	171	125
250°C, 1x10^{-4} s^{-1}	42	640	24	601
250°C, 5x10^{-4} s^{-1}	45	293	---	---
250°C, 1x10^{-3} s^{-1}	49	310	50	356
250°C, 2x10^{-3} s^{-1}	58	280	---	---
250°C, 8x10^{-3} s^{-1}	66	248	83	304
250°C, 2x10^{-2} s^{-1}	**76**	**196**	**111**	**217**
250°C, 1x10^{-1} s^{-1}	106	140	131	125
280°C, 1x10^{-4} s^{-1}	49	900	24	740
280°C, 5x10^{-4} s^{-1}	58	740	---	---
280°C, 1x10^{-3} s^{-1}	38	524	36	381
280°C, 2x10^{-3} s^{-1}	39	240	---	---
280°C, 8x10^{-3} s^{-1}	50	253	50	301
280°C, 2x10^{-2} s^{-1}	**58**	**266**	**81**	**254**
280°C, 1x10^{-1} s^{-1}	114	160	126	171
300°C, 1x10^{-4} s^{-1}	20	633	28	760
300°C, 5x10^{-4} s^{-1}	34	520	---	---
300°C, 1x10^{-3} s^{-1}	30	396	34	450
300°C, 2x10^{-3} s^{-1}	50	428	---	---
300°C, 8x10^{-3} s^{-1}	48	520	70	448
300°C, 2x10^{-2} s^{-1}	**55**	**294**	**74**	**281**
300°C, 1x10^{-1} s^{-1}	**85**	**207**	**118**	**220**

Table 3-10 Summary of the measured grain size and X-ray peak intensity ratio for the (0002) reflection over the $(10\bar{1}1)$ and $(10\bar{1}3)$ reflections for the E3 specimens.

Material condition	Grain size (μm)	$I_{(0002)}/I_{(1011)}$	$I_{(0002)}/I_{(1013)}$
As-received billet	70	0.6	5
As-extruded plate (E3)	2.5	14.6	19
Post-annealed at 150°C for 1 h	2.6	23	23
Post-annealed at 150°C for 10 h	---	60	40
Post-annealed at 200°C for 1 h	2.7	---	---
Post-annealed at 200°C for 10 h	---	---	---
Post-annealed at 250°C for 1 h	2.8	22	14.7
Post-annealed at 250°C for 10 h	---	10.7	14.7
Post-annealed at 300°C for 1 h	2.8	23	13.5
Post-annealed at 300°C for 3 h	2.9	---	---
Post-annealed at 300°C for 5 h	3.7	12.4	6.8
Post-annealed at 300°C for 10 h	3.9	10.8	5.4
Post-annealed at 350°C for 1 h	5.2	7.5	3.6
Post-annealed at 350°C for 10 h	6.5	7.5	4

Table 3-11 Schmid factors calculated for the E1 and E1B specimens.

Sample	Texture	Slip system	Average Schmid factor
E1 (42R-rod)	$<10\bar{1}0>$//ED	$\{0001\}\ <11\bar{2}0>$	0
		$\{10\bar{1}0\}<11\bar{2}0>$	0.29
		$\{10\bar{1}\bar{1}\}<11\bar{2}0>$	0.25
E1B (ECAP)	$<\bar{2}\ \bar{5}\ 76>$//ED	$\{0001\}\ <11\bar{2}0>$	0.27
		$\{10\bar{1}0\}<11\bar{2}0>$	0.14
		$\{10\bar{1}\bar{1}\}<11\bar{2}0>$	0.11

Table 4-1 The measured apparent strain rate sensitivity m_a values based on the true stress-strain curves over strain rates of $1x10^{-1}$- $1x10^{-4}$ s^{-1}.

T (^{o}C)	E1	E1B	E2	E2B	E3	E3B
150	0.11	0.20	0.13	---	0.27	0.14
200	0.26	0.26	0.23	---	0.33	0.30
250	---	---	0.31	---	0.31	0.27
300	---	---	0.39	0.32	0.35	0.44

Table 4-2 The measured apparent strain rate sensitivity m_a value for the E2B samples based on the jump strain rate tests.

T (^{o}C)	Lower strain rate 5 x 10^{-4}- 8 x 10^{-4} s^{-1}	Higher strain rate 9 x 10^{-3}- 2 x 10^{-2} s^{-1}
200	0.31	0.20
300	0.46	0.37

Table 4-3 Comparison of AZ31B and AZ91D Mg alloys processed by high-ratio (HR) extrusion and ECAP.

Item	AZ31B HR extrusion	AZ31B ECAP [58]	AZ91D HR extrusion	AZ91D ECAP [55,57]
Strain during processing	5.1	8.1	5.1	8.1
Product shape	plate	rod	plate	rod
Grain size	2.5 μm	1 μm	2 μm	1 μm
Room temp. UTS	320 MPa	270 MPa	350 MPa	---
Max room temp. elongation	50%	50%	18%	---
Max. SP elongation	900%	---	1200%	661%

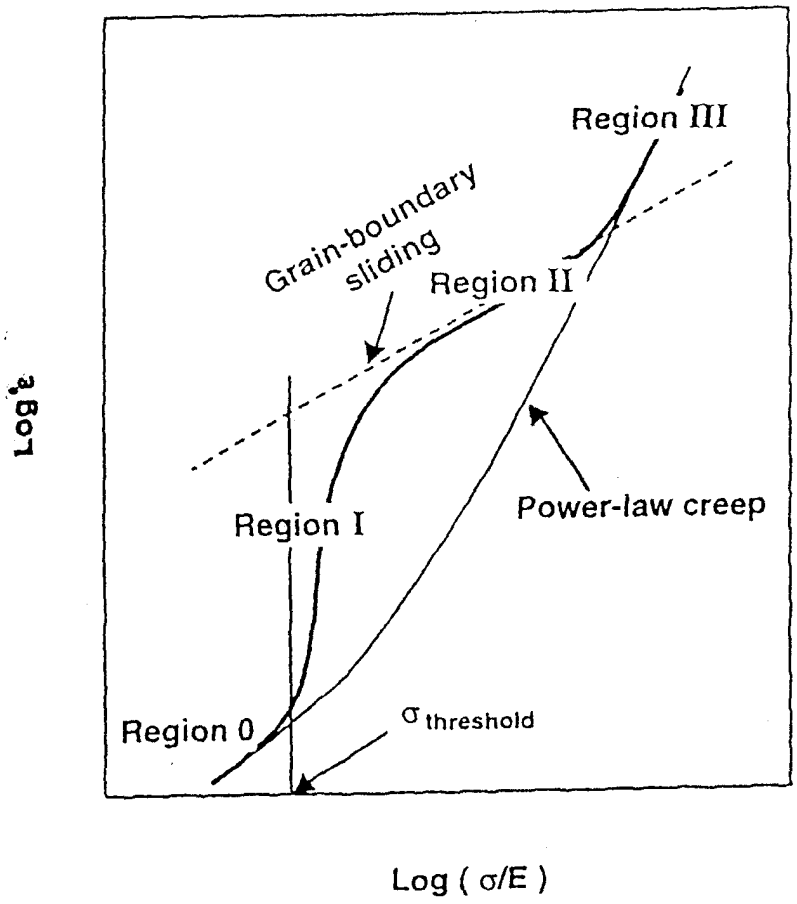

Fig. 1-1 High temperature deformation behavior of fine-grained materials [6].

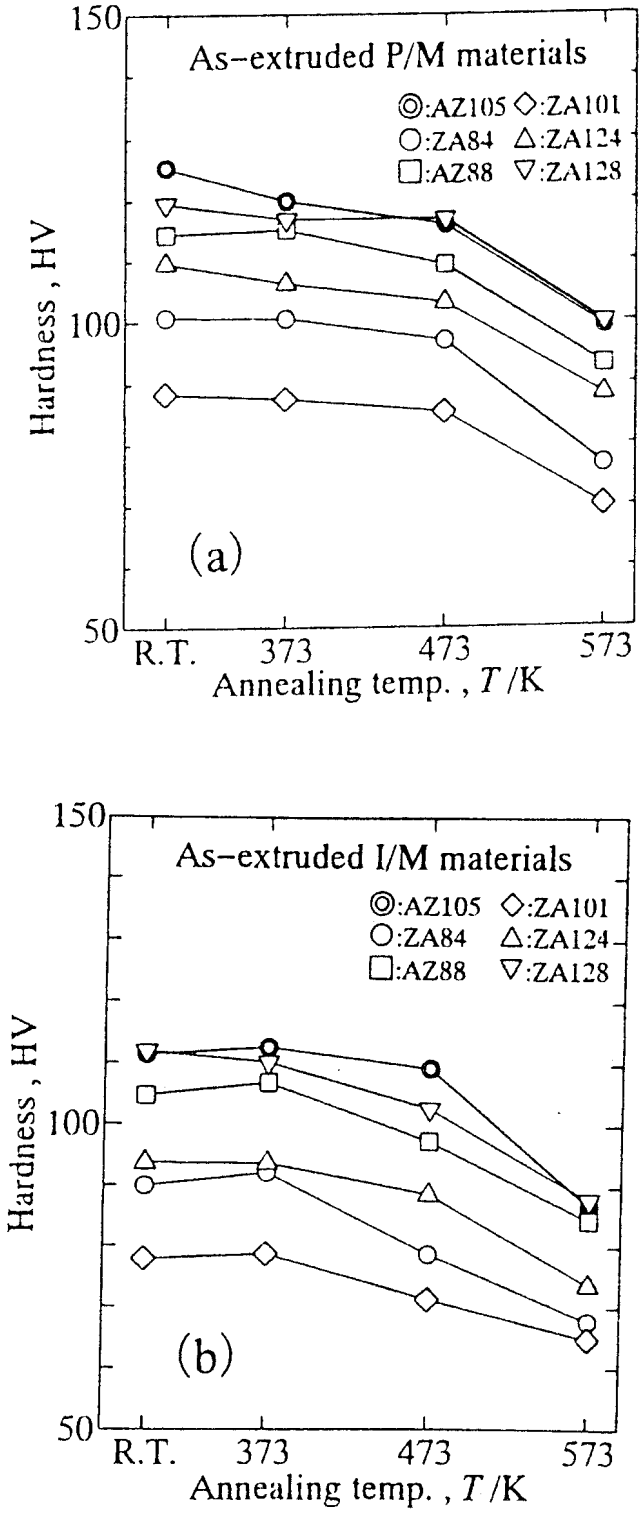

Fig 1-2 Changes in hardness after heating at various temperatures for 2 hours, (a) P/M, (b) I/M materials [47].

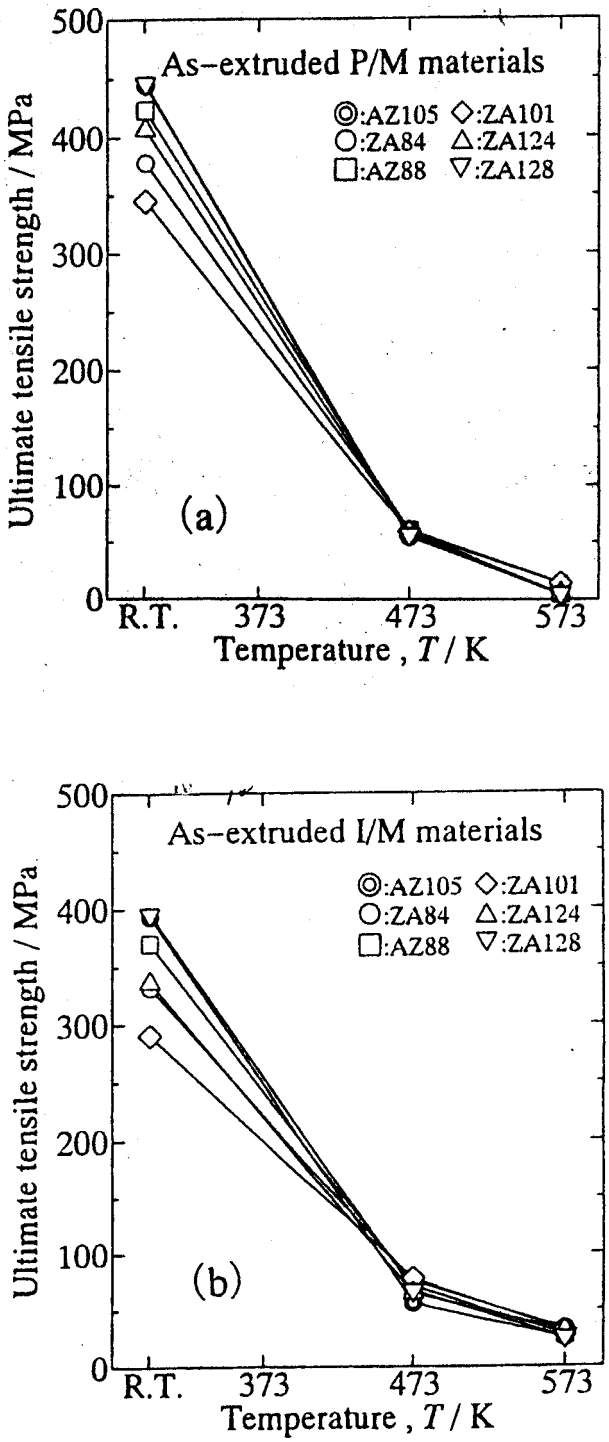

Fig. 1-3 (a)(b) Tensile strength and elongation of the P/M and I/M materials at different test temperatures [47].

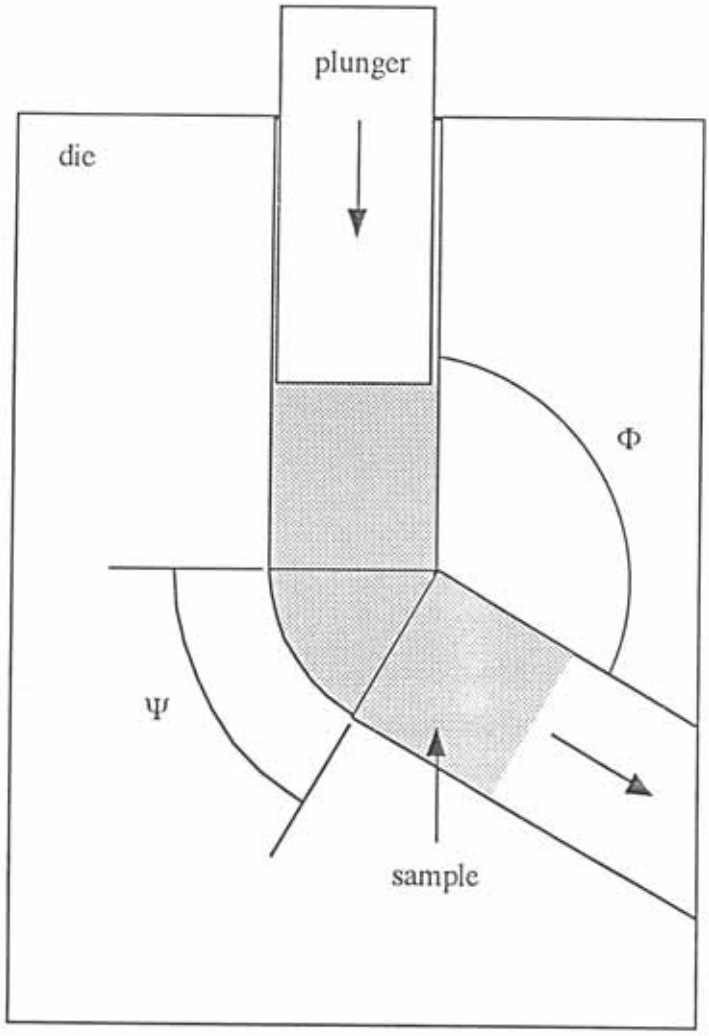

Fig. 1-4 Schematic drawing of equal channel angular pressing.

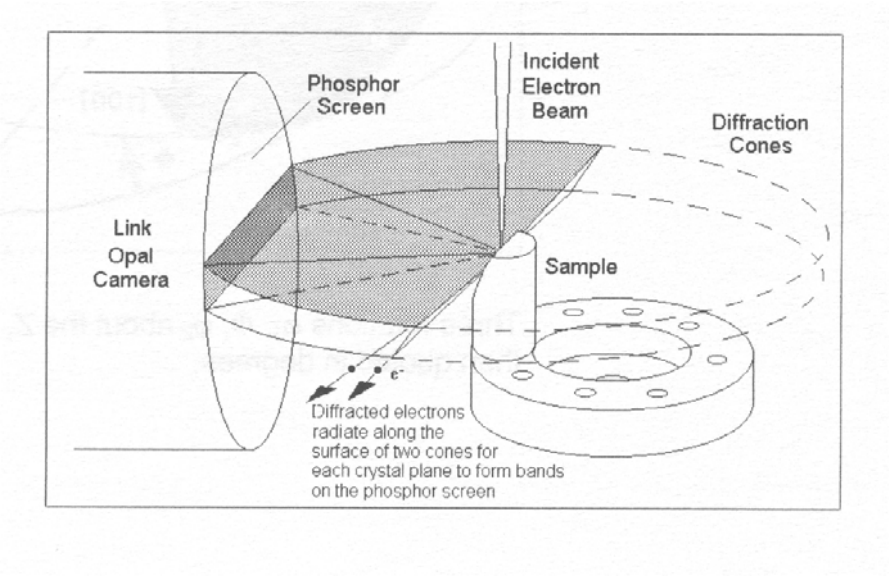

Fig 1-5 Illustration of the principle of an EBSD system [105].

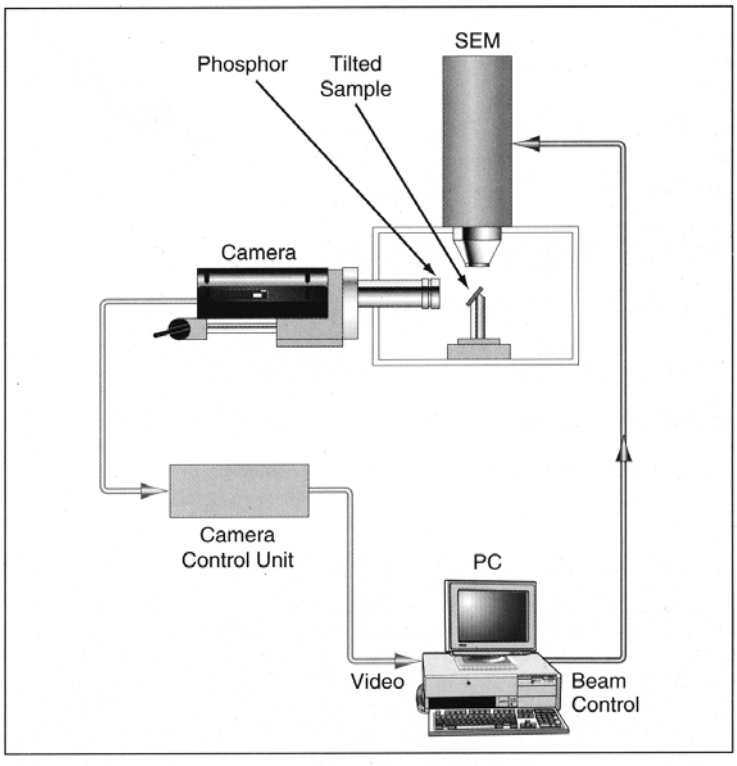

Fig. 1-6 Illustration of the set-up of an EBSD system [106].

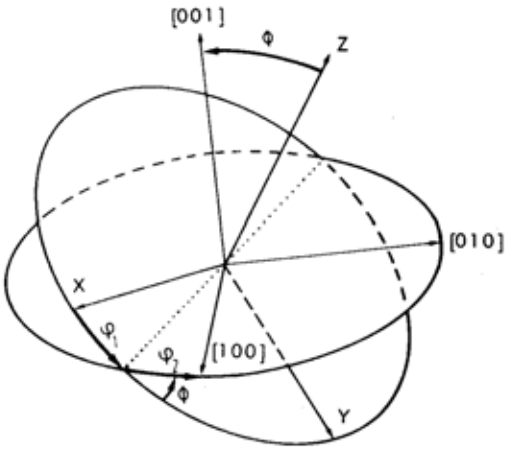

Fig. 1-7 Schematic Euler angles (φ_1, ϕ, φ_2), which would specify an orientation [107].

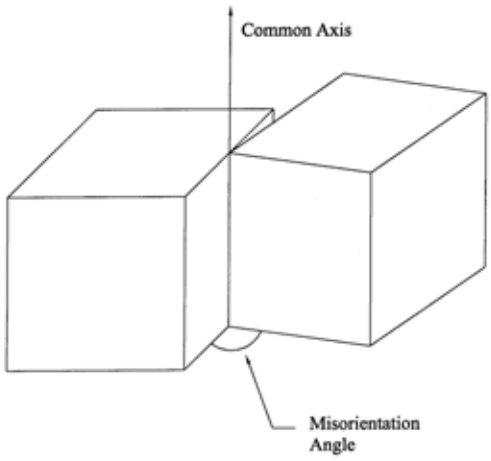

Fig. 1-8 Schematic illustration of the misorientation angle between two grains [105].

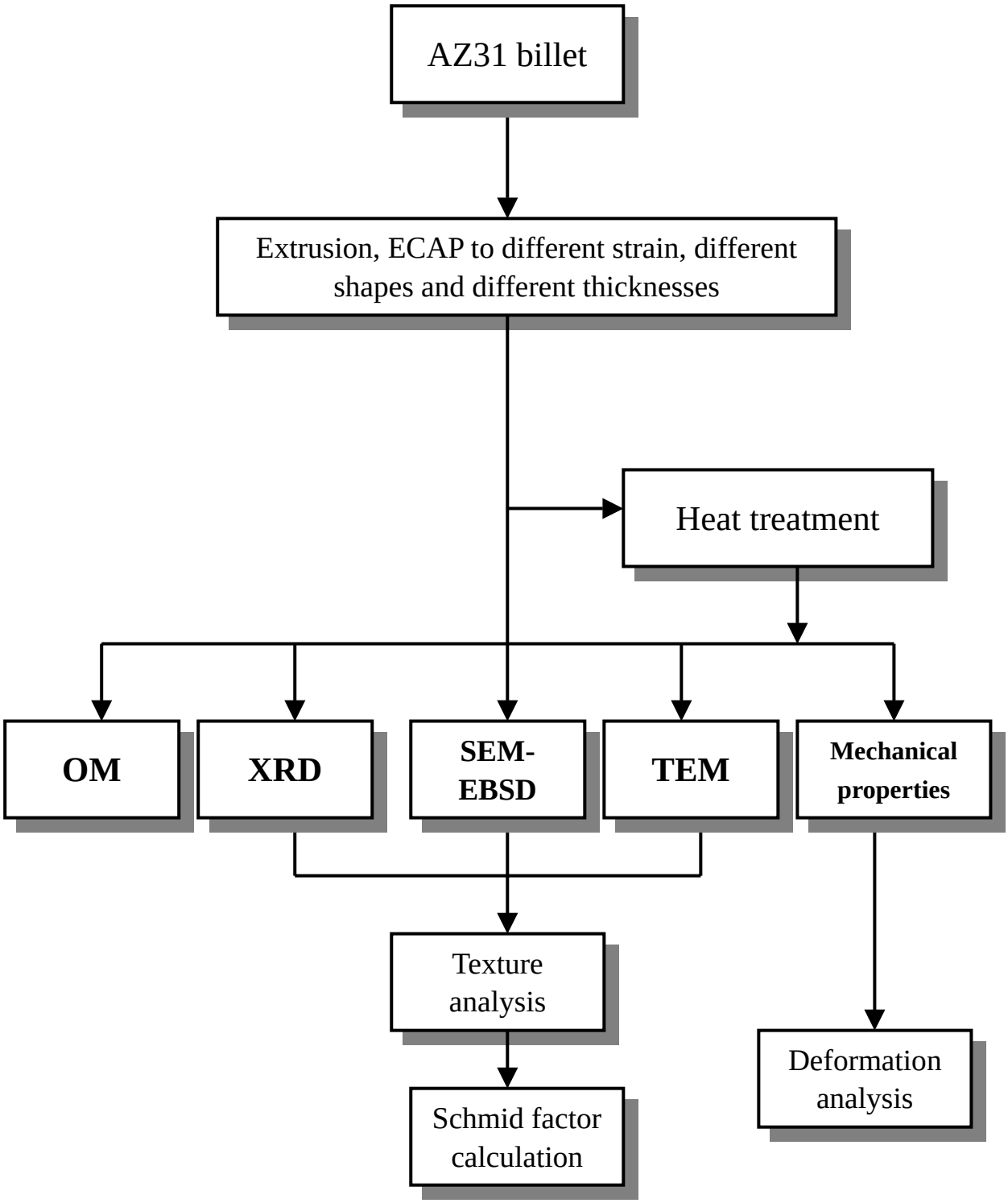

Fig. 2-1 Processing routes for this research.

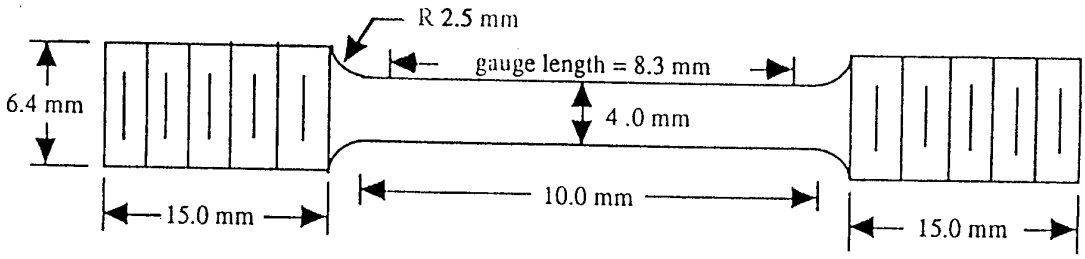

(a)

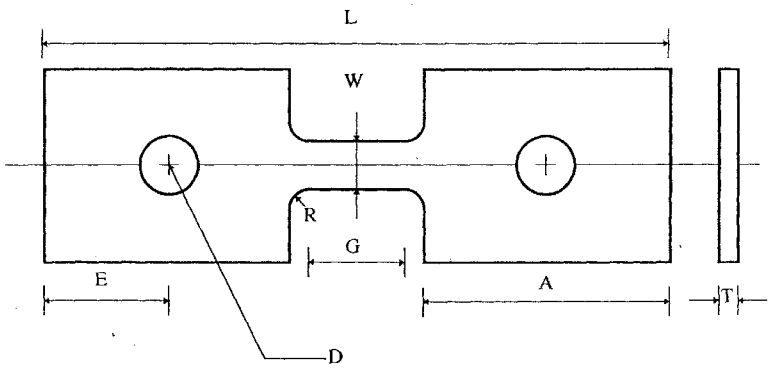

Subsize Specimen	mm
G-Gage length	5.5
W-Width	3
T-Thickness	1-2
R-Radius of fillet	0.5
L-Over all length	30
A-Length of grip section	11
B-Width of grip section	10
D-Diameter of hole for pin	3
E-Edge distance from pin	5.5

(b)

Fig. 2-2 Specimen configurations of (a) extruded rod with a gauge length of 8.3 mm and (b) extruded sheet with a gauge length of 5.5 mm.

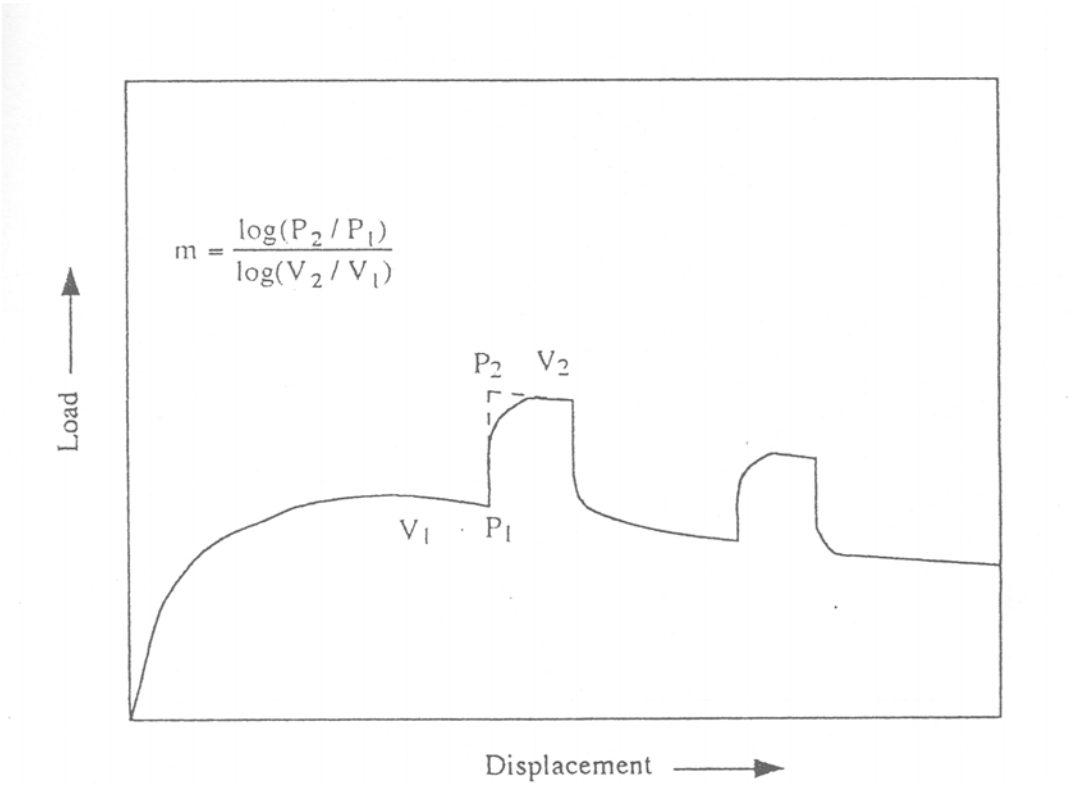

Fig. 2-3 Schematic illustration of the jump-strain-rate test.

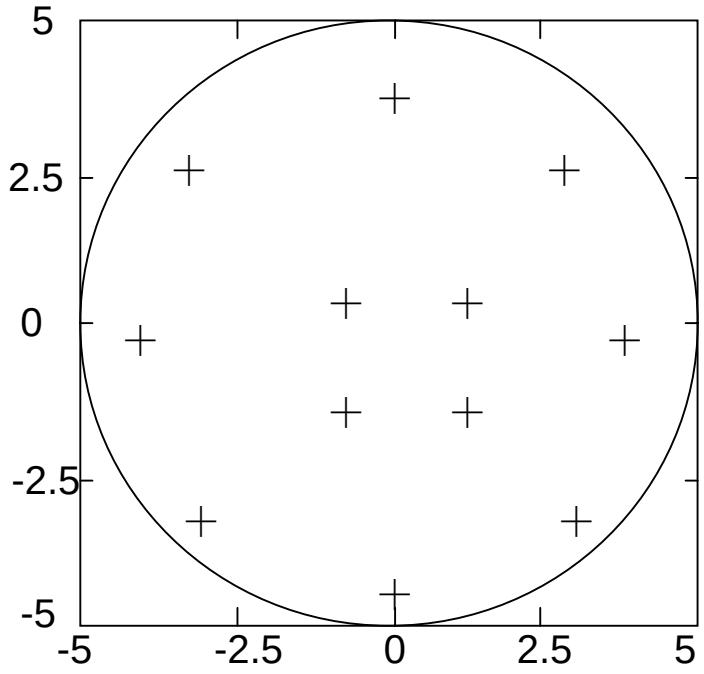

Fig. 2-4 Schematic illustration of the procedure used for taking the microhardness measurements on the transverse cross-sectional plane.

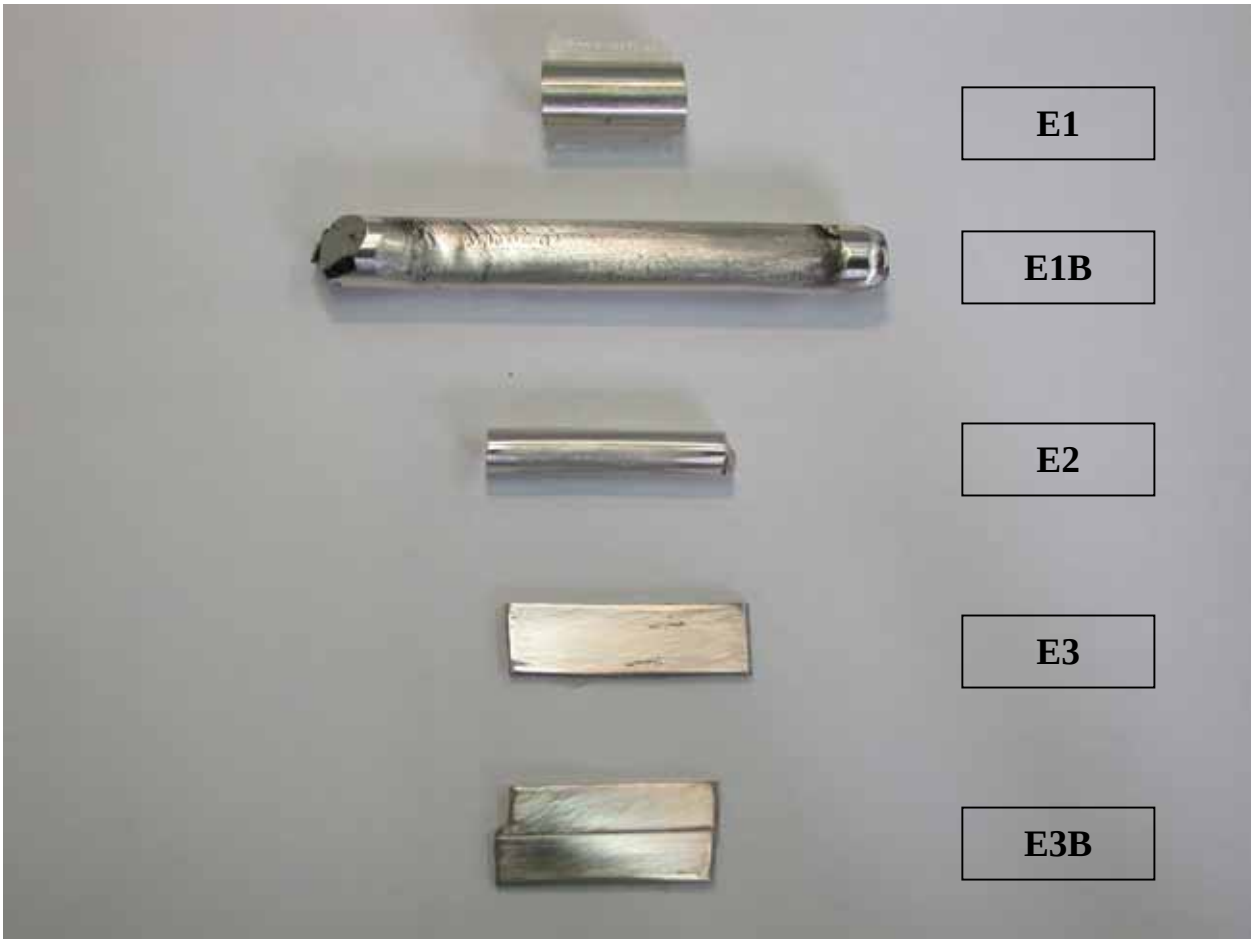

Fig. 3-1 The appearances of samples after extrusion and ECAP.

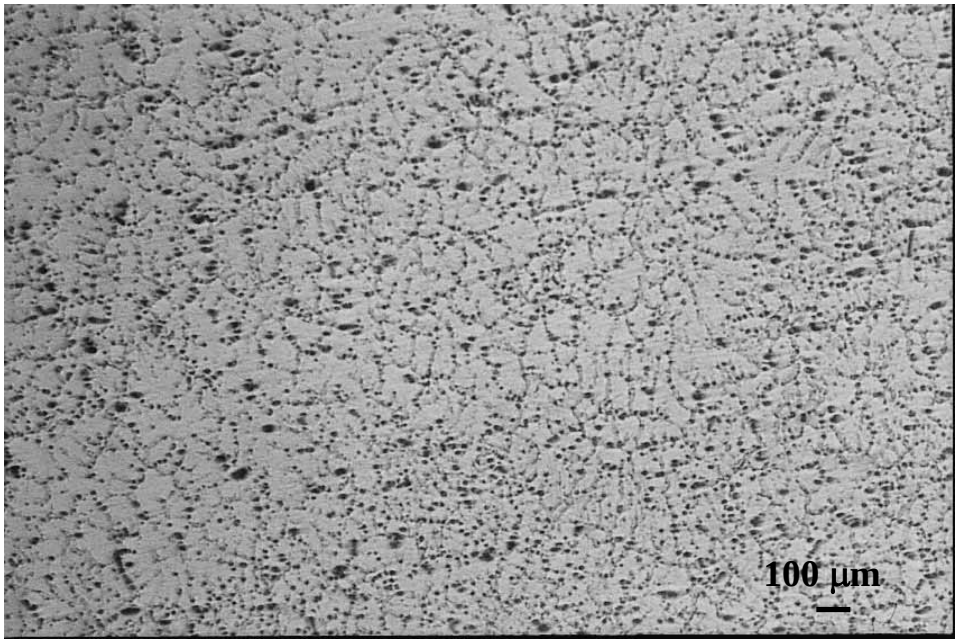

Fig. 3-2 The OM micrographs of the as-received AZ31 billet seen from the cross-sectional plane.

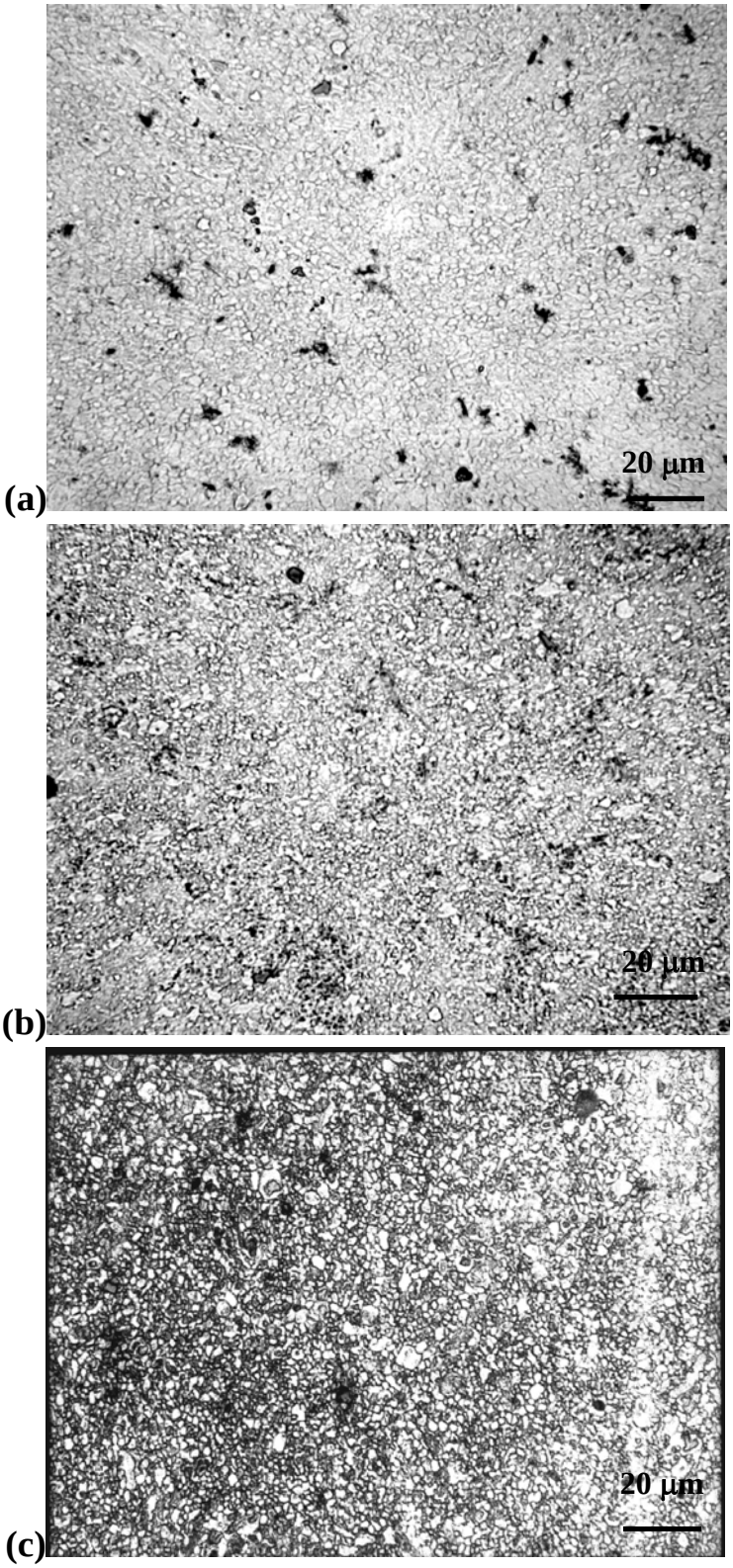

Figs. 3-3 The OM micrographs of the extruded (a) E1, (b) E1B, (c) E2, (d) E2B and (e) E3B specimens.

(d)

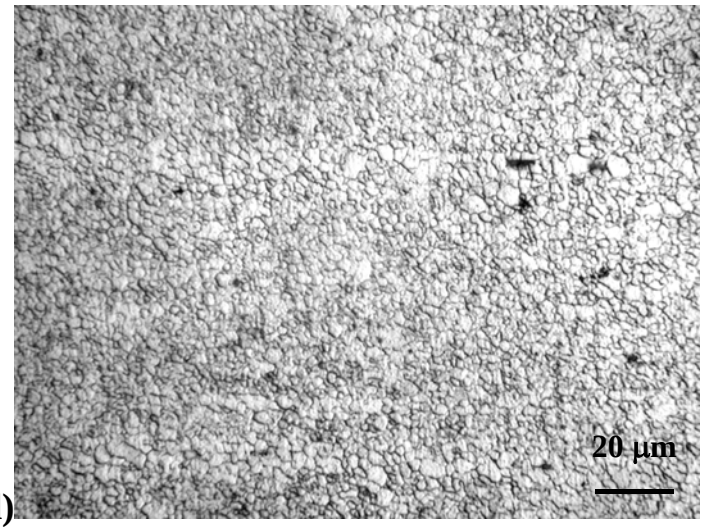

(e)

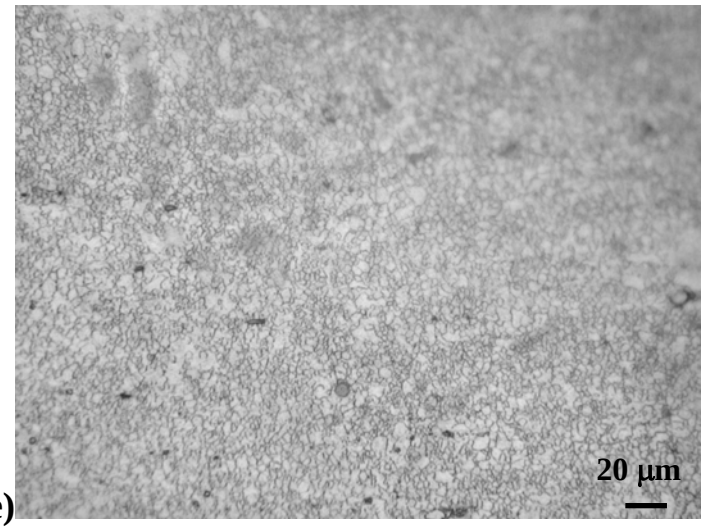

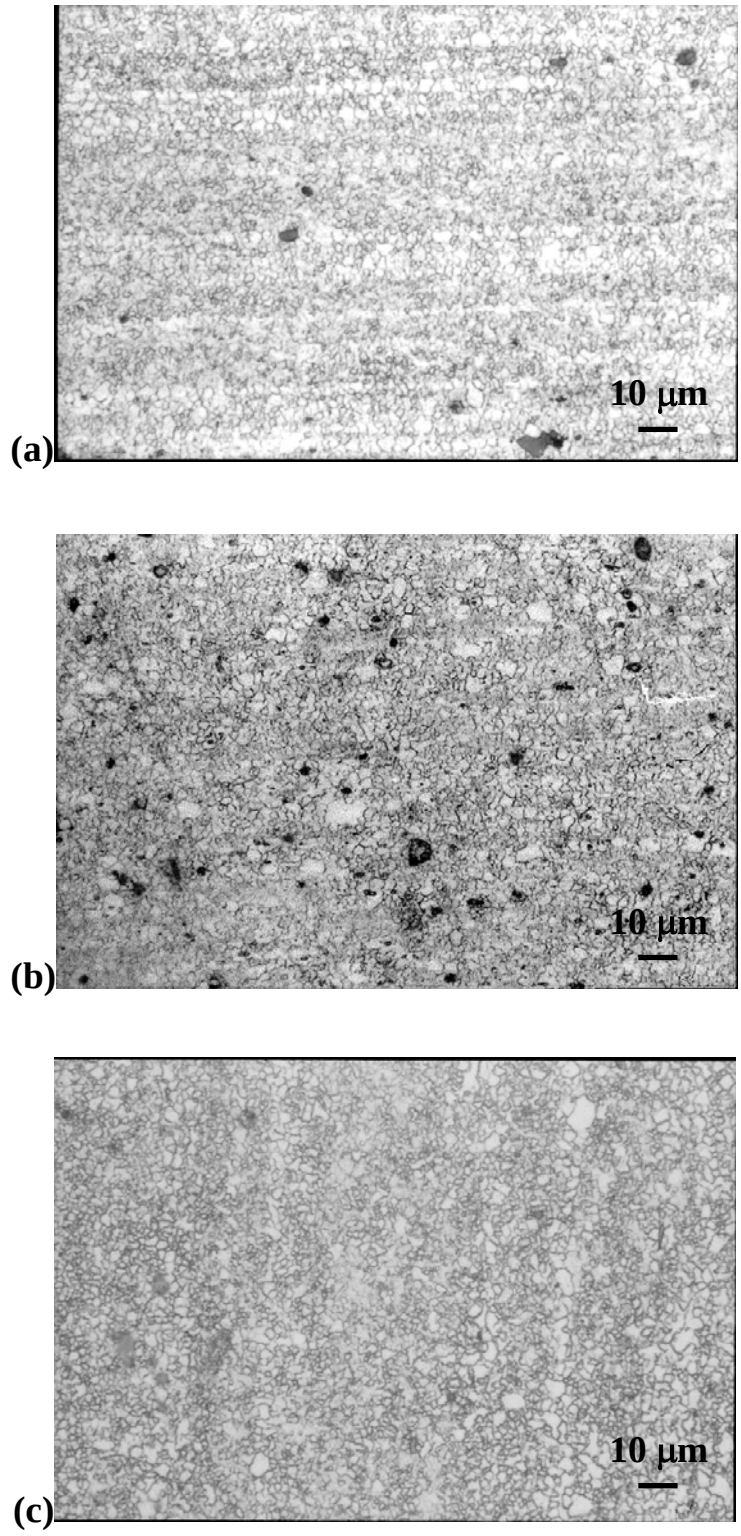

Fig. 3-4 The OM micrographs of the E3 specimens from the extrusion (a) flat, (b) longitudinal and (c) cross-sectional planes.

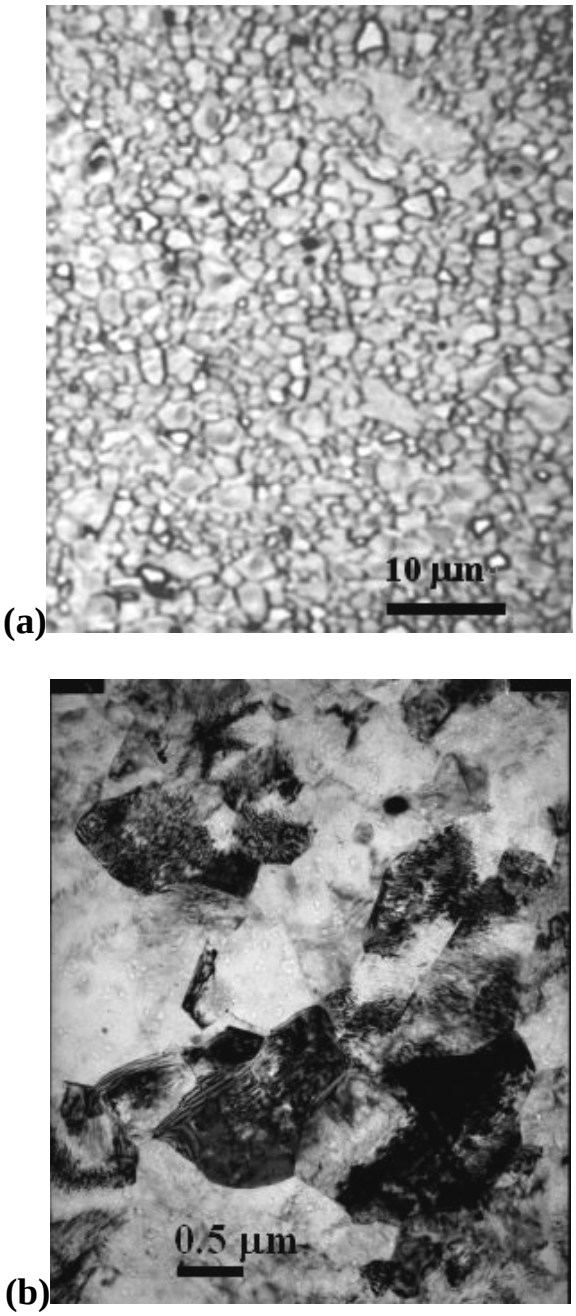

Fig. 3-5 Grain structure micrographs of the AZ31 alloy after (a) extrusion to 42:1 at 300^{o}C (OM micrograph, E1 specimen), and (b) further ECAP at 200^{o}C (TEM micrograph, E1B specimen).

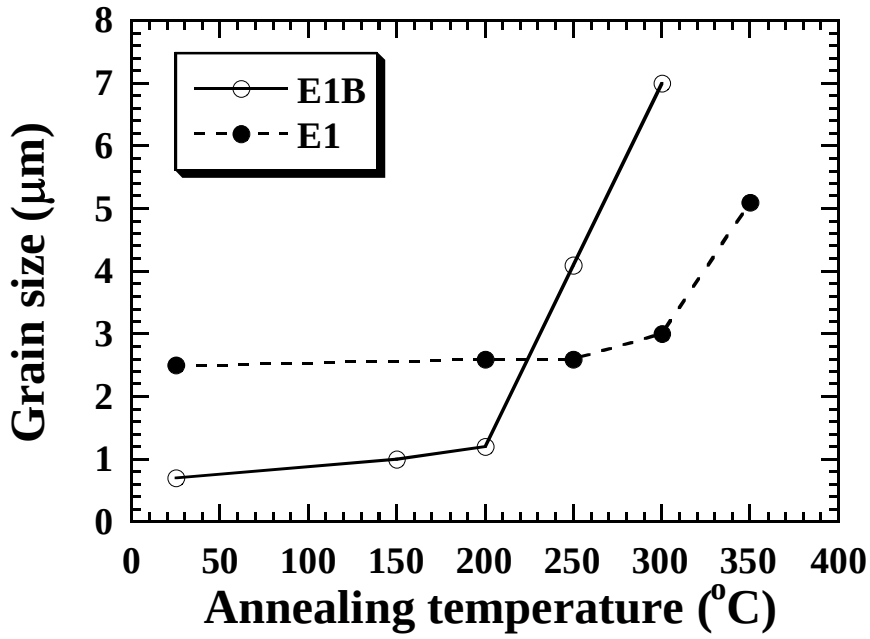

Fig. 3-6 Grain size versus annealing temperature after static annealing holding for 1 h in the extruded E1 and ECAP E1B samples.

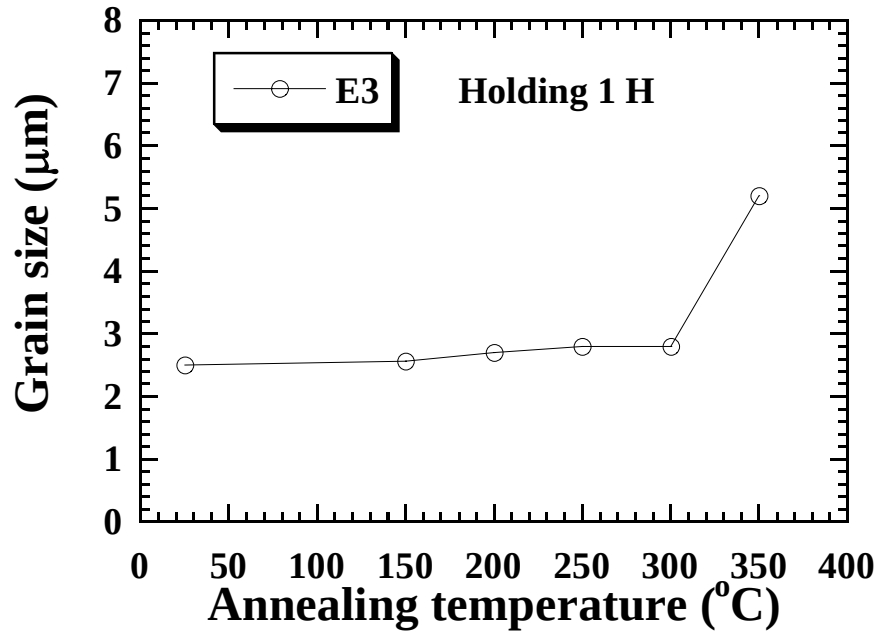

Fig. 3-7 Variation of grain size as a function of temperature in the E3 specimen after holing for 1 h in the furnace.

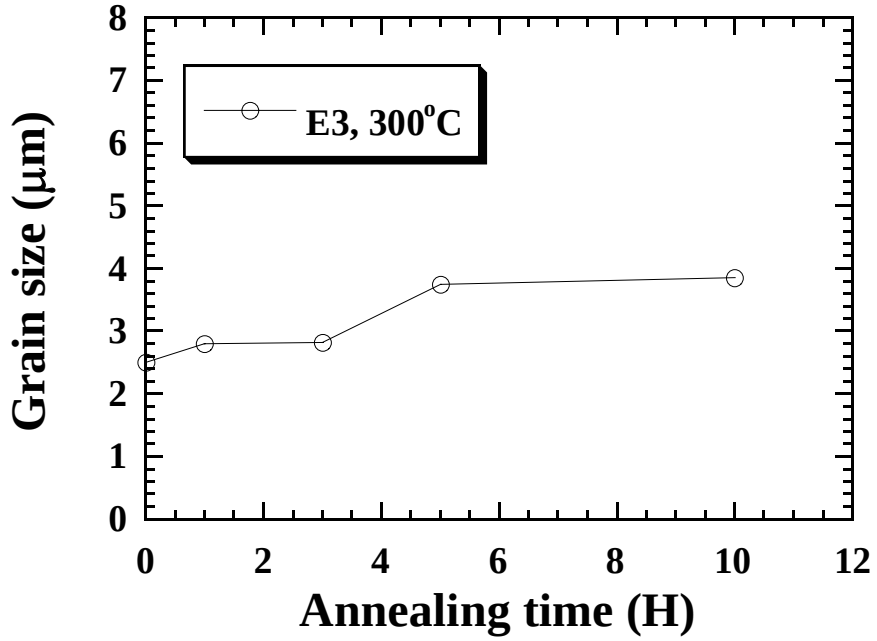

Fig. 3-8 Variation of grain size as a function of time in the E3 specimen at 300°C.

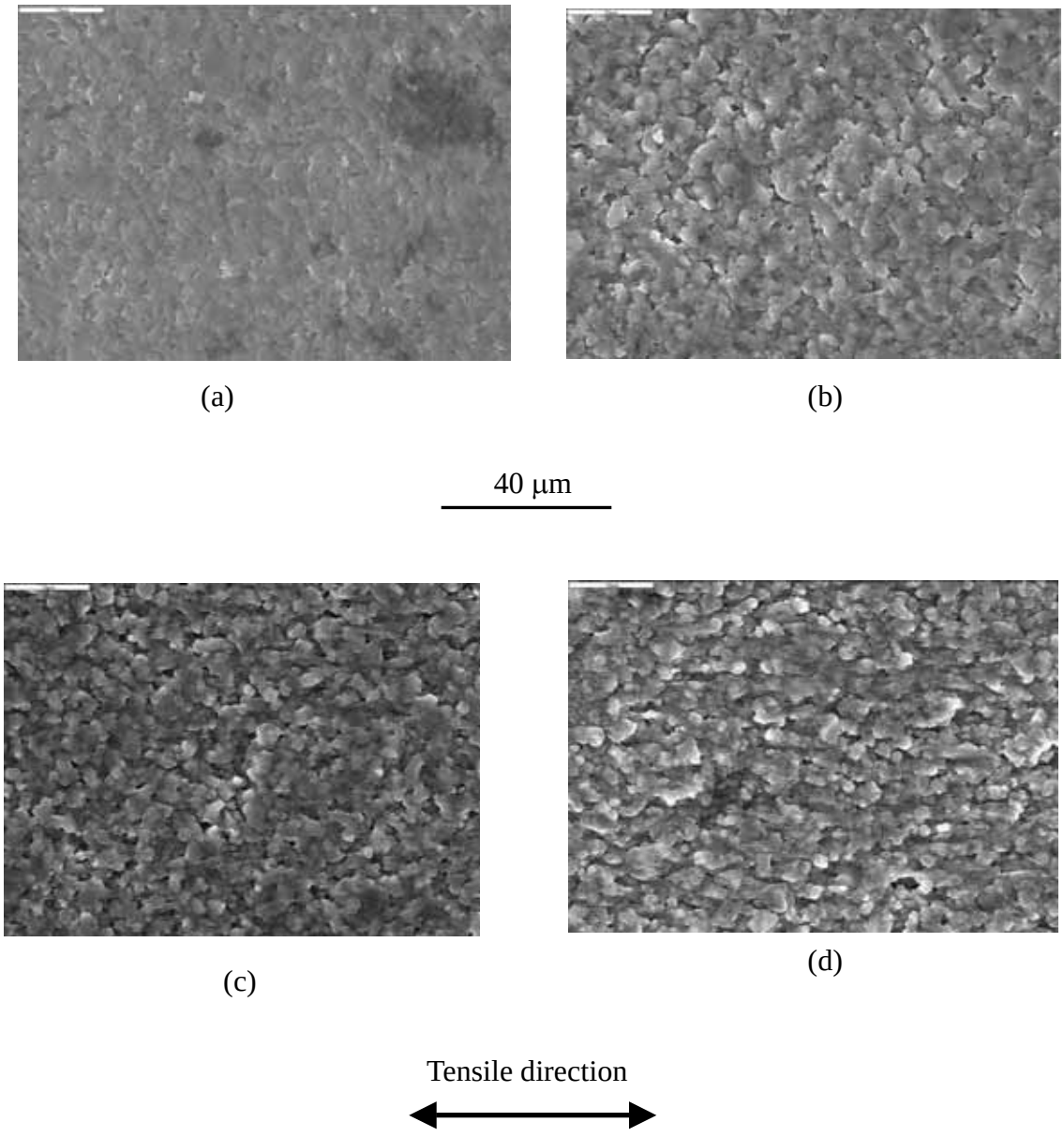

Fig. 3-9 The typical surface topography SEM micrographs taken from the E2B specimens tensile-loaded at 200^{o}C and 6x10^{-4} s^{-1} to different strains: (a) 0.29, (b) 0.71, (c) 1.12, and (d) 1.39.

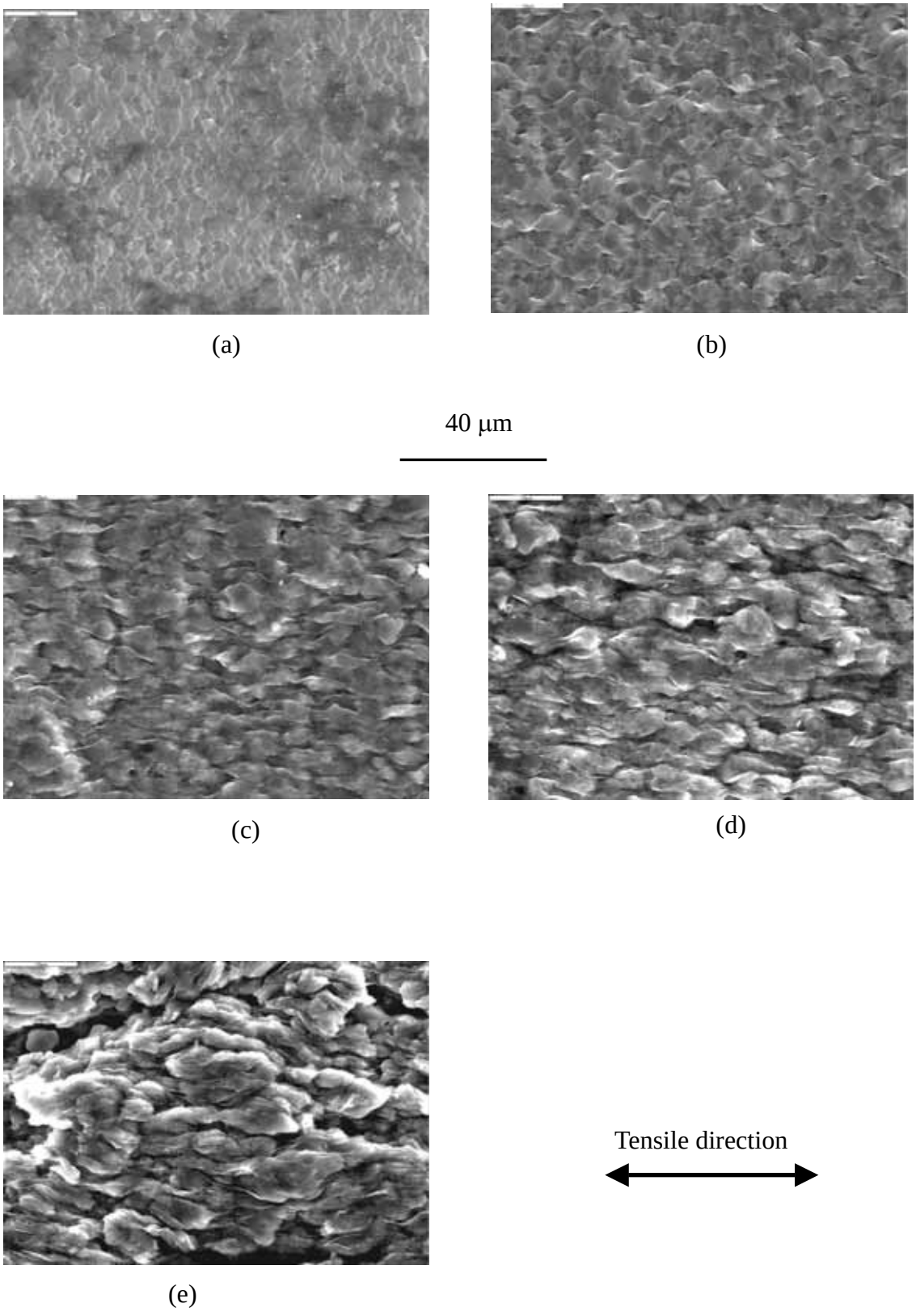

Fig. 3-10 The typical surface topography SEM micrographs taken from the E2B specimens tensile-loaded at 300°C and $6x10^{-4}$ s^{-1} to different strains: (a) 0.24, (b) 0.71, (c) 1.28, (d) 1.80, and (e) 2.03 [114].

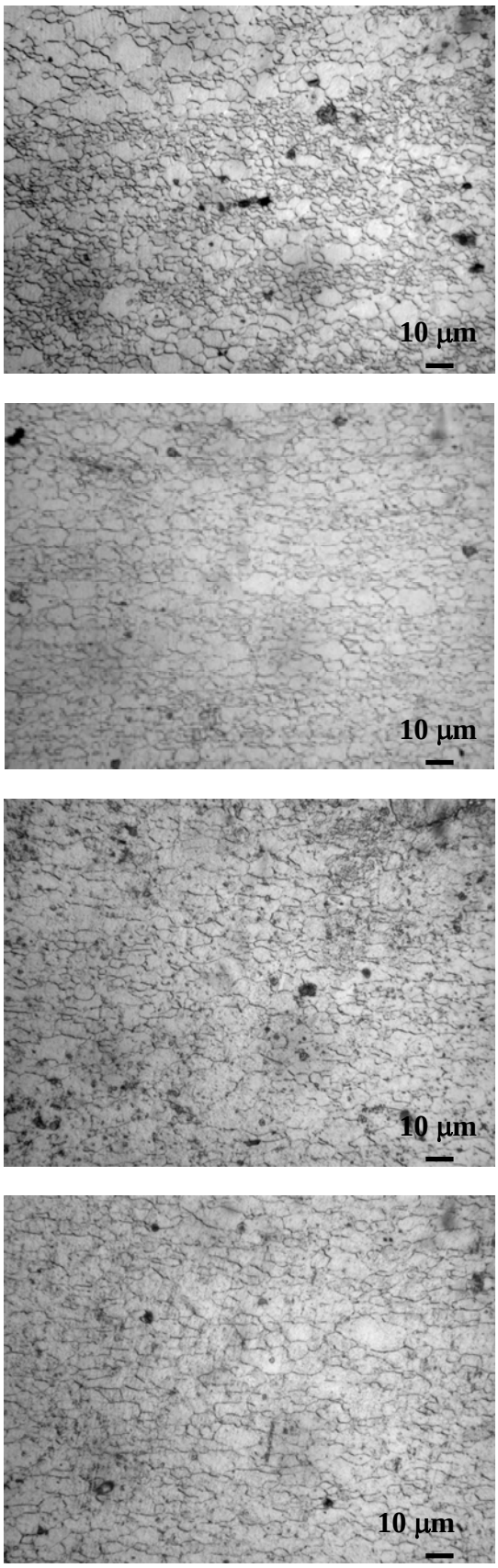

Fig. 3-11 OM micrographs of the E3 specimens tensile-loaded at 300°C and at $1x10^{-3}$ s^{-1} to different strains: (a) 0.25, (b) 0.47, (c) 0.93, and (d) 1.23.

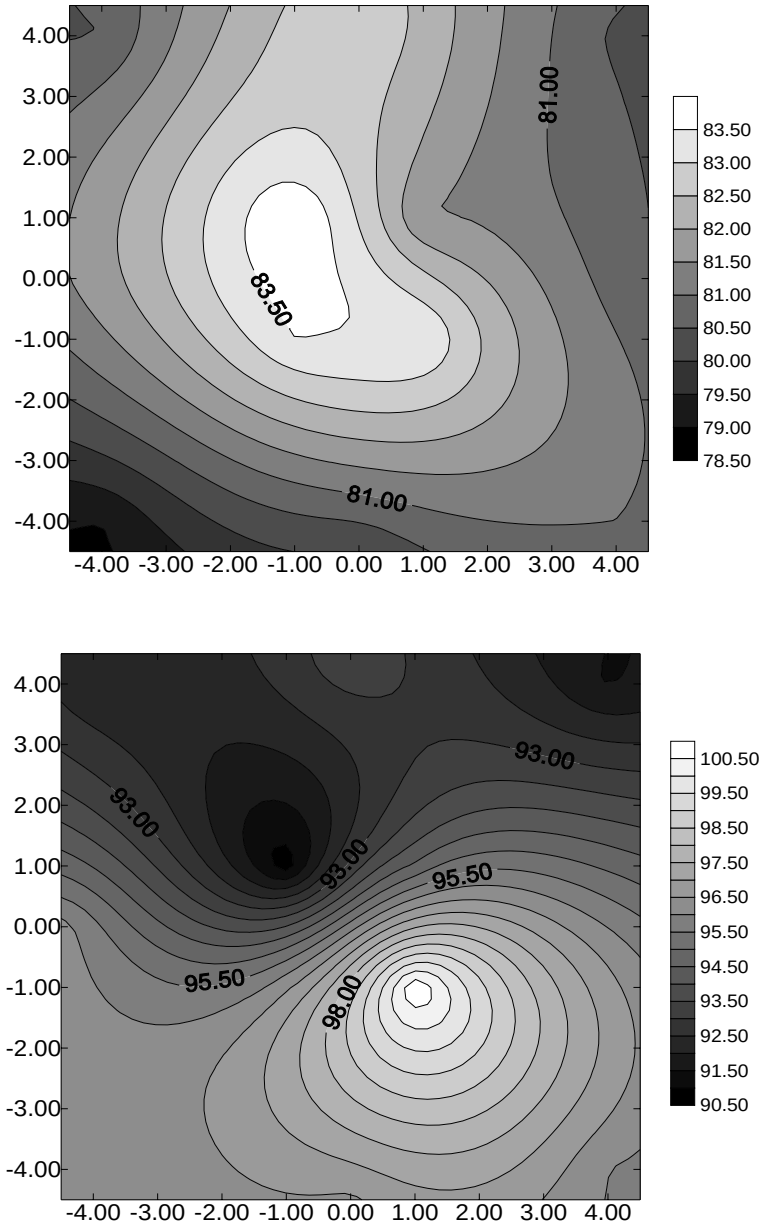

Fig. 3-12 The microhardness results taken from the transverse-sectional of samples processed by extrusion E1 (upper), and ECAP E1B (lower) specimens.

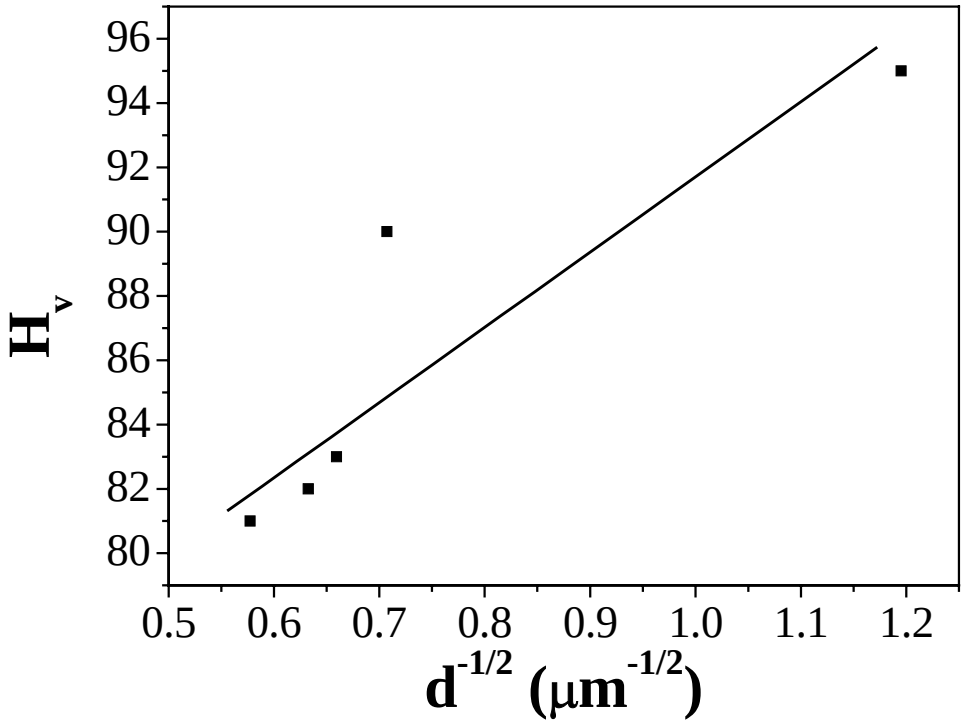

Fig. 3-13 Microhardness of the AZ31 alloy as a function of grain size.

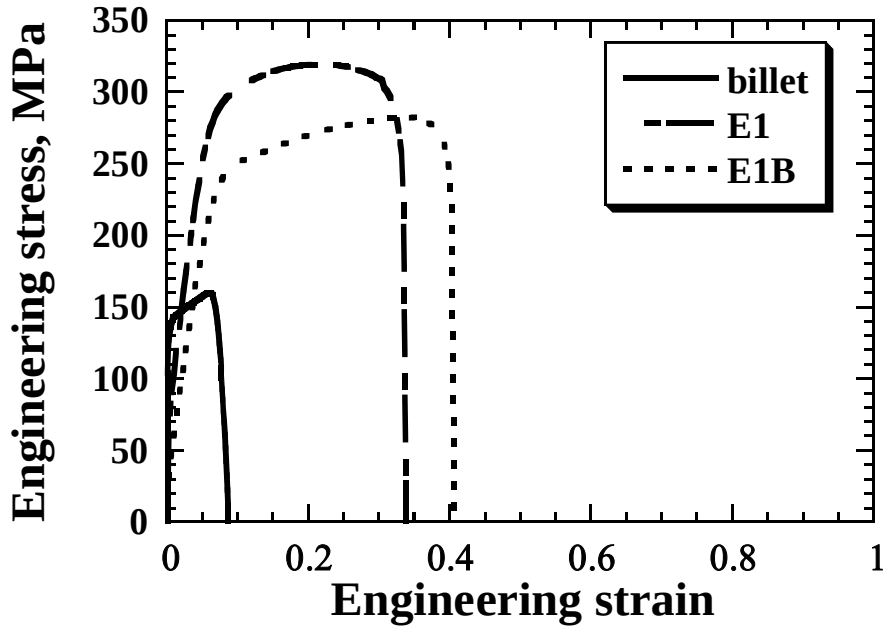

Fig. 3-14 Typical stress-strain curves for the billet, E1 and E1B specimens tensile-loaded at room temperature and 1×10^{-3} s^{-1}.

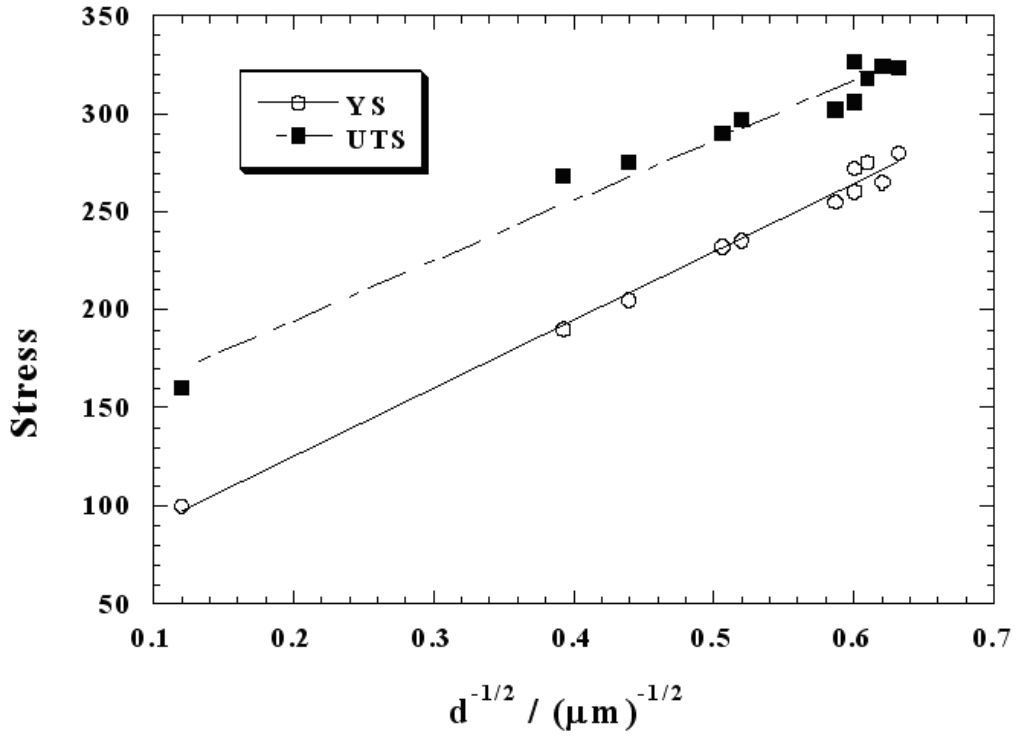

Fig. 3-15 Variation of the yield and ultimate tensile stresses of the E3 extruded plate as a function of $d^{-1/2}$ in accordance with the Hall-Petch relationship.

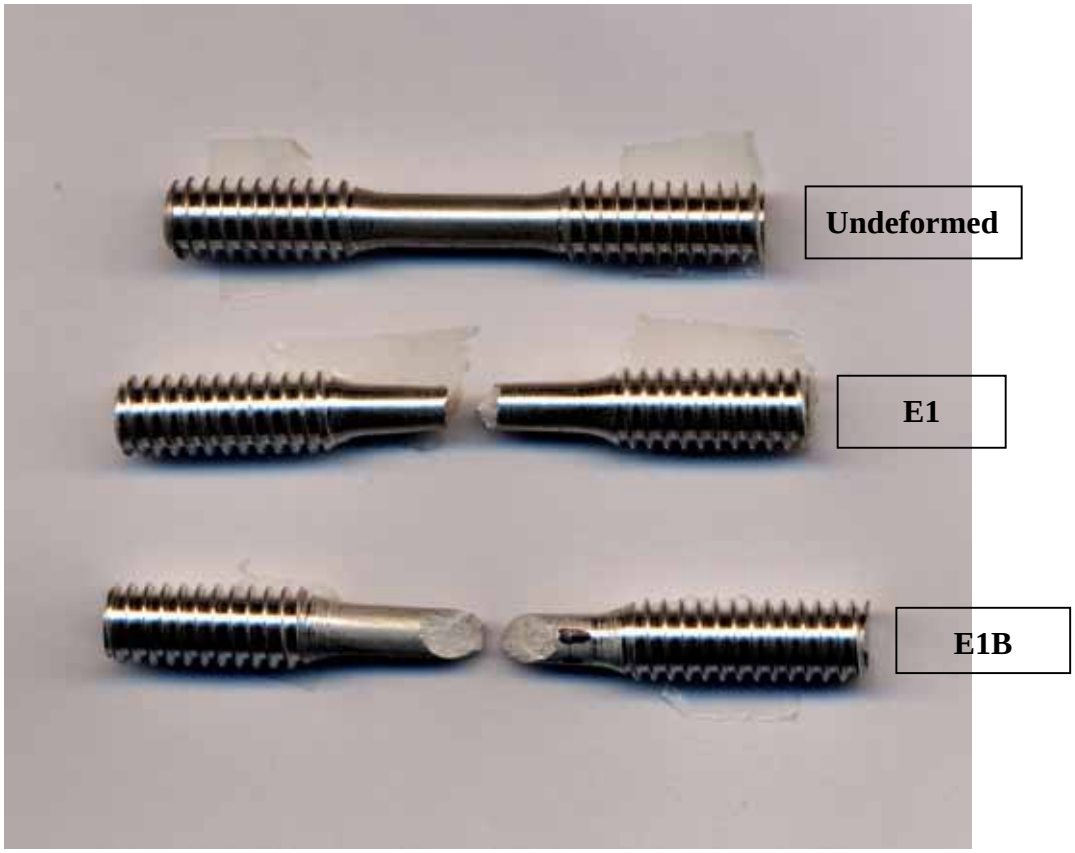

Fig. 3-16 The macroscopic fracture morphology of the E1 and E1B specimens.

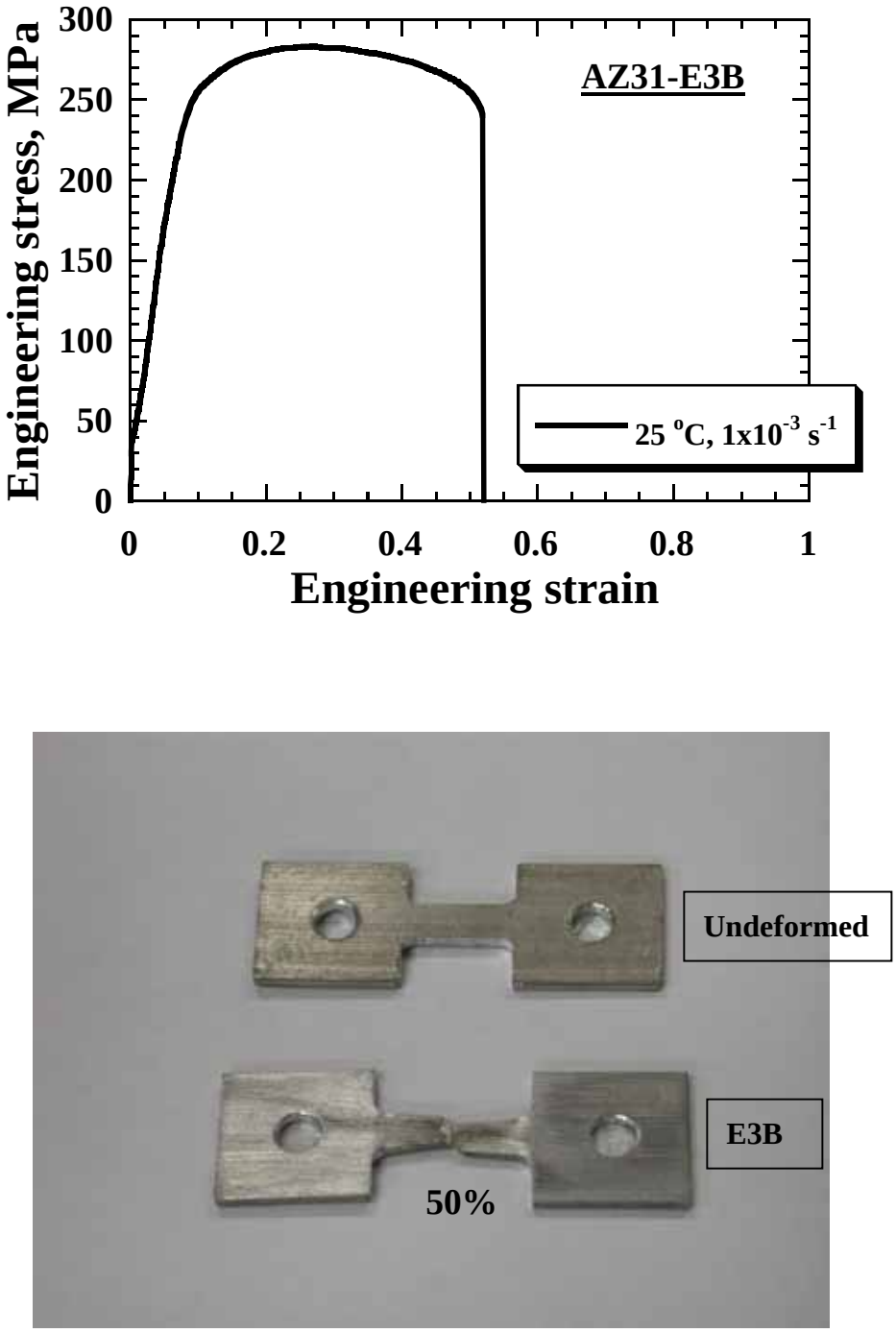

Fig. 3-17 The engineering stress versus engineering strain curves tensile-loaded at RT and the appearance of the E3B specimen after tensile testing.

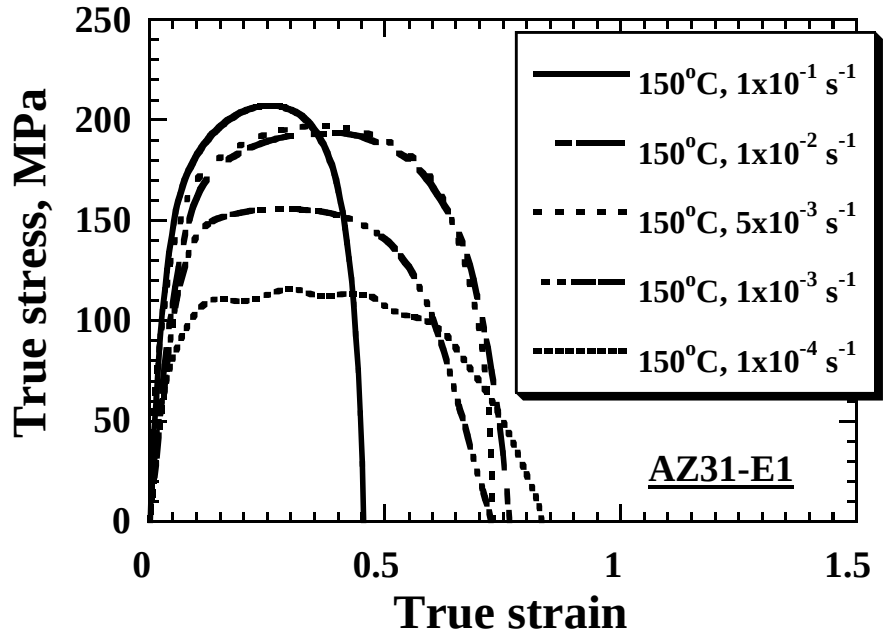

(a)

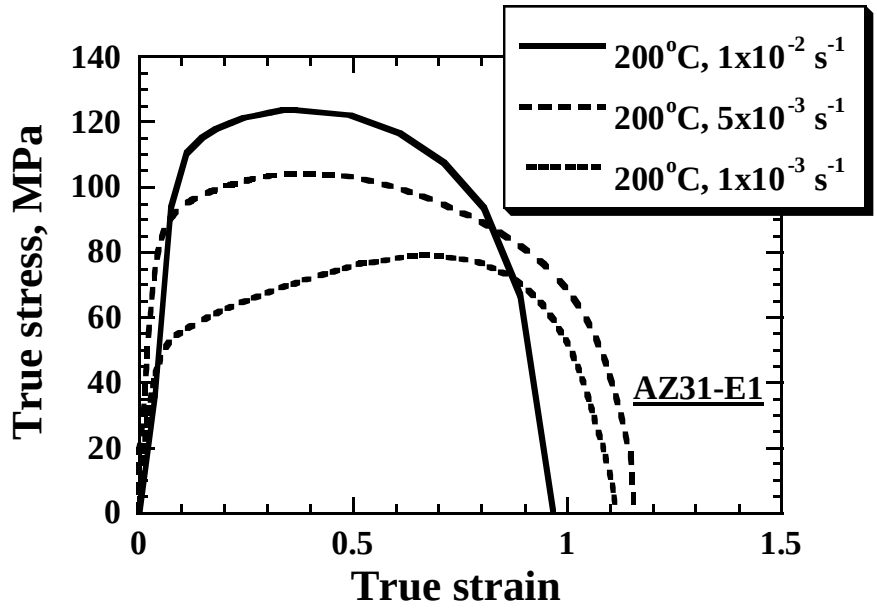

(b)

Fig. 3-18 The true stress versus true strain curves for the E1 (a)(b) and E1B (c)(d) samples tensile-loaded at 150 and 200°C.

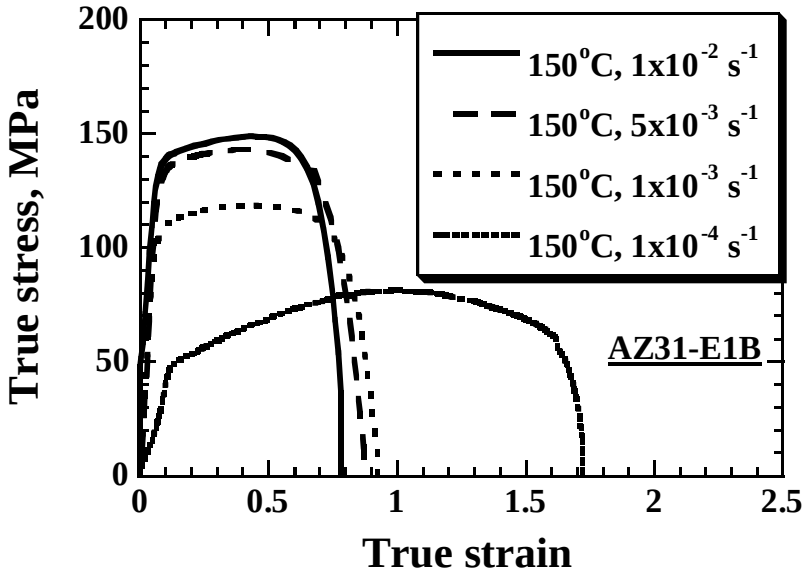
True stress, MPa
True strain
150°C, 1x10-2 s-1
150°C, 5x10-3 s-1
150°C, 1x10-3 s-1
150°C, 1x10-4 s-1
AZ31-E1B
0
50
100
150
200
0
0.5
1
1.5
2
2.5

(c)

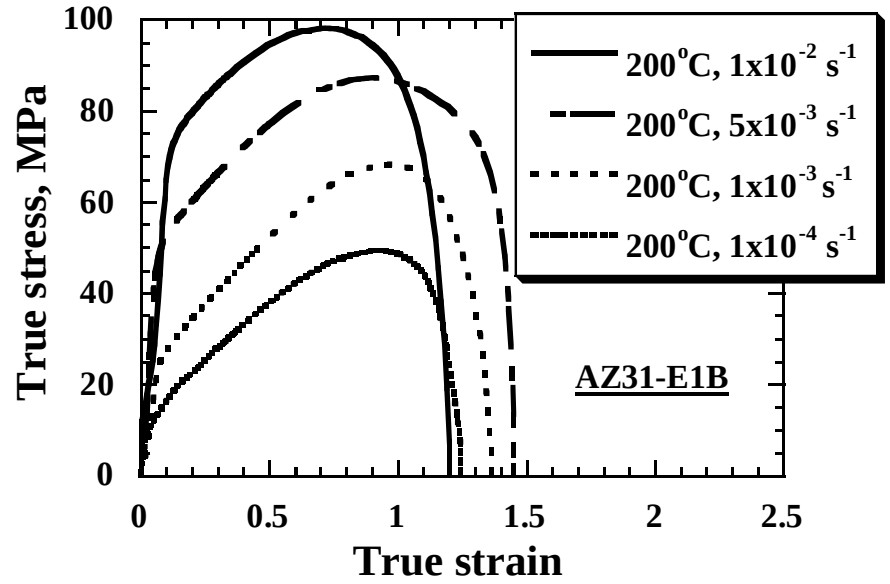
True stress, MPa
True strain
200°C, 1x10-2 s-1
200°C, 5x10-3 s-1
200°C, 1x10-3 s-1
200°C, 1x10-4 s-1
AZ31-E1B
0
20
40
60
80
100
0
0.5
1
1.5
2
2.5

(d)

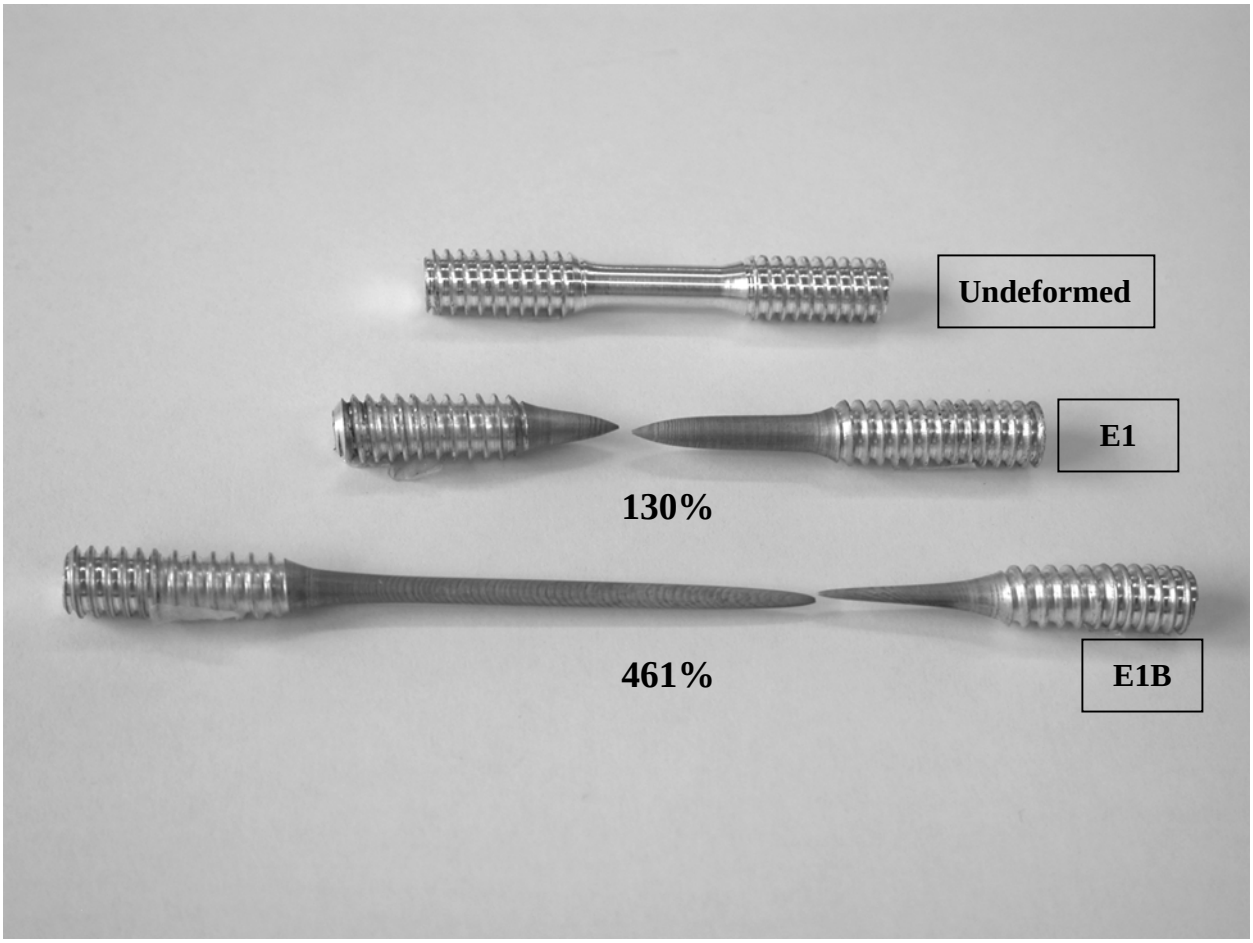

Fig. 3-19 Tensile specimens of E1 and E1B before test and tested at $1x10^{-4}$ s^{-1} and 150^{o}C.

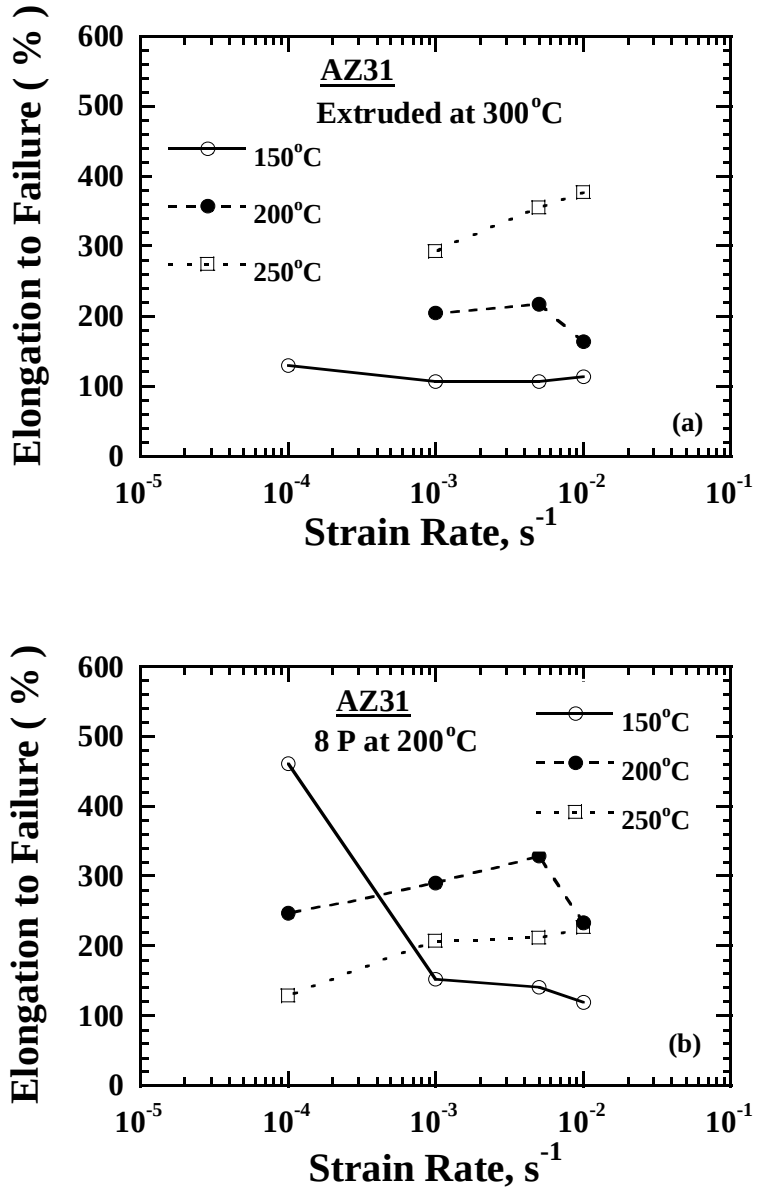

Fig. 3-20 Tensile elongation versus strain rate at 150 to 250°C for the (a) E1 and (b) E1B specimens.

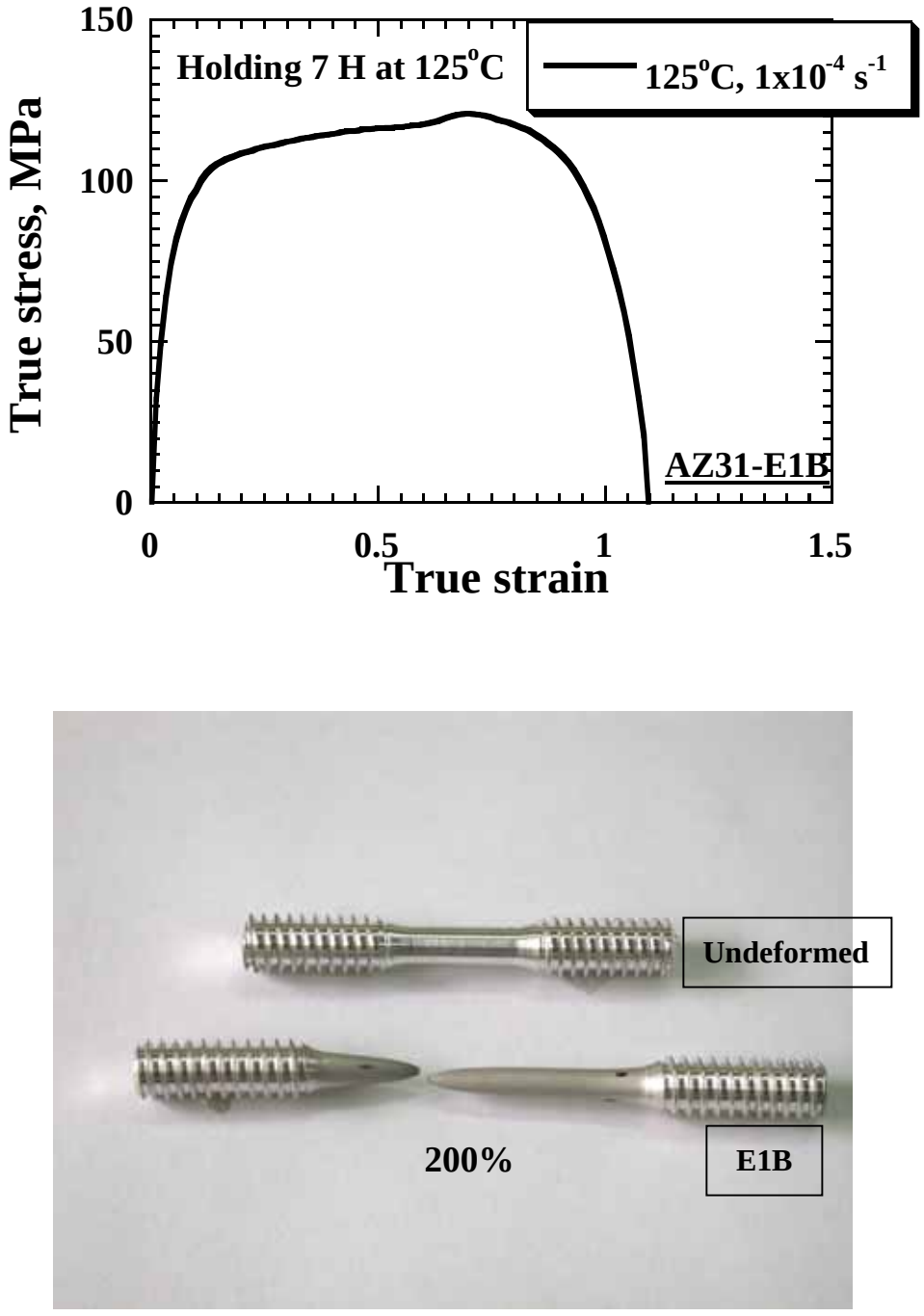

Fig. 3-21 The true stress versus true strain curves and the appearance of the E1B specimen after static annealing at 125°C for 7 h tensile-loaded at 125°C and $1x10^{-4}$ s^{-1}.

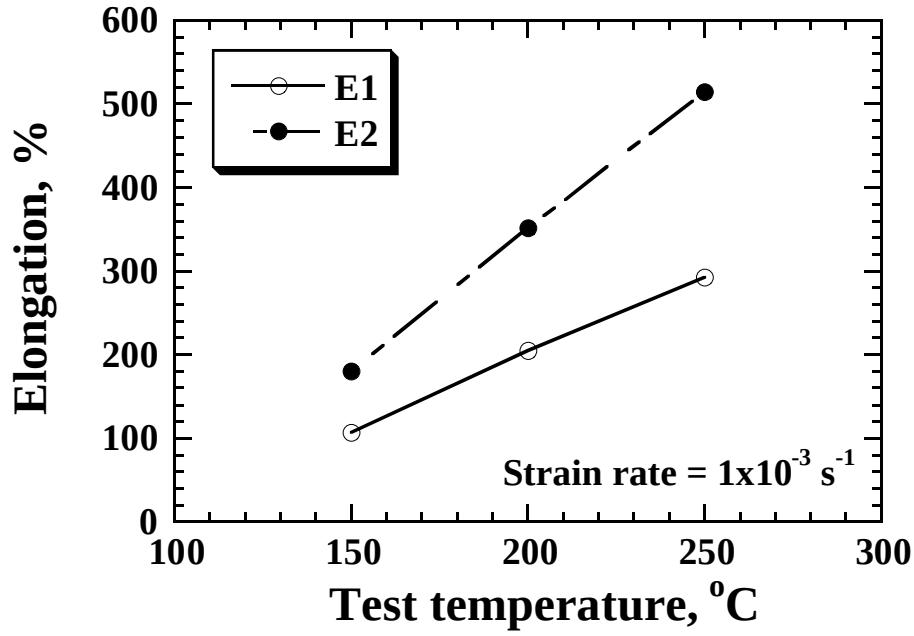

Fig. 3-22 The variation of elongation to failure as a function of test temperature.

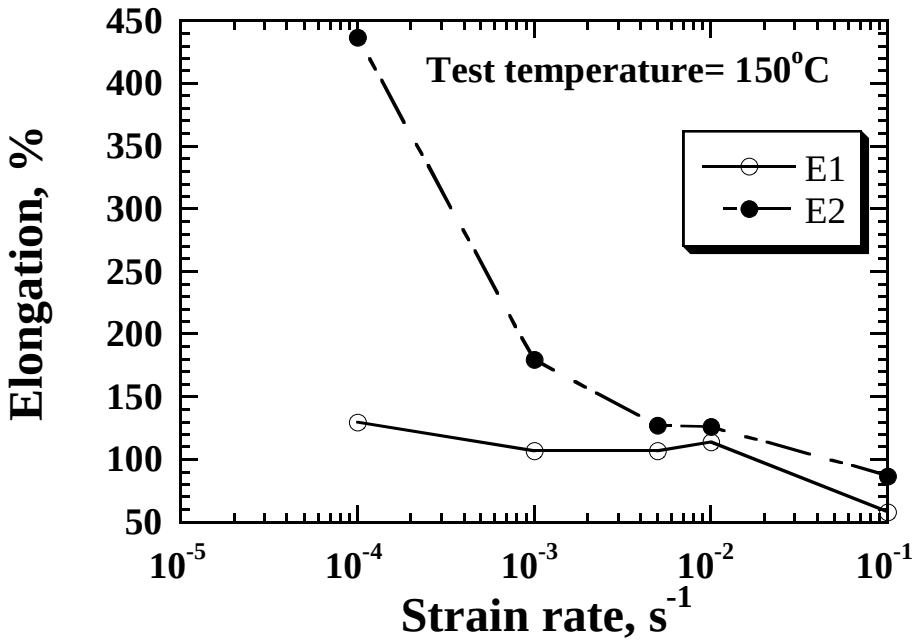

Fig. 3-23 The variation of elongation to failure as a function of strain rate.

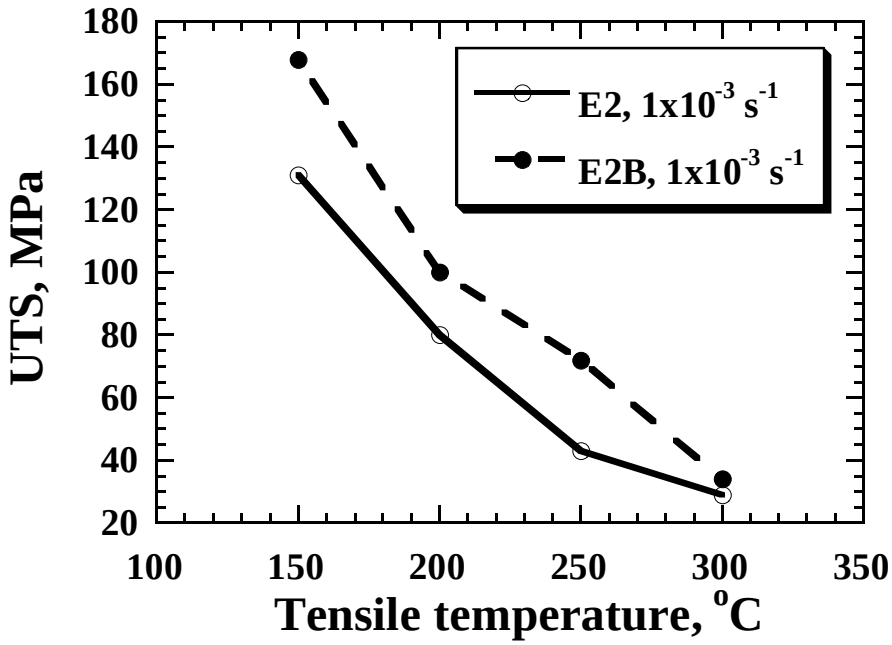

Fig. 3-24 The UTS versus tensile temperatures for the E2 and E2B specimens.

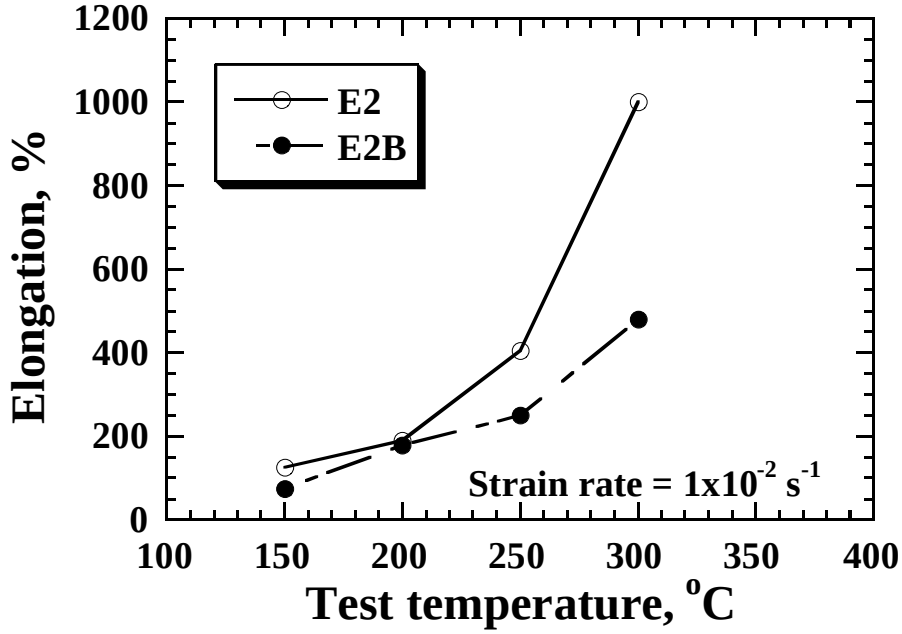

Fig. 3-25 The variation of elongation to failure as a function of test temperature for E2 and E2B.

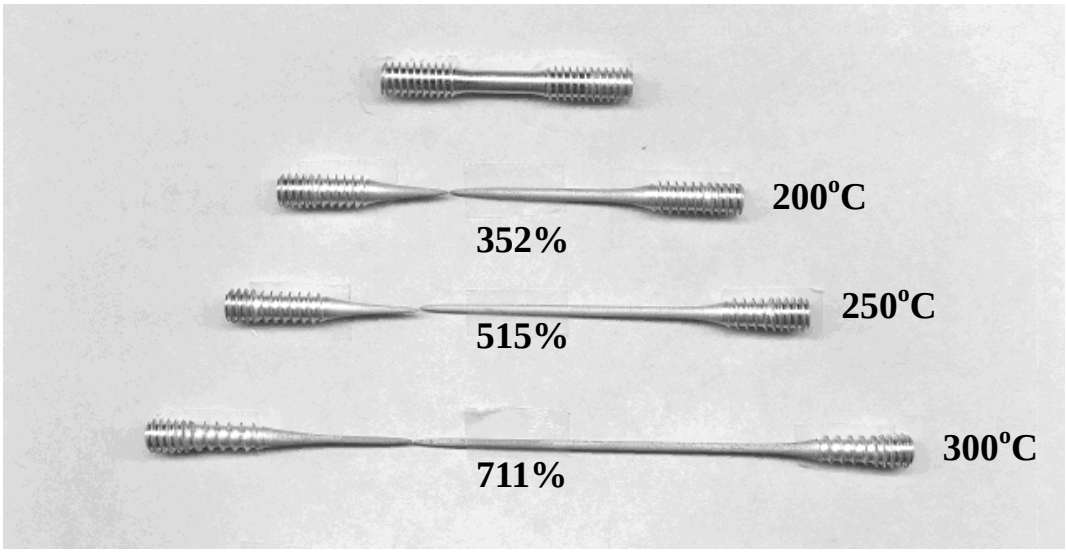

(a)

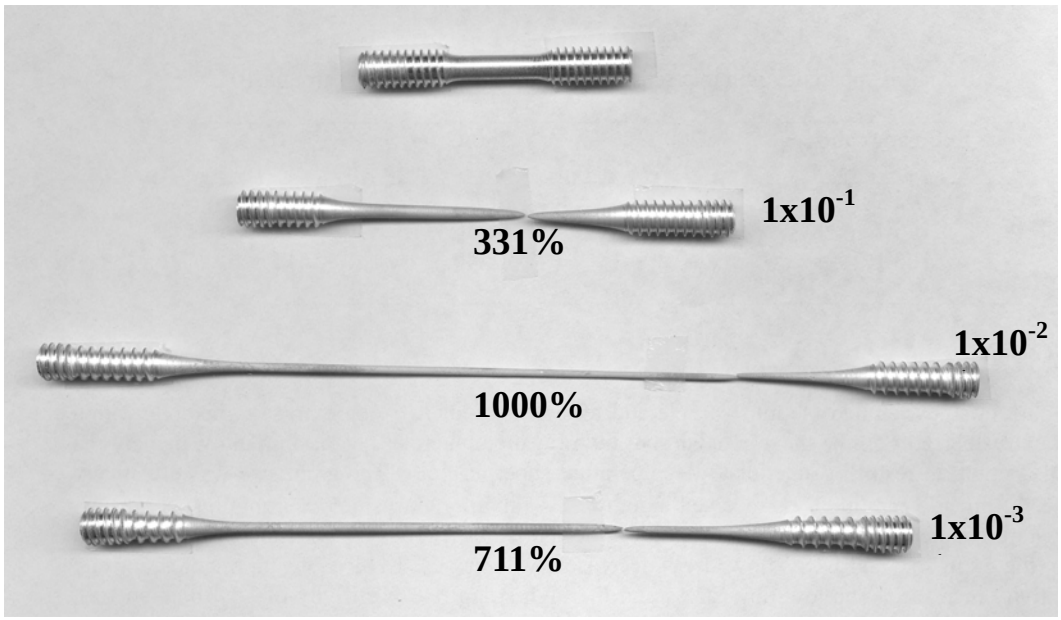

(b)

Fig. 3-26 Tensile specimens of the AZ31 E2 extruded rods: (a) fixed strain rate at $1x10^{-3}$ s^{-1} and (b) fixed tensile temperature at 300°C.

Fig. 3-27 Tensile specimens of the AZ31 E2B extruded plates fixed strain rate at $1x10^{-3}$ s^{-1}.

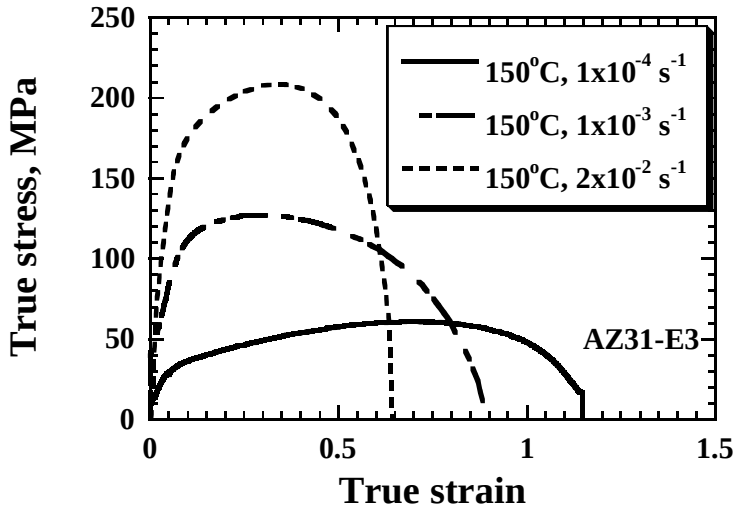

(a)

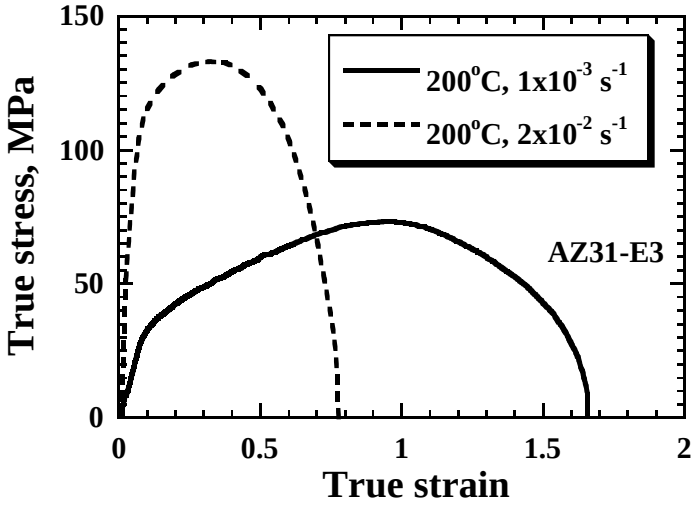

(b)

Fig. 3-28 Typical true stress and strain curves for the E3 specimens recorded from tensile tests at different initial strain rates for the loading temperatures of (a)150, (b) 200, (c) 250, (d) 280, and (e) 300°C.

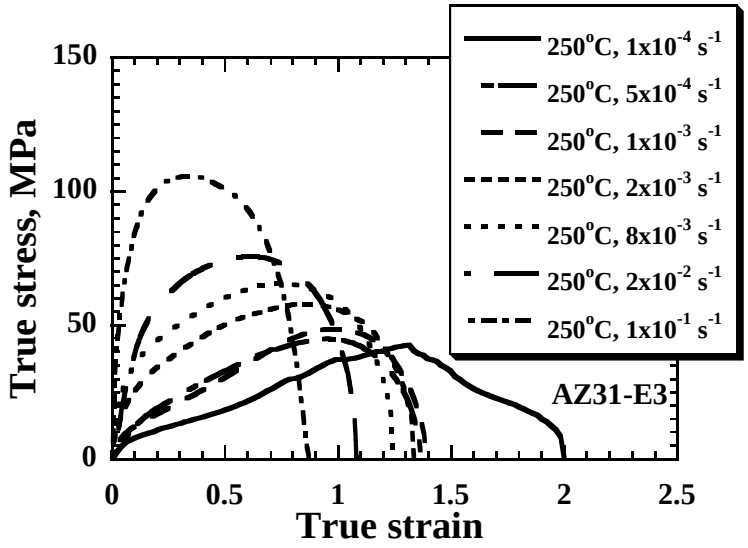
250°C, 1x10-4 s-1
250°C, 5x10-4 s-1
250°C, 1x10-3 s-1
250°C, 2x10-3 s-1
250°C, 8x10-3 s-1
250°C, 2x10-2 s-1
250°C, 1x10-1 s-1
AZ31-E3
True stress, MPa
True strain
0
50
100
150
0
0.5
1
1.5
2
2.5

(c)

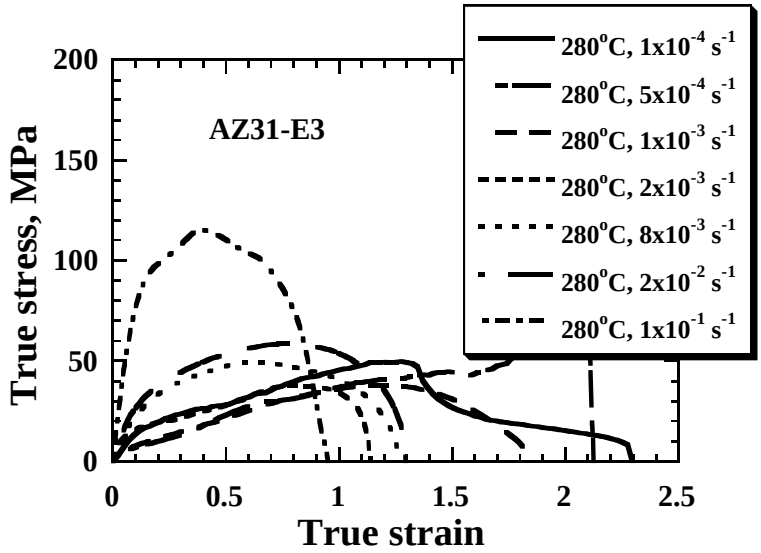
280°C, 1x10-4 s-1
280°C, 5x10-4 s-1
280°C, 1x10-3 s-1
280°C, 2x10-3 s-1
280°C, 8x10-3 s-1
280°C, 2x10-2 s-1
280°C, 1x10-1 s-1
AZ31-E3
True stress, MPa
True strain
0
50
100
150
200
0
0.5
1
1.5
2
2.5

(d)

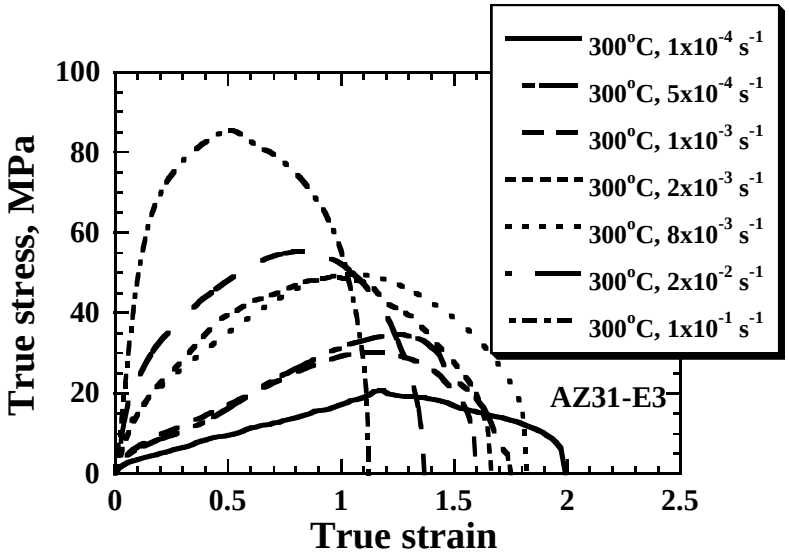
300°C, 1x10-4 s-1
300°C, 5x10-4 s-1
300°C, 1x10-3 s-1
300°C, 2x10-3 s-1
300°C, 8x10-3 s-1
300°C, 2x10-2 s-1
300°C, 1x10-1 s-1
AZ31-E3
True stress, MPa
True strain
0
20
40
60
80
100
0
0.5
1
1.5
2
2.5

(e)

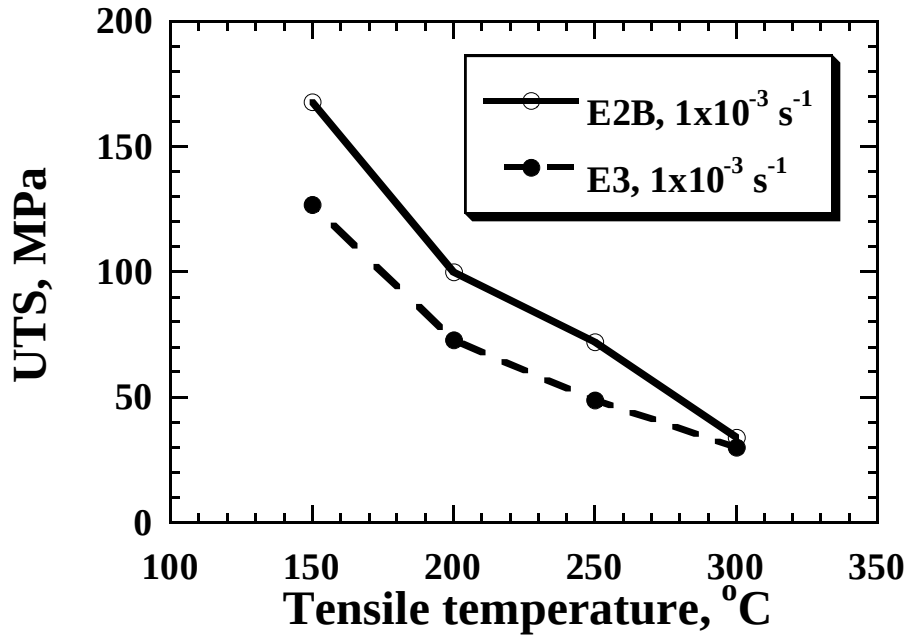

Fig. 3-29 The UTS versus tensile temperatures for the E2B and E3 specimens.

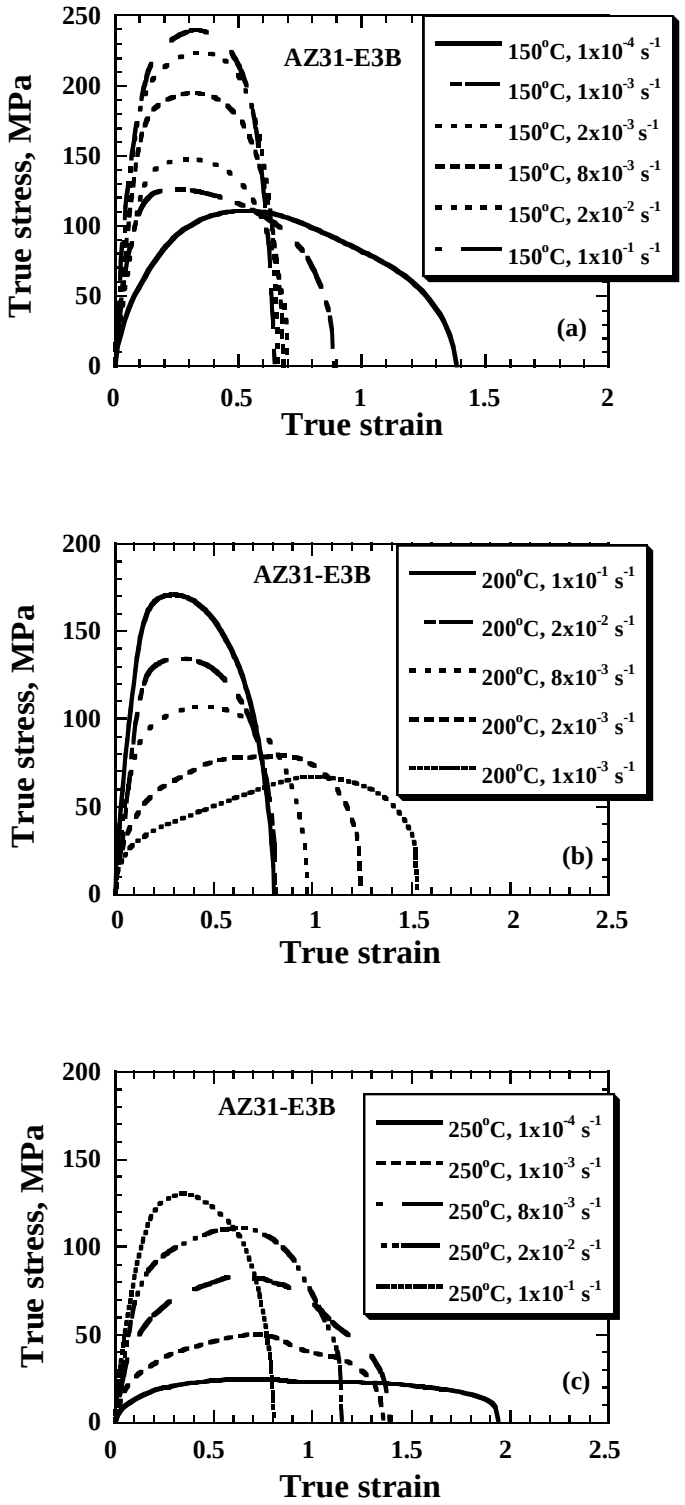

Fig. 3-30 Typical true stress and strain curves for the E3B specimens recorded from tensile tests at different initial strain rates for the loading temperatures of (a) 150°C, (b) 200°C, (c) 250°C, (d) 280°C and (e) 300°C.

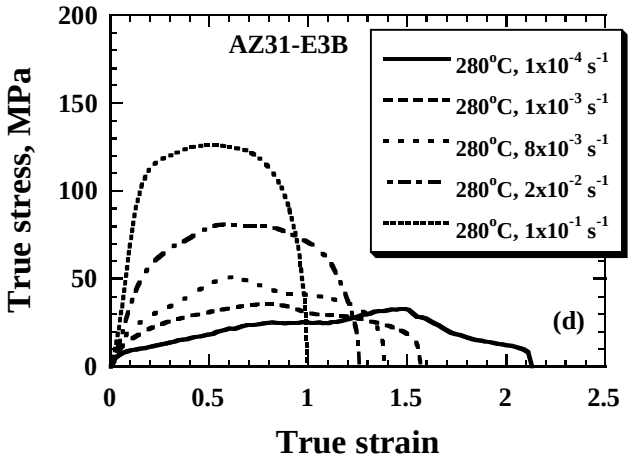
AZ31-E3B
280°C, 1x10-4 s-1
280°C, 1x10-3 s-1
280°C, 8x10-3 s-1
280°C, 2x10-2 s-1
280°C, 1x10-1 s-1
(d)
True stress, MPa
True strain
0
50
100
150
200
0
0.5
1
1.5
2
2.5

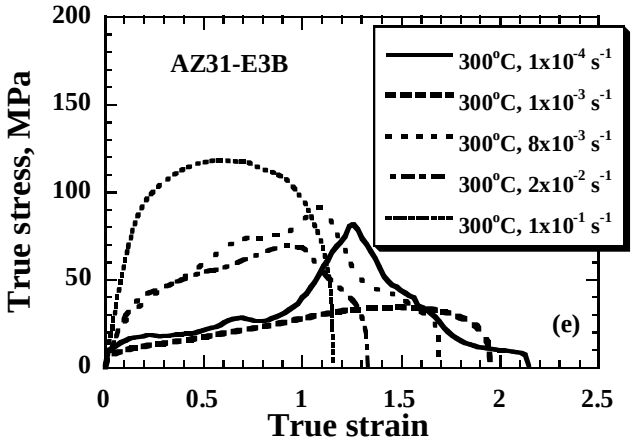
AZ31-E3B
300°C, 1x10-4 s-1
300°C, 1x10-3 s-1
300°C, 8x10-3 s-1
300°C, 2x10-2 s-1
300°C, 1x10-1 s-1
(e)
True stress, MPa
True strain
0
50
100
150
200
0
0.5
1
1.5
2
2.5

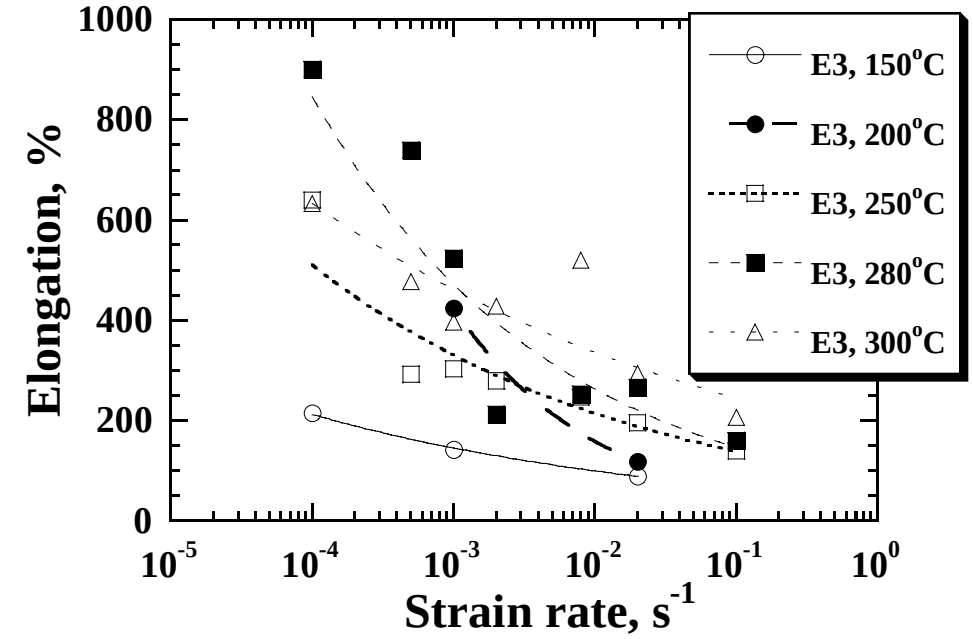

(a)

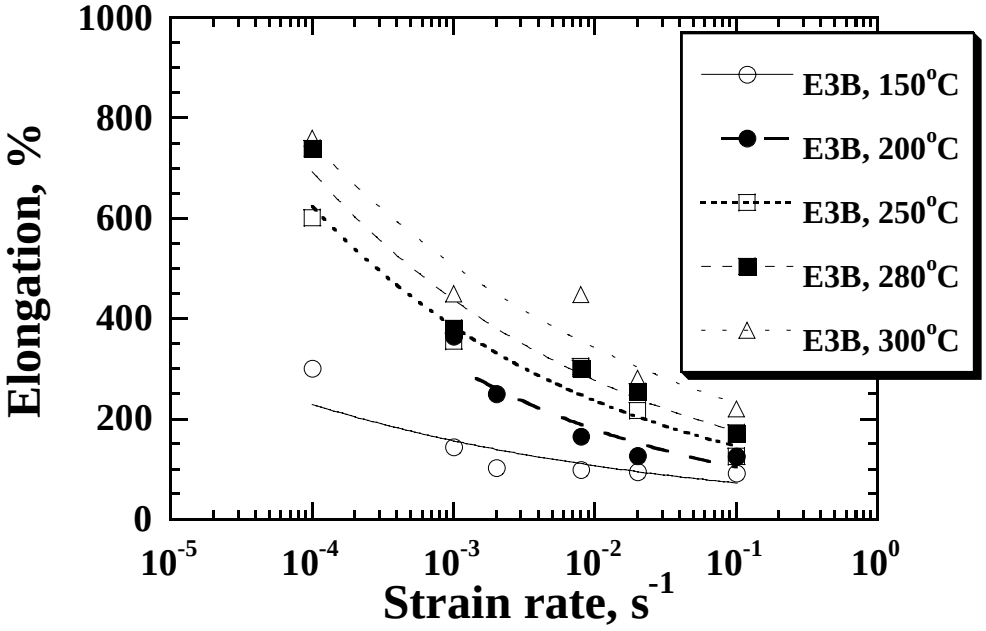

(b)

Fig. 3-31 Variation of the tensile elongation as a function of test strain rate for the AZ31 (a) E3 and (b) E3B specimens.

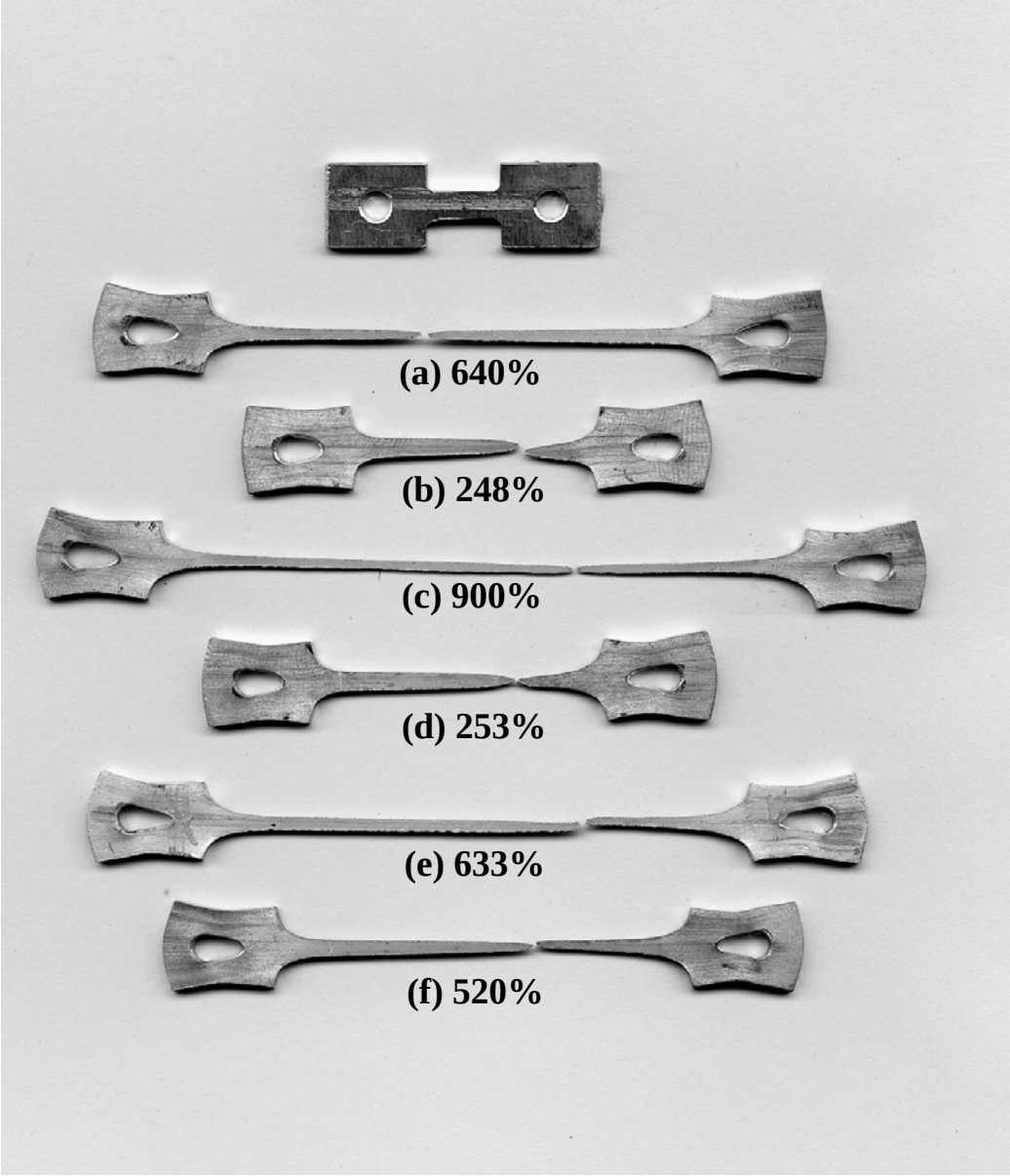

Fig. 3-32 Representative tensile specimens of the AZ31 E3 extruded plates: (a) 250^{o}C and 1x10^{-4} s^{-1}, (b) 250^{o}C and 8x10^{-3} s^{-1}, (c) 280^{o}C and 1x10^{-4} s^{-1}, (d) 280^{o}C and 8x10^{-3} s^{-1}, (e) 300^{o}C and 1x10^{-4} s^{-1}, (f) 300^{o}C and 8x10^{-3} s^{-1}.

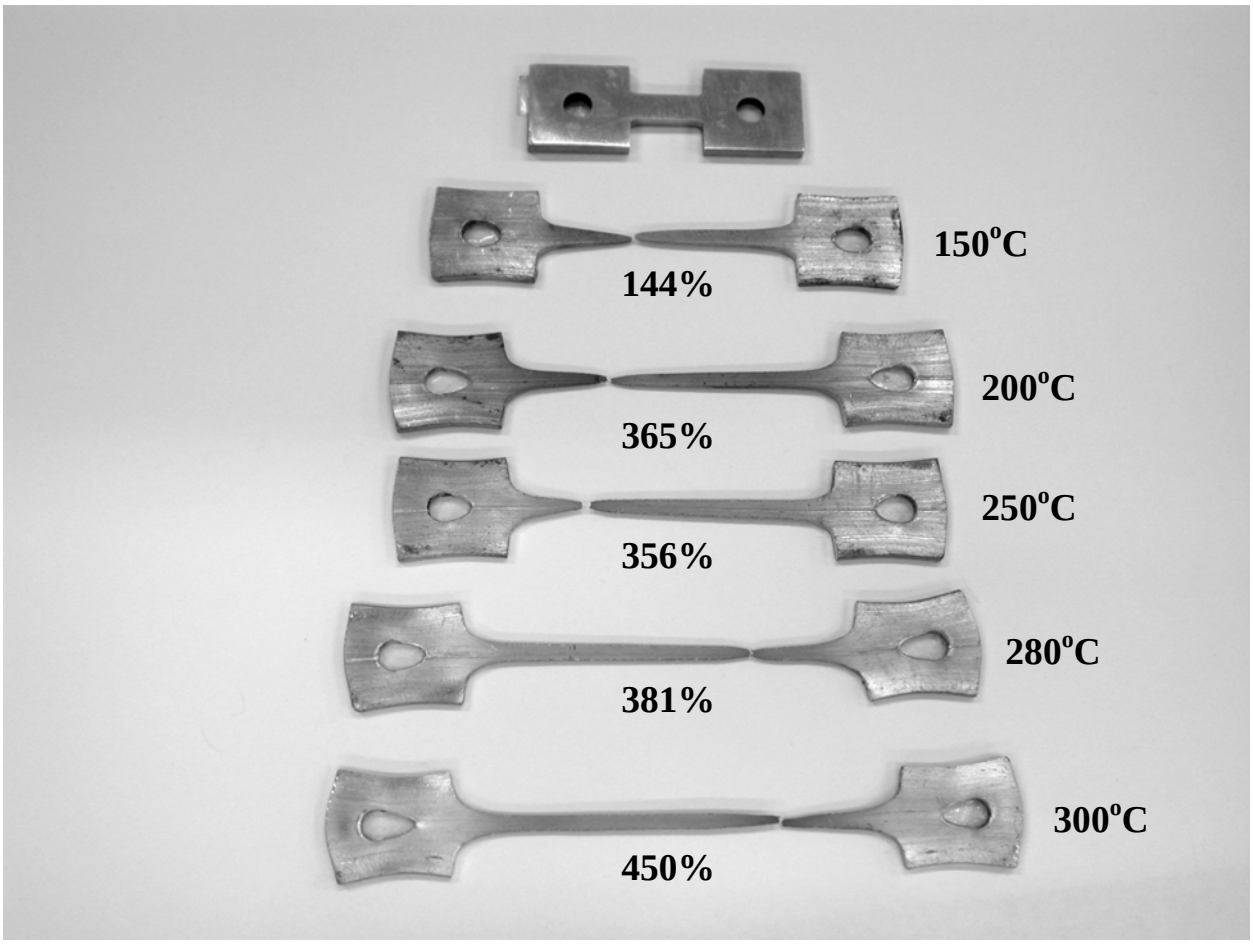

Fig. 3-33 Tensile specimens of the AZ31 E3B extruded plates fixed strain rate at $1x10^{-3}$ s^{-1}.

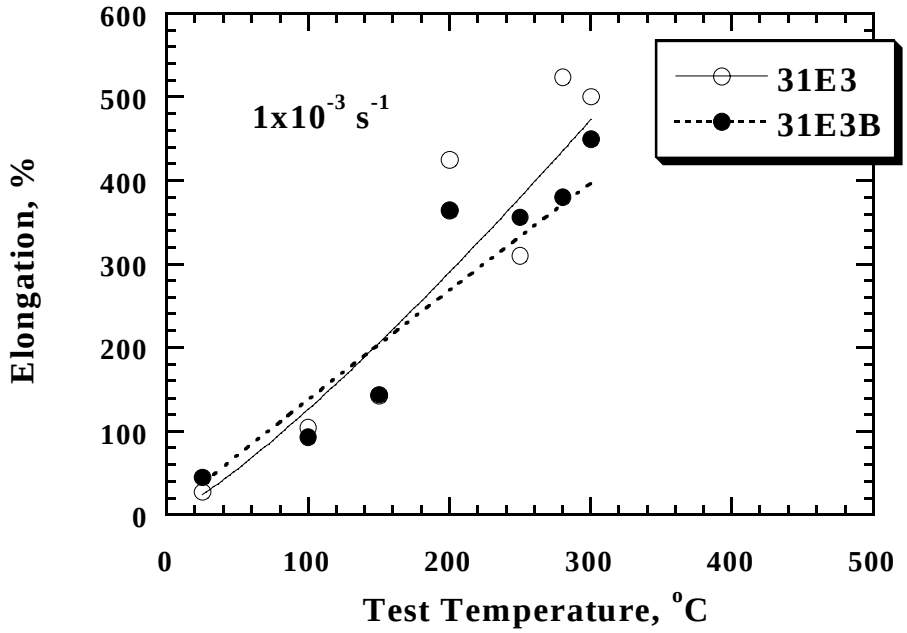

Fig. 3-34 Variation of the tensile elongation as a function of test temperature for the E3 and E3B specimens at a strain rate of $1x10^{-3}$ s^{-1}.

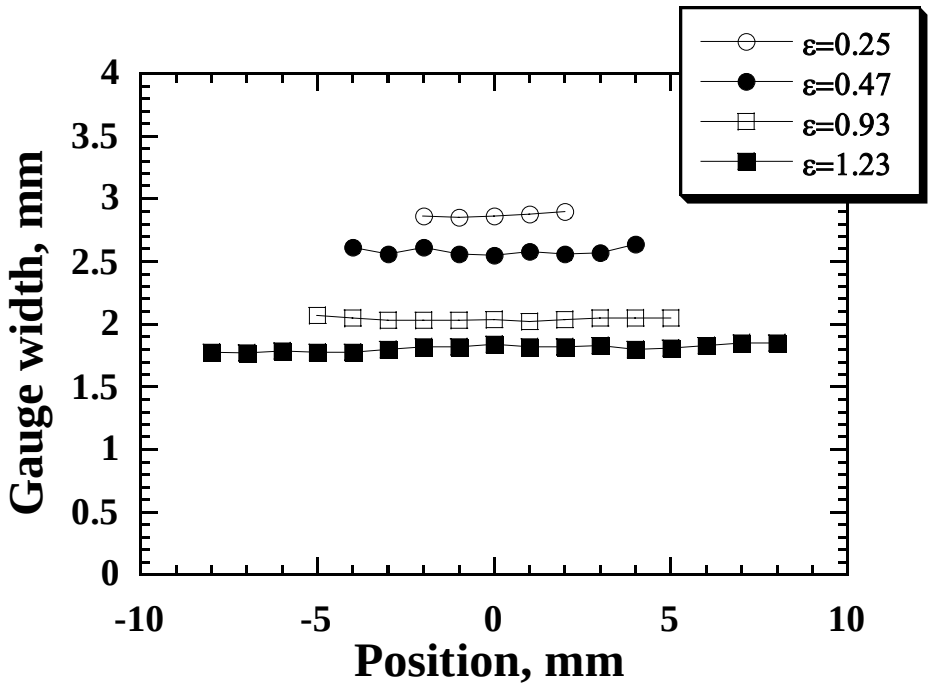

Fig. 3-35 Variation of cross-sectional area for the E3 specimens deformed at 300°C and $1x10^{-3}$ s^{-1} to tensile strains of 0.25, 0.47, 0.93, and 1.23.

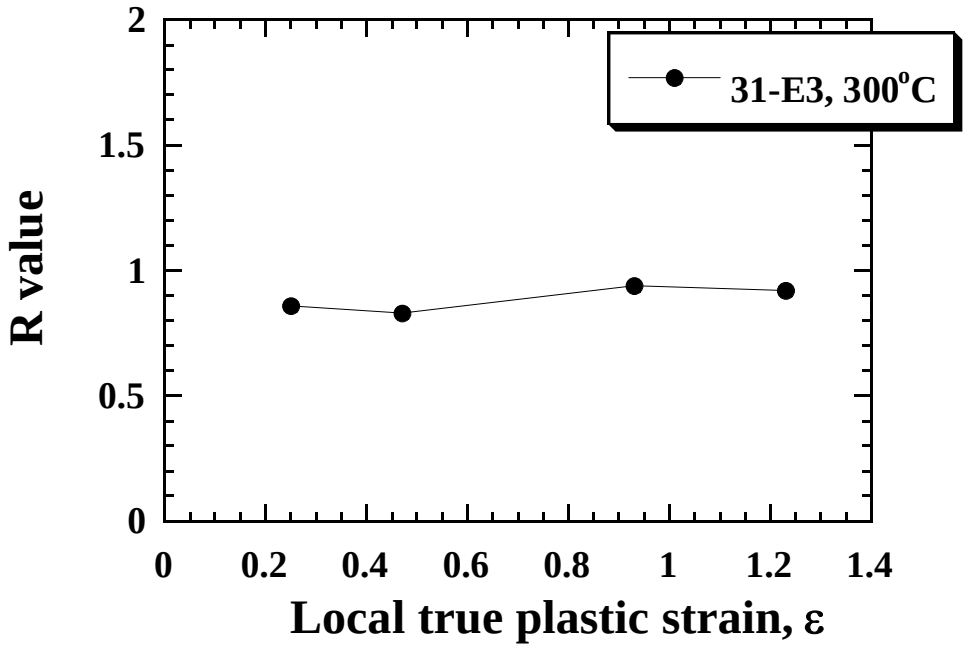

Fig. 3-36 Variation of R for the E3 specimens deformed at 300°C and $1x10^{-3}$ s^{-1} to different tensile strains.

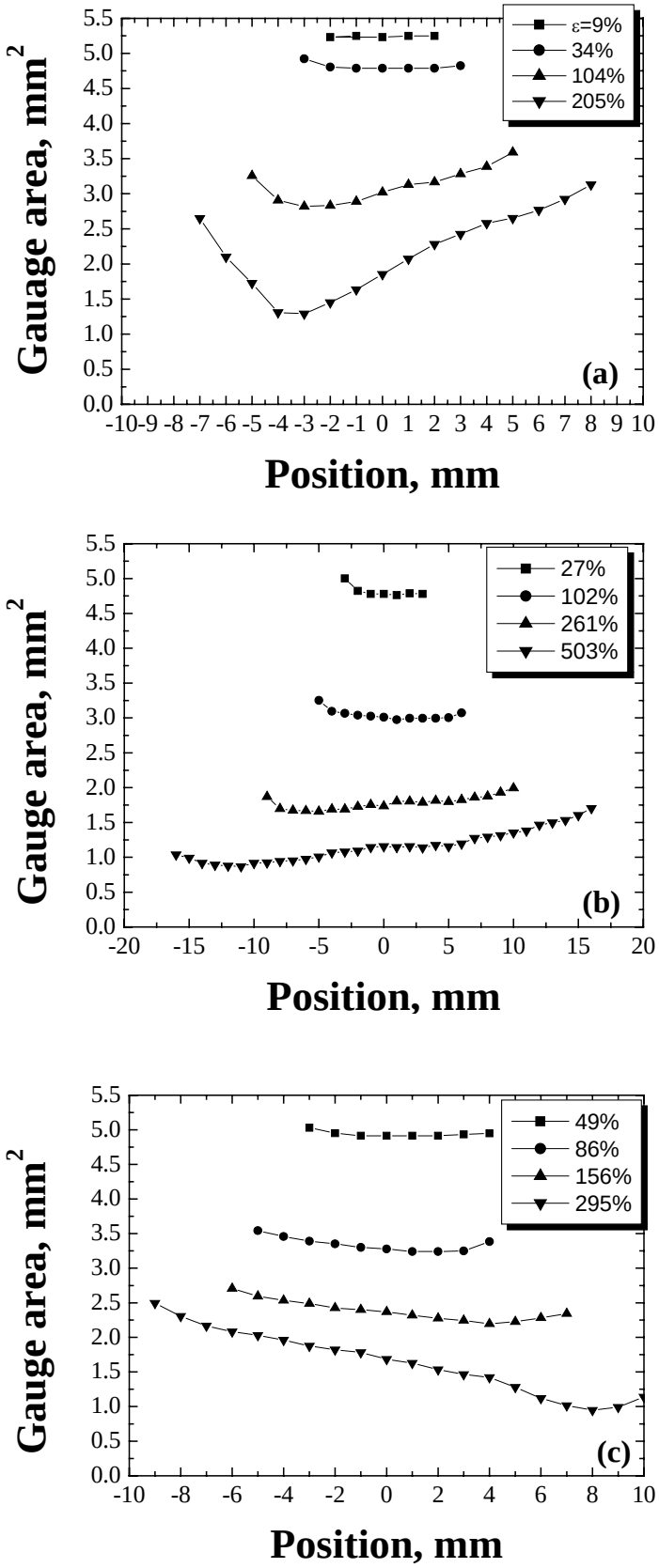

Fig. 3-37 Variation of cross-sectional area for the E2B specimens that deformed during tensile conditions: (a) 200°C, $6x10^{-4}$ s^{-1}, (b) 300°C, $6x10^{-4}$ s^{-1}, (c) 300°C, $1x10^{-2}$ s^{-1}.

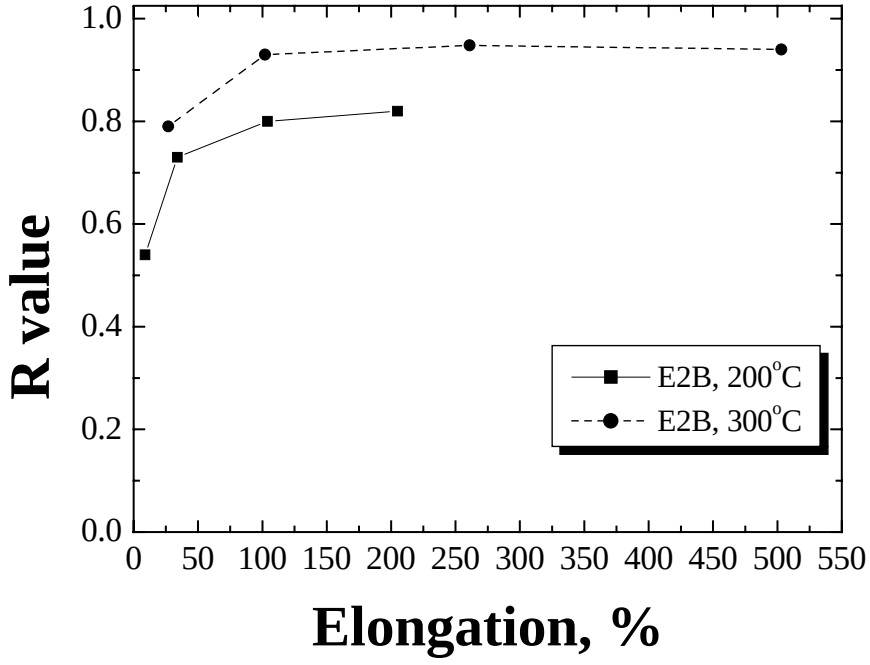

(a) E2B specimen tested at 6 x 10^{-4} s^{-1}.

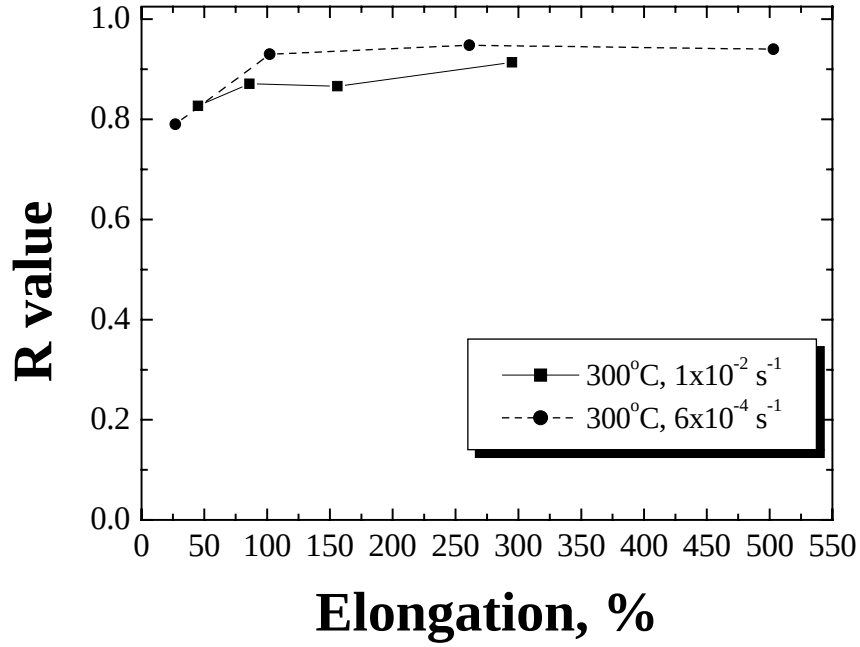

(b) E2B specimen tested at 300°C.

Fig. 3-38 Variation of R for the E2B specimens to different elongations.

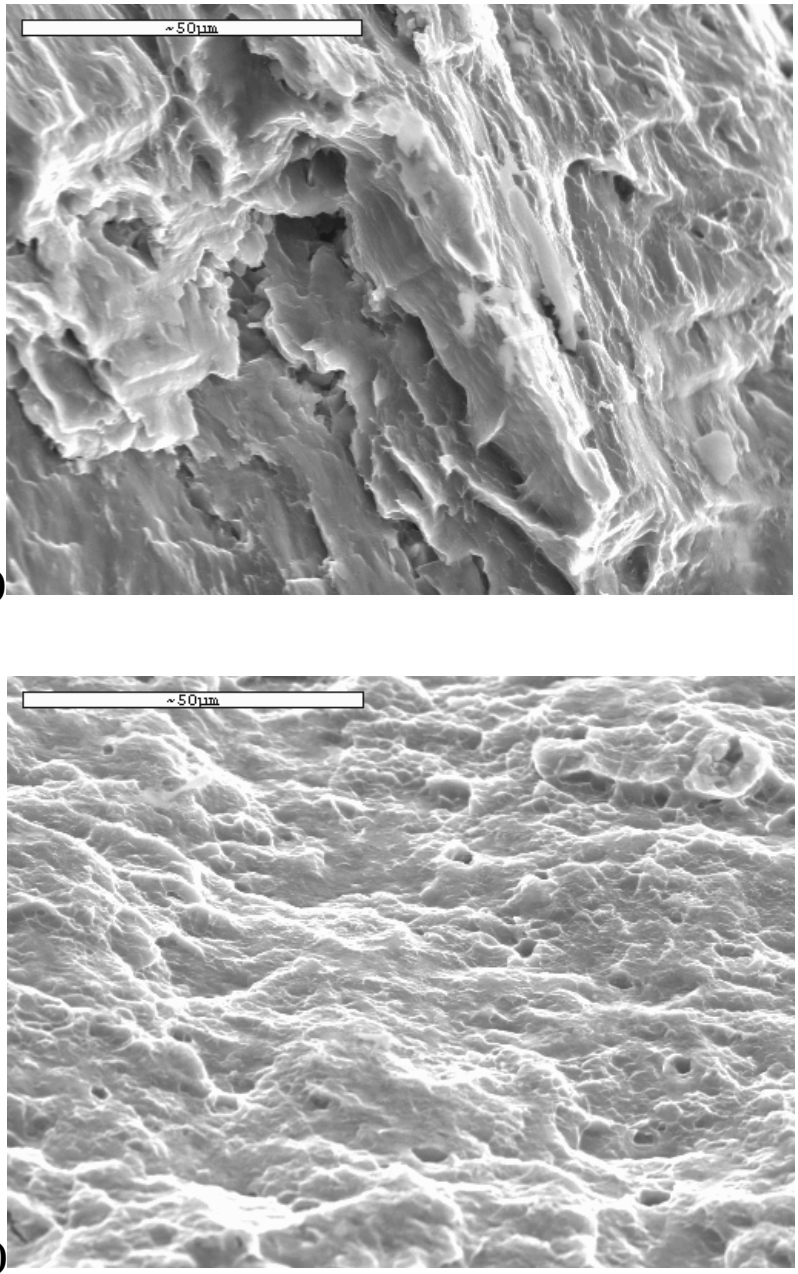

Fig. 3-39 SEM micrographs of fractures observed in the (a) billet and (b) E3B specimens after tensile test at room temperature.

(a)

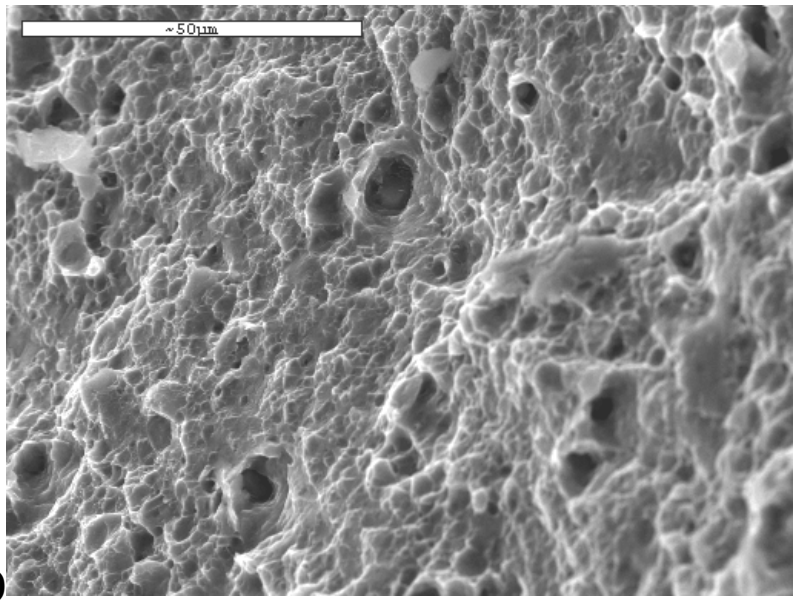

(b)

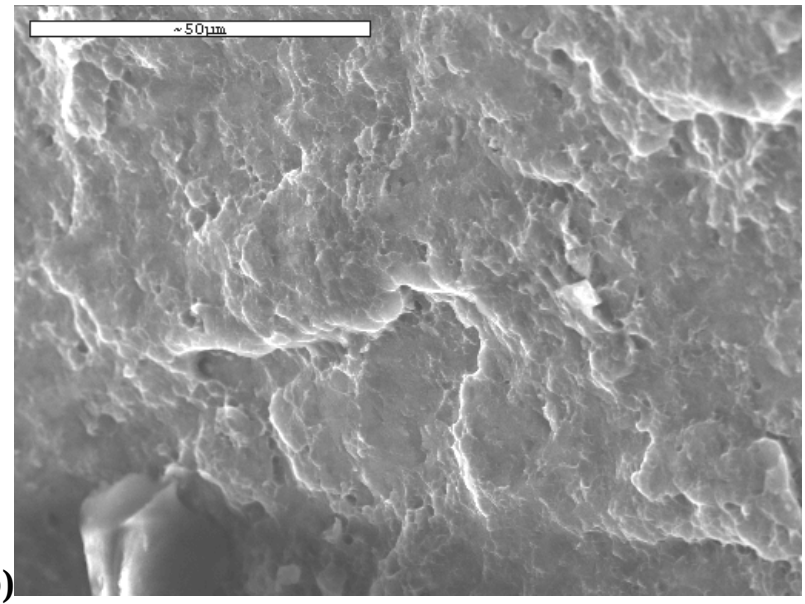

Fig. 3-40 SEM micrographs of fractures observed in the (a) E1 and (b) E1B specimens after tensile test at room temperature.

(a)

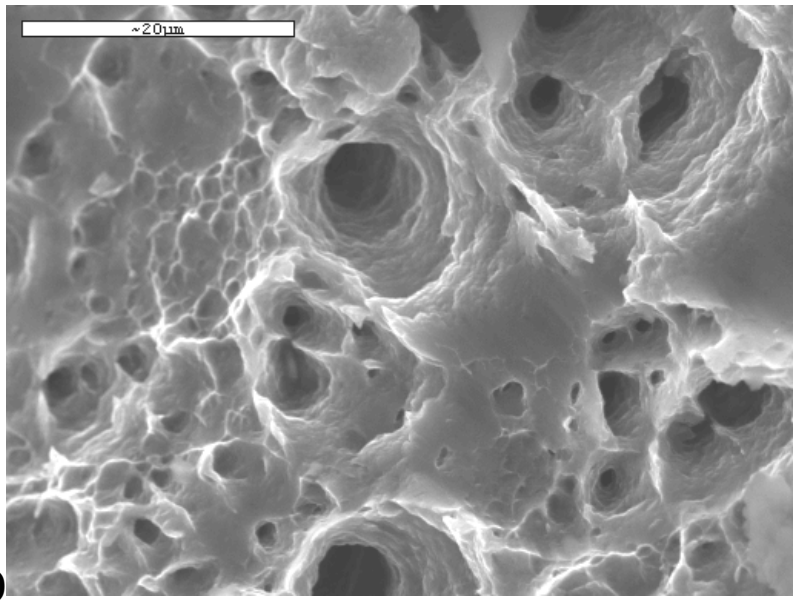

(b)

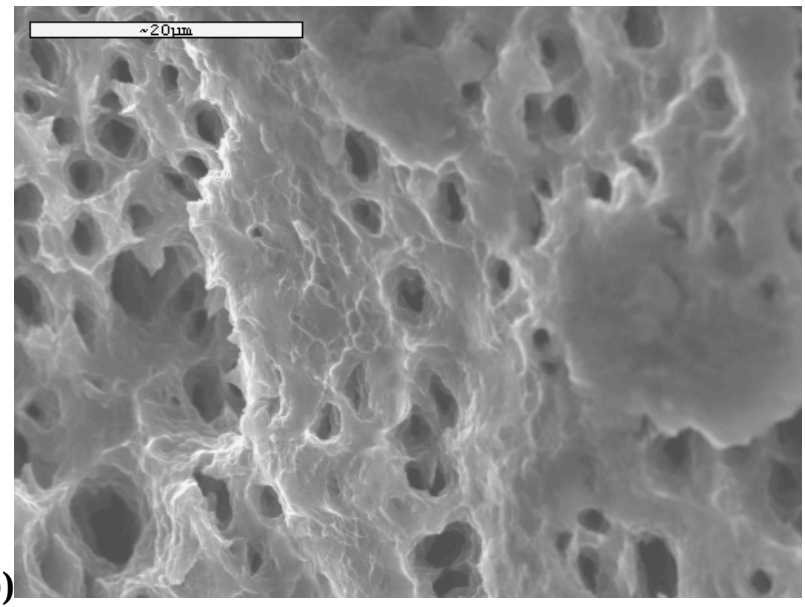

Fig. 3-41 The fracture surface of the E1B specimen after tensile testing at 150^{o}C and different strain rates of (a) 1x10^{-2} and (b) 1x10^{-4} s^{-1}.

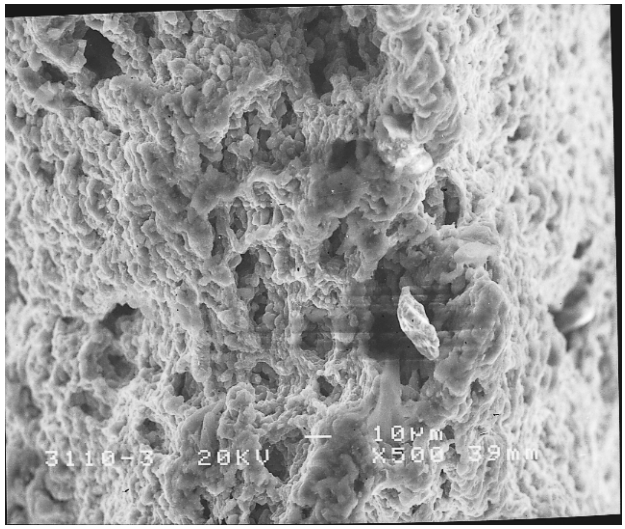

(a)

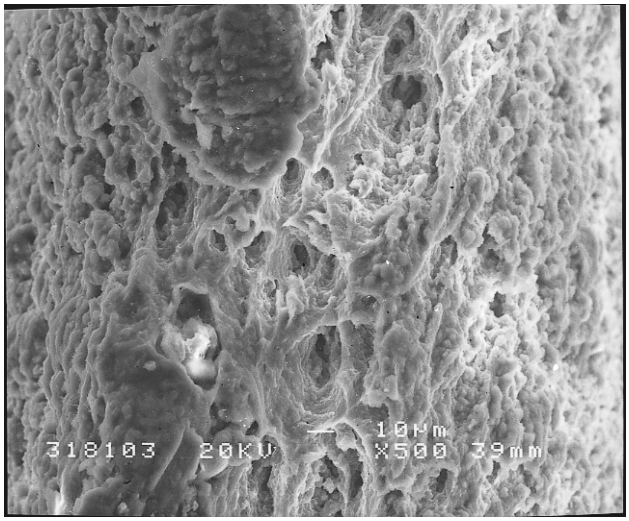

(b)

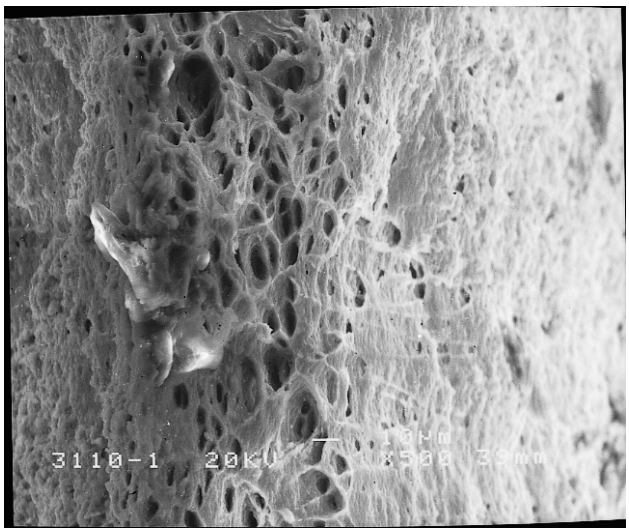

(c)

Fig. 3-42 The fracture surfaces of the E3 specimens tensile-loaded at 300°C and (a) $1x10^{-3}$, (b) $8x10^{-3}$, and (c) $1x10^{-1}$ s^{-1}.

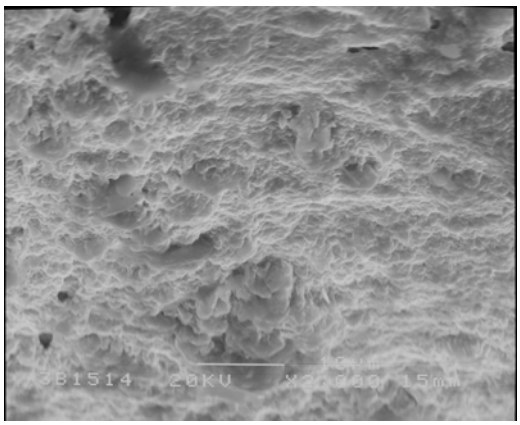

(a)

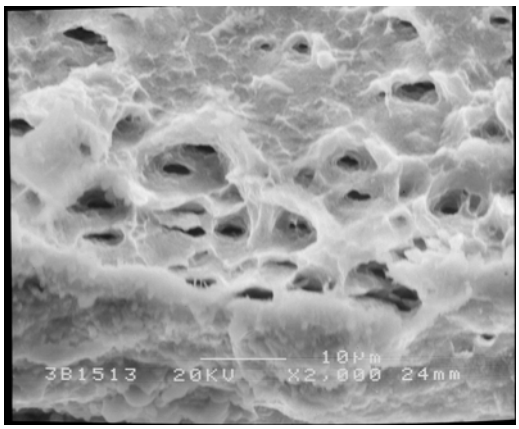

(b)

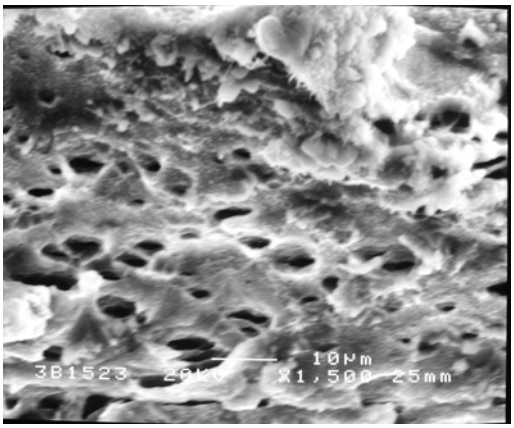

(c)

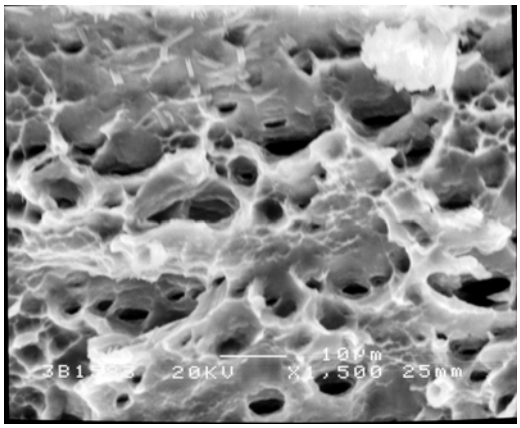

(d)

Fig. 3-43 The fracture surfaces of the E3B specimens tensile-loaded at 150°C and (a) $1x10^{-4}$, (b) $1x10^{-3}$, (c) $2x10^{-3}$ and (d) $8x10^{-3}$ s^{-1}.

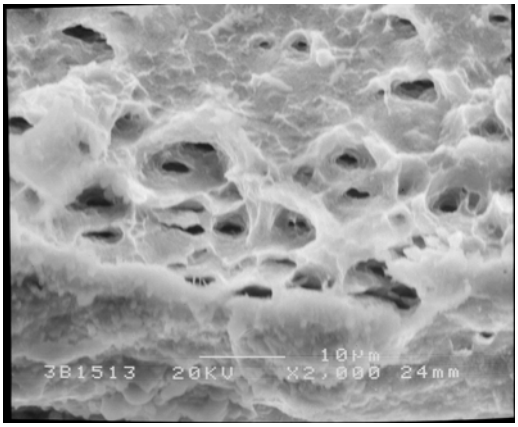

(a)

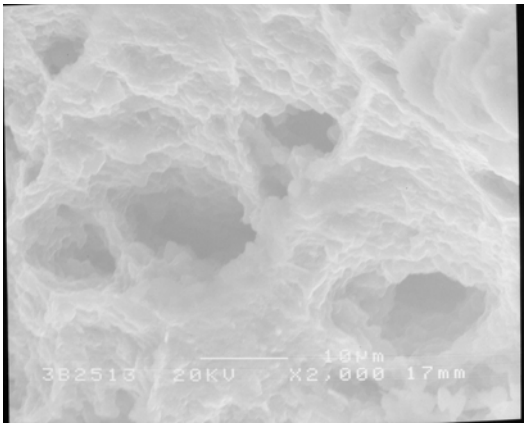

(b)

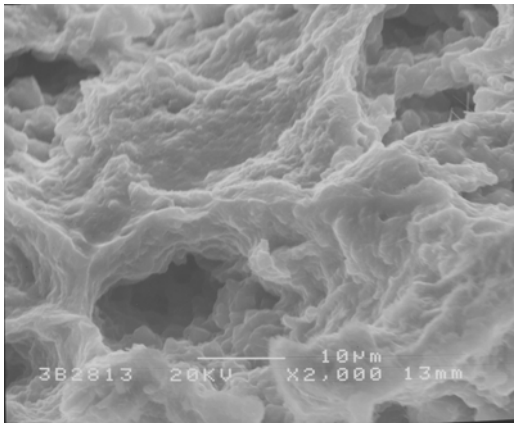

(c)

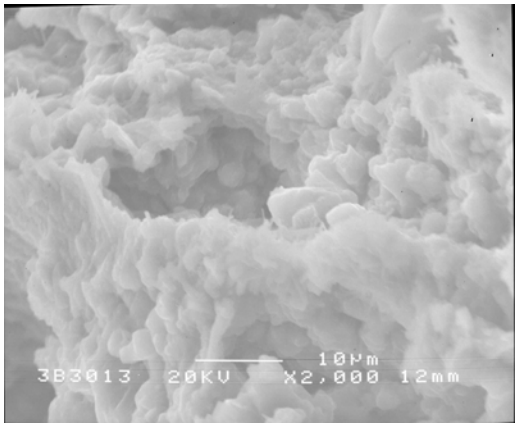

(d)

Fig. 3-44 The fracture surfaces of the E3B specimens tensile-loaded at $1x10^{-3}$ s^{-1} and (a) 150, (b) 250, (c) 280 and (d) 300^{o}C.

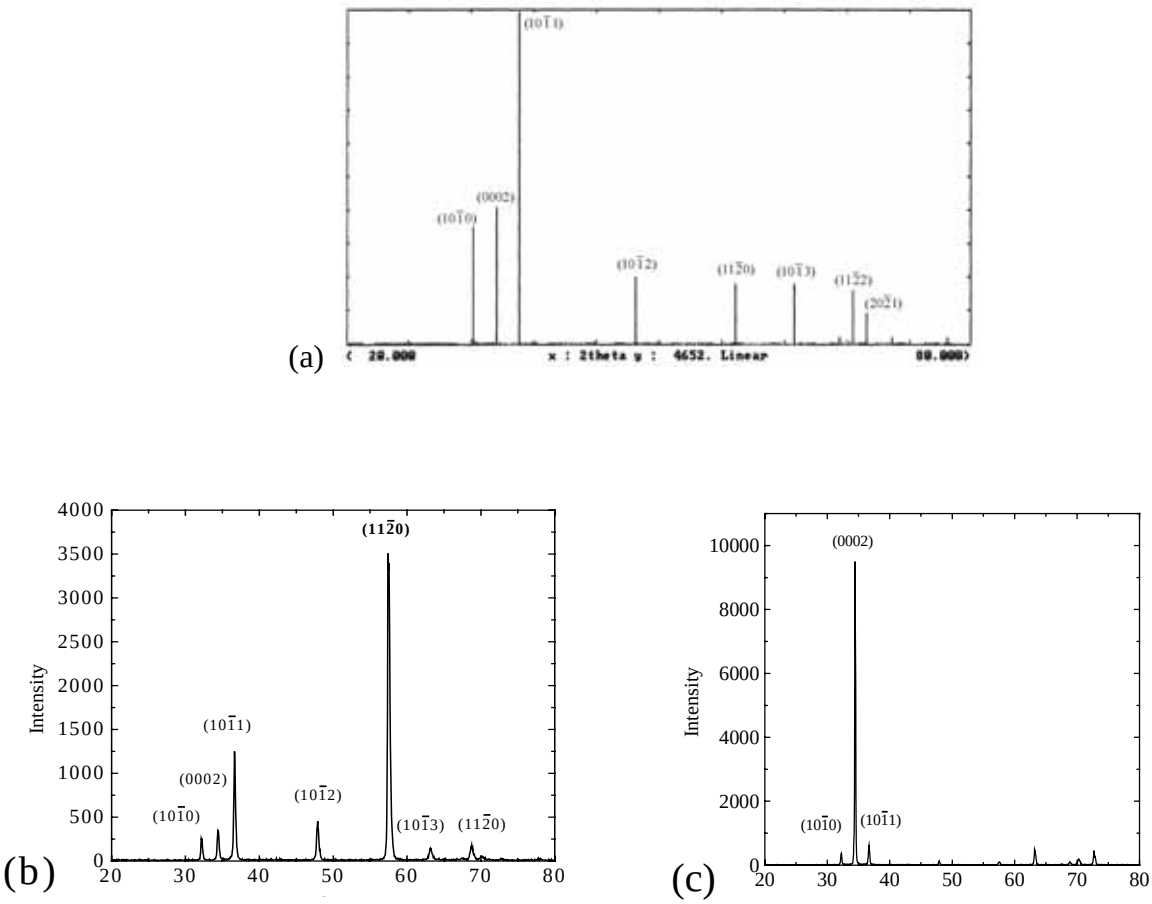

Fig. 3-45 X-ray diffraction patterns of the AZ31 Mg alloy showing the apparent change in texture after severe extrusion: (a) complete random Mg powders, (b) the cross-sectional plane of the as-received billet processed by semi-continuous casting, and (c) the flat plane of the E3 extruded plate.

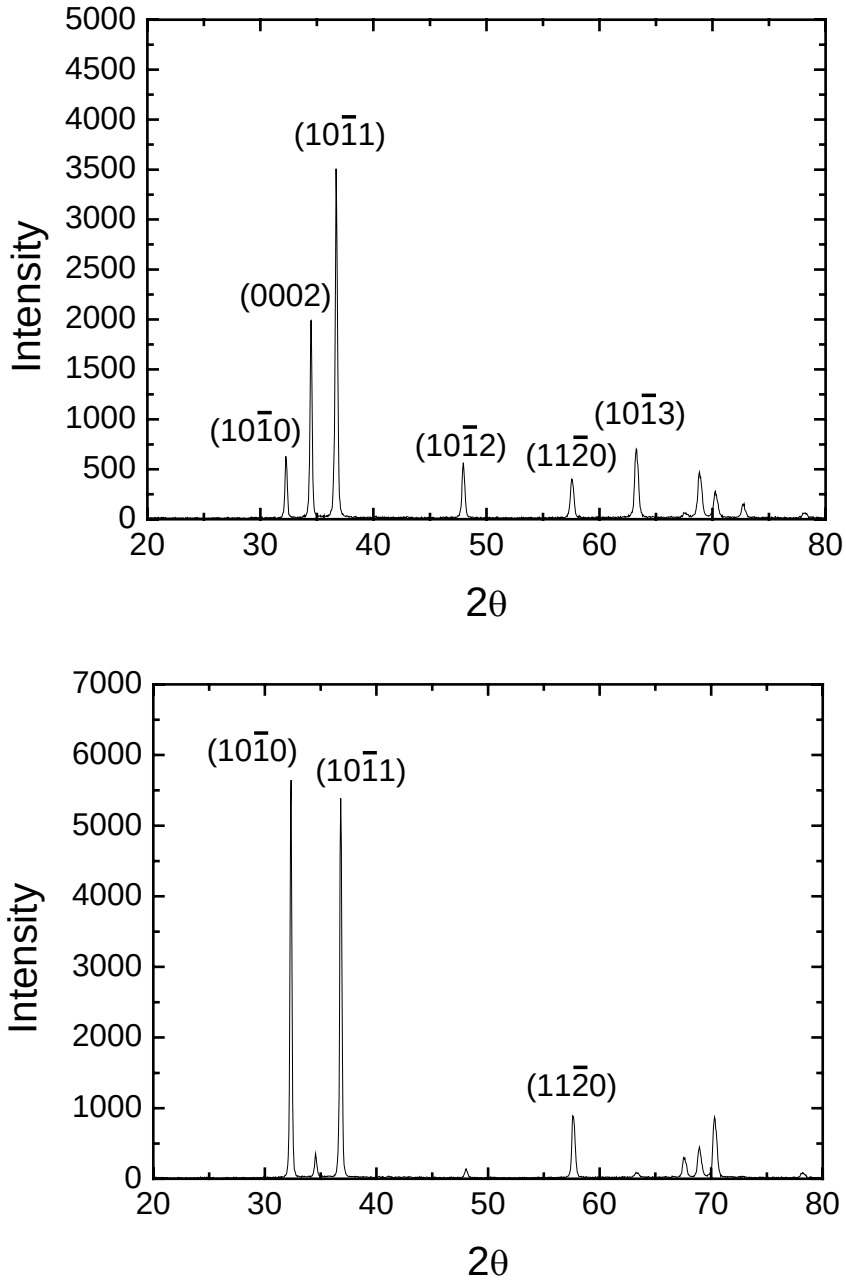

Fig. 3-46 X-ray diffraction patterns taken from the E1 sample processed with extrusion ratio of 42:1 at 300^{o}C : (a) longitudinal plane and (b) transverse cross-sectional plane.

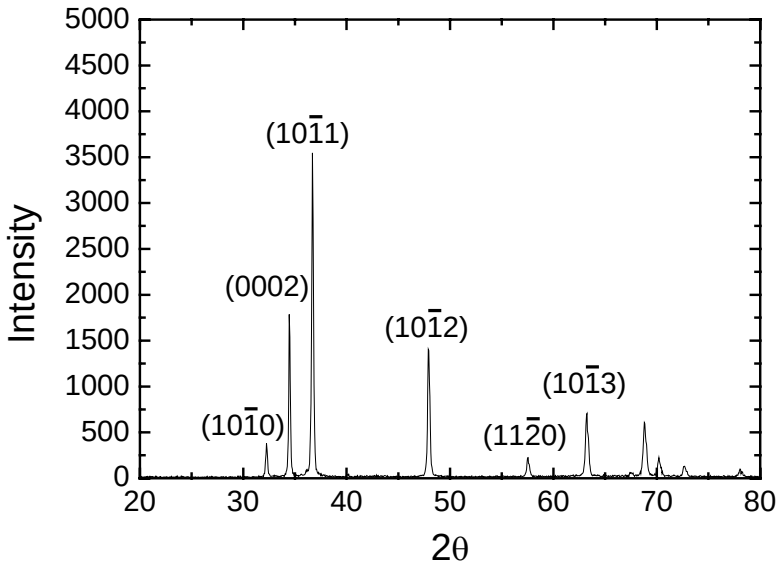

(a)

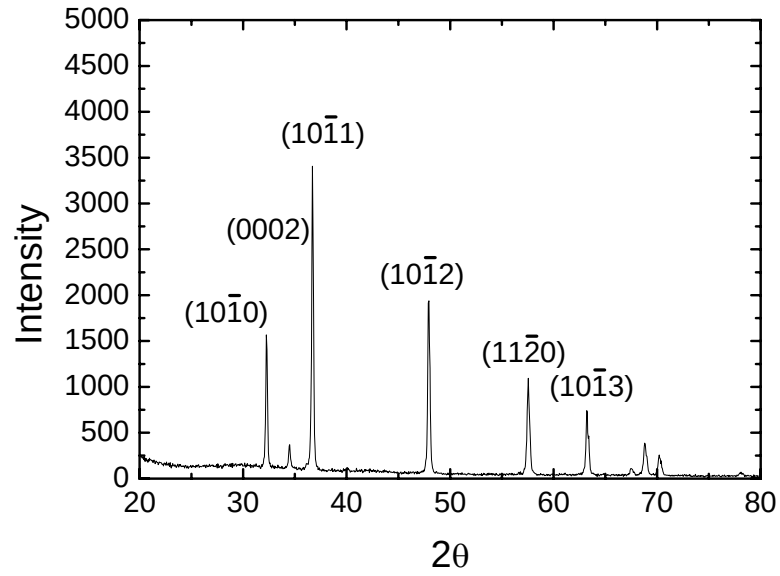

(b)

Fig. 3-47 X-ray diffraction patterns taken from the E1B sample processed after ECAP for 8 passes at 200^{o}C : (a) longitudinal plane and (b) transverse cross-sectional plane.

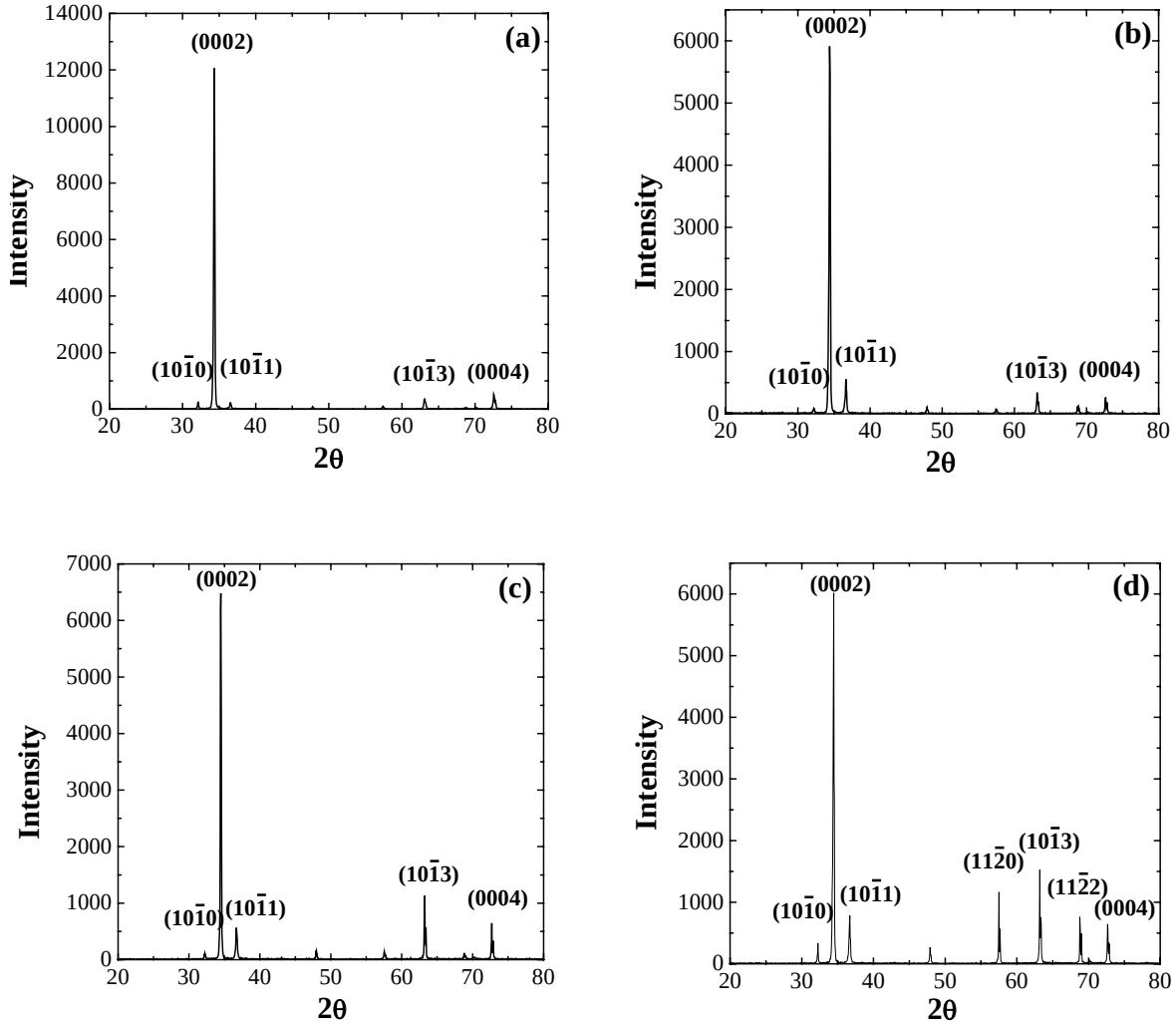

Fig. 3-48 X-ray diffraction patterns taken from the severely extruded E3 specimen after further annealing for 10 h at (a) 150°C, (b) 250°C, (c) 300°C, and (d) 350°C.

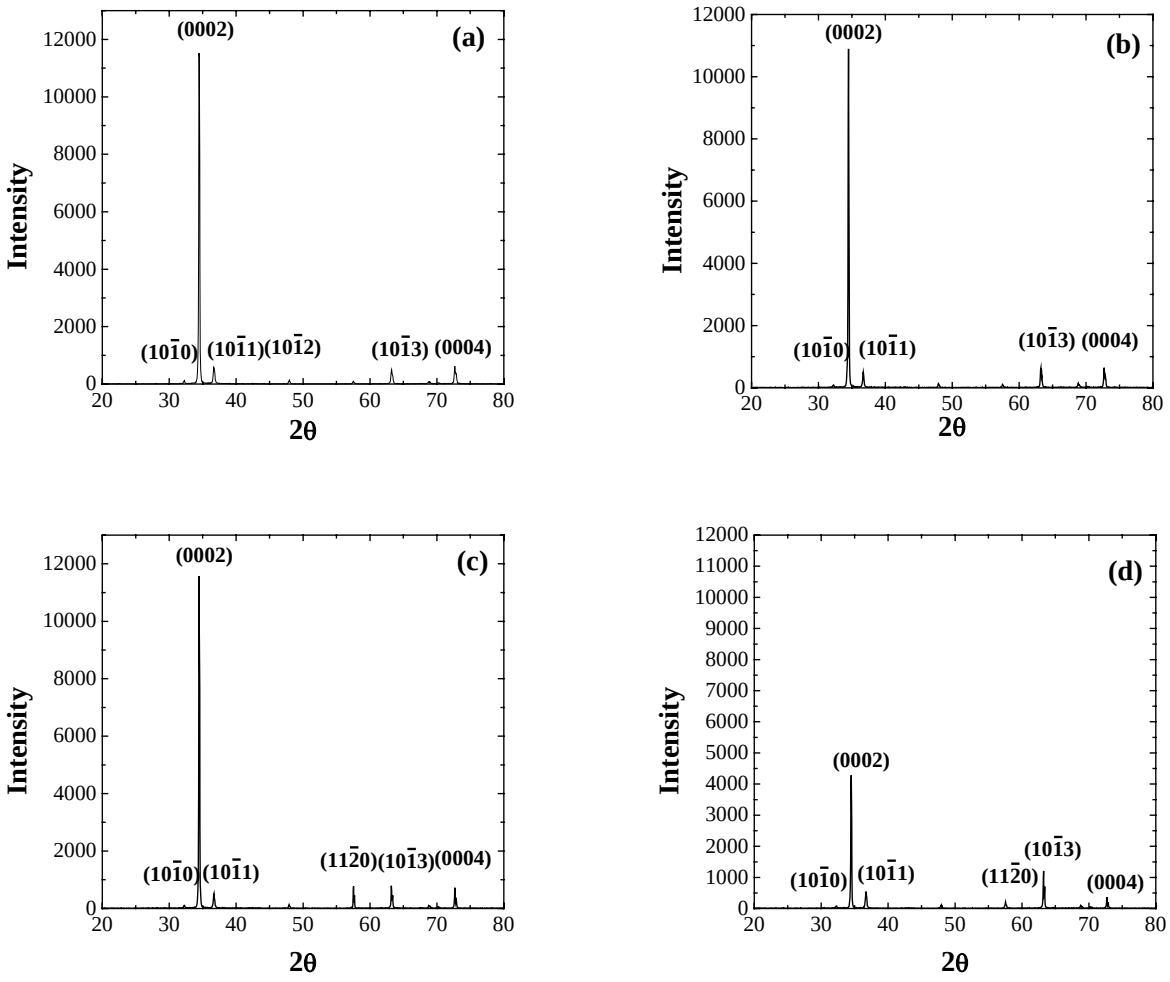

Fig. 3-49 X-ray diffraction patterns taken from the severely extruded E3 specimen after further annealing for 1 h at (a) 150°C, (b) 250°C, (c) 300°C, and (d) 350°C.

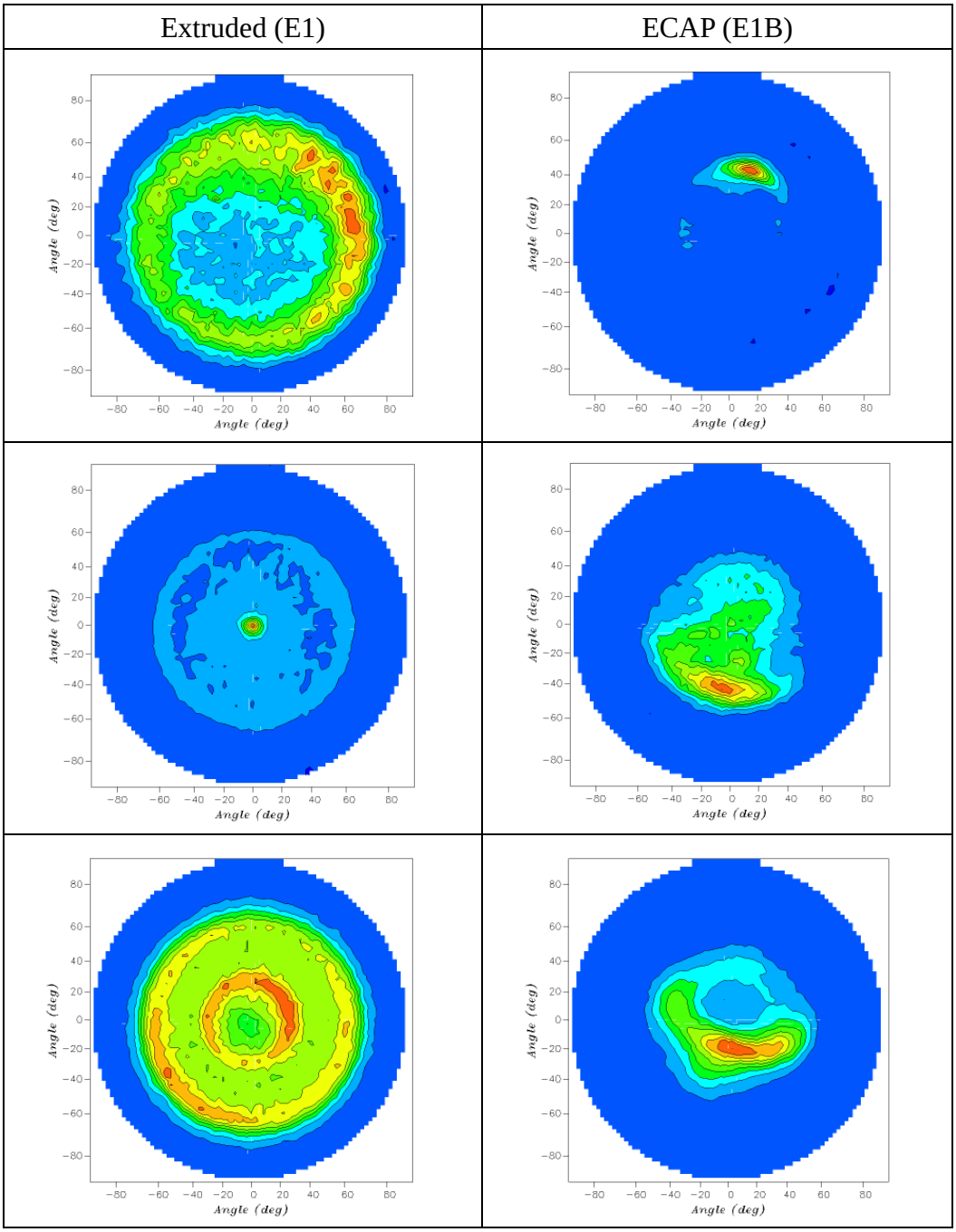

Fig. 3-50 The XRD (0002), $(10\bar{1}0)$ and $(10\bar{1}1)$ pole figures of the E1 and E1B specimens.

E2B	E3
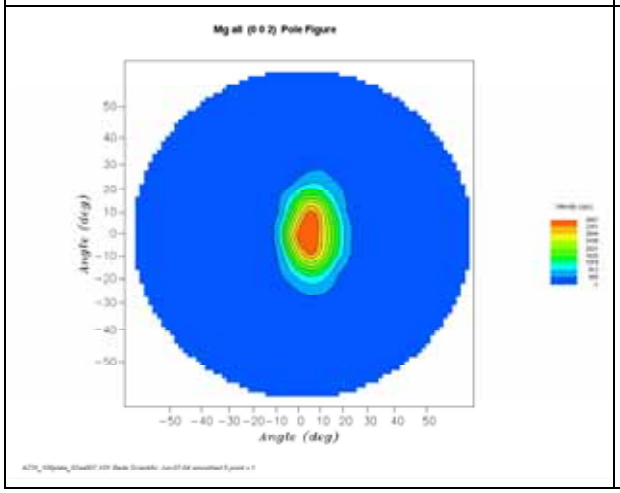	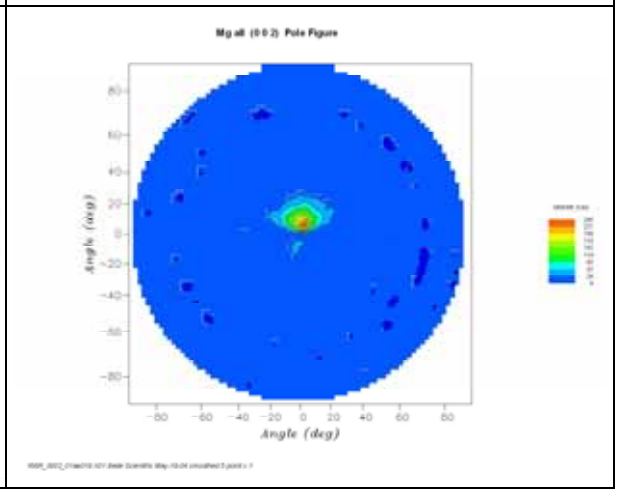

Fig. 3-51 The XRD (0002) pole figures of the E2B and E3 plate specimens.

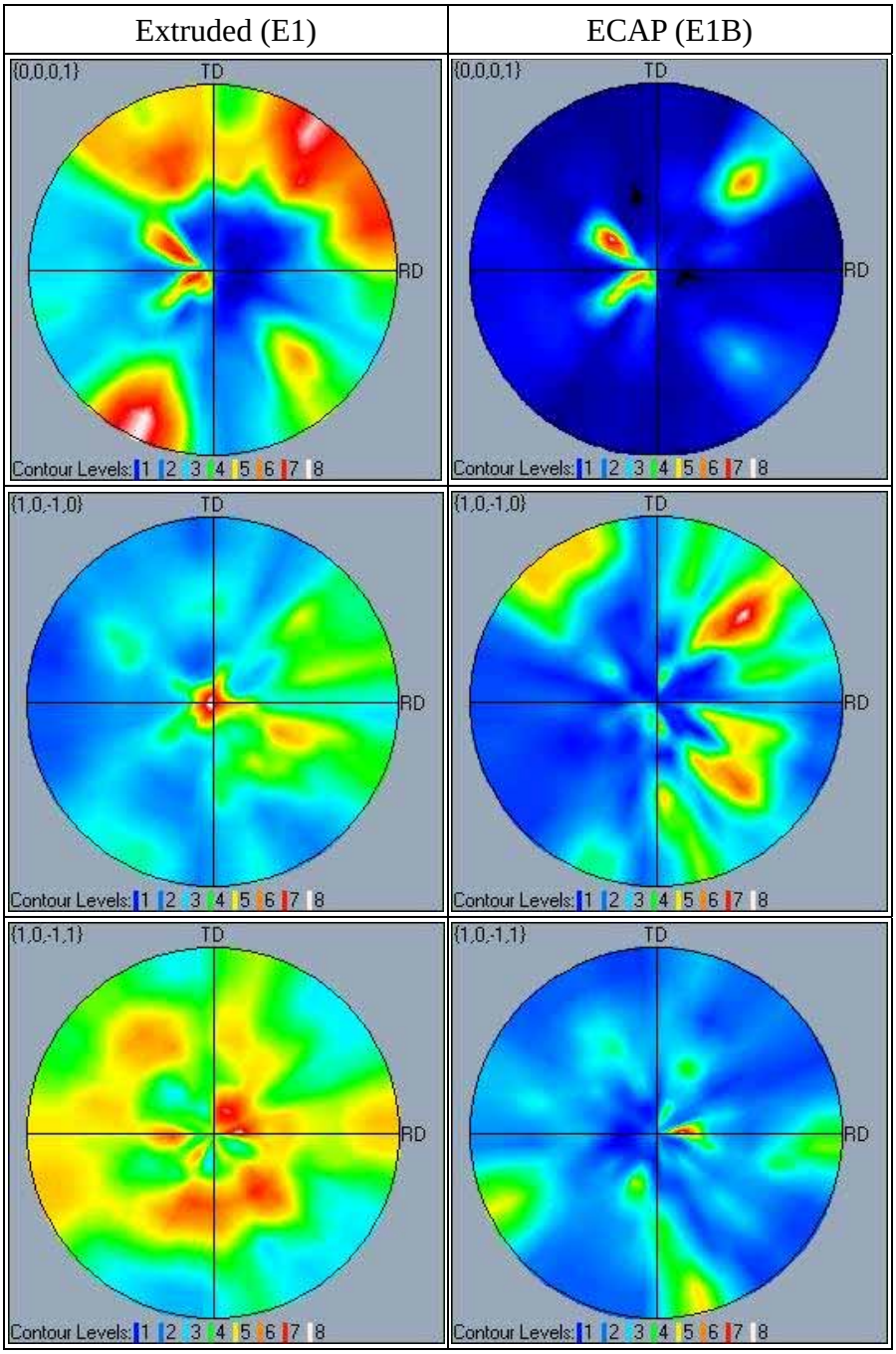

Fig. 3-52 The EBSD (0002), $(10\bar{1}0)$ and $(10\bar{1}1)$ pole figures for the extruded E1 and ECAP E1B conditions.

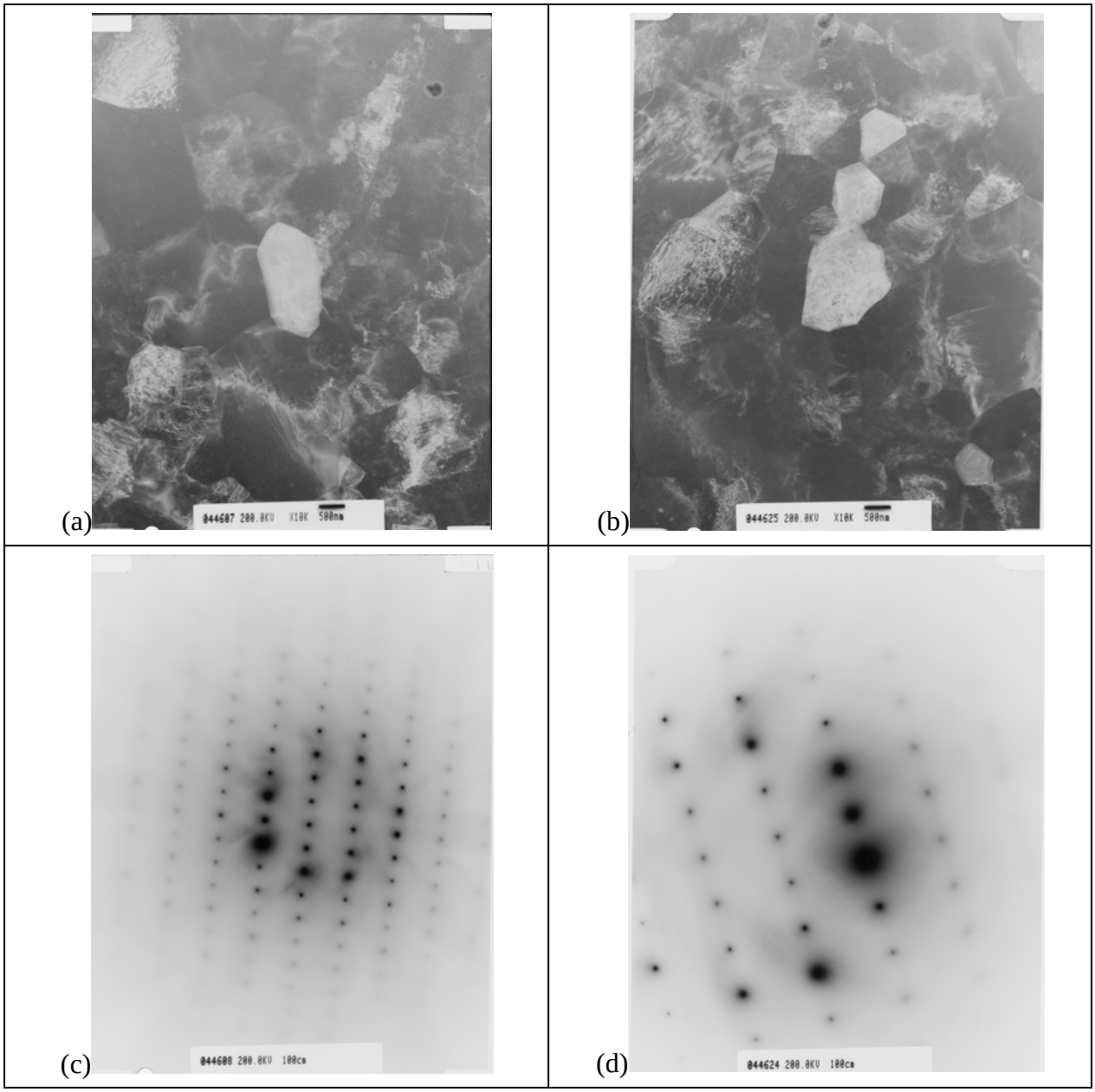

Fig. 3-53 The TEM bright field images and diffraction patterns taken from the extruded E1 condition.

(e) 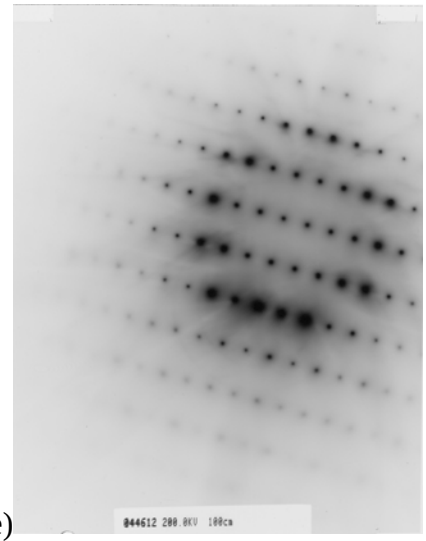	(f) 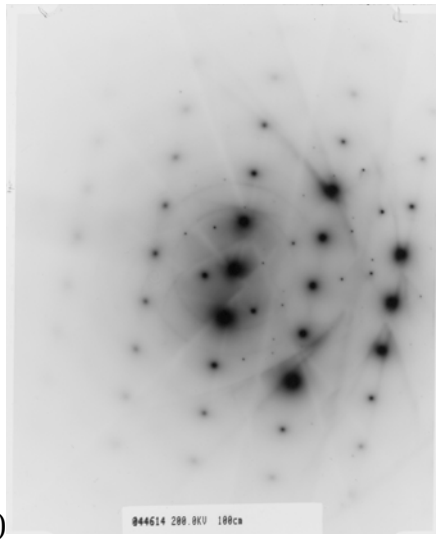
(g) 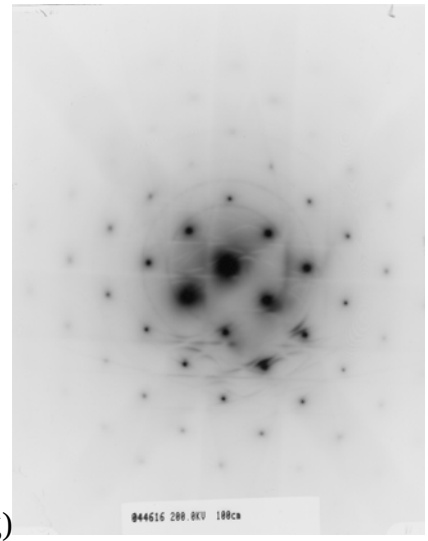	(h) 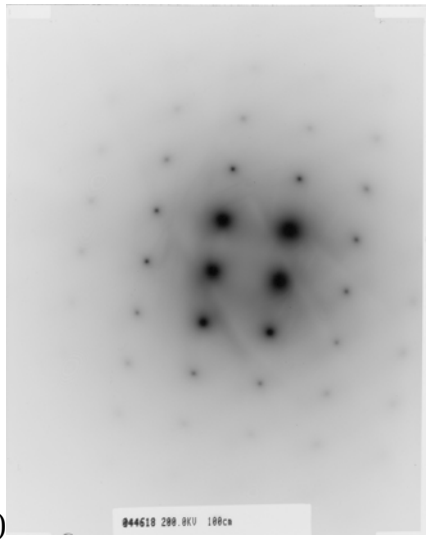
(i) 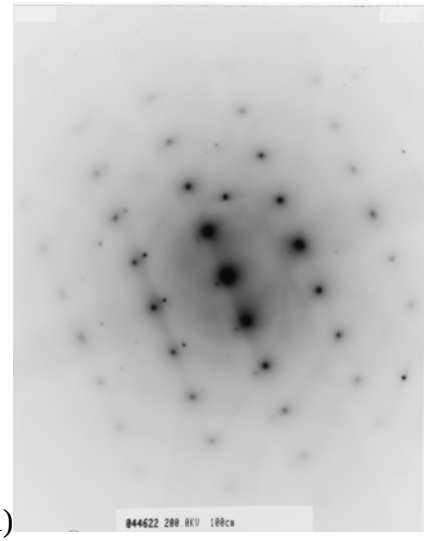	(j) 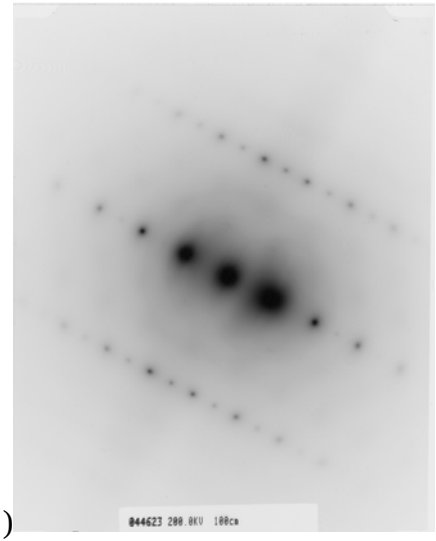

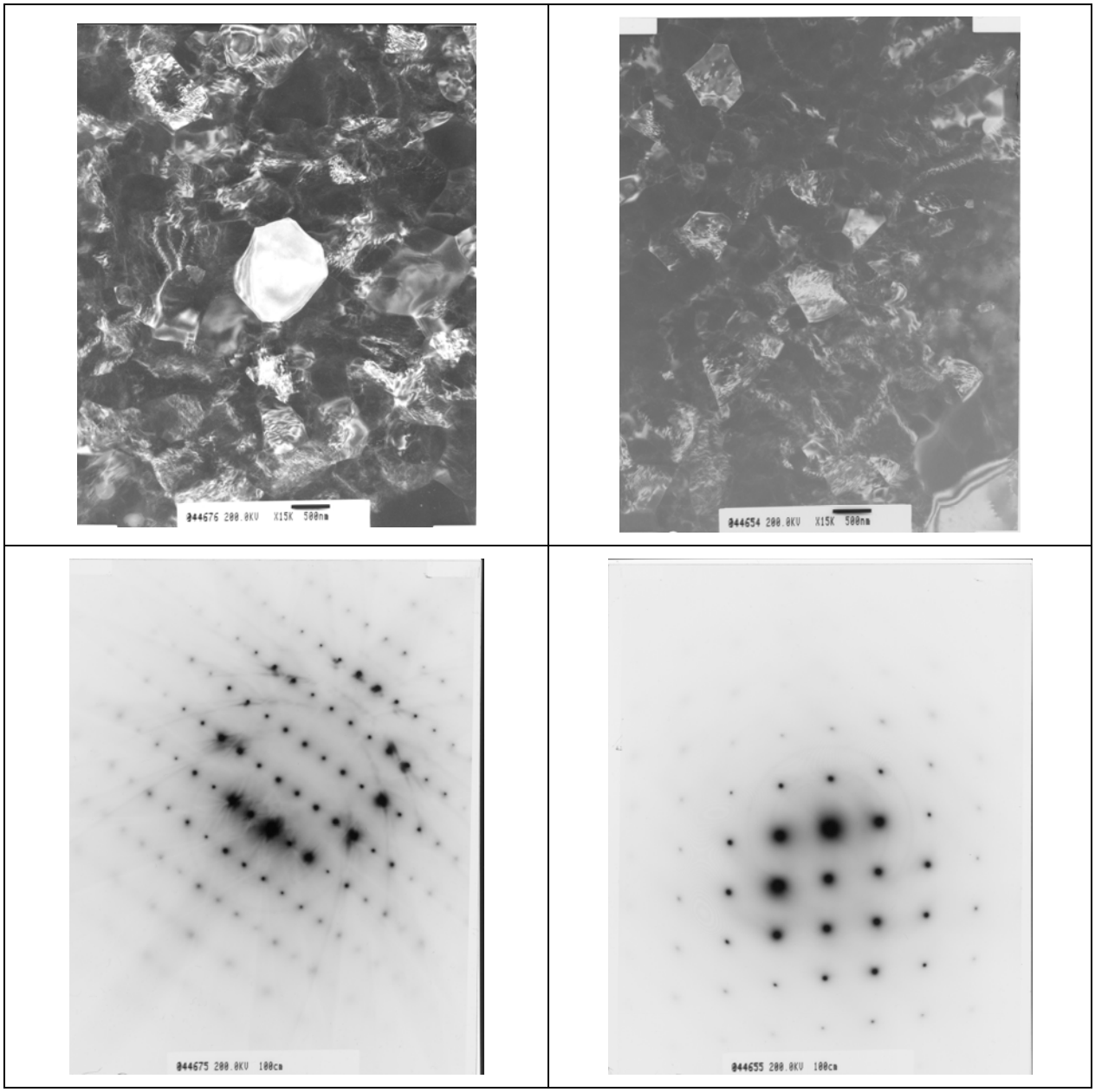

Fig. 3-54 The TEM bright field images and diffraction patterns taken from the ECAP E1B condition.

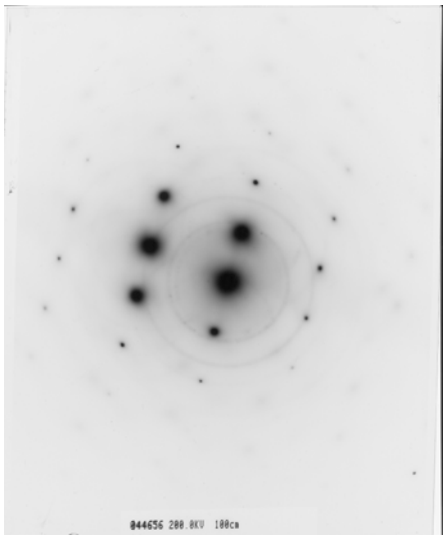
044656 200.0KV 100cm

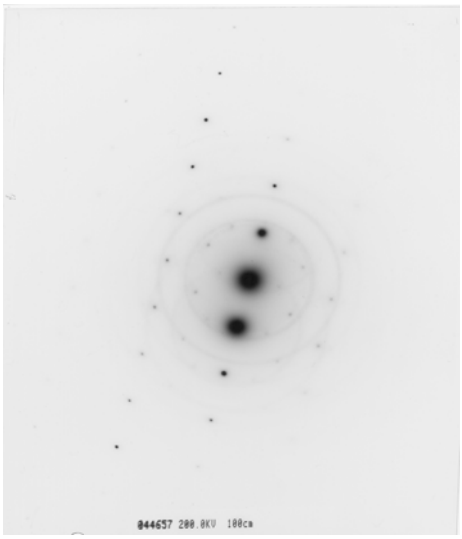
044657 200.0KV 100cm

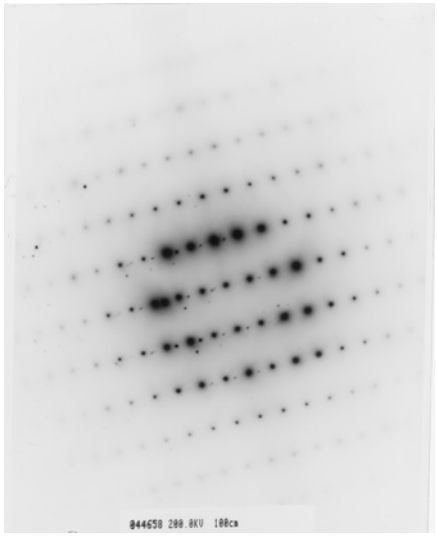
044658 200.0KV 100cm

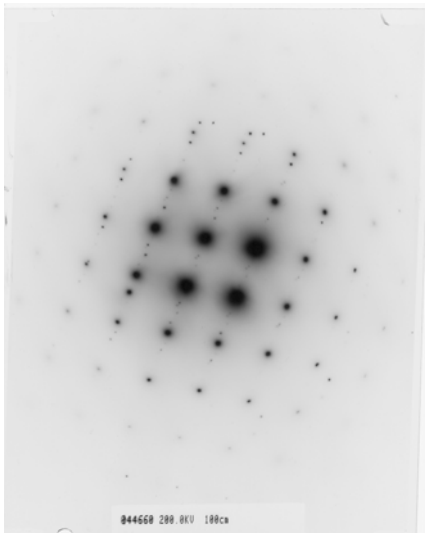
044660 200.0KV 100cm

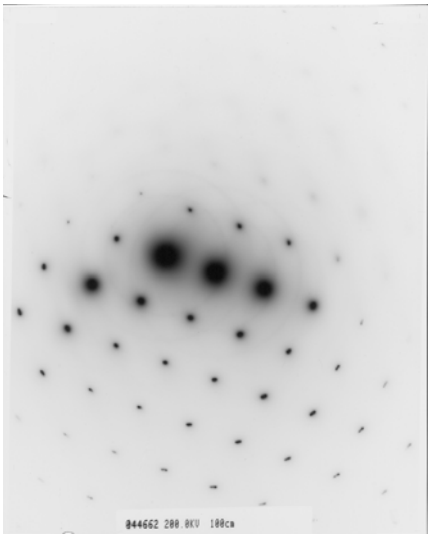
044662 200.0KV 100cm

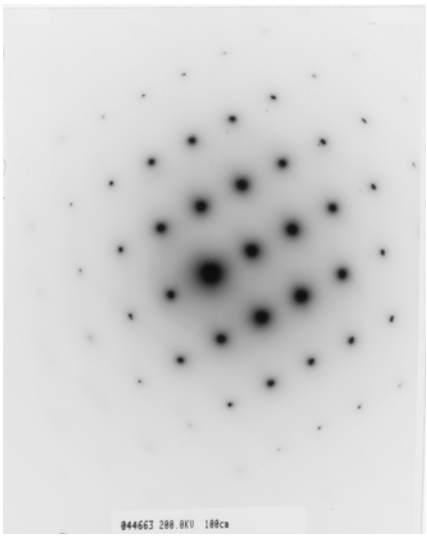
044663 200.0KV 100cm

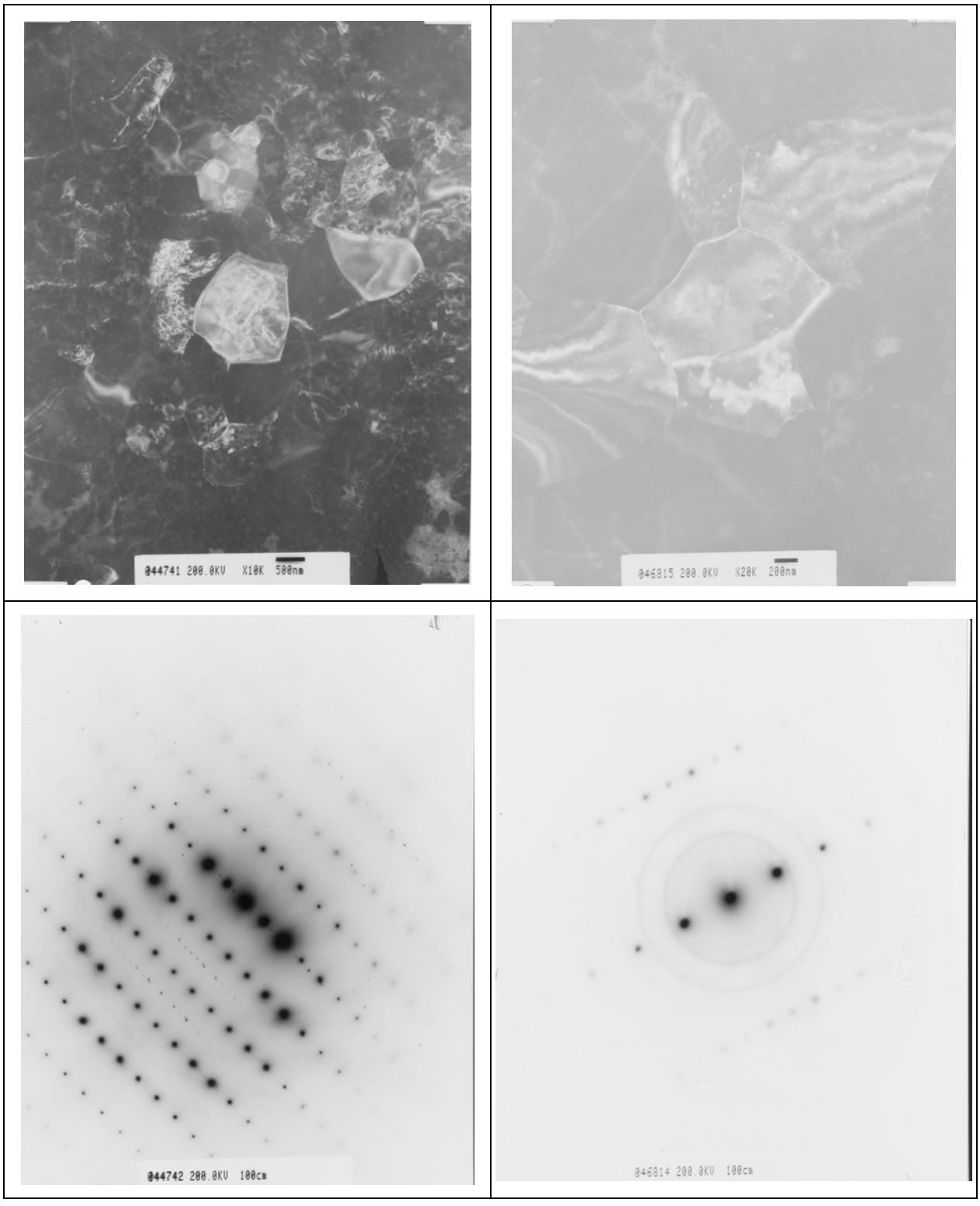

Fig. 3-55 The TEM bright field images and diffraction patterns taken from the extruded E2 specimen.

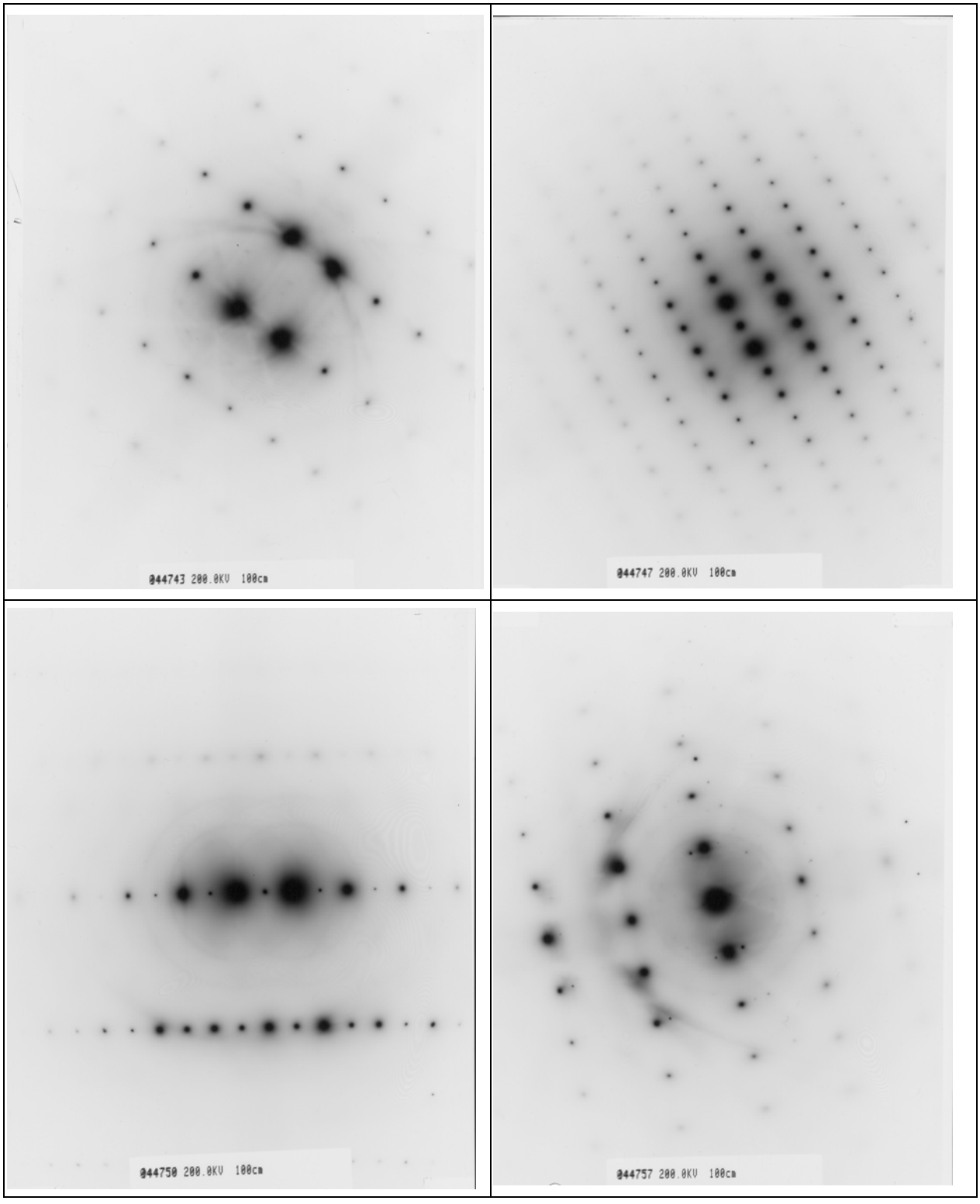
@44743 200.0KV 100cm
@44747 200.0KV 100cm
@44750 200.0KV 100cm
@44757 200.0KV 100cm

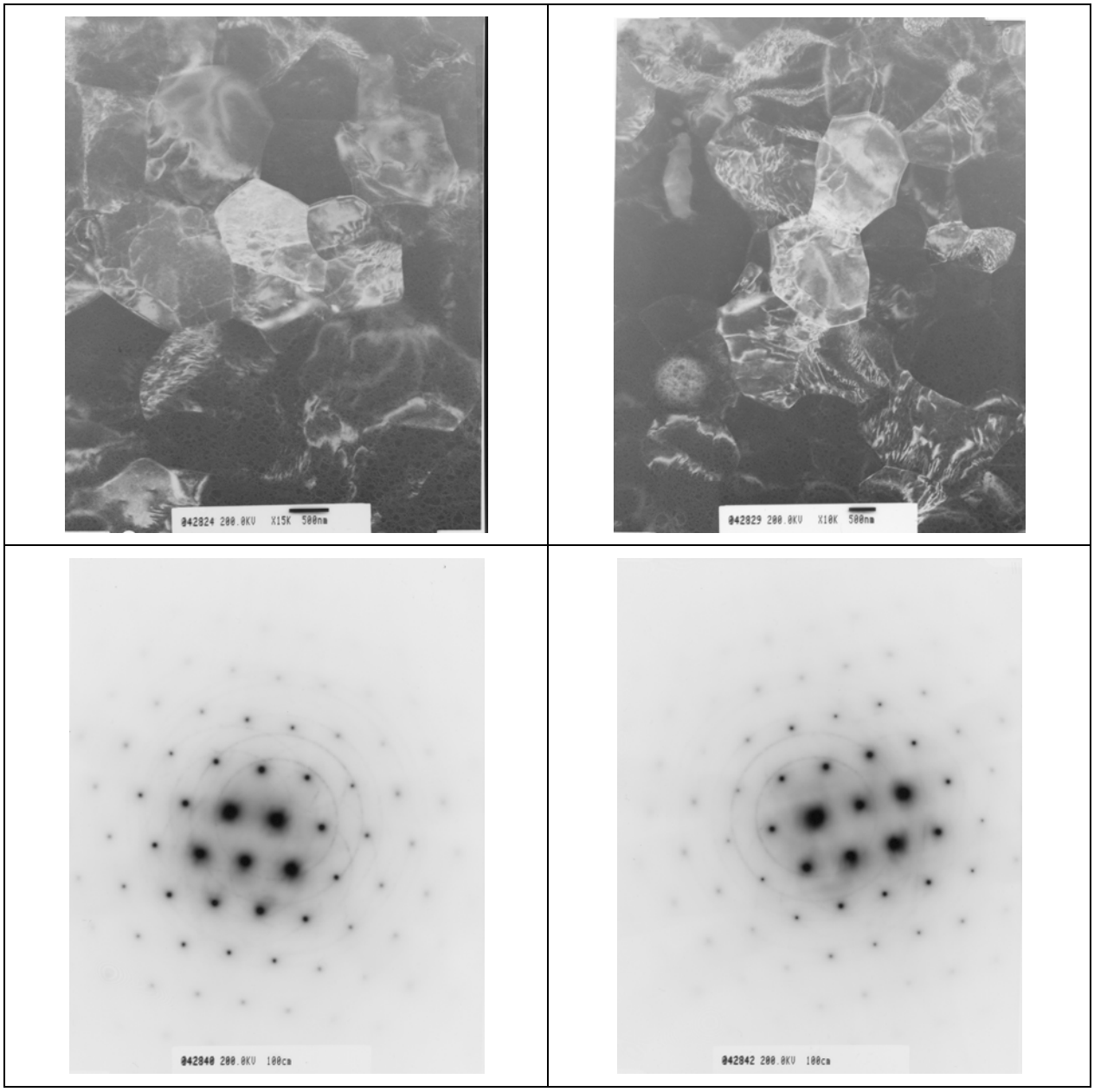

Fig. 3-56 The TEM bright field images and diffraction patterns taken from the extruded E3 specimen.

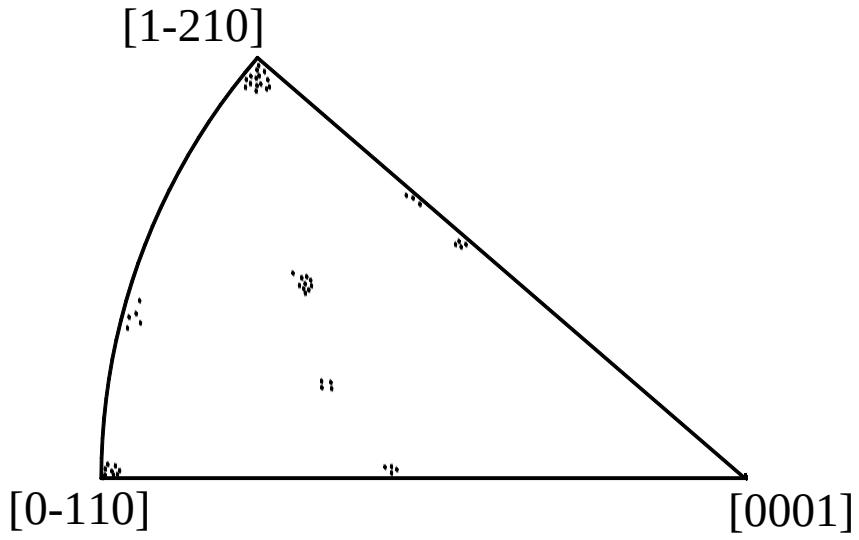

(a)

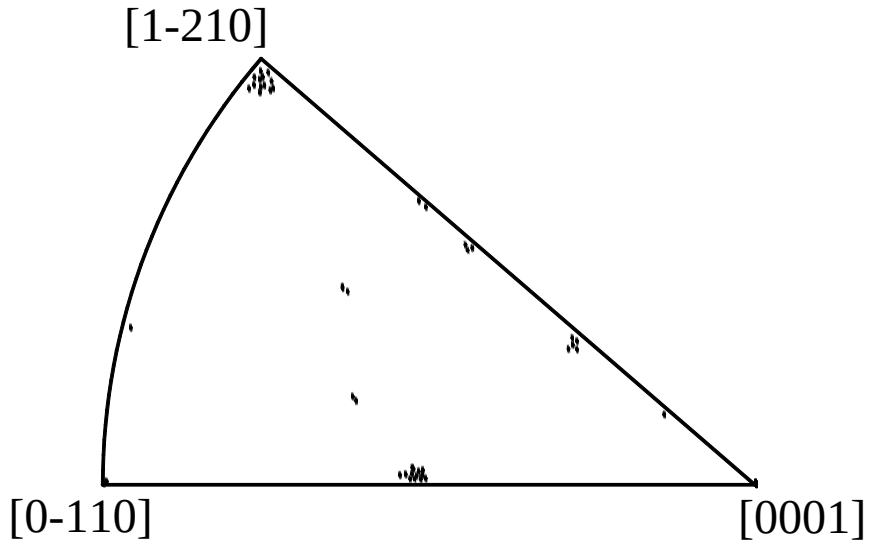

(b)

Fig. 3-57 The inverse pole figures determined by TEM diffraction pattern analysis: (a) E1 and (b) E1B specimens.

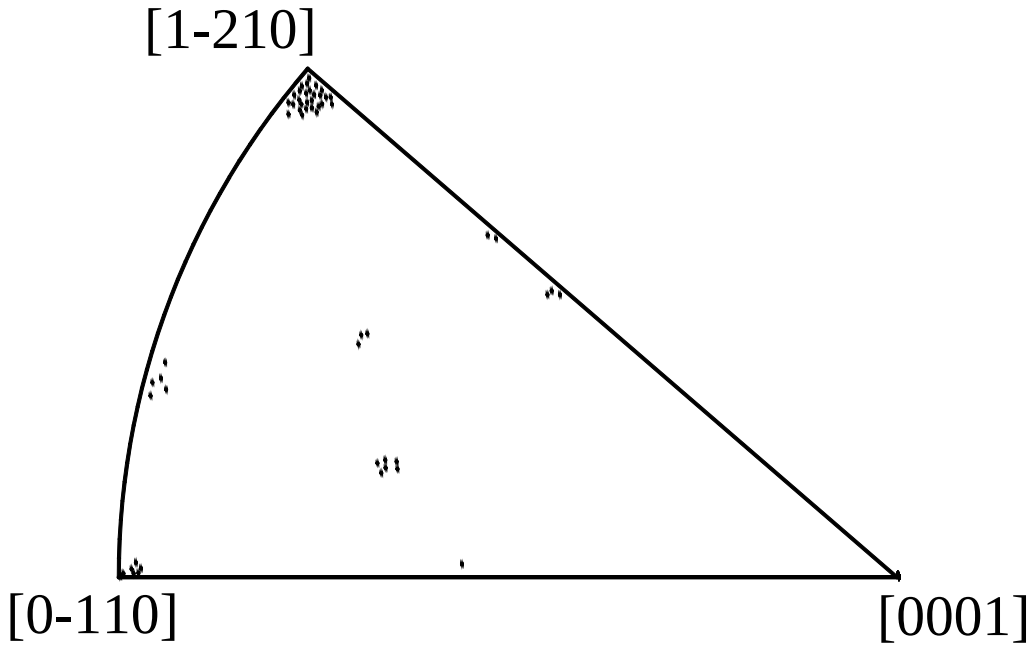

Fig. 3-58 The inverse pole figures determined by TEM diffraction pattern analysis in the E2 specimen.

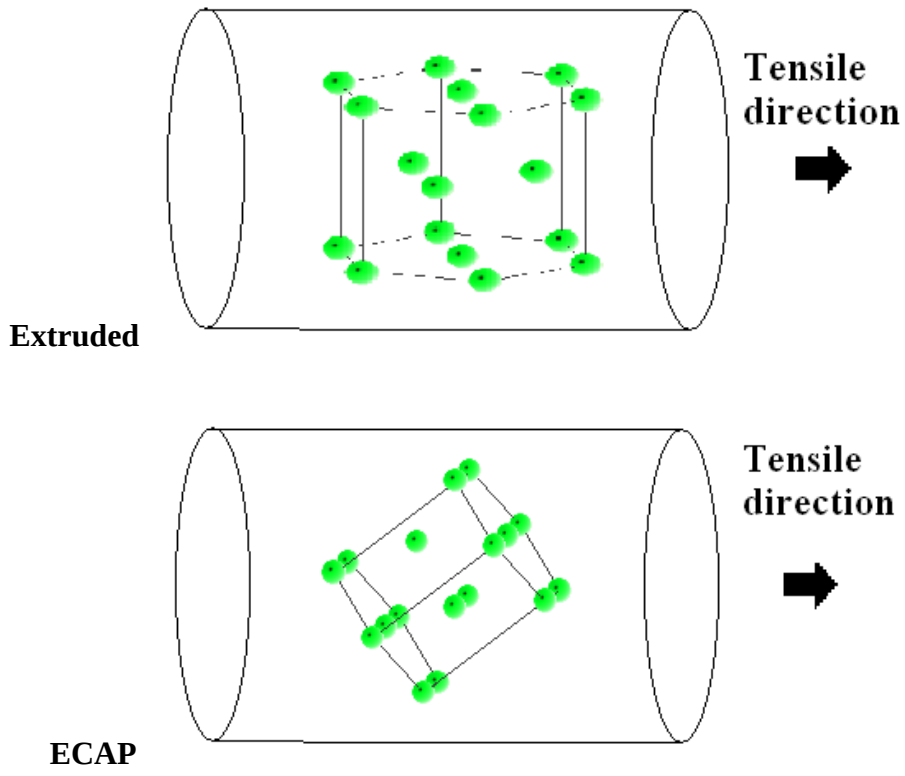

Fig. 3-59 Schematic illustration of the dominant textures in the extruded E1 and ECAP E1B conditions.

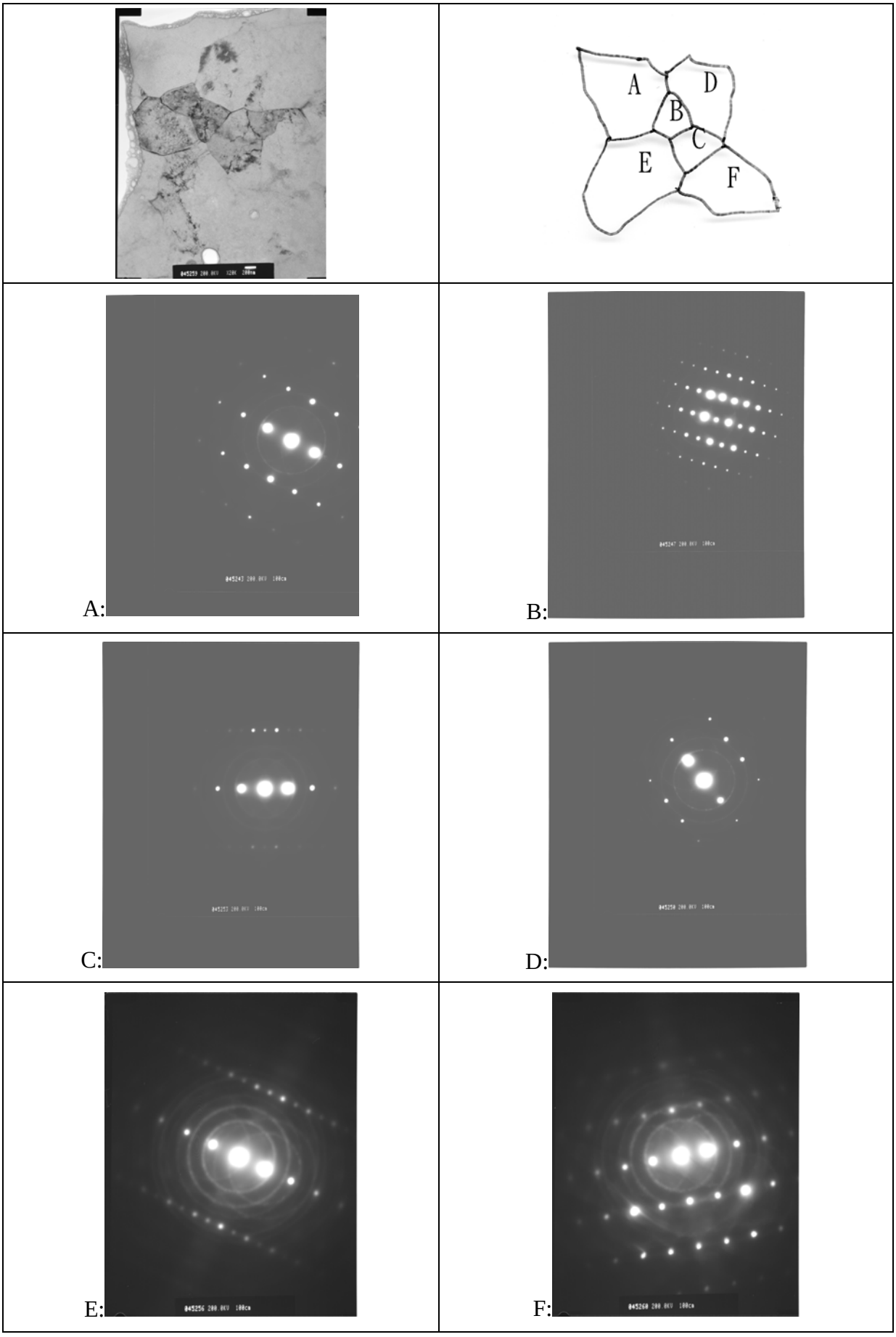

Fig. 3-60 Examples of the SAD patterns taken from various adjacent grains in E1.

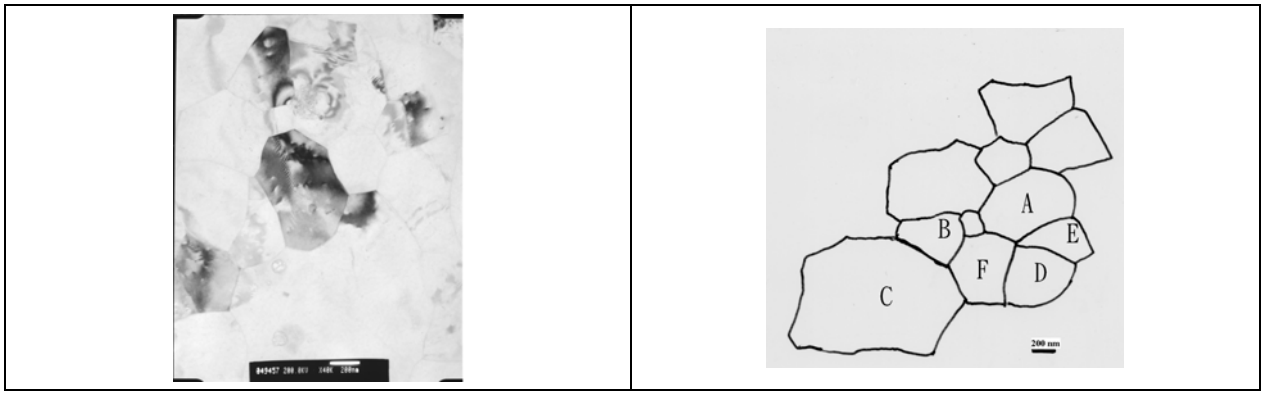

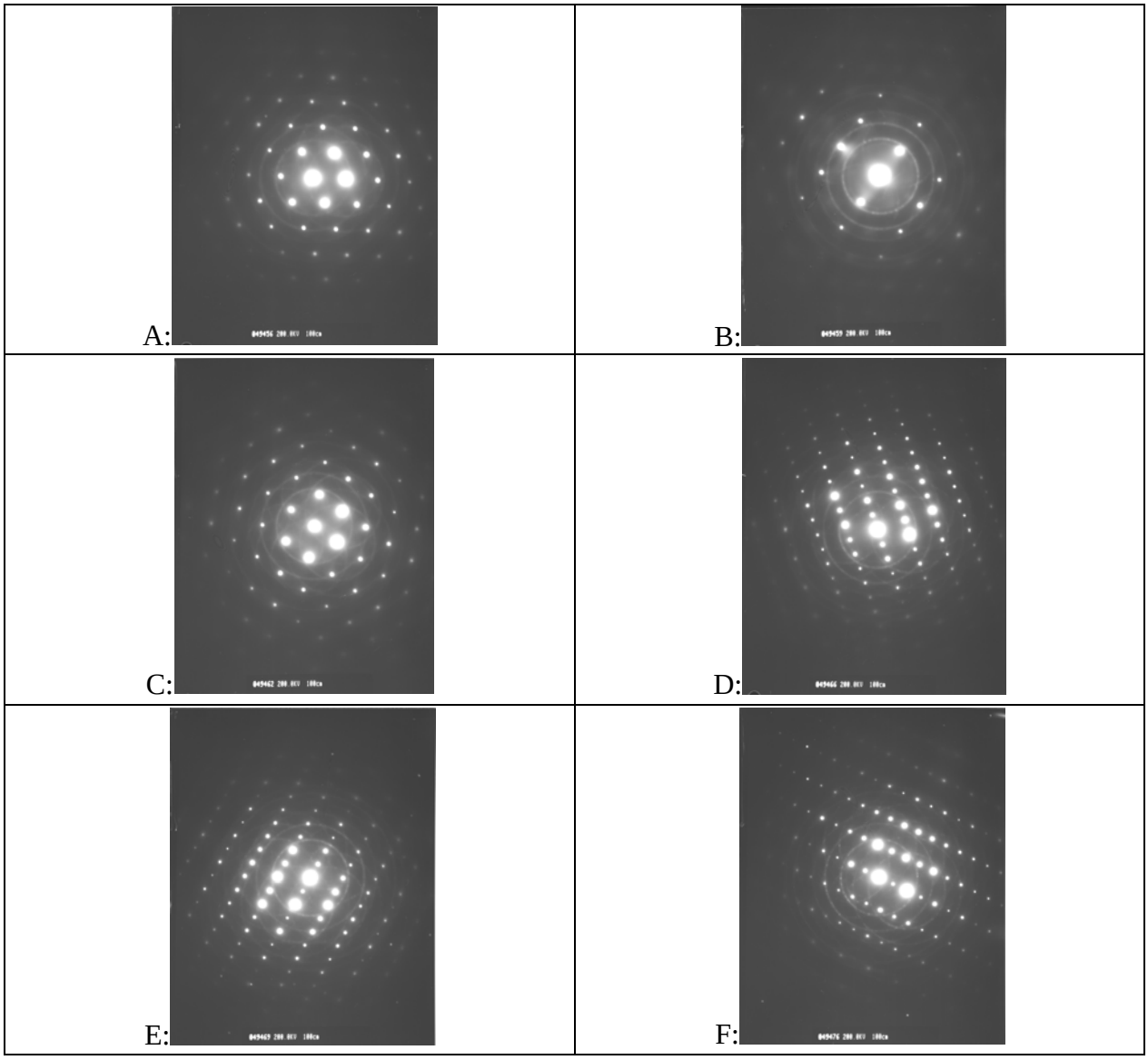

Fig. 3-61 Examples of the SAD patterns taken from various adjacent grains in the E1B specimen.

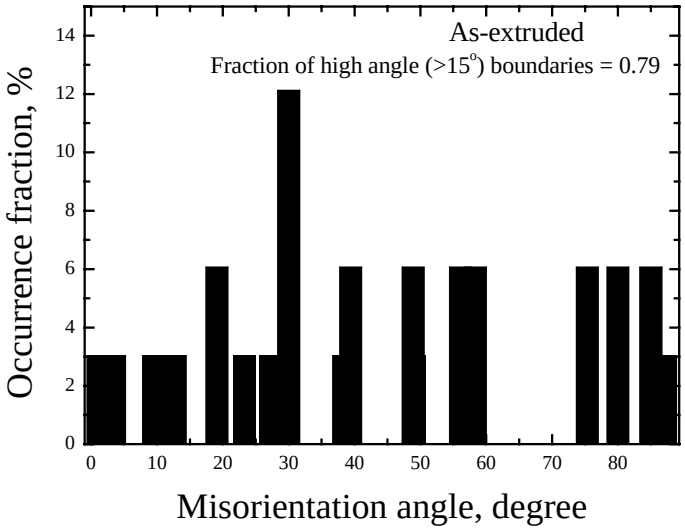

(a)

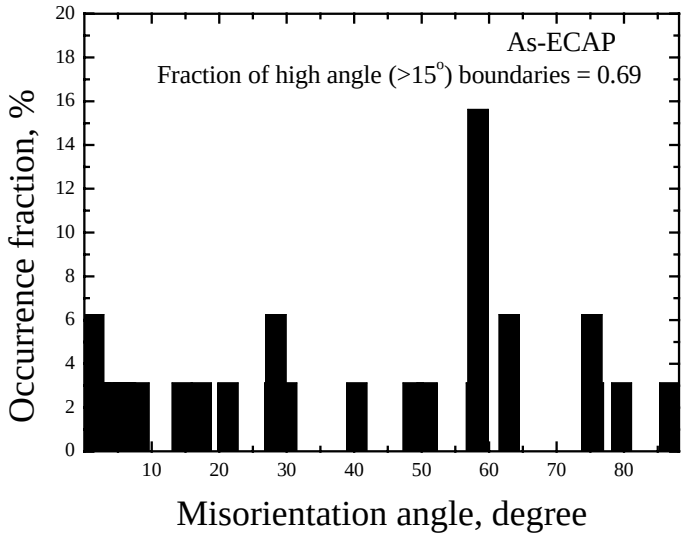

(b)

Fig. 3-62 Two representative misorientation distributions determined by TEM for the (a) E1 and (b) E1B specimens.

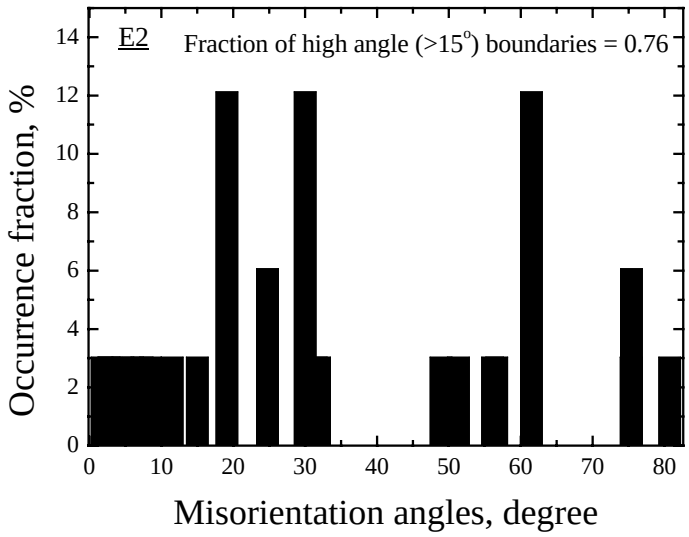

Fig. 3-63 The representative misorientation distributions determined by TEM for the E2 specimen.

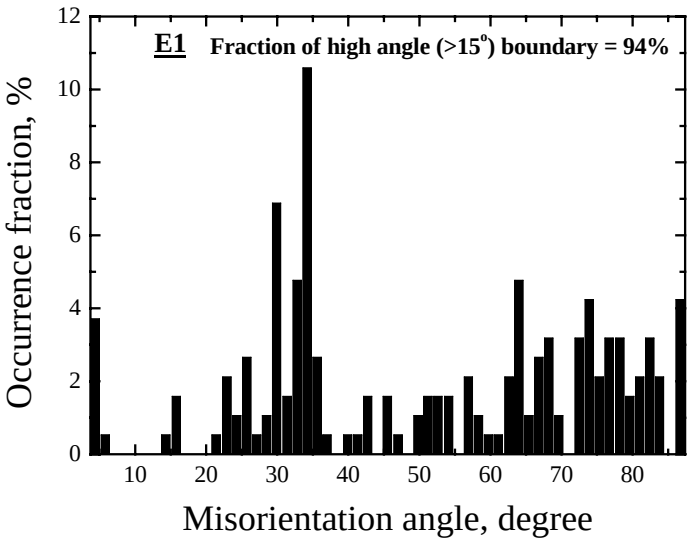

(a)

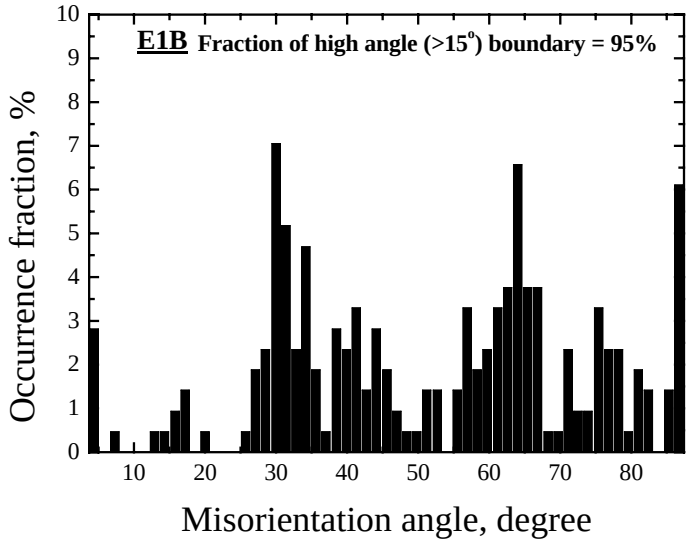

(b)

Fig. 3-64 Two representative misorientation distributions determined by EBSD for the (a) E1 and (b) E1B specimens.

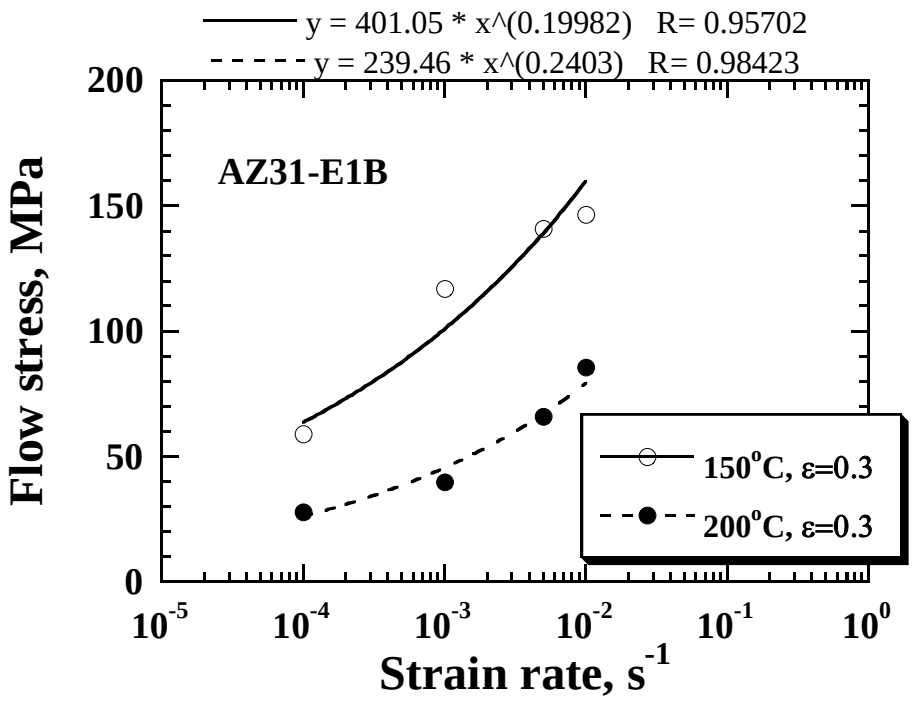

Fig. 4-1 The flow stress against strain rate curves at 150 to 200°C for the E1B specimen.

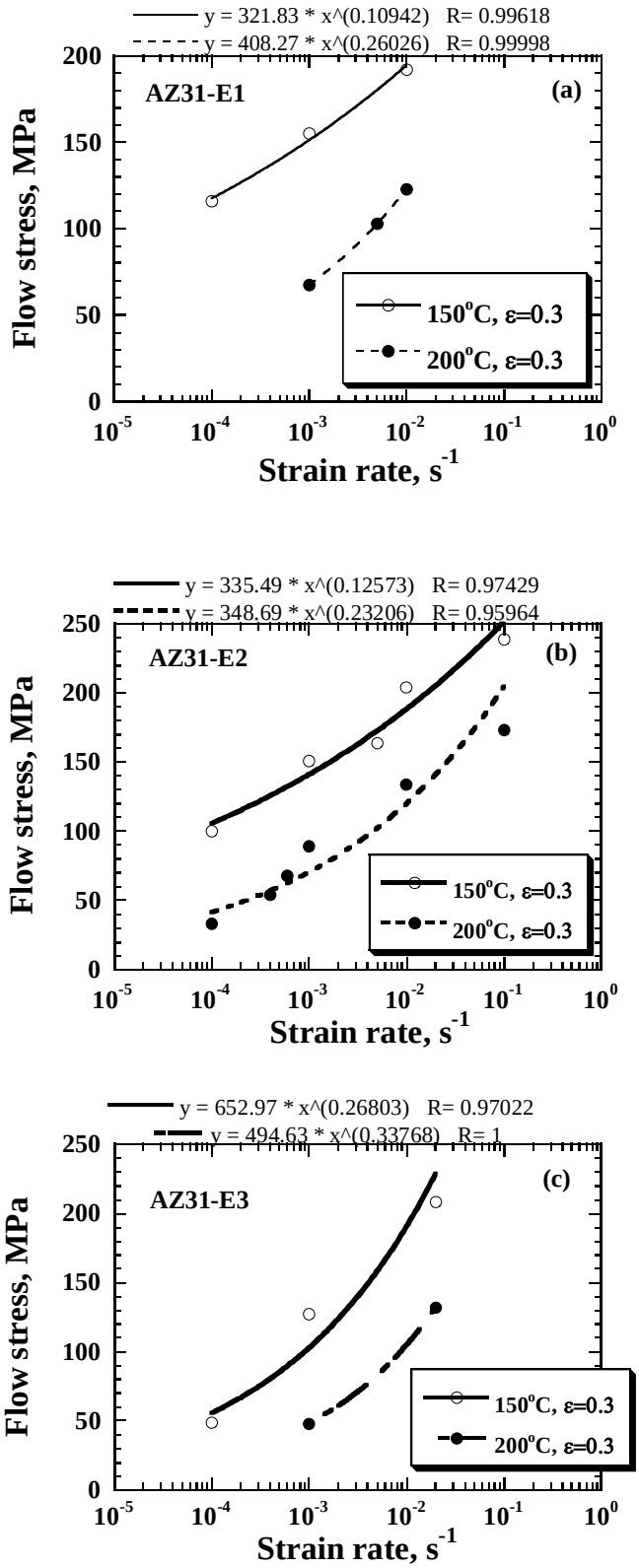

Fig. 4-2 The flow stress at ε=0.3 against strain rate curves at 150 to 200°C for the E1, E2 and E3 specimens.

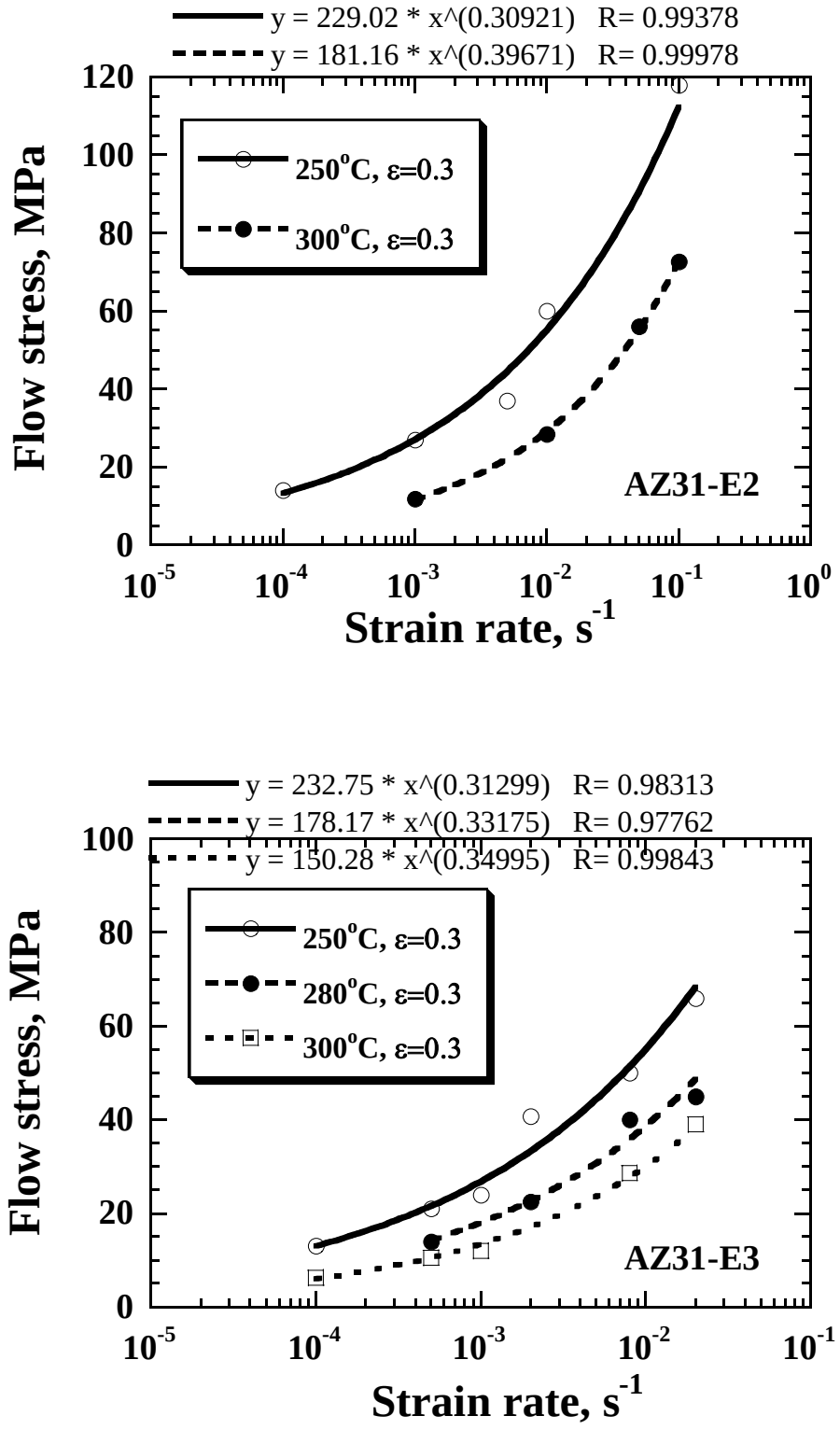

Fig. 4-3 The flow stress at ε~0.3 versus strain rate for the E2 and E3 specimens at various temperatures.

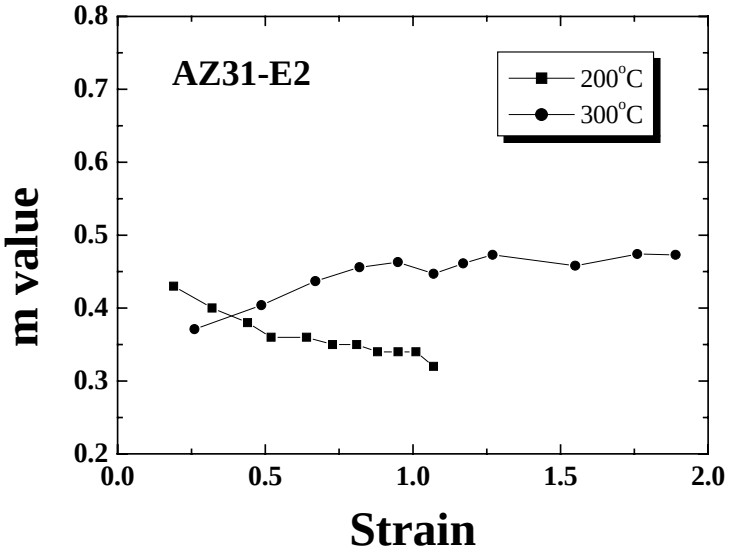

Fig. 4-4 The E2 specimen tested at $6x10^{-4} \sim 1x10^{-3}$ s^{-1}.

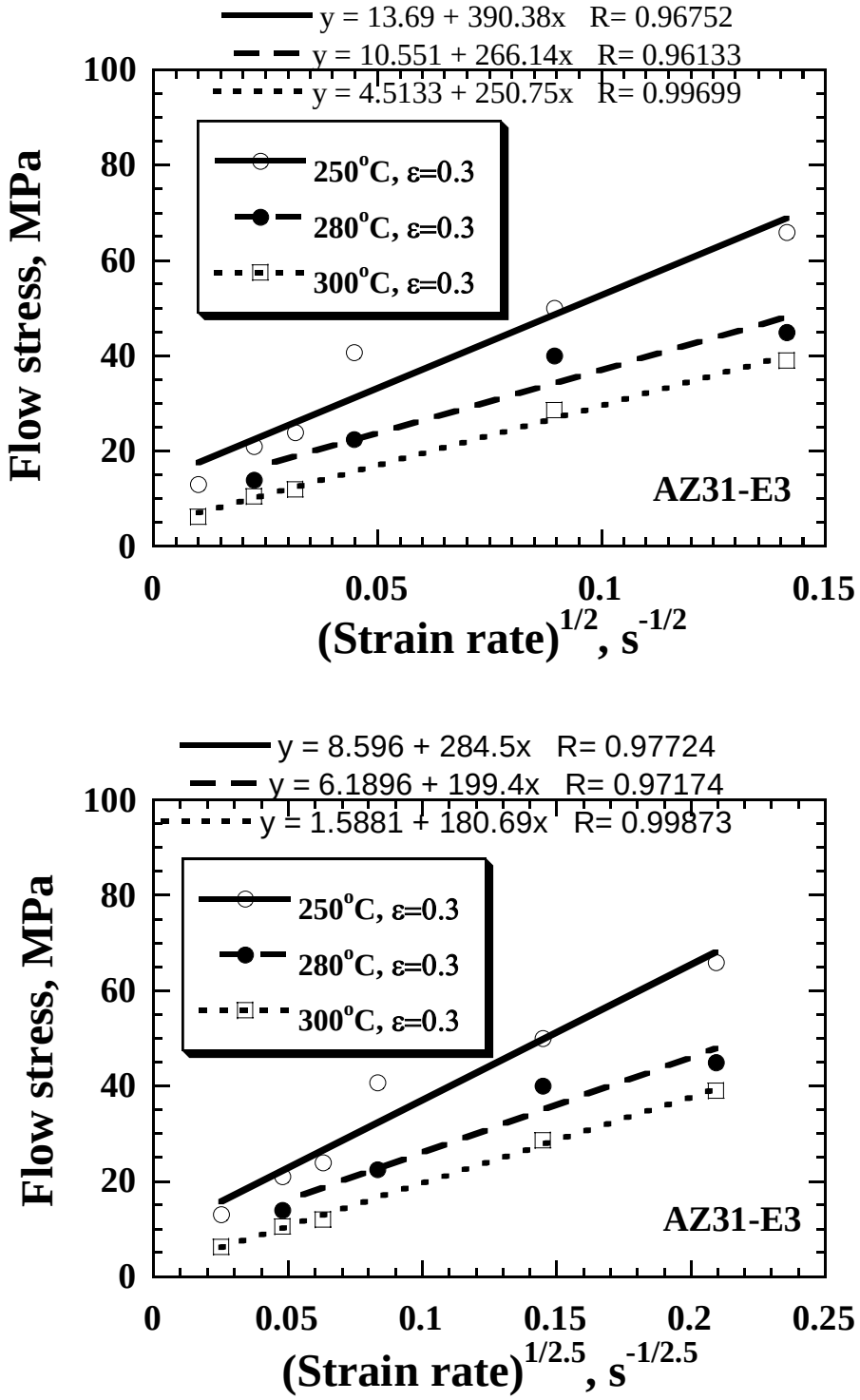

Fig. 4-5 Threshold stress for the E3 specimen.

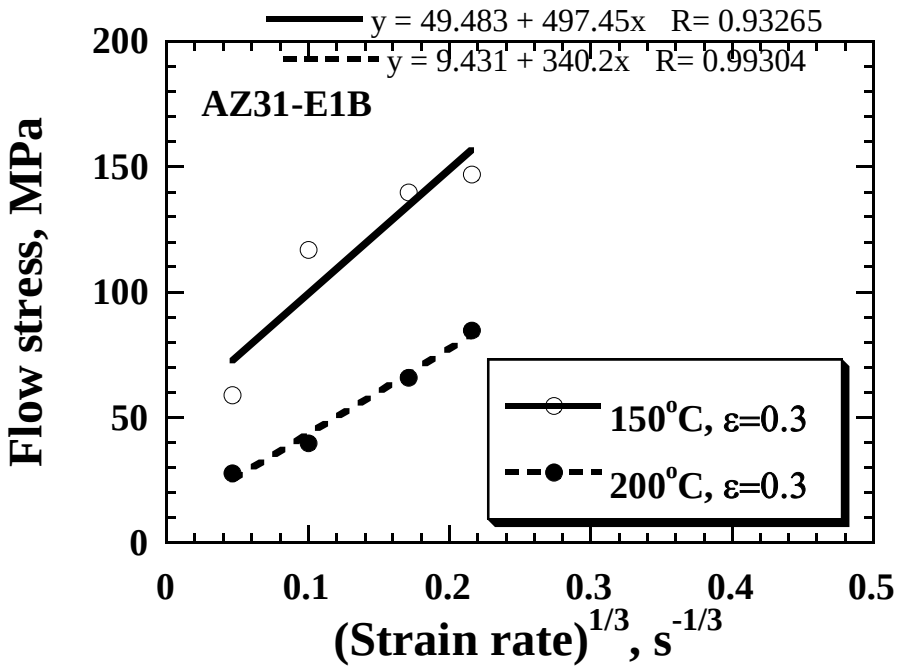

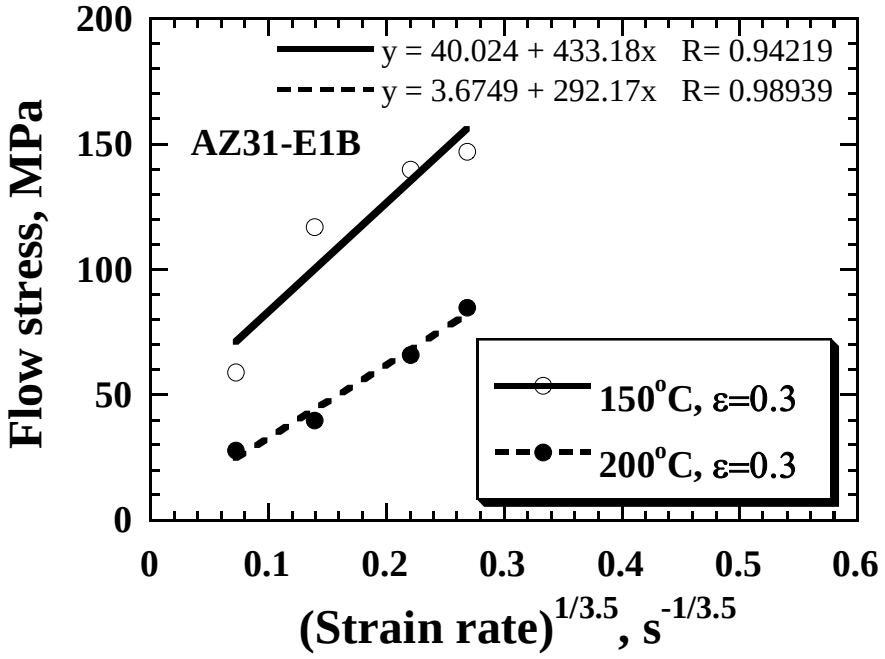

Fig. 4-6 Threshold stress for the E1B specimen.

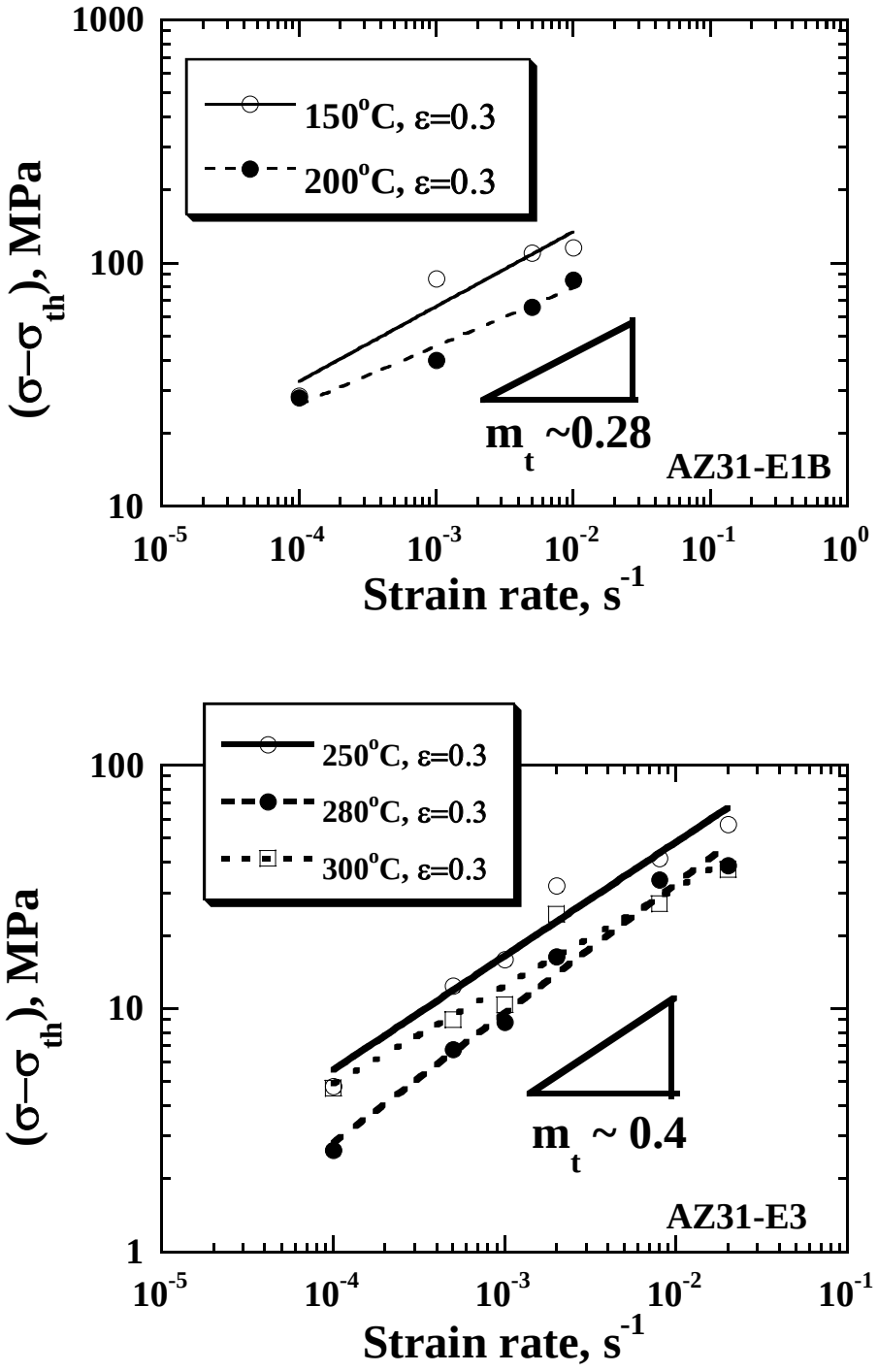

Fig. 4-7 The m_t–value could be extracted from the slope of the double logarithm plot of the flow stress versus the strain rate.

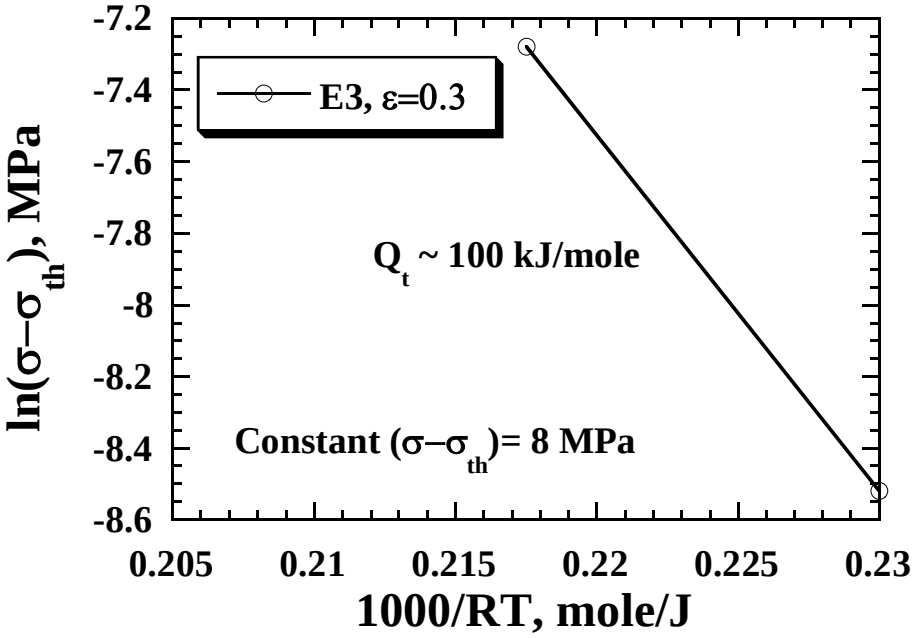

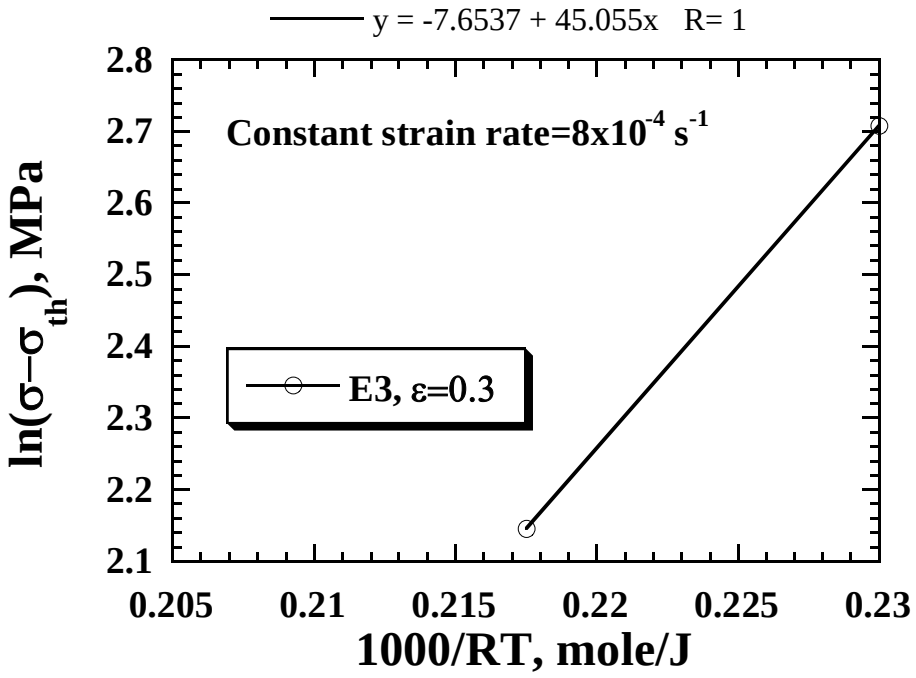

Fig. 4-8 True activation energy for the E3 specimen using the true stress exponent n_t of 2.5.

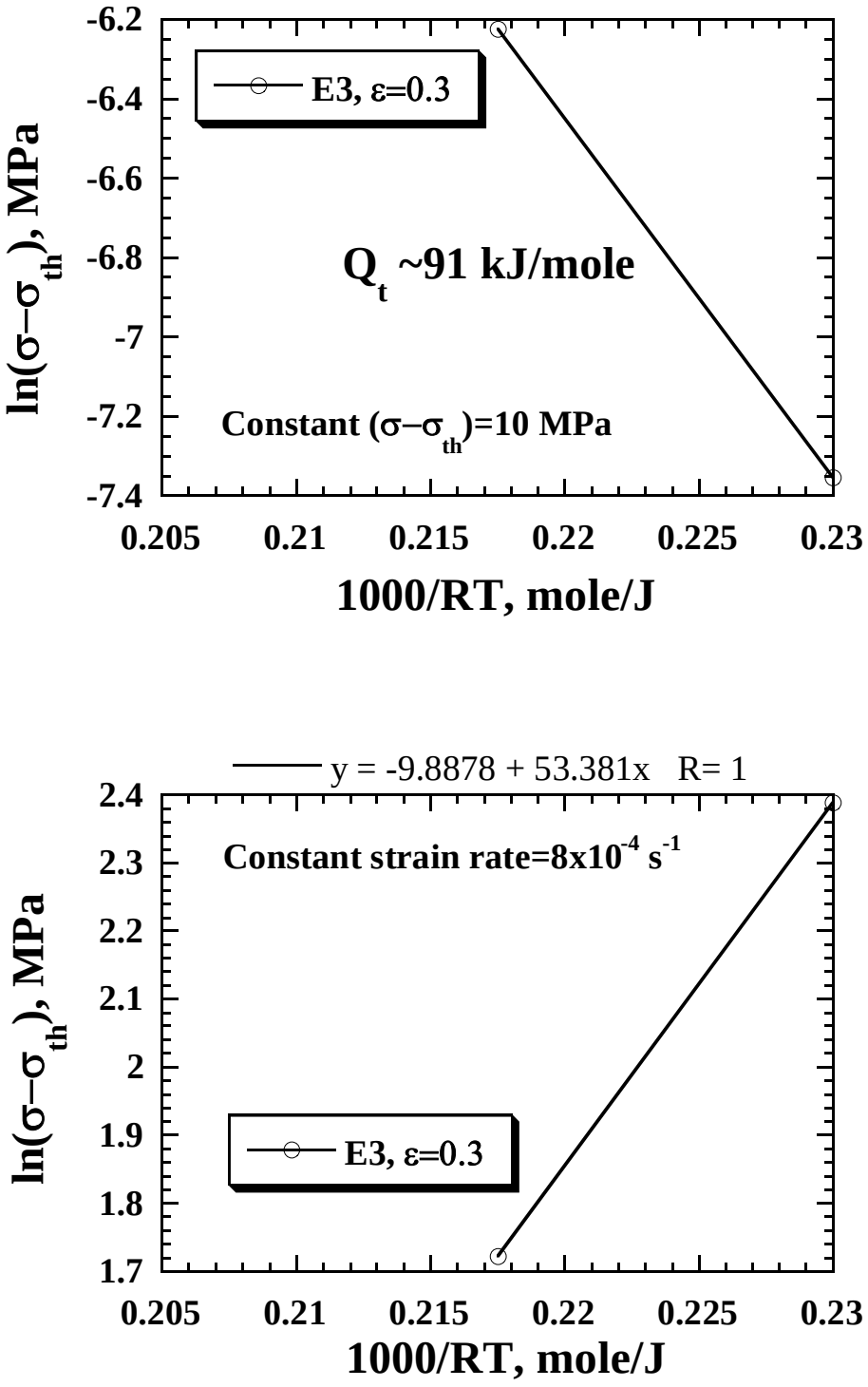

Fig. 4-9 True activation energy for the E3 specimen using the true stress exponent n_t of 2.

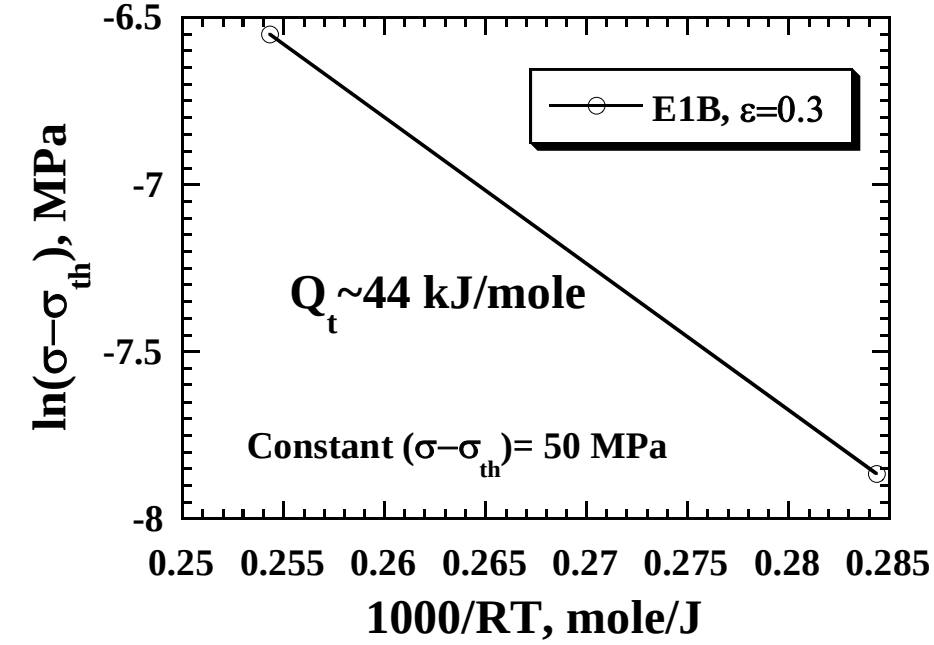

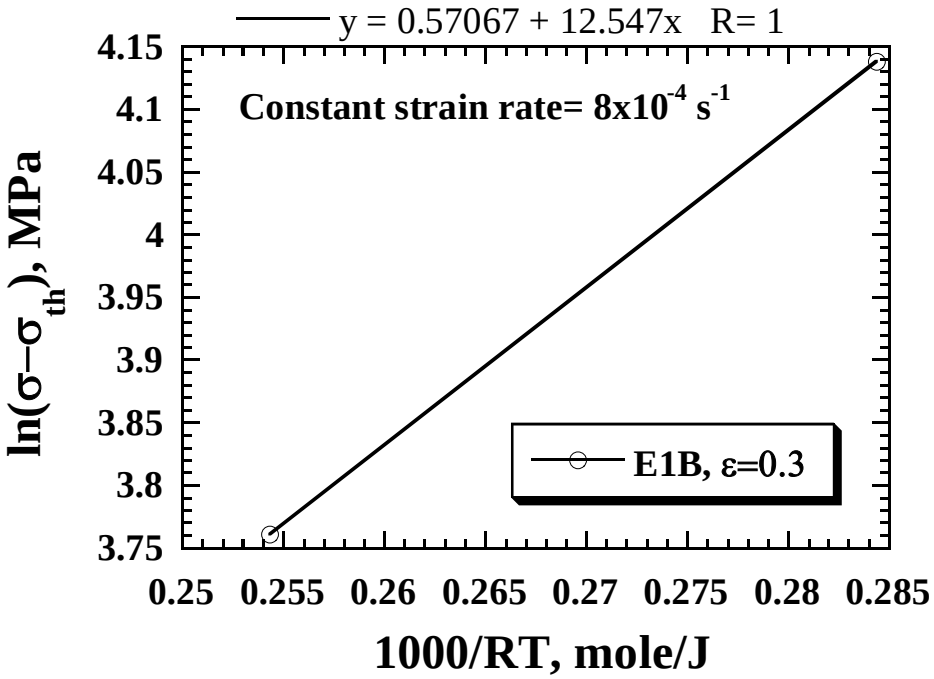

Fig. 4-10 True activation energy for the E1B specimen.

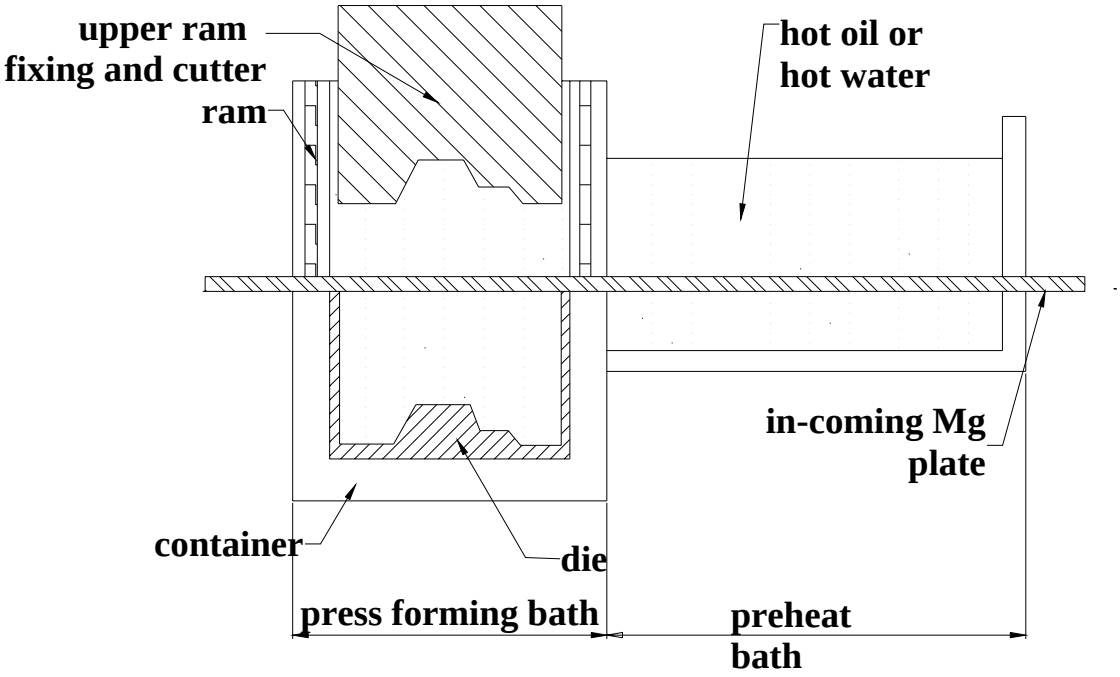

Fig. 4-11 Design of the continuous press forming using heated oil or water bath.

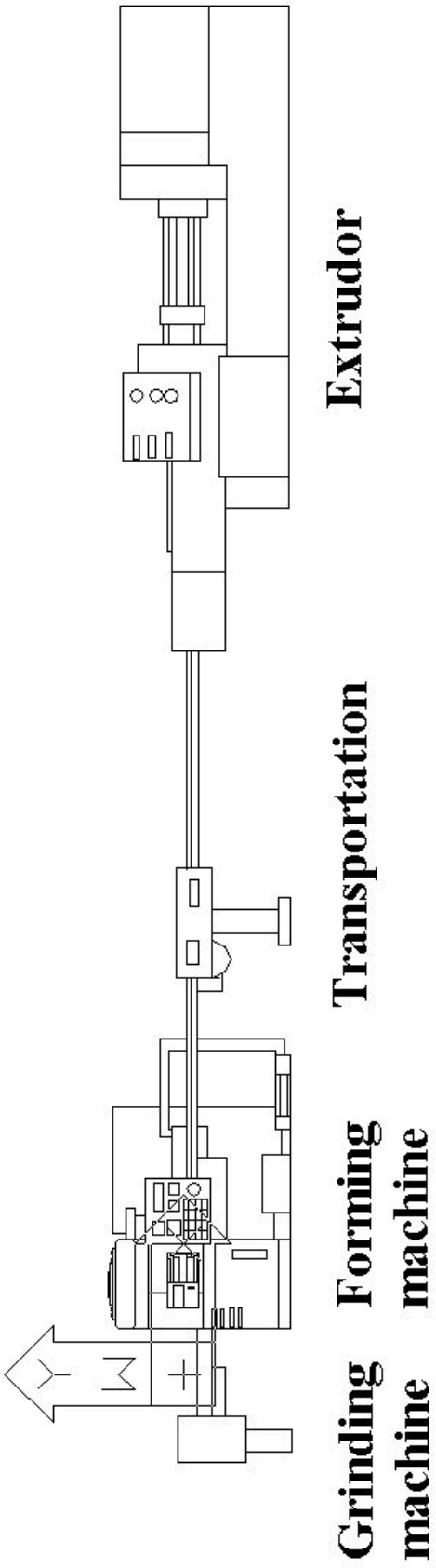

Fig. 4-12 Illustration of continuous industrial system.

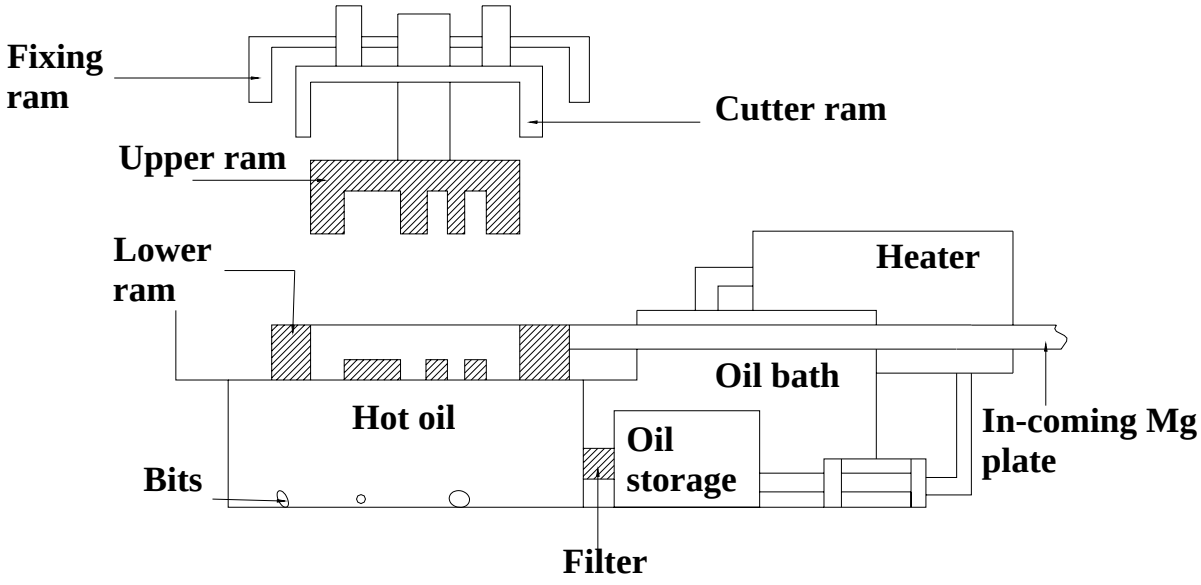

Fig. 4-13 Detailed design of the forming machine.